Cranfield University

Jude Worthy

Large Eddy Simulation Of Buoyant Plumes

School of Mechanical Engineering

PhD

Cranfield University

School of Mechanical Engineering

PhD Thesis
Academic Year 2002-2003

Jude Worthy

Large Eddy Simulation Of Buoyant Plumes

Supervisor
Dr. P. Rubini

May 2003

This thesis is submitted in partial fulfilment of the requirements
for the
Degree of Doctor of Philosophy

©Cranfield University, 2003. All rights reserved. No part of this publication may be reproduced without the written permission of the copyright holder.

Abstract

A 3d parallel CFD code is written to investigate the characteristics of and differences between Large Eddy Simulation (LES) models in the context of simulating a thermal buoyant plume. An efficient multigrid scheme is incorporated to solve the Poisson equation, resulting from the fractional step, projection method used to solve the Low Mach Number (LMN) Navier-Stokes equations.

A wide range of LES models are implemented, including a variety of eddy models, structure models, mixed models and dynamic models, for both the momentum stresses and the temperature fluxes. Generalised gradient flux models are adapted from their RANS counterparts, and also tested.

A number of characteristics are observed in the LES models relating to the thermal plume simulation in particular and turbulence in general. Effects on transition, dissipation, backscatter, equation balances, intermittency and energy spectra are all considered, as are the impact of the governing equations, the discretisation scheme, and the effect of grid coarsening. Also characteristics to particular models are considered, including the subgrid kinetic energy for the one-equation models, and constant histories for dynamic models.

The argument that choice of LES model is unimportant is shown to be incorrect as a general statement, and a recommendation for when the models are best used is given.

Acknowledgements

My thanks go firstly to Phil for quite probably being the best supervisor in the world, whose time, advice, and help have been essential and have been available on tap throughout the, ahem, three years. I'm very grateful.

Next to my parents who have been wonderful throughout the process, and whose encouragement, support, and faith, especially towards the end meant a very great deal to me. It would have been much harder without you.

Also to my brother, not only for the support, but whose fantastic handiwork can be seen in these pages in some of the early figures (note to examiners – not the results).

Lastly to the chaps and chapesses in the office, the department, and the CSA, who have become friends and who have made life that bit spicier.

Contents

List of Figures

List of Tables

Nomenclature

B	buoyancy term
c	constant
C	constant
C_p	coefficient of volumetric expansion at constant pressure
DF	diffusion term
DP	dissipation term
E	energy spectrum
F	structure function
i	internal energy, $\sqrt{-1}$
k	thermal conductivity
kc1	dissipation constant
kc2	diffusion constant
l	length scale
L	length scale
P	pressure, turbulent energy production term
q_j	subgrid flux
R	correlation term, convection/diffusion/source sum
t	time
T	temperature
T_{ij}	test-filter scale stress
u	velocity
U	velocity length scale, mean X-axis velocity
V	velocity length scale, mean Y-axis velocity
W	mean Z-axis velocity
X	horizontal Cartesian axis
Y	vertical Cartesian axis
Z	horizontal Cartesian axis

Greek Letters

a	thermal conductivity
b	coefficient of thermal expansion
d_{ij}	Kronecker delta
Δ	filter width, grid width
e	temperature difference, dissipation term
f	molecular stress term
Φ	spectrum function
h	Kolmogorov length scale
k	wavenumber
l	Taylor length scale
m	viscosity
Π	reduced pressure term
r	density
t_{ij}	stress tensor
u	kinematic viscosity

Symbols

$\Im$	Fourier transform
det	determinant

Subscripts

$X_i / X_j / X_k$	components to be summed over i/j/k dimensions
X_a	ambient value
X_0	initial / input value
X_t	turbulent value – turbulent Prandtl number or turbulent viscosity

X_b	Boussinesq
X_h	Kolmogorov
X_{ke}	kinetic energy term
X_{fke}	filtered kinetic energy term
X_{tke}	turbulent kinetic energy term
X_{ske}	subgrid kinetic energy term

Superscripts

$\overline{X}$	filtered variable with arbitrary filter
$\hat{X}$	filtered variable with arbitrary filter
$\ddot{X}$	filtered variable with arbitrary filter
$\dot{X}$	filtered variable with arbitrary filter
$\tilde{X}$	estimated variable, Favre-filtered variable with arbitrary filter
X'	fluctuating component of filtered variable

Abbreviations and Acronyms

BSmag	Buoyancy-modified Smagorinsky
CFD	Computational Fluid Dynamics
Dmixed	Dynamic mixed model
DNS	Direct numerical simulation
FKE	Filtered kinetic energy
GGDH	Generalised gradient diffusion hypothesis
KE	Kinetic energy
LDM	Localised Dynamic Model
LES	Large eddy simulation
LMN	Low Mach number
One Eq	One Equation
RANS	Reynolds-averaged Navier-Stokes

SGDH	Standard gradient diffusion hypothesis
SKE	Subgrid kinetic energy
Smag	Smagorinsky
TKE	Turbulent kinetic energy
TVD	Total-variation diminishing
URANS	Unsteady Reynolds-averaged Navier-Stokes
VLES	Very large eddy simulation

Chapter 1

Introduction

Computational Fluid Dynamics (CFD) has become a very important tool to engineers, scientists, environmentalists, and to industry. The power and potential of the subject is growing very rapidly both with the advancement of computer technology and with theoretical development. As the governing equations of fluid motion are not amenable to analytic solutions in almost all practical situations, due to complex boundary conditions, geometric or otherwise, the numerical techniques of CFD are required to predict the flow. A wide area of interrelated topics is covered by CFD. Currently, significant developments are underway in turbulence modelling, high order numerical schemes, parallel algorithms, boundary conditions, adaptive grids and reacting flows. Turbulent flows in particular can require enormous computational resources, well beyond the power even of modern day computers, and require a 'simplification' of the flow in order to make simulations feasible. This is achieved with turbulence modelling, which is the focus of this thesis. The first four major areas of research just mentioned are also encountered and constitute a significant part of the work.

One way that CFD can be classified is into the following three groupings – direct numerical simulation (DNS), large eddy simulation (LES) and Reynolds-averaged methods (RANS). The DNS often refers to turbulent simulations in which all the scales of motion are fully captured, both in time and in space. The latter two refer to the type of turbulence models which are incorporated into the governing equations.

RANS models, the first turbulence models to be developed, solve for a steady state average of the flow domain, greatly reducing the amount of information obtained, and hence computational cost, of the simulation. It is the low computational cost which allowed them to be developed first. A great deal of work has gone into the development of these models, and there are widely varying levels of complexity in the approach. LES modelling, a technique originating in meteorological research, is often

described as somewhere between RANS and DNS, although in fact it is much closer to DNS, due to its unsteady nature. The important large scales are fully resolved and the small subgrid scales, which the grid cannot capture, are modelled.

In some ways, accurate RANS modelling is far more important than LES modelling. The form of the equations are equivalent, both generating the extra terms from the filtering of the convection term – the Reynolds stresses and the subgrid stresses respectively, but the magnitudes of the Reynolds stresses are much higher than the corresponding subgrid stresses. However, the LES models do have a significant impact on the resulting large-scale motions, and still must behave suitably accurately. LES is a much more recent development than RANS modelling and although there is already a great deal of research into it, there is a lot more to be done before it becomes as widespread or acceptable as a practical tool as the RANS methods have.

There is inevitably a grey area in this classification. This comes in the form of Very Large Eddy Simulation (VLES) and Unsteady Reynolds-Averaged Navier-Stokes (URANS) models. The names are self-explanatory. Although a clear distinction is drawn between the two in their formulation, their respective limitations and benefits are unclear. In his review of these methods, Speziale (1997) argues that LES is still usually impossible and that only VLES or URANS are currently plausible. Spalart (2000) goes further, and argues that only URANS should be used at this stage, although it is the author's view that either LES or VLES should be used for any unsteady flow. In VLES, the modelling assumptions break down, but the models are still suited to unsteady flow, whereas the RANS models are designed for steady state flow – there is not a time-step scaling factor in any of the usual RANS models, which is necessary in the limit as the time-step tends to zero.

LES in particular constitutes the work of this thesis, although VLES is touched upon. RANS is important to gauge the success of LES models. Typically, LES models are much more time consuming, and are therefore deemed a bad model if the same information can be extracted at far less cost from RANS modelling. However, RANS modelling is restricted by the need for empirical constants, which the recently developed dynamic LES models eradicate altogether allowing much wider applicability of the models (although unsteady modelling is intrinsically more widely applicable anyway, due to the greater amount of information explicitly captured).

Piomelli (1999) outlines the challenges and objectives for LES modelling. These are to predict dissipation correctly, including a vanishing model in laminar flow, for the

model to be explicit, relying only on local information, and to accurately predict the energy transfer between the subgrid and grid scales. With these qualities intact the capturing of accurate large-scale motions should be achievable.

A number of models have been developed since Smagorinsky's (1963) original model, although in practical simulations it is still the most widely used. The early 90's introduced dynamic modelling, and this procedure has and will continue to have a very significant impact on the area. It is likely that this procedure in conjunction with the Smagorinsky model will become the next model as ubiquitously used for LES as the k-ε model is for RANS. However, there are significant problems with it, and although attempts have been made to address these, through extensions of the model and alternatives to the model, some are still unresolved and need to be explored. LES models are almost universally developed in the context of incompressible flows, and the turbulent channel flow is a favoured test case. However, most newly developed models compare themselves either with the Smagorinsky model or the dynamic Smagorinsky model, but not with any of the other models. A comprehensive review of the models in incompressible flow would be very useful in its own right. There is even less data concerning the models in buoyant flows. An understanding of the models in buoyant flows, through testing and comparison is necessary work, and the work of this thesis. This aspect is very similar in spirit to the work of Bastiaans et al. (2000).

It is often thought (for the reason explained above), that the accuracy of the LES model is not too important since most information is contained in the filtered scales. This implies that the choice of model is not important. It is clear that the more resolved the grid, the less significant the model becomes. On the other hand, the purpose of CFD is to give the most information with a minimum of work. It is to be expected that the coarser the grid is, the more important the subgrid model becomes, and that the more important the subgrid model becomes, the more important it becomes that the subgrid model is accurate. On relatively coarse (but suitable for LES) grids, significant differences of the models should be appreciable.

1.1 Objectives and Achievements

The objectives of this work were to develop a 3d CFD code, using state of the art numerical and computational techniques, on which to implement and investigate a wide range of the most promising and the most well-known LES models in buoyant flow simulations. The relative merits and limitations were to be assessed, and the characteristics of individual models to be considered, in conjunction with practical CFD hazards.

This work needed to be done, and a continuous process needs to be maintained, to find which models are the most effective, the most efficient, and to find areas of weakness which need to be strengthened, and to note the areas of strength which can be exploited.

These objectives are largely met. A 3d parallel CFD code has been written, solving the low Mach number (LMN) equations with a recent projection method (Najm et al., 1998), using advanced multigrid techniques for acceleration. All the most important models have been implemented and tested, with only one exception, and a superior RANS flux model, the generalised gradient diffusion model (GGDH, Daly and Harlow, 1970) has been successfully altered, implemented, and tested, and is shown to be a good alternative to the ubiquitously used standard gradient diffusion model (SGDH).

The buoyant plume was chosen as the turbulent test flow, incorporating turbulent boundary conditions, laminar flow and transition, and non-Boussinesq parameters. It provides a flow on which all of the important LES model characteristics can be observed.

Various simulations have been carried out with the different models; comparisons are made and the characteristics of the models are explored. The main LES qualities are considered – dissipation, laminar flow (and intermittency), and backscatter. Further issues are also investigated and considered including energy spectra, equation balances, Reynolds stresses, discretisations, governing equations, as well as computational and numerical effects. The impact of the models on the transition point is a major factor in the discussion and conclusions.

1.2 Code Development

A great deal of time has been devoted to the development of the code with which the LES model testing can be achieved. This development process produced a number of different codes, which eventually resulted in a single code sufficient for the task at hand. The initial idea was for a structured non-uniform (stretched in each axis) 3d parallel LES code, using multigrid acceleration for the Poisson solver. After rash initial attempts to write the final code from scratch, a more tempered approach was taken. The Poisson solvers were always developed separately, and integrated in to the main code afterwards. A scalar uniform 2d Boussinesq equation code with multigrid Poisson solver was written. Following this the 3d non-uniform parallel multigrid Poisson solver was written. Bad convergence was found on Neumann boundary conditions. Nevertheless, this was implemented into the correspondingly written 3d parallel non-uniform Boussinesq code. The process of debugging, speeding up the solution on Neumann conditions, and extending the main code to the low Mach number (LMN) equations continued for some time, with apparently successful simulations eventually crashing, and the LMN part of the code not working at all. Considerations of greater efficiency and scalability of a code if a new multigrid Poisson solver was written led to an alternative uniform formulation of the multigrid Poisson which worked on an even number of grid nodes (the previous worked on an odd number). A new main code was written for the new multigrid code, using a stable scheme for LMN equations reported in the literature, Najm et al. (1998). This code, whilst algorithmically more efficient, turned out to be less computationally efficient due to the use of modules rather than automatic arrays, although the Poisson Neumann boundary conditions were resolved. Coarse grids made central schemes and even upwind schemes in the temperature equation unstable, and TVD schemes had to be introduced. In the process of debugging the original code was updated to include the LMN solver and also to resolve the Neumann boundary condition issue on the Poisson solver. It was also reduced to a uniform grid in this process, and ended up being the first of the fully debugged codes, and is consequently the one used. The various LES models were then implemented into the code.

1.3 Thesis Structure

It is desirable to present a fully sequential text, with everything following from what has gone before. However, with a number of aspects overlapping and referring to one another in their own development there is necessarily a certain amount of forward referencing. The structure attempts to keep this to a minimum.

The first half of the thesis is broken up as follows. Chapter 2 presents the governing equations, from the compressible Navier-Stokes equations to the Low Mach number (LMN) equations to the incompressible Boussinesq equations for completeness, followed by the introduction to and the formalism of large eddy simulation. Chapter 3 briefly provides the basic background turbulence theory required to understand the LES models and their derivation. The introduction to Fourier space and the energy spectrum is a critical part of the analysis of turbulence and LES models. The LES models are given in chapter 4, after the presentation of the transport equations of various levels of kinetic energy – kinetic energy, grid-scale energy, subgrid-scale energy, and turbulent kinetic energy, which provide insight into the behaviour of the scales of motion. The models investigated are given in detail, and a review of their applications is given towards the end of the chapter.

Chapter 5 presents the numerical methods involved in this work, and some particular coding details, including issues of parallelism. Although the latter are not directly relevant to the LES model results presented, these issues represent a considerable amount of work, and are pertinent to anyone embarking on work in the field. A further review of LES simulations is given.

The second half of the thesis presents the results of the simulations. Chapter 6 gives validation of the code and of the LES models on laminar plumes, and follows this through with a discussion and presentation of the issues involved in the turbulent simulations. The final chapters give the full results. Chapter 7 gives the static model simulation results, and chapter 8 presents the dynamic model results. Chapter 9 considers further relevant issues through further simulations. A summary and discussion of the conclusions is given in chapter 10, finished with a discussion of future work.

This is illustrated in fig. 1.1 below.

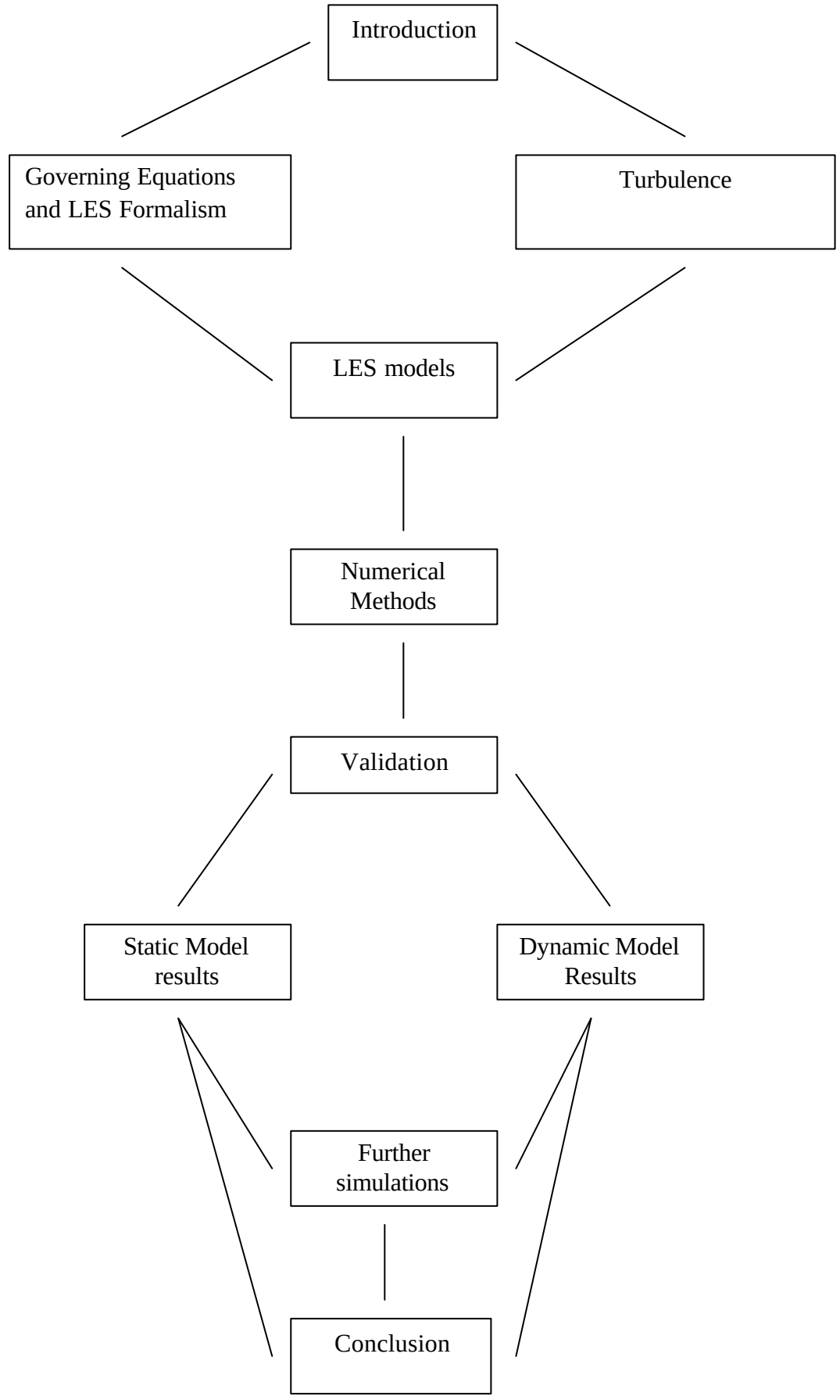

Figure 1.1 Thesis structure flow chart.

Chapter 2

Governing Equations and LES Formalism

2.1 Introduction

This chapter introduces the governing equations, shows how to form the LES equations with the filtering process which defines turbulence modelling in general, and considers the formalism issues which are associated. These are given for both the incompressible equations and the Low Mach number (LMN) equations. Some plume simulations (for example Webb and Mansour, 2000) use the Boussinesq equations where the assumptions do not hold, i.e. the density variation is not small, and the effect is considered.

2.2 Navier-Stokes Equations

Although the incompressible Navier-Stokes equations were historically developed first, it makes more sense to start from the fully compressible equations and reduce them. The dimensional compressible Navier-Stokes equations (comprising the continuity equation, momentum equations, internal energy equation, and equation of state) are given by the following, a good derivation of which is provided in Versteeg & Malalasekera (1995). These govern an ideal single component fluid for all speeds, allowing shock waves, and are hence discontinuous. These are (should be) the starting point for all other single component fluid equations, which are some sort of reduction of these[1]

[1] Of course there are numerous different formulations, but these are typically as general as they get. The only frequently used source term not included is the Coriolis term, in meteorology generated by the rotation of the earth.

$$\frac{\partial r}{\partial t}+\frac{\partial r u_i}{\partial x_i}=0 \tag{2.1}$$

$$\frac{\partial r u_i}{\partial t}+\frac{\partial r u_i u_j}{\partial x_j}=-\frac{\partial P}{\partial x_i}+\frac{\partial j_{ij}}{\partial x_j}+r g_i \tag{2.2}$$

$$\frac{\partial i}{\partial t}+\frac{\partial u_j i}{\partial x_j}=\frac{k}{r}\frac{\partial^2 T}{\partial x_j^2}-\frac{P}{r}\frac{\partial u_i}{\partial x_j}+2u(e_{ij}e_{ij}-\tfrac{1}{3}e_{ii}e_{jj}) \tag{2.3}$$

$$P=rRT \tag{2.4}$$

$$j_{ij}=2me_{ij}-\frac{2}{3}d_{ij}me_{kk}\,. \tag{2.5}$$

$$e_{ij}=\tfrac{1}{2}\left(\frac{\partial u_i}{\partial x_j}+\frac{\partial u_j}{\partial x_i}\right) \tag{2.6}$$

Equation 2.5 is Stokes Hypothesis. The second term is included due to the requirement that the normal stresses sum to zero.

The dimensional Low Mach number Navier-Stokes (LMN) equations follow. Rehm and Baum (1978) developed the equations initially for fire simulations. Later, Paulucci (1982) derived similar equations completely and formally, through the Taylor expansion of the (non-dimensionalised) compressible N-S variables in terms of the Mach number. The energy equation is reformulated as a temperature equation before the expansion using the following assumption for ideal liquid and gases.

$i=C_pT$, where C_p is constant.

$$\frac{\partial r}{\partial t}+\frac{\partial r u_i}{\partial x_i}=0 \tag{2.7}$$

$$\frac{\partial r u_i}{\partial t}+\frac{\partial r u_i u_j}{\partial x_j}=-\frac{\partial \Pi}{\partial x_i}+\frac{\partial j_{ij}}{\partial x_j}+(r-r_a)g_i \tag{2.8}$$

$$\frac{\partial T}{\partial t}+u_j\frac{\partial T}{\partial x_j}=\frac{k}{rc_p}\frac{\partial^2 T}{\partial x_j^2} \tag{2.9}$$

$$rT=r_aT_a \tag{2.10}$$

$$\Pi=P-P_a+r_ag_i \tag{2.11}$$

Π, given by 2.11, is the reduced pressure, representing only the dynamic pressure and the hydrostatic buoyancy term. A consequence of the Taylor expansion is that the static pressure does not vary spatially, taking it out of the momentum equations and the equation of state. The inclusion of the hydrostatic pressure in the reduced pressure is numerically beneficial.

The temperature equation is considerably simplified. The last term in equation 2.3, as well as the spatial derivatives of pressure, goes to zero. A time derivative for pressure does remain, but this is also zero so long as any heat introduced can escape from the domain. The term is unnecessary for an open plume.

The reduced pressure term is elliptic, which can be interpreted as pressure waves travelling at infinite speed.

Equation 2.9 is a transport equation for temperature rather than the internal energy or enthalpy. This is a non-conservative formulation, but is a good approximation for the flows considered. This is akin to the incompressible equations below and is the form solved in this work.

The dimensional incompressible Navier-Stokes equations, with the buoyancy term added are the Oberbeck-Boussinesq equations (Paulucci,1982), but are more often just referred to as the Boussinesq equations. The Boussinesq assumption is that the variation in the density is slight enough as to be insignificant in all terms apart from the buoyancy force. This obviously limits the temperature difference that can be correctly described by the equations. Contrary to intuition, up to 15% change in temperature in air, and up to 2% change in water results in less than 1% error in the flow field (Ferziger and Peric, 1999). However, these equations take out the difficulty of the time derivative in the continuity equation. Natural convection ventilation is a good example of the utility of these equations. There are interesting applications where the error in the approximation is limited to only a tiny part of the domain. The turbulent plume is one. The effect of the error of the approximation on the rest of the flow domain is sometimes ignored but is not well understood.

$$\frac{\partial u_i}{\partial x_i} = 0 \qquad (2.12)$$

$$\frac{\partial u_i}{\partial t} + u_j \frac{\partial u_i}{\partial x_j} = -\frac{1}{r_a}\frac{\partial \Pi}{\partial x_i} + u\frac{\partial^2 u_i}{\partial x_j^{\,2}} + r_b g_i \qquad (2.13)$$

$$\frac{\partial T}{\partial t} + u_j \frac{\partial T}{\partial x_j} = \frac{k}{r c_p}\frac{\partial^2 T}{\partial x_j^{\,2}} \qquad (2.14)$$

$$r_b = -\frac{T - T_a}{T} \qquad (2.15)$$

$$r_b = -b(T - T_a) \qquad (2.16)$$

Equation 2.15 is for gases, 2.16 for liquids.

2.3 Non-Dimensionalisation

Typically, the equations are non-dimensionalised. With buoyant flows, there are a number of useful approaches. Using constants taken from the simulation in which L is a length scale and U is a velocity scale, (for example these respectively are the inlet diameter and inlet velocity typically for a jet flow), let

$$x_i^{\,*} = Lx_i \;\; ; \;\; t^* = \frac{L}{U}t \;\; ; \;\; u_i^{\,*} = Uu_i \;\; ; \;\; T^* = T_0 T \;\; ; \;\; r^* = r_0 r \;\; ; \;\; g_i^{\,*} = g_0 g_i$$

$$\Pi^* = r_0 U^2 \Pi$$

m, the viscosity, k, the thermal conductivity, c_p, the specific heat at constant pressure, and g_0, the gravity modulus, are considered constant parameters. The following non-dimensional parameters are defined.

$\mathrm{Re} = \dfrac{r_0 UL}{m}$; Reynolds number

$\mathrm{Pr} = \dfrac{u}{a_0}$; Prandtl number

$Fr = \dfrac{U^2}{gL}$; Froude number

$Gr = \dfrac{bg\Delta TL^3}{u^2}$; Grashof number

$Ra = \frac{gL^3 e}{u a_0}$; Rayleigh number

$a = k / rc_p$ is the thermal diffusivity, $e = \frac{\Delta T}{T_0}$ is the temperature difference, and $b = \frac{1}{r}\frac{\partial r}{\partial T}$ is the coefficient of thermal expansion.

Then this results in, for the LMN equations solved in this work:

$$\frac{\partial r}{\partial t} + \frac{\partial r u_i}{\partial x_i} = 0 \tag{2.17}$$

$$\frac{\partial r u_i}{\partial t} + \frac{\partial r u_i u_j}{\partial x_j} = -\frac{\partial \Pi}{\partial x_i} + \frac{1}{\mathrm{Re}}\frac{\partial s_{ij_i}}{\partial x_j} + B \tag{2.18}$$

$$\frac{\partial T}{\partial t} + u_j \frac{\partial T}{\partial x_j} = \frac{1}{r}\frac{1}{\mathrm{Re}\,\mathrm{Pr}}\frac{\partial^2 T}{\partial x_j^{\,2}} \tag{2.19}$$

$$rT = 1 \tag{2.20}$$

$$B = \frac{1}{Fr}(r - 1) g_i , \tag{2.21a}$$

$$\text{or } B = \frac{Gr}{\mathrm{Re}^2 b\Delta T}(r - 1) g_i , \tag{2.21b}$$

$$\text{or } B = \frac{\mathrm{Pr}\, Ra}{e}(r - 1) g_i . \tag{2.21c}$$

The Rayleigh number formulation requires the extra condition $U = a_0 / L$. Then $1/\mathrm{Re} = \mathrm{Pr}$ further simplifying the equations. Different authors use different formulations.
The Grashof formulation is usually used with liquids.

For the incompressible equations the results are equivalent.

2.4 Large Eddy Simulation

DNS simulations of high Reynolds number flows are well known to require vast grids, requiring vast resources beyond the capability of modern machines, although Friedrich et al. (2001) give a review of the recent successes in flows of practical interest at moderate Reynolds numbers. This is due to the amount of detail incorporated in the rapidly varying (spatially and temporally) turbulent field of motion. The main idea behind LES is to filter out the fine or high frequency scales of motion and leave the large scales to be solved directly. The small scales of turbulence are assumed to be isotropic. The effect of the subgrid scales is then modelled based on turbulence theory.

Smagorinsky (1963), Lilly (1962,1967), and Deardorff (1970) were the first to develop and utilise LES models. Leonard (1974) introduced the formalism of the filter function as it is used today, which Ferziger (1977) reviews. Germano (1992) gives the most complete account of filtering, generalising the filter to include the time dimension. This puts LES and RANS on the same footing, with the former using a spatial filter, the latter a temporal filter. Recent developments (Carati and Wray, 2000) explore the conjunction of the use of fully four-dimensional filters.

2.4.1 Definitions

An exact definition of LES is as elusive as one for turbulence in general, but here are three perspectives (these are not the respective authors views, but views that they have presented).
A large eddy simulation is one in which

1. 80% of the dynamic energy is resolved accurately (Pope, 2000).
2. The scales of motion resolved are at most of the order of the Taylor microscale (Ferziger, 1977).
3. The subgrid scales are within the inertial subrange (Ferziger, 1977).

These are very similar, each providing a notion of the length scales to be fully resolved. This reflects the maximum scale at which the turbulence is assumed to be isotropic, and amenable to general modelling.

2.5 Filtering

The filtering process is the essence of turbulence modelling, both for RANS and LES. The damping of the high frequency oscillations, either temporal or spatial, occurs by integrating the terms of the Navier-Stokes with a filter function.

The LES filter is formally defined:

$$\bar{f}(x_i - x_i', t) = \int_{-\infty}^{\infty}\int_{-\infty}^{\infty}\int_{-\infty}^{\infty} G(x_i - x_i', t) f(x_i - x_i', t)\partial x_i', \tag{2.22}$$

with $\int_{-\infty}^{\infty}\int_{-\infty}^{\infty}\int_{-\infty}^{\infty} G(x_i - x_i', t)\partial x_i' = 1$, (2.23)

where G is the filter function.

With the filter defined, we can define the 'fluctuating' component, form the instantaneous variable and its filtered counterpart.

$$f' = f - \bar{f} \tag{2.24}$$

The name stems from the RANS formulation, where the filter gives the mean velocity, which does not fluctuate. In LES, the filtered component is an instantaneous value that also fluctuates in time (and space depending on the filter), which is slightly misleading.

The filter is required to have a number of properties, which are required for the manipulation of the governing equations to arrive at the filtered governing equations.

$\overline{f + g} = \bar{f} + \bar{g}$

$\overline{af} = a\bar{f}$, a is a scalar.

$\overline{f_{,t}} = \bar{f}_{,t}$

2.5.1 Filters

The most frequently used are the box, Gaussian, and cutoff filters.

$$G(box) = \begin{cases} 1/\Delta^3 & -\Delta/2 \le (x_i - x_i') \le \Delta/2 \\ 0 & otherwise \end{cases} \tag{2.25}$$

$$G(Gaussian) = \frac{\exp(-|x_i - x_i'|^2 / s^2)}{(s\sqrt{p})^3} \tag{2.26}$$

$$G(cutoff) = \begin{cases} 1 & |k| \le k_c \\ 0 & otherwise \end{cases} \tag{2.27}$$

The box or top hat filter is described in physical space. This is the most natural filter to use with a finite difference or finite volume scheme, since the filtered quantity is just the average quantity in the cell when the filter width is equal to the cell width.

The Gaussian is also described in physical space but is used in spectral space also.

The cutoff filter is described in spectral space. Most LES models are based on analyses using this filter.

All numerical schemes provide an additional unspecified implicit filter which are dependent on the scheme. These act as a varying cutoff filter dependent on grid width and time scale. This is a useful occurrence given the lack of models developed with the top-hat filter in mind.

These filters are not commutative under differentiation when a non-uniform grid is used on an inhomogeneous flow domain (Ghosal, 1999). This can be a significant problem, introducing errors of $O(\Delta^2)$, which has only recently started to be explored again (Ghosal, 1996). Van der Ven (1994) gives a family of suitably commutative filters, as does Valsilyev (1998 – referenced in Ghosal 1999).

The significance of using different filters is largely unexplored in practical simulations, although Germano (1992) believes them to lead to similar results. Salvetti and Beaux (1998) have gone some way to showing different results with different filters. Pope (2000) quotes a significant difference between spectral space filters. To maintain 80% of the turbulent kinetic energy the Gaussian filter requires a filter width 2/3 the length of the filter width required by the cutoff filter.

2.6 Filtered Navier-Stokes Equations

The filtered Boussinesq equations with the Froude number non-dimensionalisation are given by the following.

$$\frac{\partial \overline{u}_j}{\partial x_j} = 0 \tag{2.28}$$

$$\frac{\partial \overline{u}_i}{\partial t} + \frac{\partial \overline{u}_i \overline{u}_j}{\partial x_j} = -\frac{1}{r_a}\frac{\partial \overline{\Pi}}{\partial x_i} + \frac{1}{\mathrm{Re}}\frac{\partial^2 \overline{u}_i}{\partial x_j^{\,2}} + \frac{1}{Fr}\overline{r}_b g_i - \frac{\partial t_{ij}}{\partial x_j} \tag{2.29}$$

$$\frac{\partial \overline{T}}{\partial t} + \overline{u}_j \frac{\partial \overline{T}}{\partial x_j} = \frac{1}{\mathrm{Re}\,\mathrm{Pr}}\frac{\partial^2 \overline{T}}{\partial x_j^{\,2}} - \frac{\partial q}{\partial x_j} \tag{2.30}$$

$$\overline{r}_b = 1 - \frac{1}{\tilde{T}} \tag{2.31}$$

This gives the turbulent stresses or subgrid terms in the momentum equation, and the subgrid temperature fluxes.

$$t_{ij} = \overline{u_i u_j} - \overline{u}_i \overline{u}_j \tag{2.32}$$

$$q_j = \overline{u_j T} - \overline{u}_j \overline{T}\,. \tag{2.33}$$

It is these terms that are the prime focus of LES modelling and where the vast majority of research has focused. The distinction is made here, with the Boussinesq formulation since these are essentially identical to the incompressible equations (i.e. only the addition of the buoyancy term and temperature equation), since almost all fundamental turbulence research not concerned with high speed flows attempts to solve these equations.

Note that the Favre average is required for the Boussinesq relation, defined by the following, since the density is multiplied with the temperature (2.31 comes from 2.20).

$$\tilde{f} = \frac{\overline{rf}}{\overline{r}} \tag{2.34}$$

It is necessary due to the fact that, for a general filter $\overline{\frac{1}{f}} \neq \frac{1}{\bar{f}}$.

We make the assumption that *the density varies slowly through space* and then can approximate $\bar{f} = \tilde{f}$. This term is then consistent.

The Favre averaging and the previous approximation are used in attaining the filtered LMN equations, which are as follows:

$$\frac{\partial \overline{r}}{\partial t} + \frac{\partial \overline{r}\tilde{u}_i}{\partial x_i} = 0 \tag{2.34}$$

$$\frac{\partial \overline{r}\tilde{u}_i}{\partial t} + \frac{\partial \overline{r}\tilde{u}_i\tilde{u}_j}{\partial x_j} = -\frac{\partial \overline{\Pi}}{\partial x_i} + \frac{1}{\mathrm{Re}}\frac{\partial^2 \tilde{u}_i}{\partial x_j^{\,2}} + \frac{1}{Fr}(\overline{r} - 1)g_i - \frac{\partial \overline{r}\, t_{ij}}{\partial x_j} \tag{2.35}$$

$$\frac{\partial \tilde{T}}{\partial t} + \tilde{u}_j\frac{\partial \tilde{T}}{\partial x_j} = \frac{1}{\overline{r}}\frac{1}{\mathrm{Re}\,\mathrm{Pr}}\frac{\partial^2 \tilde{T}}{\partial x_j^{\,2}} - \frac{\partial q_j}{\partial x_j} \tag{2.36}$$

$$\overline{r}\tilde{T} = 1 \tag{2.37}$$

These subgrid terms in the momentum equations differ from before in that they contain density terms. (The double bar represents the Favre average also)

$$t_{ij} = \overline{\overline{u_i u_j}} - \tilde{u}_i\tilde{u}_j \tag{2.38}$$

$$q_j = \overline{\overline{u_j T}} - \tilde{u}_j\tilde{T} \tag{2.39}$$

2.6 Subgrid Decomposition

A significant difference between RANS and LES is the decomposition of the spatially filtered or time averaged convection term. Leonard (1977) formalised the following split. Regardless of the filtering type, the subgrid scale term can be found and decomposed into the following parts, through the filtering of the non-linear

convection term. By splitting the velocities (and/or scalar if appropriate) into their grid scale and subgrid scale components it can be seen that:

$$\overline{u_i u_j} = \overline{\bar{u}_i \bar{u}_j} + \overline{u_i' \bar{u}_j} + \overline{\bar{u}_i u_j'} + \overline{u_i' u_j'} \tag{2.39}$$

Substituting 2.39 into 2.32 gives

$$t_{ij} = \overline{u_i u_j} - \bar{u}_i \bar{u}_j \tag{2.40}$$

$$= \overline{\bar{u}_i \bar{u}_j} - \bar{u}_i \bar{u}_j \quad \text{Leonard term} \tag{2.41}$$

$$+ \overline{u_i' \bar{u}_j} + \overline{\bar{u}_i u_j'} \quad \text{Cross term} \tag{2.42}$$

$$+ \overline{u_i' u_j'} \quad \text{Reynolds term} \tag{2.43}$$

In RANS modelling, the Leonard and Cross terms go to zero. This is in general the case for LES, although using the cutoff filter in spectral space results in only the Reynolds term. The top hat filter does not have this property, but effectively does when the filter width is equal to the cell spacing[2], which can cause numerical complications. The decomposition affects the derivation of the turbulent kinetic energy equations. Many modelling approaches guided by RANS modelling are based on only the Reynolds terms.

The Leonard term and Cross term are approximately equal. Salvetti and Banerjee (1995) show this to be true across a range of filter widths (i.e. across the inertial subrange). Liu et al. (1995) also demonstrate this to be true in their experiments on turbulent jets.

The Leonard term can be approximated by $\overline{\bar{u}_i \bar{u}_j} \approx \bar{u}_i \bar{u}_j$ as found by Lily (1967), although Leonard (1974) gives a Taylor expansion for more accuracy. The term can be computed directly from the resolved field, though, and does not have to be modelled.

After the initial work on the Leonard and Cross terms they were typically dropped from consideration because their order of magnitude was the same as the order of

[2] This occurs if a finite volume cell is considered in which the filtered variable represents all points in that cell, so that applying the same top hat filter over a non-varying volume does not change the value of the filtered variable.

magnitude of the discretisation error. The Leonard model entry in chapter 4 gives more details of this.

2.7 Other Issues

The governing equations have symmetries; that is to say that under certain transformations the form of the equations remains the same. This is also called invariance. The NS equations are invariant under a fixed translation, a reflection, and a rotation. Also under a Galilean transformation, in which the frame of reference is moving at a constant velocity relative to the comparative frame. Speziale (1985) shows that the filtered NS equations also have these properties. Consequently all subgrid models should have these properties. However, he also showed that when the subgrid terms are considered after decomposition, the Leonard and Cross terms are not Galilean invariant, although their sum is. So this is not a restriction on models for *only those terms*, although it is still necessary for the complete subgrid model. The significance of this is seen if the simulation is such that the equations are stiff, i.e. that the time scales between the different equations in the system are significantly different. Galilean coordinate transforms can be made to alleviate strict time step restrictions.

Another consideration is that of realizability. Schumann (1977) introduced the notion for the Reynolds stress. It is clear that the stress tensor is semipositive definite. That is that the components of the trace are greater than or equal to zero. The next two realizability conditions follow directly from that.

$$t_{ij} \geq 0 \ , \ i = j \tag{2.44}$$

$$t_{ij}^{\ 2} \leq t_{ii} t_{jj} \ , \ i \neq j \tag{2.45}$$

$$\det(t_{ij}) \geq 0 \tag{2.46}$$

Vreman et al. (1994b), extends the work to prove that the necessary condition for the subgrid stresses to be positive semi-definite is that the filter operation is always non-negative. This is true for the top-hat filter and the Gaussian filter, but not for the cut-

off filter. Subgrid models should not be able to break these rules when appropriate filters are used.

An attempt has been made to find sufficient conditions for LES modelling to capture accurate average flow values. Meneveau (1993) showed the outcome to be equivalent to the closure problem of the NS equations. For each equation to be satisfied, accurate capturing of higher moments is needed.

Germano (1992) notes and Salvetti and Beaux (1998) investigate the implicit nature of filters in finite difference schemes. The use of different discretisations for different terms in the equations leads to a necessary inconsistency in the filter. This has not been explored in any detail. They do give different correlations for different discretisations of the SGS term, however.
Piomelli et al. (1988) show the importance with some models of choosing appropriate filters to be consistent. The essence of this consistency is that where the model has a length scale in it, this must correspond to the length scale associated with the filter. Hartel and Kleiser (1997) investigate the effect of the invariance and filter type in the near wall region. Previous authors including Piomelli et al. (1988) had found that the SGS behaviour was dependent on the filter in the near wall region (elsewhere it was independent). Hartel and Kleiser show this dependence was due to the uses of non-invariant SGS models. Also the Leonard term was shown to be small in this region.

Chapter 3

Turbulence

3.1 Introduction

To understand LES modelling it is necessary to understand the turbulence theory on which it is based. This chapter briefly introduces the fundamental notions of turbulence and the quantities which are possible to investigate. The energy spectrum is particularly important and is discussed. More detailed presentations on most of the issues here can be found, for example, in Pope (2000) or Mathieu and Scott (2000).

A satisfactory definition of turbulence is still elusive, although we know intuitively what it is. We see it in the breakdown of orderly laminar flow into a chaotic flow where the motion is highly unpredictable to say the least. The chaotic nature of turbulence is clearly seen in weather simulations, where predictions become highly inaccurate after relatively short amounts of time. The slightest change in input parameters will lead to drastically different results. However, when viewed from a greatly magnified perspective, we could consider the flow laminar again, when the smallest scales of motion are clearly distinguishable.

Consider an experimental turbulent channel flow. Each experiment will result in different instantaneous velocity fields, although the average field will remain constant. This led Taylor (1935) to propose that the turbulence could be modelled with random functions over a steady field (but note the Navier-Stokes equations are still deterministic, and *not* random, in that the computational solutions are exactly reproducible). Later, he showed that the correlation of two velocities gives an energy spectrum in Fourier space (see below). This led to a great deal of research into the transfer of energy between the Fourier modes. The turbulent motion is considered in terms of eddies, large, small, and many in between, a superposition of which results in a turbulent field. The energy in each mode can be considered to be representative of

the energy contained in a particular eddy size. The energy cascade describes the behaviour of the flow. The energy of the large eddies transfer into the smaller eddies which in turn transfer to smaller eddies, until the energy is dissipated through viscosity.

3.2 Theory

There are just a handful of underlying principles from which the majority of current thinking stems. These are still rather limited, however, and it is important to remember these restrictions: that the hypotheses are developed for isotropic, homogeneous turbulence. The buoyant plume has neither of these properties.
The following is considered so important by Tennekes (Frost and Moulden, 1979), that he considers it the 'first law'.

First Law: The turbulent dissipation rate is proportional to the lifetime of the largest eddies.

$$e = O(u'^3 / l_0) \qquad (3.1)$$

u' is the fluctuating (from the mean) component and l_0 is the integral length scale, the scale associated with the largest eddies.
The turbulent energy is $O(u'^2)$, and the lifetime of the largest eddies is $O(u'/l_0)$.
The significance is that the dissipation rate is independent of viscosity. Even though there is no rigorous derivation of the above, it has been thoroughly validated by experiment.
This law leads to the notion of the universal equilibrium range. In this range the amount of turbulent energy put in from the large scales will immediately be counterbalanced by the small-scale dissipation. This is possible as the small-scale motions have much shorter time scales, and react quickly to dissipate the energy. Kolmogorov's hypotheses (Pope, 2000) stem in part from these ideas and are the foundation of modern turbulence theory.

Kolmogorov's hypothesis of local isotropy: At sufficiently high Reynolds number, the small-scale turbulent motions $l << l_0$ are statistically isotropic.

Kolmogorov's first similarity hypothesis: At sufficiently high Reynolds number, the statistics of the small-scale turbulent motions can be uniquely described by the viscosity, u, and the dissipation rate e.

Kolmogorov's second similarity hypothesis: At sufficiently high Reynolds number, the statistics of the small-scale turbulent motions in the range $l_0 >> l >> h$ can be uniquely described by e alone.

h is the Kolmogorov length scale, at which viscous dissipation occurs.

The essence of these is to divide the eddies into ranges about which more quantifiable statements can be made. Fig. 3.1 shows these in spectral space, in which the eddy length scales can be clearly distinguished with wavenumber.

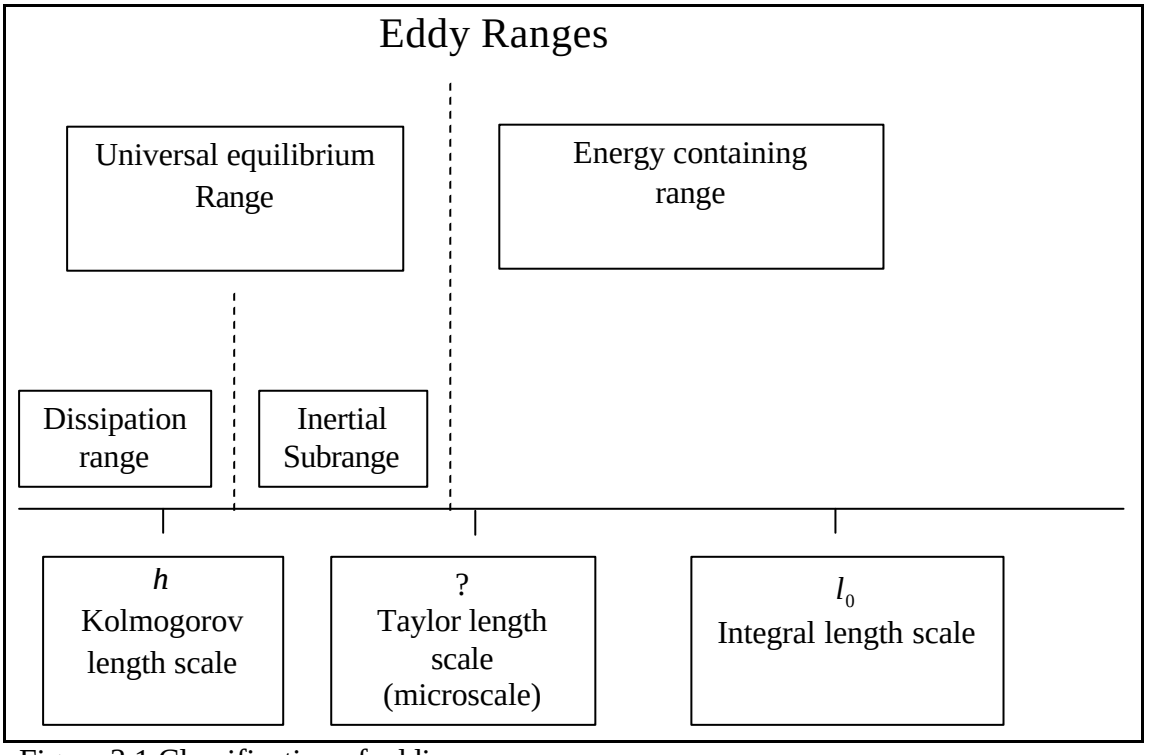

Figure 3.1 Classification of eddies.

The key point of the hypothesis of local isotropy is that the characteristics of the small scales of motion are universal in nature, and not dependent on the dynamics of the large scales. This is the premise for LES, which attempts to exploit the universal

nature of the small scales with modelling, and to capture the large scales explicitly. It must be remembered that this is only a hypothesis, and although it has been shown to be true in practical flows such as channel flow it may not hold elsewhere. Near wall regions do not have small-scale isotropy.

It is assumed that the range in which the local isotropy assumption holds is similar to that of the Universal Equilibrium range. That this Universal Equilibrium range exists is more often termed the equilibrium assumption, and is equally important to LES modelling.

The similarity hypotheses indicate two small-scale ranges. The first is the dissipation range, acting at the Kolmogorov scales and the second is the inertial subrange, the latter of which LES models are also very reliant. These are not divisions of the Universal Equilibrium range, although they have a similar range, and are often presented pictorially as such.

3.3 Length and Time Scales

The Kolmogorov scales of turbulence can be estimated from his hypotheses and from dimensional reasoning (hence the name). The dissipation (length) scale, corresponding velocity, and corresponding time scales are as follows.

$$h = O(u^3 / e)^{1/4} \tag{3.2}$$

$$u_h = O(eu)^{1/4} \tag{3.3}$$

$$t_h = O(u / e)^{1/2} \tag{3.4}$$

DNS simulations which capture all the flow detail (rather than letting DNS simulation refer to simulations without a subgrid model) must be resolved to these scales of space and time. It is worth noting that whilst LES models are expected to resolve all the time scales of the filtered field, these are larger than the Kolmogorov time scale.

As well as the integral length scale, there is the Taylor microscale. It can be defined as follows (Mathieu and Scott, 2000), in which an average for the indexes can be used.

$$l = O(u_i' / \frac{\partial u_i}{\partial x_j}) \tag{3.5}$$

The physical interpretation is not clear, although it can used to define LES (see section 2.4), since it is an approximation to the beginning of the universal equilibrium range (Ferziger, 1977).

From the definition:

$$e = u\overline{\frac{\partial u_i'}{\partial x_j}\frac{\partial u_i'}{\partial x_j}} \tag{3.6}$$

The energy dissipation can then be expressed:

$$e = O(u\frac{\overline{u_i'^2}}{l^2}) \tag{3.7}$$

From these, and the first law, we can obtain the relations below.

$$\frac{h}{l_0} = \mathrm{Re}_{l_0}^{-3/4} \tag{3.8}$$

$$\frac{l}{l_0} = \mathrm{Re}_{l_0}^{-1/2} \tag{3.9}$$

$$\frac{t_h}{t_0} = \mathrm{Re}_{l_0}^{-1/2} \tag{3.10}$$

where $\mathrm{Re}_{l_0} = \frac{u'l_0}{u}$. (3.11)

3.4 Measuring Turbulence and Energy Spectra

Experiments and DNS simulations provide an understanding of turbulence, around which turbulence models can be evaluated, although DNS simulations are still limited to only moderate Reynolds numbers on the fastest computers.

LES model simulations should be able to capture identically the large scale motions found through these methods, and ultimately be capable of being used as an

alternative to DNS in certain circumstances as a tool for the fundamental study of turbulence.

The most basic measurements that can be taken are the average flow quantities – the average velocity, temperature, and pressure fields. The averaging process also yields the second moments – the average of the fluctuating components. These are the Reynolds stresses, $RS_{ij} = \overline{u_i' u_j'}$ where u_i' is the deviation from the mean and the overbar is the time average. In the temperature equation, these are given by the temperature fluxes, $TF_i = \overline{u_i' T'}$. These values have been extensively researched in widely varying fields. The turbulent kinetic energy (TKE), $k = \frac{1}{2}\overline{u_i'^2}$, is also critical to the study of turbulence. Third moments are harder to capture but effort in this direction is currently underway.

In practical flow simulations it is usually only the first moments which are required, and are naturally the most important to capture correctly. However, to obtain these we need to know the second moments, which in turn require the third moments. This is, of course, the closure problem of turbulence modelling, discussed further in Wilcox (1993).

RANS models model these, either explicitly of through transport equations. These models are well developed and can give very good results for first and second moment terms across a range of complex flow situations. It is important that LES models, as well as giving detail of the unsteady flow, accurately give the information RANS models can.

Equation balances can also be taken, which average the individual components contributing to the momentum and temperature equations. The LES simulation balances are different to the RANS balances, but the RANS balance information can also be extracted from the results.

The turbulent kinetic energy is studied through the energy spectrum. This essentially considers the TKE in Fourier space, where the energy is distributed across wavenumbers, which correspond to the eddies' physical length scale. The energy of a certain size of eddy is roughly represented by the energy contained in the

wavenumber (region) that is the inverse of the physical length scale. Thus the TKE is the integral across Fourier space of the energy contained in different eddy sizes.
In isotropic, homogeneous turbulence, the energy spectrum is given by the following (see Appendix A).

$$E(k) = 2p k^2 \Phi_{ii}(k) \tag{3.12}$$

$$k = \int_0^\infty E(k) \partial k \tag{3.13}$$

Φ_{ij} is the Fourier transform of the spatial second order velocity correlation.

Kolmogorov's second similarity hypothesis states that (in a certain region) the statistics of small-scale turbulence can be entirely described by e. In Fourier space this implies that the spectrum can be fully described as a function of e and k. This leads, through dimensional reasoning (remembering that k has units m^{-1}), to the Kolmogorov energy spectrum.

$$E(k) = Ce^{2/3} k^{-5/3} \tag{3.14}$$

This is the –5/3 power law.

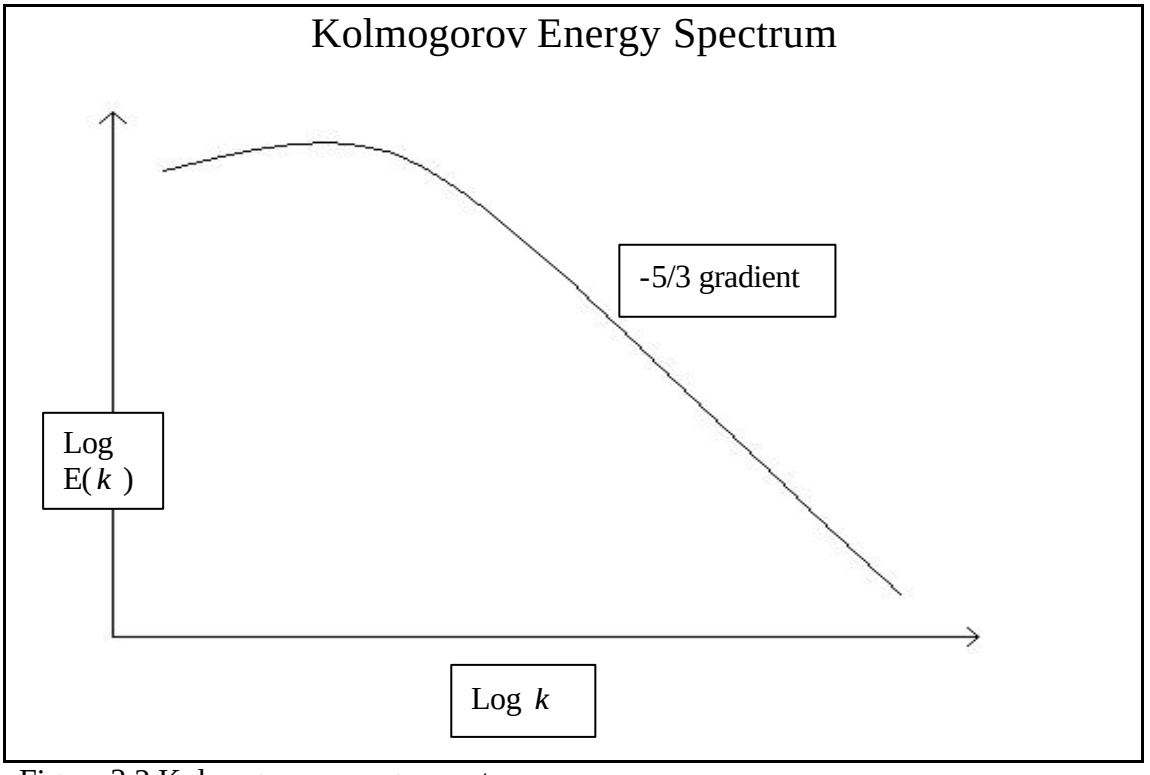

Figure 3.2 Kolmogorov energy spectrum.

Fig. 3.2 shows the full energy spectrum. On the log plot, the Kolmogorov spectrum appears as a straight line. The stronger the turbulence is the larger the inertial subrange is. As the turbulence becomes weaker the region is vanishingly small. In low Reynolds number turbulence, where the inertial subrange does not exist, the modelling assumptions used for some LES models break down. Also in non-isotropic, non-homogeneous turbulence the power law can break down. Pope (2000) finds the value of the power law varies between –1 and –2, and requires extra functions to compensate as the spectra deviates from the straight line. Nevertheless the –5/3 law is an excellent general guide, and most situations will result in a good approximation to it.

Buoyant turbulence in generally studied in the context of Rayleigh-Benard convection – buoyancy induced motion between heated plates. Two main phenomena are found distinctive form isothermal turbulence. Yanagita and Kaneko (1995) discuss the present thinking on buoyant turbulence and report that there is still a great deal yet to fully understand, and find that transition occurs through a number of different mechanisms dependent on the Prandtl number and the aspect ratio. In the fully turbulent region two types of turbulence are found, 'hard' and 'soft' (Xia and Qiu, 1999). This distinction is a recent discovery, and further regions were investigated although evidence against 'ultrahard' turbulence has been put forward by Glazier et al. (1999). The distinction is in the Nusselt number relation to Rayleigh number., where the Nusselt number, Nu, the non-dimensional heat flux is defined by $\frac{HD}{k(T_1 - T_2)}$ where the terms are respectively from top to bottom, the heat transfer per unit area per unit time, a length scale (the distance between the two plates), the thermal conductivity, and the temperatures of the plates.

$Nu \propto Ra^{1/3} \qquad Ra < 10^9$

$Nu \propto Ra^{2/7} \qquad Ra > 10^9$

The former is 'soft', and the latter 'hard'. The second phenomenon is in the temperature fluctuation spectra. Zhou et al (2001) show two distinct spectra regions, one with a –5/3 power law, and the second with a –3 power law. This is clearly related to the following investigations. The question remains open as to what causes the turbulent kinetic energy in buoyant flows – the buoyancy or the shear (Zhou and

Xia, 2001). They suggest two regions within the inertial subrange, each dominated by one of these, and further work by Shang and Xia (2001) suggests the first region has a –11/5 power law, and at the smaller scales the usual –5/3 law.

3.5 Taylor's Hypothesis

It is very difficult to take the above measures experimentally. Taylor's hypothesis is normally used to overcome this. '*The time correlation can be connected to the spatial correlation if the turbulent fluctuations are small compared with the mean velocities*' (Bradshaw, 1971). In this situation the time correlation would be equal to the spatial correlation, where the distance between the two points (in the direction of the mean velocity) is equal to the time difference multiplied by the mean velocity. This is because the turbulence would not distort the large eddies significantly in the time it takes to pass the point of measurement. So $\frac{\overline{u(x,t)u(x,t+h)}}{\overline{u^2(x,t)}} \approx \frac{\overline{u(x,t)u(x+hU,t)}}{\overline{u^2(x,t)}}$ holds under these conditions, where U is the mean velocity of the large eddy and h is a time scale.

Similarly we take the Fourier transform, in this case obtaining time-scale spectra of the turbulence. The physical time scales are related to the physical length scales via $\Delta t = U\Delta x$ in Taylor's Hypothesis.

So let $R_{ii}(t,t+\Delta t) = \overline{u_i'(t)u_i'(t+\Delta t)}$ be the new correlation function fixed in space. Again $R_{ii}(0)$ is the TKE, which can be expressed in wave space.

$$R_{ii}(t) = \Im^{-1}(\Phi_{ii}(k)) \qquad (3.15)$$

$$\Phi_{ii}(k) = \Im(R_{ii}(t)) \qquad (3.16)$$

The idea of length scales corresponding to their wavenumber counterparts is very useful. However, since Taylor's hypothesis is not always useable, and since the time spectra can usually be evaluated (so long as there is no intermittency), it seems to make more sense to concentrate on the time spectra, in which the time wavenumbers can equally be seen as corresponding to lengthscales regardless of the formality of transforming into spatial spectra.

3.5 Other Issues

The energy cascade is a simplified view of energy transfer. Most energy goes from large scales to smaller scales, but some energy goes from small scales to large scales. This phenomenon is called backscatter, although it more particularly refers to the energy transfer in LES simulations from the subgrid-scales back up to the grid scales. Piomelli et al. (1991) investigated this and showed extensive backscatter in a channel flow. The amount varied with filter type, but all had a considerable amount of backscatter. To accurately account for this behaviour is still a challenge for LES modelling.

The unsteady flow features are typically not reported beyond the energy spectra. With the need to test LES models, more characteristics to qualify their unsteady accuracy should be studied. The statistics of intermittency are one such example. An intermittent region is a region which has periods of turbulence and laminar flow passing over it. It makes spectra evaluation impossible, and provides a challenge for dynamic LES models.

Chapter 4

LES Models

4.1 Introduction

There are too many different LES models to complete an exhaustive review, so a selection of the most important from the development perspective, and the most promising of the recently developed models are presented. The 1960's and 1970's saw the pioneering work and the initial development of LES modelling and simulation. The lack of computing power and the significant progress made in RANS modelling led to a lull in the amount of activity in the 80's. The 90's saw a considerable resurgence in the area which can be largely attributed to the Germano relation (Germano, 1992), and the introduction of dynamic modelling (Germano et al., 1991), as well as the increased amounts of computing power.

This work has resulted in LES modelling being on the brink of becoming a significant engineering tool, similarly to RANS. Computational cost is still a very significant issue. The dynamic models are between marginally more expensive and considerably more expensive than their static counterparts. Both are usually local in nature however, although methods such as the estimation model (Domaradzki and Saiki, 1997) and the model introduced by Shah and Ferziger (1996), which consistently evaluate the pre-filtered momentum and scalar fields must solve global equations, making them the most expensive to solve. It is important to see what gain is achieved, and at what cost.

It should be noted that there is usually no non-dimensional parameter to scale the turbulent stress, since it comes from the filtering of the convective term.

The subgrid models are usually developed with the incompressible equations. In the LMN equations, effects of density are taken into account as a scaling factor, assuming that stresses calculated with the Favre averages are allowable.

The modelling of the scalar fluxes, and in particular that of the temperature flux, has received relatively little attention. Fortunately the extension of the stress models to

this end is either straightforward or there is no conflict using an alternative model, for example using an eddy stress model and a structural flux model (although the choice of flux model is limited by the choice of stress model – it is not sensibly possible to use a structural stress model and an eddy flux model).

4.2 Kinetic Energy Equations

A number of models, using the equilibrium assumption, are derived balancing the kinetic energy equations. They are useful or essential to see the derivation. It is, in fact, the subgrid kinetic energy equation which is used in the 'one equation' model and its derivatives. The following are derived from the dimensional incompressible equations.

Often the dissipation and production terms are written in terms of $S_{ij} = \frac{1}{2}(\frac{\partial u_i}{\partial x_j} + \frac{\partial u_j}{\partial x_i})$ instead of $\frac{\partial u_i}{\partial x_j}$. Due to symmetry of the tensors and the summation over three equations, these are equivalent.

The kinetic energy is $k_{ke} = \frac{1}{2}u_i^{\,2}$, and its transport equation is found by multiplying the unfiltered momentum equations by the unfiltered velocities, u_i.

$$\frac{\partial k_{ke}}{\partial t} + u_j \frac{\partial k_{ke}}{\partial x_j} = -\frac{1}{r_a}\frac{\partial u_j \Pi}{\partial x_i} + u\frac{\partial^2 k_{ke}}{\partial x_j^{\,2}} - e_{ke} + B_{ke} \qquad (4.1)$$

$e_{ke} = 2u\frac{\partial u_i}{\partial x_j}\frac{\partial u_i}{\partial x_j}$ is the viscous dissipation.

$B_{ke} = u_j \Theta g_j$ is the kinetic energy produced through buoyancy forces.

$\Theta = \frac{r}{r_a} - 1$ is the density differential.

The filtered kinetic energy (the kinetic energy contained by the filtered scales, not the kinetic energy after it has been filtered) is found by multiplying the filtered equations by $\overline{u}_i$, $k_{fke} = \frac{1}{2}\overline{u}_i^{\,2}$.

$$\frac{\partial k_{fke}}{\partial t} + \overline{u}_j \frac{\partial k_{fke}}{\partial x_j} + \frac{\partial \overline{u}_i t_{ij}}{\partial x_j} = -\frac{1}{r_a}\frac{\partial \overline{u}_j \Pi}{\partial x_i} + u\frac{\partial^2 k_{fke}}{\partial x_j^{\,2}} - e_{fke} - \Pr_{fke} + B_{fke} \qquad (4.2)$$

There is an extra convective term of the turbulent stresses on the lhs from splitting the stress term into two. This term is small.

$e_{fke} = 2u\frac{\partial \overline{u}_i}{\partial x_j}\frac{\partial \overline{u}_i}{\partial x_j}$ is the viscous dissipation.

$\Pr_{fke} = -t_{ij}\frac{\partial \overline{u}_i}{\partial x_j}$ is the production of subgrid scale kinetic energy (sink term).

$B_{fke} = \overline{u}_j \Theta g_j$ is the production of grid scale kinetic energy due to buoyancy.

The subgrid energy production is a significantly greater sink term than the viscous dissipation if the Reynolds number is high enough.

The subgrid kinetic energy of the filtered equations, defined $k_{sgs} = \frac{1}{2}(\overline{u_i^{\,2}} - \overline{u}_i^{\,2}) = \frac{1}{2}t_{ii}$, is found by reducing $\overline{u_i M_i} - \overline{u}_i\overline{M}_i$, where M_i are the momentum equations.

$$\begin{aligned}&\frac{\partial k_{sgs}}{\partial t} + \overline{u}_j\frac{\partial k_{sgs}}{\partial x_j} + \frac{\partial \overline{u}_i t_{ij}}{\partial x_j} = -\frac{\partial}{\partial x_i}(\overline{u_i\Pi} - \overline{u}_i\overline{\Pi}) + u\frac{\partial^2 k_{sgs}}{\partial x_j^{\,2}} \\ &-\frac{\partial}{\partial x_j}\left(\frac{\overline{u_i^{\,2}u_j}}{2} - \frac{\overline{u_i^{\,2}}\,\overline{u}_j}{2} - \overline{u}_i\overline{u_i u_j} + \overline{u}_i^{\,2}\overline{u}_j\right) - e_{sgs} + P_{sgs} + B_{sgs}\end{aligned} \qquad (4.3)$$

The pressure terms are clearly derived, the viscous terms are all from the original viscous terms; the four triple products are from the convection term. The stress term splits in two as before.

$e_{sgs} = 2u\left(\overline{\frac{\partial u_i}{\partial x_j}\frac{\partial u_i}{\partial x_j}} - \frac{\partial \overline{u}_i}{\partial x_j}\frac{\partial \overline{u}_i}{\partial x_j}\right)$ is the viscous dissipation.

$\Pr_{sgs} = -t_{ij}\frac{\partial \overline{u}_i}{\partial x_j}$ is the turbulent production (source term).

$B_{sgs} = (\overline{u_j\Theta} - \overline{u}_j\overline{\Theta})g_j$ is the turbulent production due to buoyancy.

The turbulent kinetic energy, $k = \frac{1}{2}\overline{u_i'^2}$, is the energy studied in turbulent energy spectra, when a time filter is used. This also simplifies the transport equation, since $\overline{u_i'} = 0$, and $\overline{\overline{u}}_i = \overline{u}_i$. This is found with $\overline{u_i'M_i} - \overline{u_i'\overline{M}_i}$.

$$\frac{\partial k}{\partial t} + \overline{u}_j\frac{\partial k}{\partial x_j} = -\frac{\partial}{\partial x_i}\overline{u_i'\Pi'} + u\frac{\partial^2 k}{\partial x_j^{\,2}} - \frac{\partial}{\partial x_j}\overline{u_i'^2u_j'} - e_{tke} + P_{tke} + B_{tke} \qquad (4.4)$$

$$e_{tke} = 2u\overline{\frac{\partial u_i'}{\partial x_j}\frac{\partial u_i'}{\partial x_j}}$$

$$P_{tke} = -\overline{u_i'u_j'}\frac{\partial \overline{u}_i}{\partial x_j}$$

$$B_{tke} = \overline{u_i'\Theta}g_i$$

.

Note that $k_{ke} \neq k_{fke} + k_{sgs}$ (4.5)

Eqn. 4.5 is a good approximation however. k_{sgs} would have to be redefined as $k_{ske} = \frac{1}{2}(u_i^{\,2} - \overline{u}_i^{\,2})$ for the relation to hold but this would lose the more useful relation $k_{ske} = \frac{1}{2}t_{ii}$.

Various authors have made proposals for the modelling of the unknown correlations but it is acknowledged (Lilly, 1967, Hoiruti, 1985) that they are not well understood and not modelled accurately. It is thought the higher the order of the correlation the less significance the term has, and so the accuracy of the modelling of these correlations is not too important. The models are given section 4.8.

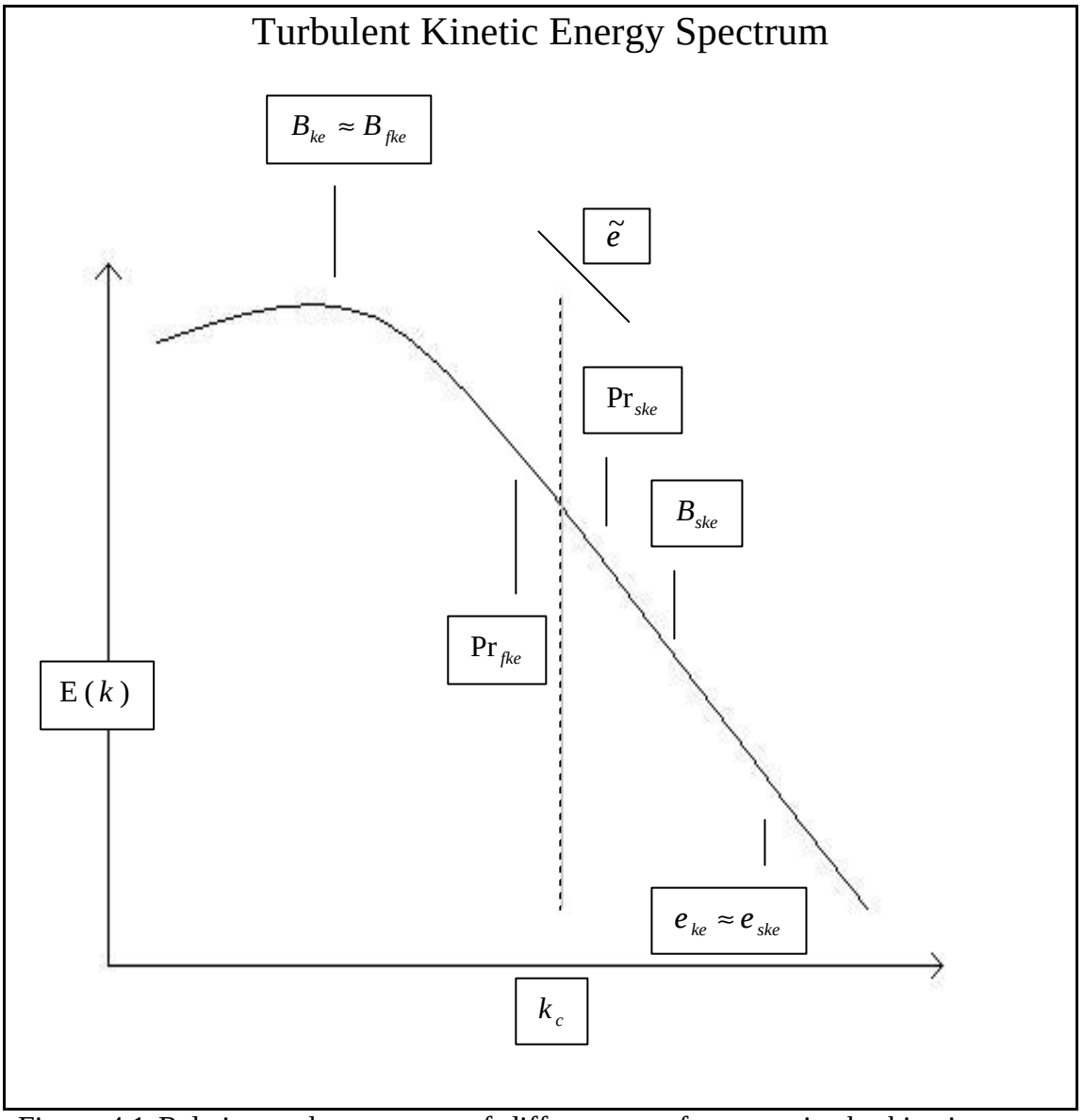

Figure 4.1 Relation and movement of different transfer terms in the kinetic energy equations in a buoyancy driven flow.

Pope (2000) considers the dominant source and sink terms in the kinetic energy (KE) and filtered kinetic equations (FKE) in a non-buoyant flow. Assuming the total amount of kinetic energy dissipated is similar to the amount of filtered grid scale energy passed on to the subgrid scales, we have

$$e_{ke} = \Pr_{fke} \tag{4.6}$$

Lilly (1967) considers the subgrid kinetic energy equation (SKE) (without buoyancy) for stationary, isotropic, homogeneous flow (i.e. the transport terms go to zero), which reduces to:

$$e_{sgs} = \Pr_{sgs} \tag{4.7}$$

Assuming no buoyancy again, the production term of the SKE and sink term of the FKE are equal.

$$\mathrm{Pr}_{fke} = \mathrm{Pr}_{sgs} \tag{4.8}$$

The Reynolds averaged equation, 4.4 governs the turbulent kinetic energy (TKE). This has come under a great deal of scrutiny in RANS modelling, and is also a reduced form of the SKE equation.

It is interesting to note that although there is a production term due to buoyancy in the SKE equation (4.3) there is no equivalent dissipation term in the filtered equation. This shows the buoyancy generating turbulence at all scales, and is illustrated in fig. 4.1 above. These equations help to understand the mechanisms involved in turbulence generation and dissipation at the different scales.

4.3 The Boussinesq Hypothesis

The Boussinesq hypothesis (1877) is *that the turbulent terms can be modelled as directly analogous to the molecular viscosity terms using a 'turbulent viscosity'*. Recalling Stokes hypothesis, the turbulent terms are given by:

$$t_{ij} = -2u_t \bar{S}_{ij} + \frac{2}{3} d_{ij} \frac{\partial u_k}{\partial x_k} \tag{4.9}$$

$$\text{or } t_{ij} - \tfrac{1}{3} d_{ij} t_{kk} = t_{ij}^{a} = -2u_t \bar{S}_{ij} \tag{4.10}$$

Normally only the anisotropic part is used in computations in which case the isotropic component can be interpreted as being amalgamated into the pressure term, otherwise the right hand side of equation 4.10 can define the complete hypothesis. The increased viscosity provides a clear mechanism to dissipate the turbulent energy.

For computational purposes, a total viscosity can be made, $u_{tot} = u + u_t$. This is more efficient than evaluating the whole tensor separately. Since non-Boussinesq models are also use, this method is not used in this work.

The equivalent model for the temperature flux is more simply:

$$q_j = \frac{u_t}{\mathrm{Pr}_t}\frac{\partial T}{\partial x_j} \tag{4.11}$$

This latter term is referred to as the standard gradient diffusion hypothesis (SGDH) or as the eddy diffusivity model.

These are the most widely used turbulence models, and a great deal of research has gone into developing these, originally for RANS, and now for LES. Within this model are numerous sub-models, evaluating the turbulent viscosity differently.

Dimensional reasoning shows

$$u_t = C\tilde{e}^{1/3}\Delta^{4/3} \tag{4.12}$$

$\tilde{e}$ is the energy transfer through the cutoff shown in fig. 4.1, and is equal to the usual viscous dissipation e_{ke} by the local equilibrium assumption. Δ is a length scale which is chosen to be the filter width. The evaluation of $\tilde{e}$ is the key to closure, and eqn. 4.12 is referred back to in the model derivations.

By analogy to the viscous dissipation, the turbulent dissipation is given by

$$\tilde{e} = \int_0^{k_c} u_t k^2 E(k)\partial k \tag{4.13}$$

This will also be referred back to.

4.4 Generalised Gradient Diffusion Hypothesis

Before going on to the main LES stress models, an alternative to the standard gradient diffusion hypothesis is given, which has been found in RANS modelling (Sanderson, 2001) to give significant improvements.

Daly and Harlow (1970) were among the first to report a more complex model, the general gradient diffusion hypothesis (GGDH). The model is derived from balance considerations from the scalar flux equation (the equivalent of the TKE equation for the temperature fluctuations), assuming steady homogeneous turbulence, and assuming that higher order correlations are negligible, although the temperature (or scalar) flux is itself of the order of the neglected terms. The model reads, leaving out subscripts which can be read either as TKE or SKE:

$$q_j = c_t \frac{k^2}{e} t_{jk} \frac{\partial T}{\partial x_k} \qquad (4.14)$$

$c_t = O(1)$

The LES models currently used do not include a transport equation for the turbulent dissipation, e. e can be modelled in a number of ways. The most immediate is to use equation. 4.7, $e = \frac{1}{2} t_{ij} S_{ij}$. This leads to the S_{ij} term in the denominator which is very unstable. The alternative comes from the first law, with the constant taken from the modelling of the dissipation term in the turbulent energy transport equation (see section 4.8. That is

$$e = \frac{k^{3/2}}{\Delta} \qquad (4.15)$$

The turbulent energy can be evaluated directly from its definition, when the subgrid energy equation is not in use.

$$k = \frac{1}{2} t_{ii} \qquad (4.16)$$

Substitution results in the following.

$$q_j = -c_t \Delta k^{0.5} t_{jk} \frac{\partial T}{\partial x_k} \qquad (4.17)$$

$$\text{or } q_j = -c_t \Delta (\tfrac{1}{2} t_{ii})^{0.5} t_{jk}^{1.5} \frac{\partial T}{\partial x_k} \qquad (4.18)$$

Equation 4.17 is labelled GGDH_1, due to having fewer requirements for it's implementation, and equation 4.18 is GGDH_2.

4.5 Smagorinsky's model

The first model always cited is that of Smagorinsky (1963), although Lilly (1962) was using variants of it already, notably the buoyancy modified Smagorinsky model described in the next section. This has been the most widely used model. It has been extensively tested and utilized across a broad range of simulations from combusting flows cases to atmospheric flows (for which it was developed) to building flows. Almost all newly developed models are tested against this. The turbulent viscosity takes the form:

$$u_t = C\Delta^2 \left|\overline{S}\right| \ , \ \left|\overline{S}\right| = (2\overline{S}_{ij}\overline{S}_{ij})^{1/2} \qquad (4.19)$$

Lilly (1967) shows the model to be consistent with the Kolmogorov spectrum if the correct constant is chosen. Consideration of an isotropic, homogeneous, stationary, no-buoyant flow gives equation 4.7 again, $e = \frac{1}{2} t_{ij} \overline{S}_{ij}$. Substituting equation 4.19 into 4.10, and then into 4.7, using the Fourier integral approximation $\left|\overline{S}\right|^2 \approx 2\int_0^{p/\Delta} k^2 E(k)\partial k$ (Lilly, 1967) in conjunction with the Kolmogorov energy spectrum, shows the constant to be about 0.03, although a constant of 0.01 is typically used.

The model has had considerable success, but has a number of failings. The constant does not allow for backscatter. This leads to bad correlations in a priori testing of the models, in which the constant would vary significantly. However, it is simple, very robust, and does give good overall dissipation.
The constant used is found from experiment rather than theory, and the optimal value varies between simulations. In laminar flow it should tend to zero, but can't since it is constant, and will give extra dissipation. The Smagorinsky model gives bad results in shear flows according to Bardina et al. (1980).
Wall modelling provides another difficulty, which is not dealt with in this work, since no turbulent wall boundaries are simulated.

The SGDH is usually used together with the Smagorinsky model. This has the same problems, and the GGDH or even non-gradient models can be used instead. Zhou et al. (2001) use the SGDH with a turbulent Prandtl number of 0.4, although values between 0.4 and 0.7 are found in the literature.

4.8 Buoyancy Modified Smagorinsky Model

This was developed by Lilly (1962), and is the only model explicitly using buoyant terms in the stress tensor to date. Note the buoyancy term does reintroduce a non-

dimensional flow parameter into the model. The original derivation makes an approximation only suitable for low Mach number flows.

$$u_t = C\Delta^2(2\overline{S}_{ij}\overline{S}_{ij} - \frac{1}{Fr\,\mathrm{Pr}_t}\frac{\partial\overline{T}}{\partial x_i}d_{ij})^{1/2} \qquad (4.20)$$

Bastiaans (2000) finds the model the worst of a collection of models in the simulation of enclosed thermal plumes (including the unmodified model). The simulations are very coarse, and good inertial range spatial spectra are not found for any of the models, although the time spectra are good.

This model works for unstable stratification and neutral stratification, and Eidson (1985) suggests fixing the constant to zero in any situation where the stable positive stratification term is greater than the positive definite strain term. i.e. when the square root of a negative value is calculates in eqn. 4.20, the model should be fixed to zero.

However, balancing the equations as for the Smagorinsky model, with the buoyancy production term, B_{ske}, and a buoyancy correction term, B_u, added to the turbulent viscosity gives

$$e = -2C\Delta^2(\left|\overline{S}_{ij}\right| + B_u)\overline{S}_{ij}^{\,2} + B \qquad (4.21)$$

This provides an algebraic expression which can be used to develop buoyancy modified models consistent with the flux model used, after substituting it into eqn. 4.21, and without the low Mach number restriction. Also other stress models can be substituted. An expression linking the temperature gradient to the dissipation rate would be very beneficial.

4.7 Structure Function model

The structure function in physical space is an extension of the spectral eddy viscosity model, developed by Metais and Lesieur (1992), although it can be derived independently. It takes the following form (Lesieur and Metais, 1996).

$$u_t = \frac{2}{3}C_k^{-3/2}(\frac{E(k_c)}{k_c})^{1/2} \qquad (4.22)$$

With the cutoff in the inertial range, $E(k_c) = 1.4e^{2/3}k^{-5/3}$ according to Kolmogorov's hypotheses. Substitution of this into 4.9 gives 4.23 above. In physical space, we assume the grid width is associated with the cut-off filter, so $k_c = p/\Delta$.

$$u_t = \frac{2}{3}C_k^{-3/2}(\frac{\Delta}{p})^{1/2}E(p/\Delta)^{1/2} \tag{4.23}$$

Let $\|r\| = \Delta$,where the double bar is the magnitude of the vector, and define F_2, the second order structure function

$$F_2(x,\Delta) = <\|\bar{u}(x,t) - \bar{u}(x+r,t)\|^2> \tag{4.24}$$

and <.> is a spatial average.

Assuming local isotropy, the function is related to the energy spectrum with Batchelor's (1953) formula.

$$F_2(x,\Delta) = 4\int_0^{k_c} E(k)[1 - \frac{\sin(k\Delta)}{k\Delta}]\partial k \tag{4.25}$$

All values above k_c are zero, since the filtered (with cutoff) equations are used.

Again, substituting the Kolmogorov energy and rearranging gives

$$u_t = 0.105C_k^{-3/2}\Delta(F_2(x,\Delta))^{1/2} \tag{4.26}$$

$C_k = 1.4$. F_2 is evaluated using the average of the values made using the surrounding six grid nodes. They suggest using it with a turbulent Prandtl number of 0.6.

They have found good results with simulations of a growing wake, and for the separated flow of the backward facing step. In the latter case the results are an improvement on the Smagorinsky model. It has also been successfully tested on supersonic flow. Nevertheless, it cannot handle backscatter, and with the empirical constant, can be dissipative in laminar flows.

Grenoble and David (1993) attempt to overcome this problem by introducing a switch to turn the model on or off locally. The angles between the vorticity of the grid node and the vorticity of the surrounding six nodes are averaged. If this is greater than 20^o then the model is utilised. This switch has numerical difficulties near stagnation points where the angles cannot be calculated without numerical error.

4.8 One Equation Model

The one equation model, first introduced in an LES context by Schumann (1975) is directly analogous to its RANS counterpart. A transport equation is derived for the turbulent kinetic energy and the eddy viscosity is modelled with the following reasoning.

$$k_{sgs} = \int_{k_c}^{\infty} E(k)\partial k \tag{4.27}$$

After integration with the Kolmogorov spectrum and letting $k_c = p/\Delta$

$$k_{sgs} \propto \tilde{e}^{2/3}\Delta^{2/3} \tag{4.28}$$

Substituting 4.28 into 4.12 gives

$$u_t = C_m \Delta (k_{sgs})^{1/2} \tag{4.29}$$

$C_m = 0.069$, and is a theoretically derived value (Sagaut, 2000). However, values between 0.04 and 1 have been used (Schmidt and Schumann, 1989).
The transport equation is given in section 4.2, and the terms are modelled as by Lilly (1962, 1967). Early one-equation modellers Yoshizawa (1982) and Hoiruti (1985) use the k_{tke} form of the equation rather than the k_{sgs}. This simply assumes that the Leonard and Cross terms are zero. Menon et al. (1995) and Ghosal et al. (1995) use the latter. Although the latter is better developed, the unknown components in each equation are modelled equivalently.

The extra diffusion term is modelled, although it is acknowledged as having little justification. In both equations (k_{tke} and k_{sgs}, read k as either below) all unknown higher order correlations are put into this term. It is expected to be an insignificant term.

$$DF = C_2 \frac{\partial}{\partial x_j}(\Delta(k)^{1/2}\frac{\partial k}{\partial x_j}) \tag{4.30}$$

$$DP = e = \frac{u}{2}\overline{\frac{\partial u_i'}{\partial x_j}\frac{\partial u_i'}{\partial x_j}} = C_1\frac{(k)^{3/2}}{\overline{\Delta}} \tag{4.31}$$

The constants are found to take the values $C_1 = 1$ and $C_2 = 0.1$. The first law is used to model the turbulent dissipation. Lilly (1967) finds the constant to be unity from a similar method to the derivation of the Smagorinsky constant.

The buoyancy term is given by the density flux and is modelled according to whichever method is preferred. It was usually modelled with the standard gradient diffusion hypothesis, but in RANS plume simulations, the effect of the buoyancy term was investigated by Sanderson (2001) and Worthy et al. (2001), and it was shown that the general gradient diffusion hypothesis is a significant improvement in a plume simulation, the former giving near zero production values.

This gives the turbulent kinetic energy equation.

$$\frac{\partial k}{\partial t} + \frac{\partial u_j k}{\partial x_j} = +u\frac{\partial^2 k}{\partial x_j \partial x_j} + P - DP + DF + B \tag{4.32}$$

It is possible for the energy to take a negative value from numerical or modelling errors. This is clearly unphysical, and must not be allowed to occur. It is easily stopped in an algorithm.

Schumann (1975) found it no improvement over the Smagorinsky model. Hoiruti (1985) also used this model. Both were in spectral space, for a channel flow. The latter finds that the model is not over-diffusive and suggests the Smagorinsky model can be.

Even though the coefficient doesn't go to zero in laminar flow, the energy does, which should be sufficient to stop excess dissipation.

A transport equation exists for the summed scalar fluxes (Daly and Harlow, 1970), but a model for the Prandtl number, or some other such, based on this has not yet been developed.

.

4.9 Note on the use of the Kolmogorov Spectrum

The Leonard decomposition has not been mentioned in the above models. However, the terms from the Leonard decomposition which are modelled can be seen from the way in which the energy spectrum is integrated. The Smagorinsky model integrates over the filtered scales leaving all decomposed terms incorporated in the model. The structure function model likewise integrates over the filtered field to find the velocity function and so can be deemed to model the whole stress tensor. The one-equation model integrates over the subgrid scales themselves, and models just those terms, leaving the Leonard and possibly the Cross terms not modelled.

4.10 Bardina Model

The Bardina model (Bardina et al., 1980) was the first of the scale similarity models. The basic principle behind them is that the structure of the smallest resolved scales, given by the filtered subgrid component, is similar to the structure of the largest unresolved scales, given by the subgrid component. This allows the following assumption, remembering the notation is for the LES filter and its respective difference term, rather than the mean velocity and it's time fluctuation.

$$\overline{u}_i' \approx u_i'$$

With this substituted into the decomposed subgrid term, the Leonard term remains the same, whilst the Reynolds and Cross terms reduce. This leaves the model in a calculable form.

$$t_{ij} = \overline{\overline{u}_i \overline{u}_j} - \overline{\overline{u}_i}\,\overline{\overline{u}_i} \qquad (4.33)$$

Two extensions have been proposed. One, by Hoiruti (1997), was simply to re-filter the whole term. Liu et al. (1994) proposed the other, using a different second filter, given in equation 4.34 below.

$$t_{ij} = \overleftrightarrow{\overline{u}_i \overline{u}_j} - \overleftrightarrow{\overline{u}_i}\,\overleftrightarrow{\overline{u}_j} \qquad (4.34)$$

In physical space, where the filter width is usually the cell width and a top hat filter is used, this is a necessary extension, since the original model could give a zero value if the simplest numerical filter is applied. The second and subsequent filtering operations would not alter the values further than the first filter. Alternatively, the first filter can be given a width wider than the cell width.

These models give good correlation with the actual subgrid terms, as found with a priori testing, and can describe backscatter. Winckelmans (1998) has shown the model to have a priori correlation with DNS of 0.7 upwards, using the same filter, but with a second filter twice the width the correlation is reduced to 0.5. Also, they are found not to be dissipative enough in actual simulations. This is a serious problem, overcome with mixed models. This had led to recommendations of the use of a multiplicative constant to increase the dissipation. However, the model would lose its Galilean invariance (Speziale, 1985).

4.11 Leonard Model

Leonard (1974) introduced a model through the Taylor expansion of the filtered components, which has a number of variants. The original and second listed models use a Gaussian filter, the last uses with a box filter, width $\overline{\Delta}$.

$$\overline{\overline{u}_i\overline{u}_j} = \overline{u}_i\overline{u}_j + \overline{\Delta}^2 \frac{\partial \overline{u}_i}{\partial x_k}\frac{\partial \overline{u}_j}{\partial x_k} + O(\overline{\Delta}^4) \quad \text{Leonard (1974)} \quad (4.35)$$

$$\overline{u_i u_j} = \overline{u}_i\overline{u}_j + \overline{\Delta}^2 \frac{\partial \overline{u}_i}{\partial x_k}\frac{\partial \overline{u}_j}{\partial x_k} + O(\overline{\Delta}^4) \quad \text{Winckelmans (1998)} \quad (4.36)$$

$$\overline{\overline{u}_i\overline{u}_j} = \overline{u}_i\overline{u}_j + \frac{\overline{\Delta}^2}{24}\frac{\partial^2 \overline{u}_i\overline{u}_j}{\partial x_k{}^2} + O(\overline{\Delta}^4) \quad \text{Kwak et al. (1975)} \quad (4.37)$$

Prior to this, Lilly (1967) had suggested the use of the first term in the expansion. In the Leonard and Kwak versions the Cross and Reynolds terms were not modelled. The difference in the coefficients is dependent on the choice of filter, and the function to be expanded. Leonard uses the Gaussian filter, whereas Kwak uses the box filter. The Leonard model expands the velocity variables and multiplies them together,

whereas the Kwak version expands the multiple, $\overline{u}_i\overline{u}_j$, as a single function, resulting in the second derivative term, rather than the first derivative terms. The Winckelmans (1998) formulation does incorporate all the terms, but the derivation is mysterious. The $O(\overline{\Delta})$, $O(\overline{\Delta}^3)$ terms vanish due to the symmetry of the filter functions.

Winckelmans notes that the Cross terms have been found to be of similar magnitude to the Leonard term and Liu et al. (1994) show this experimentally to be the particular case of jets and plumes. Also that increasing the order of accuracy of the expansion beyond second does not result in any improvement.

Leonard's formulation with the box filter is used because it clearly adheres to the realizability conditions, which the Kwak model is not constrained to.

The scalar fluxes can be modelled analogously.

$$\overline{\overline{u}_i\overline{T}} = \overline{u}_i\overline{T} + \frac{\overline{\Delta}^2}{12}\frac{\partial\overline{u}_i}{\partial x_k}\frac{\partial\overline{T}}{\partial x_k} + O(\overline{\Delta}^4) \qquad (4.38)$$

A formula for the Cross terms was derived in a similarly to Kwak et al. (1975).

$$\overline{\overline{u}_i u'_j} = \frac{\overline{\Delta}^2}{24}\overline{u}_i\frac{\partial^2\overline{u}_j}{\partial x_k{}^2} + O(\overline{\Delta}^4) \qquad \text{Clark et al. (1977)} \qquad (4.39)$$

The benefits and limitations of the model are essentially the same as for the Bardina model.

4.12 Mixed Models

There are two natural types of mixed model.

$t_{ij} = \frac{1}{2}(A+B)$ Type 1 (4.40)

$t_{ij} = L + C + R$ Type 2 (4.41)

Bardina et al. (1980) were the first to propose a mixed model. They proposed a type 1 model using the Smagorinsky combined with the Bardina. This is appropriate since

both are models for the whole stress, and it combines the dissipation of the Smagorinsky with the structural accuracy of the Bardina.

$$t_{ij} = \tfrac{1}{2}(-2u_{sgs}\bar{S}_{ij} + \overline{\bar{u}_i\bar{u}_j} - \bar{\bar{u}}_i\bar{\bar{u}}_j) \qquad (4.42)$$

Although little used until they were revived with the advent of dynamic models, these were probably the best models available. However, since in practical simulations the correlation between the SGS models and their real counterpart is less important than the main flow characteristics being captured, the Smagorinsky model dominated.

Type 2 models mix separate models of the different components of the Leonard decomposition. The Cross terms can be modelled as identical to the Leonard term. An example would be the one-equation model with the Leonard model, with or without explicitly modelling the Cross terms.

4.13 Estimation Model

A more recent model is the estimation model, introduced by Domaradzki and Saiki (1997). This is a similarity model, like the Bardina model, but estimates a finer velocity field from which to evaluate the SGS terms. Extensive experimental work, such as Domaradzki and Rogello (1990), and by Kerr et al. (1996), show that about 75% of the energy transfer and interaction from the SGS motion to the grid scale motion is due to eddies with no more than double the frequency of the cutoff filter frequency. The original model was developed in spectral space. Domaradzki and Loh (1999) extend this to physical space. Here, the assumption is that estimating the velocity on a grid with the cell width being half that of the LES grid cell width, is enough to provide most of the information required for accurate LES modelling.

$$t_{ij} = \overline{u_i u_j} - \bar{u}_i\bar{u}_j \approx \overline{\tilde{\bar{u}}_i\tilde{\bar{u}}_j} - \tilde{\bar{u}}_i\tilde{\bar{u}}_j \qquad (4.43)$$

The tilde, $\tilde{u}_i$, denotes the velocity at this fine grid region.

There are two steps in the procedure, although only the first is necessary. The first is to estimate the fine grid filtered velocity field. This must have the property that

$\tilde{\bar{u}}_i = \bar{u}_i$

The solution of the tridiagonal system

$$[\tilde{u}_i(x_{n-1}) + 4\tilde{u}_i(x_n) + \tilde{u}_i(x_{n+1})]/6 = \bar{u}_i \tag{4.44}$$

gives the estimated field values. This assumes that the estimate filter is a top hat with a filter width equal to twice that of the coarse grid cell width and that Simpsons rule is used for integration. Other methods can also be used. With this field, the SGS terms can be evaluated. Note that this filter is in one dimension only. The effect of a full deconvolution in all axes has not been considered, and would be considerably more computationally expensive.

However, this process does not include any information from frequencies higher than those extracted in the initial filter process of the governing equations. The 'dynamic' step involves these. The convective term doubles the frequency of the modes in spectral space. In physical space these can be fully resolved on a grid cell width half that of the original. The velocity field evaluated in step one is interpolated on to the fine mesh.

Let C be the convective term.

$$C = -\tilde{u}_j \frac{\partial \tilde{u}_i}{\partial x_j} \tag{4.45}$$

We need to derive only the subgrid scale effects from this term. The large-scale advection term is taken out, and then the term is filtered and the difference taken, leaving only scales less than those on the original grid.

$$N' = N - \overline{N} \tag{4.46}$$

where $N = -(\tilde{u}_j - \overline{\tilde{u}}_j)\frac{\partial \tilde{u}_i}{\partial x_j}$ (4.47)

These small scales provide a significant dissipative effect. It is these that give it its advantage over other similarity models, which do not provide enough dissipation. Here though, the dissipative effect is added directly to the estimated velocity field. This does not damage the accuracy of the SGS terms.

It is assumed the fluctuations occur over the time period of a single large eddy, and the correction term can be incorporated as

$$\tilde{u}_i^{corrected} = \tilde{u}_i + \tilde{u}_i' \tag{4.48}$$

where

$$\tilde{u}_i' = qN' \tag{4.49}$$

and q is the time scale. This is evaluated by assuming that the local subgrid scale energy is equal to the energy of the smallest resolved scales.

$$q = R(\frac{(\tilde{u}_i - \tilde{\bar{u}}_i)^2}{N'^2})^{1/2} \quad (4.50)$$

and $R = 0.5$

This model has been tested in channel flow and found to give good results, for both the dissipation and the SGS terms. The dissipation is lowered without the dynamic step leading to less accurate large scale dynamics. It has not yet been used with the energy equation, although the extension is straightforward. The approximated pre-filtered field is calculated with the same tridiagonal system as above, and the correction terms for the temperature equation are evaluated as follows.

$$N = -(\tilde{u}_j - \tilde{\bar{u}}_j)\frac{\partial \tilde{T}}{\partial x_j} \quad (4.51)$$

$$q = R(\frac{(\tilde{T} - \tilde{\bar{T}})^2}{N'^2})^{1/2} \quad (4.52)$$

4.14 Dynamic models

Dynamic models have caused somewhat of a stir in the development of SGS models, and have given a new lease of life to otherwise forgotten models. The appeal is two-fold. Firstly, their general applicability to any model, stress, flux, or otherwise, which has an empirical constant, and secondly, their ability to overcome many of the problems associated with empirical constants. The first published account was the dynamic Smagorinsky model of Germano et al. (1991), based on an algebraic identity, which Germano (1992) generalises for use with any other appropriate model.
Considering the double filtering of the NS equations he observed the following relation.

$$\overleftrightarrow{u_i u_j} - \overleftrightarrow{\bar{u}_i \bar{u}_j} = \overleftrightarrow{u_i u_j} - \overleftrightarrow{\bar{u}_i \bar{u}_j} + \overleftrightarrow{\bar{u}_i \bar{u}_j} - \overleftrightarrow{\bar{u}_i \bar{u}_j} \quad (4.53)$$

This can be rewritten

$$T_{ij} = \overleftrightarrow{t}_{ij} + L_{ij} \quad (4.54)$$

where $T_{ij} = \overleftrightarrow{u_i u_j} - \overleftrightarrow{\bar{u}}_i \overleftrightarrow{\bar{u}}_j$ (4.55)

$$t_{ij} = \overleftrightarrow{u_i u_j} - \bar{u}_i \bar{u}_j \quad (4.56)$$

and $L_{ij} = \overleftrightarrow{\overline{u}_i \overline{u}_j} - \overleftrightarrow{\overline{u}_i}\overleftrightarrow{\overline{u}_j}$ (4.57)

This relates exactly the subgrid stress of the double filtered field to the filtered (with the second filter) subgrid stress of the single filtered field via a quantity calculable from the filtered variables.

Putting an arbitrary SGS model into the stress tensors, which takes a form such that $t_{ij} = Cf(\overline{u}_i)$, and $T_{ij} = Cf(\overleftrightarrow{\overline{u}}_i)$ we find

$$Cf(\overleftrightarrow{\overline{u}_i}) = \overleftrightarrow{Cf(\overline{u}_i)} + L_{ij} \tag{4.58}$$

This over-prescribes the value of C, since a group of equations are found.

It has been suggested (Ghosal, 1999) that a lack of similarity in the filter causes problems for these relations. It is true that for the top hat filter, a double filter does not result in another top hat filter, but this does not appear to be a problem. Carati and Eijnden (1997) reformulate the dynamic procedure in a consistent manner, without altering the form of any of the equations. The filter is no longer a top hat filter, though.

$$Cf(\overleftrightarrow{\overline{u}_i}) = C\overleftrightarrow{f(\overline{u}_i)} + L_{ij} \qquad \text{Type 1 evaluation.} \tag{4.59}$$

$$C^{n+1} f(\overleftrightarrow{\overline{u}_i}) = \overleftrightarrow{C^n f(\overline{u}_i)} + L_{ij} \qquad \text{Type 2 evaluation.} \tag{4.60}$$

n in the type 2 evaluation is the time step. A problem is that the constant is typically taken out the filter term, to form the type 1 evaluation. Since it is only locally a constant, this is not strictly allowed. Lilly (1991) proposes that if the flow has at least one homogeneous axis, the constant can be evaluated consistently by filtering only in the homogeneous axes. Ghosal et al. (1995) provide an iterative method, suitable for completely inhomogeneous flows, such as the thermal plume to overcome this. This method can be unstable. Piomelli and Liu (1995) and Davidson (1997) use the type 2 evaluation which is marginally more accurate than type 1, and state that it is more stable than that of Ghosal.

The dynamic models assume that the filter and test filter are in the inertial range. There is a problem with the constant tending to zero with grid refinement (Meneveau

and Lund, 1996). If the filter is in the dissipation range, then the constant will be evaluated to match the dissipation of the test filter width, i.e. there will be too much dissipation. The point is that if the grid is too fine, but not very much too fine, errors will be introduced.

4.15 Dynamic Smagorinsky Model

Germano et al. (1991) introduced the model for incompressible flow. The extension to compressible flow and scalar transport followed shortly after by Moin et al. (1991). The scalar transport (temperature equation) is resolved using the Germano identity for the turbulent Prandtl number.

The SGS for the momentum equations is found first, solving for C with type 1 evaluation.

Equation 4.55 is rewritten.

$$L_{ij} = T_{ij} - \overleftrightarrow{t}_{ij} = \overleftrightarrow{\overline{u}_i \overline{u}_j} - \overleftrightarrow{\overline{u}}_i \overleftrightarrow{\overline{u}}_j \tag{4.61}$$

$$\overline{t_{ij}} = -2C\Delta^2 \overleftarrow{\left|\overline{S}\right| \overline{S}_{ij}} \tag{4.62}$$

$$T_{ij} = -2C\overleftrightarrow{\Delta}^2 \left|\overleftrightarrow{\overline{S}}\right| \overleftrightarrow{\overline{S}}_{ij} \tag{4.63}$$

The usual Smagorinsky model is put into the stress tensors.

$$\text{Let } M_{ij} = (-2\overleftrightarrow{\Delta}^2 \left|\overleftrightarrow{\overline{S}}\right| \overleftrightarrow{\overline{S}}_{ij} + 2\Delta^2 \overleftarrow{\left|\overline{S}\right| \overline{S}_{ij}}) \tag{4.64}$$

$$\text{Then } C = \tfrac{1}{2} L_{ij} / M_{ij} \tag{4.65}$$

This gives six separate equations for C. This is over-specified for the eddy viscosity, and needs to be evaluated (although nobody has yet tried the different constants for the different stresses). The denominator, M_{ij}, can go to zero causing instability and ill definition. Lily (1992) suggested a least squares method, minimising the error. This has become the standard method.

$$C = \tfrac{1}{2}(L_{ij} M_{ij} / M_{kl} M_{kl}) \tag{4.66}$$

This is an improvement but does not alleviate the problem entirely.

An early claim was that the model would be able to represent backscatter, and indeed the constant does become negative at points giving a negative eddy viscosity. The turbulent viscosity is usually larger than the molecular viscosity resulting in a negative effective viscosity. Lund et al. (1993) investigate the numerical stability of negative viscosities. With implicit Euler time-marching they show it is necessarily unstable. Using an explicit 2nd order scheme, it is shown that the negative viscosities can remain stable so long there is only a small-time correlation for the variable constant; the stronger the turbulence, the shorter the stable time-correlation. The essential conclusion is that the constant must be clipped, ensuring a non-negative value, in order to produce a stable result.

The instability caused by near zero denominators in laminar flow can also be a problem. Balaras and Benocci (1992), simulating a square duct flow, find that the constant has to be bounded above in some cases.

The turbulent Prandtl number is evaluated similarly. Let Ψ_k be the flux Leonard term, q_k be the flux, and Q_k be the test flux.

$$\Psi_k = Q_k - \overline{q_k} = \hat{\bar{u}}_k \hat{T} - \hat{\bar{u}}_k \hat{\bar{T}} \tag{4.67}$$

$$q_k = \overline{u_k T} - \bar{u}_k \bar{T} \tag{4.68}$$

$$Q_k = \hat{\overline{u_k T}} - \hat{\bar{u}}_k \hat{\bar{T}} \tag{4.69}$$

The scalar fluxes take identical form to the turbulent stresses.

Using the SGDH model for the temperature SGS flux terms gives the following.

$$\overline{q_k} = \frac{-C\Delta^2}{\mathrm{Pr}_t} \left|\bar{S}_{ij}\right| \frac{\partial \bar{T}}{\partial x_k} \tag{4.70}$$

$$Q_k = \frac{-C\hat{\Delta}^2}{\mathrm{Pr}_t} \left|\hat{\bar{S}}\right| \frac{\partial \hat{\bar{T}}}{\partial x_k} \tag{4.71}$$

$$\text{Let } \Xi_k = \left(-\Delta^2 \left|\hat{\bar{S}}\right| \frac{\partial \hat{\bar{T}}}{\partial x_k} + \Delta^2 \left|\bar{S}\right| \frac{\partial \bar{T}}{\partial x_k}\right) \tag{4.72}$$

$$\text{Then } 1/\mathrm{Pr}_t = \Psi_k / C\Xi_k \tag{4.73}$$

Again, least squares should be used for a more stable evaluation.

$$1/\mathrm{Pr}_t = \Psi_k \Xi_k / C\Xi_l \Xi_l \tag{4.74}$$

where C is the constant in the momentum flux.

A straightforward extension was proposed by Zhang and Chen (1999, 2000), the filtered dynamic Smagorinsky model (FDSM). Rather than using the regular Germano identity, they also filter it.

$$\hat{T}_{ij} - \hat{\bar{t}}_{ij} = \hat{L}_{ij} \tag{4.75}$$

Simulating indoor airflow with the Boussinesq equations, they find the error to be significantly reduced from the non-filtered model, where the errors are defined as follows.

$$\hat{err}_{ij} = \hat{L}_{ij} - \hat{T}_{ij}^{\mathrm{mod}\,el} + \hat{\bar{t}}_{ij}^{\mathrm{mod}\,el} \tag{4.76}$$

$$err_{ij} = L_{ij} - T_{ij}^{\mathrm{mod}\,el} + \bar{t}_{ij}^{\mathrm{mod}\,el} \tag{4.77}$$

They suggest that this does not have any problems with inhomogeneity, although the problems associated with the formulation of the constant under the filter are not eradicated.

Although the expectation of resolving the backscatter issue is unfulfilled by this model, it remains a considerable improvement over the Smagorinsky model. Jimenez (1995) looks into why the dynamic models work, and suggests that the effect of the dynamic relation is to choose the constant to maintain the local equilibrium balance.

4.16 Dynamic Mixed Models

The dynamic mixed model appeared soon after the Germano identity. Zang et al. (1993) use the original mixed model of Bardina et al. (1980), combining the Bardina model with the Smagorinsky model as the base model for the dynamic procedure. However, it is used in a type 2 formulation with the Smagorinsky model representing the Reynolds stresses and the Bardina model the Leonard term. The form is:

$$\bar{t}_{ij} = -2C\overline{\Delta}^2 \overleftarrow{\left|\overline{S}\right|\overline{S}_{ij}} + \overleftarrow{B_{ij}(\overline{u}_i, \overline{u}_j)} \tag{4.78}$$

$$T_{ij} = -2C\overleftrightarrow{\overline{\Delta}}^2 \left|\overleftrightarrow{\overline{S}}\right| \overleftrightarrow{\overline{S}}_{ij} + B_{ij}(\overleftrightarrow{\overline{u}}_i, \overleftrightarrow{\overline{u}}_j) \quad (4.79)$$

where $B_{ij}(\overline{u}_i, \overline{u}_j) = \overleftarrow{\overline{u}_i \overline{u}_j} - \overleftarrow{\overline{u}}_i \overleftarrow{\overline{u}}_j$ (4.80)

or $B_{ij}(\overline{u}_i, \overline{u}_j) = \overline{\overline{u}_i \overline{u}_j} - \overline{\overline{u}}_i \overline{\overline{u}}_j$ (4.81)

Equation 4.80 gives the formulation with an unspecified second filter, and Vreman et al. (1994a) give the form in equation 4.81. The distinction is that in equation 4.80, the top filter (the single arrowhead is different from the double arrowhead filters) does not depend on the filters used 'below' whether a single filter, or a double filter as is the case for the test filter. The second formulation, equation 4.81, uses whichever filter or filters are used for the variable, so for the test filter this would incorporate a total of four filter layers.

Let $G_a = \overline{\Delta}^2 \overleftarrow{\left|\overline{S}\right| \overline{S}_{ij}}$ (4.82)

$$G_b = \overleftrightarrow{\overline{\Delta}}^2 \left|\overleftrightarrow{\overline{S}}\right| \overleftrightarrow{\overline{S}}_{ij} \quad (4.83)$$

$$H_a = \overleftarrow{B_{ij}(\overline{u}_i, \overline{u}_j)} \quad (4.84)$$

$$H_b = B_{ij}(\overleftrightarrow{\overline{u}}_i, \overleftrightarrow{\overline{u}}_j) \quad (4.85)$$

Then $C = (L_{ij} + H_a - H_b)/(G_a - G_b)$ (4.86)

It was tested in a turbulent recirculating flow. The averaged results were the same as for the dynamic Smagorinsky model. The constant still needs to be clipped. Although backscatter can now occur through the addition of the Bardina model in a stable manner, since it is not a diffusive (2^{nd} derivative) term. This is acceptable; the backscatter will be mainly due to the largest of the subgrid scales, given by the Leonard term, whilst the Reynolds term we would expect to be mainly diffusive, and are given by the purely diffusive (after clipping) Smagorinsky or other eddy model.

4.17 Localized Dynamic Model

This model is the dynamic version of the one-equation model. A number of authors have developed it independently with different considerations (Wong, 1992, Ghosal et

al, 1995, Kim and Menon, 1995, Davidson, 1997), although the derivation of Ghosal et al. (1995) is the most thorough and is the most cited reference.

The first part applies the Germano identity to the subgrid model.

$$t_{ij} = C\overline{\Delta}k^{1/2}\overline{S}_{ij} \tag{4.87}$$

$$T_{ij} = C\hat{\overline{\Delta}}K^{1/2}\hat{\overline{S}}_{ij} \tag{4.88}$$

Using type 1 evaluation for C, let

$$M_{ij} = \hat{\overline{\Delta}}K^{1/2}\hat{\overline{S}}_{ij} - \overline{\Delta}\overbrace{k^{1/2}\overline{S}_{ij}} \tag{4.89}$$

Then

$$C = \frac{L_{ij}M_{ij}}{M_{kl}M_{kl}} \tag{4.90}$$

K can be evaluated from a second transport equation, or from the relation

$$K = \hat{k} + L_{ii} \tag{4.91}$$

This is all that is required for the eddy viscosity constant, but the models used in the transport equation can also be dynamically calculated. Following Ghosal et al. (1995), adding buoyancy terms, and using type 2 constant evaluation, we consider the subgrid kinetic energy transport equation and the test filtered subgrid energy transport equation.

$$TRANS(k) = P_k - C_1\frac{k^{3/2}}{\overline{\Delta}} + C_2\frac{\partial}{\partial x_j}(\overline{\Delta}k^{1/2}\frac{\partial k}{\partial x_j}) + B_k \tag{4.92}$$

$$TRANS(K) = P_K - C_1\frac{K^{3/2}}{\overline{\Delta}} + C_2\frac{\partial}{\partial x_j}(\overline{\Delta}K^{1/2}\frac{\partial K}{\partial x_j}) + B_K \tag{4.93}$$

The buoyancy term may introduce a third constant. If this has not been established already, the Bardina or Leonard model may be used to eliminate the need to evaluate the constant.

Wong (1992) gives a dynamic relation for the dissipation constant C_1, but Ghosal et al. (1995) find it unusable for high (turbulent) Reynolds numbers, since information in the equation is lost to more dominant terms.

C_2 is attained with the following relation.

$$F_j - \overleftrightarrow{f}_j = Z_j \equiv \overleftrightarrow{\bar{u}}_j \overrightarrow{(\bar{p} + k + \bar{u}_i \bar{u}_i / 2)} - \overrightarrow{\bar{u}_j (\bar{p} + k + \bar{u}_i \bar{u}_i / 2)} \quad (4.94)$$

Substituting the flux models into F_j and f_j gives

$$C_2^{n+1} = (Z_j + \overleftarrow{\bar{\Delta} C_2^n k^{1/2} \frac{\partial k}{\partial x_j}})(\overleftrightarrow{\bar{\Delta}} K^{1/2} \frac{\partial K}{\partial x_j})^{-1} \quad (4.95)$$

$$F_j = C_2 \bar{\Delta} K^{1/2} \frac{\partial K}{\partial x_j} \quad (4.96)$$

$$f_j = C_2 \bar{\Delta} k^{1/2} \frac{\partial k}{\partial x_j} \quad (4.97)$$

C_1 can now be calculated by substituting 4.92 into 4.93 and filtering 4.92. It is slightly simpler just to assume the filtered transport of k is equal to the transport of K.

$$C_1^{n+1} = (\overleftrightarrow{P_k} + P_K + \frac{\partial \overleftrightarrow{f_j}}{\partial x_j} + \frac{\partial F_j}{\partial x_j} + \overleftrightarrow{B}_k + B_K + \overleftarrow{C_1^{n+1} \frac{k^{3/2}}{\bar{\Delta}}}) / (\frac{K^{3/2}}{\overleftrightarrow{\bar{\Delta}}}) \quad (4.98)$$

Davidson's (1997) formulation lets $C_2 = 0$, assuming it is a negligible term. This also simplifies the evaluation of C_1.

As mentioned earlier the eddy viscosity and the subgrid energies must not be allowed to become negative. These are the only constraints on the model.

4.18 Other Models

Sagaut (2000) gives a thorough review of the current models, although they are being developed very rapidly. Ding et al. (2001) develop two-component eddy viscosity and eddy diffusivity models, used in the atmospheric simulations, which split the turbulent viscosity and Prandtl numbers respectively into mean and fluctuating components. The earliest model overlooked in this work is the full subgrid transport modelling of Deardorff (1973). There have not been any attempts so far to bridge the gap between the one equation models and six equation full models similarly to the RANS models, where two, three, and four transport equation models can be found. There are a number of non-linear models – Lund and Novikov (1992) give one such approach using a Taylor expansion akin to the Leonard model. Jaberi and Colucci (2003)

extend the Bardina model to the 'serial decomposition' model using structural approximations for the Reynolds and Cross terms also. Scotti and Meneveau (1997) introduced a fractal interpolation scheme. Using an iterative fractal-generating scheme, relating to the grid scale structures, the subgrid scales are explicitly approximated and the filtered subgrid terms can be calculated directly. Sagaut et al. (2000) derive the dynamic relations between models with N parameters, through the addition of more filters in accordance with the number of extra parameters, resulting in a solvable set of algebraic equations.

The MILES (Monotonically Integrated LES) model (Fureby and Grinstein, 2002), uses TVD discretisations to implicitly model the subgrid term. It has received better attention than Kawamura's (1985) suggestion that a subgrid model was not needed.

Chester et al. (2001) recently introduced dynamic modelling without the use of test filters. Taylor expansions are used to evaluate directly the required filtered quantity.

4.19 Review of Model Applications

There have been many applications of LES modelling, covering as diverse fields as wind power engineering (Murikami, 1997), nuclear power , fire simulations (Baum et al., 1994), electrical engineering, and many more. Some of these simulations are reviewed and the key issues are raised.

Using the (non-dynamic) mixed Smagorinsky-Bardina model, Piomelli et al. (1989) performed simulations of transpired channel flow. They found the simulation to be in good agreement with experiment. A Gaussian filter was used. Madabhushi and Vanka (1991) simulated a square duct using the fixed Smagorinsky model, and showed the secondary recirculating flow to be well captured. This had not been possible for RANS simulations of less complexity than the algebraic stress models, until Speziale (1987) developed the non-linear k-ε model (Sanderson, 2001). However, these have a varying number of empirical constants, and the lack of these is considered a significant advantage in LES. The RANS models require a significant amount of tweaking to accurately capture the flow. McGratten et al. (1996) demonstrate the capturing of secondary circular motions, simulating a smoke plume above an oil fire.

They use the static Smagorinsky model and successfully capture the two counter-rotating vortices found experimentally in such flows.

Ansari and Strang (1996) find that 'a subgrid-scale model that correctly represents the effect of the subgrid-scales on the large scales has not been available'. They simulate a mixing layer with both a finite volume low Mach number scheme and a pseudo-spectral incompressible scheme. They find the pseudo-spectral code gives good results, while the LMN scheme gives satisfactory results for all results. They support the findings that the dynamic mixed models give better a priori results than pure dissipation models, but that the average quantities are not significantly affected. Also, they find transition damped in the LMN code by the LES models, although in high-resolution simulations they find that the static Smagorinsky model is overly dissipative, and results in an exaggeration of the turbulent fluctuations.

For the Smagorinsky model and various dynamic versions, Salvetti and Bannerjee (1995) show a significant improvement in the a priori modelling when the Leonard terms are included, and the Cross terms are modelled as equal to the Leonard terms.

Bastiaans et al. (1998), simulating confined thermal plumes, use the Smagorinsky model and the dynamic Smagorinsky model. Demonstrating considerable intermittency, they conclude the necessity of the dynamic model, but use a fixed temperature flux model, suggesting the (non-turbulent) Prandtl number should be above unity to become a significant term, and necessitate the use of the dynamic procedure. Harvat et al. (2001) show that the Prandtl number is more important to conduction rather than convection dominated flows, but that its significance increases with Rayleigh number.

Zang et al. (1993) tested their dynamic mixed model in a 3d lid-driven cavity and found their model to be, a posteriori, an improvement over the dynamic Smagorinsky. The model constant was significantly reduced in the mixed version.

Moin and Kim (1982) performed a channel flow simulation, using a Fourier solution technique on stretched grids. They demonstrated that the mixed Leonard models do give improved results over the pure eddy models *so long as the discretisation schemes are higher than second order*. This is clear from their definition since the model is identical to a second order truncation error. While it will not change the formal accuracy of the model, it does not seem a sufficient reason to exclude the model. It can be viewed as doubling the error by excluding it. They find good turbulent statistics of the resolved scales, i.e. the Reynolds averages of the grid scale variables

and second moments are good. They successfully used the predecessor to the anisotropic cell width of Scotti et al. (1993), just using the cell width in the mean flow direction (Deardorff, 1970).

The fully localised dynamic model is shown to be a slight improvement over the dynamic one equation model in which the constants are not locally evaluated dynamically, by Krajnovic et al. (1999), simulating flow over a cubic obstacle. They run the simulation without a SGS model, and show significant degradation of the results.

A dynamic (non-mixed) similarity model is compared with the dynamic Smagorinsky by Cottet and Vasilyev (1998). The similarity model is found to be more dissipative in channel flow, better capturing the anisotropic behaviour of near-wall flow. The cost of this is breaking the Galilean invariance property of the model.

4.20 Other Issues

It has been shown that the constant found using the dynamic models adjusts according to the numerical scheme used. Najjar and Tafti (1996) show a more dissipative 5^{th} order upwind scheme had a lower value than the non-dissipative 2^{nd} order central scheme, resulting in similar overall dissipation.

The problems of backscatter have been discussed earlier. If an eddy model is to be used, the turbulent (more exactly, the total) viscosity must be non-negative. Carati et al. (1995) introduce a random component to the viscosity, similarly to Lund et al. (1993) who had already shown the method to be stable. They find the energy spectra to be improved by the inclusion of this term. However, the nature of this random term is arbitrary, and not based on any physics. In this case white noise is added, ensuring the time correlation is low for stability.

The effect of the numerical scheme is obviously an important issue in a simulation. Ragab et al. (1992) investigate a number of finite difference schemes through the simulation of a compressible mixing layer. A MacCormack scheme, 2^{nd} order in time and 4^{th} order in space for the convective terms, and 2^{nd} order for the subgrid terms is considered alongside a 2^{nd} order Runge-Kutta scheme with a 3^{rd} order upwind convective scheme, again with 2^{nd} order evaluation of the subgrid components. The MacCormack scheme crashes without a subgrid model. This is due to a build-up of

energy in the high frequency modes which has no mechanism for dissipation, which is shown in the time histories of different energy ranged modes. The subgrid model, here the Smagorinsky, is necessary for the dissipation of this energy. Using a mixed model, the Leonard term is found not to affect the small-scale energy distribution with the MacCormack scheme and is not considered further. The Smagorinsky model does affect the modes in both cases, but in order to have equal spectrum distributions resulting the usual constant of 0.1 with the central schemes have to be reduced to a value of 0.05. In this work, the square of the constants are usually taken, giving the usual 0.01 a reduction to 0.0025, indicating the dissipative nature of the scheme has left only a quarter of the energy left for the subgrid term to deal with. This is a clear sign of the importance of the dynamic models, but also gives credence to the work of Kawamura (1985) in which he uses a 3^{rd} order upwind convective scheme to simulate channel flow and a transitional duct flow without the use of a subgrid model. He reports satisfactory results; that the laminar flow and the transition are well captured, and that the averages are reasonable. There is room for improvement, but approximate results are easily and reasonably accurately captured.

Peng and Davidson (2001) use a 2^{nd} order central implicit scheme, and use the dynamic Smagorinsky, the dynamic buoyancy-modified Smagorinsky, and the dynamic SGDH model to simulate buoyant cavity flow. These are compared to their static counterparts. The static buoyancy-modified Smagorinsky model gives a degradation of results when compared with the static Smagorinsky, but its dynamic version is equal to the dynamic Smagorinsky. The dynamic SGDH model is not found to give any significant improvement over the static model.

Chapter 5

Numerical Method

5.1 Introduction

The numerical method is inevitably very important to the results. Three main qualities are desirable – accuracy, speed, and simplicity. However, the first choice was whether to use finite difference or finite volume techniques. Finite difference methods were chosen for this work mainly due to the history of LES being developed (when not using spectral methods, which are not used for their lack of grid flexibility) with finite difference schemes (Smagorinsky (1963), Ferziger (1977), Kim and Moin (1985)), although finite volume methods are now used equally, for example Bastiaans et al. (2000).

Typically in DNS high order schemes are used for both space and time discretisations. In LES 2^{nd} order time discretisations are almost always used, although the spatial discretisations range from 2^{nd} order upwards. Harlow and Welch (1965) introduced a Poisson solver method on a staggered grid, the likes of which have been widely used since. This scheme combined with a predictor-corrector method, Ferziger and Peric (1999), was used to solve the Boussinesq equations initially in this work, but the extension to the LMN equations was found to be unstable. Alternative methods are the Runge-Kutta schemes, 2^{nd} or 4^{th} order in time, or the projection schemes as introduced by Chorin (1968). Brown et al. (2001) report the boundary conditions of Runge-Kutta methods to be difficult to handle, and develop the projection methods to arbitrary accuracy. Semi-implicit projection schemes were developed by Kim and Moin (1985) in which the viscous terms are implicitly handled in the discretisation while the convective terms are explicitly handled. Another method which is a semi-implicit scheme, but in which all variables, including the pressure term, are calculated locally, was developed by Bravo et al. (1999). This was investigated with a 2d serial

code, but appeared not to be suitable for parallelisation. Since it is not a well-tested method, it was not pursued further.

A reduced form of the semi-implicit fractional step, projection method of Najm et al. (1998) was used. It is the scheme used by Zhou et al. (2001), and Boersma (1998). The convective and diffusive terms are evaluated locally, and the usual Poisson equation is required for the pressure terms. Staggered grids were used and simulations were run on a uniform grid.

The general idea behind incompressible and LMN solvers is presented. An informal combination of differential terms and discretised terms is used, similarly to the notation of Ferziger (1977). Remembering the continuity and momentum equations:

$$\frac{\partial r}{\partial t}+\frac{\partial r u_i}{\partial x_i}=0 \tag{5.1}$$

$$\frac{\partial r u_i}{\partial t}+\frac{\partial r u_i u_j}{\partial x_j}=-\frac{\partial \Pi}{\partial x_i}+\frac{\partial^2 u_i}{\partial x_j{}^2}-\frac{\partial t_{ij}}{\partial x_j} \tag{5.2}$$

Discretising the time derivative of the momentum equation can be given by

$$(ru_i)^{n+1}-(ru_i)^n=\Delta t(R_i^n-\frac{\partial \Pi^n}{\partial x_i}) \tag{5.3}$$

if R_i is the sum of the convection, diffusion and any source terms (including the subgrid stresses). Taking the divergence of the three momentum equations and rearranging gives

$$\nabla^2\Pi^n=\nabla R_i^n-(\nabla(ru_i)^{n+1}-\nabla(ru_i)^n)/\Delta t \tag{5.4}$$

The critical point is to ensure continuity is maintained at time-step n+1. This is done by substituting the continuity equation in at n+1, giving

$$\nabla^2\Pi^n=\nabla R_i^n-(-\frac{\partial r}{\partial t}^{n+1}-\nabla(ru_i)^n)/\Delta t \tag{5.5}$$

This is the Harlow and Welch (1965) formulation extended to the LMN equations, and is identical to the fractional step principle mathematically, except that all the terms are added together to make the next velocity in a single step. For the fractional step method the first calculation is made

$$ru_i^{n^*}=ru_i^n+\Delta t R_i \tag{5.6}$$

and substituting this gives

$$\nabla^2 \Pi^n = (\frac{\partial r}{\partial t}^{n+1} - \nabla(ru_i)^{n^*})/\Delta t \tag{5.7}$$

5.2 Numerical Scheme

Najm et al's (1998) scheme was developed for the LMN equations but is clearly easily altered for the Boussinesq equations also. It is an extension and particular implementation of the general form just given.

$$\text{Let } R_i = -\frac{\partial r u_i u_j}{\partial x_j} + \frac{1}{\text{Re}}\frac{\partial^2 u_i}{\partial x_j^{\,2}} + \frac{1}{Fr}(r-1)g_i - \frac{\partial t_{ij}}{\partial x_j} \tag{5.8}$$

$$\text{Let } L = -\frac{\partial u_j T}{\partial x_j} + \frac{1}{r\,\text{Re}\,\text{Pr}}\frac{\partial^2 T}{\partial x_j^{\,2}} - \frac{\partial q_j}{\partial x_j} \tag{5.9}$$

Predictor part:

1. Evaluate $R_i \equiv \frac{\partial r u_i}{\partial t} + \frac{\partial \Pi}{\partial x_i}$ and $L \equiv \frac{\partial T}{\partial t}$ at time-step n, storing values for previous time step, using 5.1 and 5.2 above.

2. Evaluate density time derivative (this comes from taking the derivative of the equation of state).

$$\frac{\partial r}{\partial t} = -\frac{r}{T}\frac{\partial T}{\partial t} \tag{5.10}$$

$$\left.\frac{\partial r}{\partial t}\right|^n = -\frac{r}{T}L^n \tag{5.11}$$

at time-step n, storing values for previous time step.

3. Evaluate predicted density, r^*

$$\frac{r^* - r^n}{\Delta t} = \frac{3}{2}\left.\frac{\partial r}{\partial t}\right|^n - \frac{1}{2}\left.\frac{\partial r}{\partial t}\right|^{n-1} \tag{5.12}$$

4. Calculate predicted temperature from equation of state.

5. Calculate intermediate velocity field

$$\frac{r^{*}\hat{u}_i - r^{n}u_i^{n}}{\Delta t} = \frac{3}{2}R_i^{n} - \frac{1}{2}R_i^{n-1}. \tag{5.13}$$

6. Solve the Poisson equation for the current time step. This ensures the continuity of the predicted velocity.

$$\nabla^2\Pi^{n} = \frac{1}{\Delta t}[\nabla.(r^{*}\hat{u}_k) + \left.\frac{\partial r}{\partial t}\right|^{*}] \tag{5.14}$$

$$\left.\frac{\partial r}{\partial t}\right|^{*} = \frac{1}{2\Delta t}(3r^{*} - 4r^{n} + r^{n-1}). \tag{5.15}$$

7. Evaluate the predicted velocities

$$\frac{r^{*}u_i^{*} - r^{*}\hat{u}_i}{\Delta t} = -\frac{\partial\Pi^{n}}{\partial x_i} \tag{5.16}$$

Corrector part:

8. Calculate predicted temperature derivative, L^{**}, using predicted variables.

9. Evaluate new predicted density derivative $\left.\frac{\partial r}{\partial t}\right|^{**}$ at time step $n+1$ with predicted values.

10. Evaluate r at time step $n+1$ with

$$\frac{r^{n+1} - r^{n}}{\Delta t} = \frac{1}{2}\left.\frac{\partial r}{\partial t}\right|^{n} + \frac{1}{2}\left.\frac{\partial r}{\partial t}\right|^{**} \tag{5.17}$$

11. Evaluate corrected temperature at time step $n+1$, again with equation of state.

12. Calculate a new intermediate velocity:

$$\frac{r^{n+1}\hat{u}_i - r^{n}u_i^{n}}{\Delta t} = \frac{3}{2}R_i^{n} - \frac{1}{2}R_i^{n-1} \tag{5.18}$$

13. Solve the corrected Poisson equation

$$\nabla^2\Pi^{n} = \frac{1}{\Delta t}[\nabla.(r^{*}\hat{u}_k) + \left.\frac{\partial r}{\partial t}\right|^{**}] \tag{5.19}$$

14. Evaluate corrected velocities from

$$\frac{r^{n+1}u_i^{n+1} - r^{n+1}\hat{u}_i}{\Delta t} = -\frac{\partial\Pi^{n+1}}{\partial x_i} \tag{5.20}$$

This is a two-part method. Najm et al. (1998) assert its stability, if only the first part is used, if the maximum temperature is less than double the minimum temperature. This

method is fully 2nd order in time, even when using only the first step. This is what is done unless stability requires otherwise.

When the scheme is reduced for the Boussinesq equations, the following is used to march the temperature field.

15. $$\frac{T^{n+1}-T^{n}}{\Delta t}=\frac{3}{2}L^{n}-\frac{1}{2}L^{n-1} \qquad (5.21)$$

The projection methods have similar same boundary problems as the Runge-Kutta methods, but only at one step (the usual 4th order RK method has 5 steps, 4 of which would need special treatment, and higher order methods would have more). The problem is that the intermediate velocity term is not actually a velocity, and as such the boundary conditions given to the velocities are not strictly suitable for them. These are often overlooked as is done here, although Kim and Moin (1985) give details on how to correct the boundaries. The Harlow and Welch method avoids these boundary condition issues, but is only first order accurate in time. The above method, similar to Minion's (1991) method can also be made arbitrarily formally accurate. As many back values of R_i can be stored to make a backward time difference of any order. A predictor value could also be included in this.

The pressure term has no time derivative. Nevertheless it has been found (Brown et al. 2001) to be only first order in time. Spatial discretisations of arbitrary order can be used. 2nd order central are used in this work.

The convection and diffusion discretisations are as follows. The uniform spatial discretisations are usually 3rd order upwind for momentum convection, 4th order central for incompressible momentum diffusion, 2nd order central for LMN momentum diffusion, 2nd order TVD (Total Variation Diminishing)(superbee, see Appendix B) for temperature convection, and 4th order central for temperature diffusion.

These were chosen from a variety of available schemes. Second order TVD schemes (Sweby, 1984) are the highest order TVD schemes currently available, although 3rd order schemes are under development (Schroll, 2002). ENO (Essentially Non-

Oscillatory) schemes have higher order but do not have the absolute stability of TVD schemes. The compact schemes introduced by Lele (1992) are currently being widely implemented, particularly in DNS, giving almost spectral like accuracy, covering differing scales on arbitrary grids. The cost is that the schemes are non-local, and slower to calculate.

5.3 Boundary Conditions

Boundary conditions are clearly critical for the success of any CFD simulation. The (open) thermal plume simulations have four boundary types to consider. The inflow of the heated fluid, the turbulent outflow at the top of the domain, the entrainment inflow boundaries at the sides, and the wall boundary at the bottom surrounding the jet inflow. The wall is no-slip and does not cause any grid resolution problems typical of wall bounded LES flows because the flow is laminar there (early test simulations with free slip boundaries demonstrated the same negative average vertical velocity around the base of the plume).

5.3.1 Formulation of Boundary Conditions

Sani and Gresho (1994) review an incompressible boundary condition minisymposium, with bleak conclusions, although with a clear idea of where the important focus of future research should be. 'We believe that the most important issue for incompressible flows is that the incompressibility constraint is all-pervasive and even shows up (or should) on open boundaries', i.e. that continuity is ensured on the boundaries also, 'with the concomitant (and often awkward) result of coupling the pressure and the normal velocity there'.

In the review, the BCs $\frac{\partial u_n}{\partial n} = 0$, $P = 0$ are dismissed as over-prescribed. In 2d this is certainly the case as continuity necessitates that the tangential velocity component is also zero, since $\frac{\partial u_t}{\partial t} = 0$ (this is a spatial derivative rather than temporal, the subscript and derivative terms are tangential). This results in the boundary behaving as a wall. In 3d, the two tangential components are not so constrained leaving the normal

component also unconstrained, and *do* result in satisfactory laminar flow and continuity is ensured. If the velocity is fixed at the boundary (i.e. here, at the wall and the jet inflow) then the pressure must take a Neumann condition otherwise continuity will be broken. Both pressure and velocity being fixed is incorrect (although it can be correct in flows such as channel flow).

Using gradient boundaries for pressure and velocity (with one reference pressure point fixed) is suggested as not over-prescribed. Early test simulations in the present work found them to be very slowly divergent. This is probably due to the under-prescription, i.e. non-uniqueness of the BC's. This allows round-off errors in the pressure to very slowly push the plume over, and when it interacts with the entrainment boundaries continuity is broken and the solution diverges.

5.3.2 Inflow

Prescribing known inflow conditions is straightforward. Turbulent inflow conditions are more difficult. In most of the experiments of thermal plumes, the flow is laminar at the inlet but very rapidly becomes turbulent (typically no more than one diameter downstream, George et al., 1977, Shabbir and George, 1994). The issue becomes not to prescribe accurate turbulent data at the inlet, but just to cause sufficient instability for the onset of transition. Pera and Gebhart (1971) show that high frequency instabilities are damped, and low frequency instabilities are those that develop into turbulence in laminar plumes. Also, depending on the Grashof number the strength of temperature fluctuations can add to the speed of transition, although these effects are less at very high Grashoff numbers (high Grashoff number is similar to low Froude number in terms of strength of buoyancy). Basu and Mansour (1999) use high frequency noise to cause rapid transition along with a very fine grid around the source. This noise is not as effective on coarser grids, which are necessary with uniform grids. A successful method has been to use the function given by Menon and Rizk (1996). Zhou et al. (2001) utilise this method and find rapid transition.

The form is given by

$$v' = AV(r)\sum_{n=1}^{N} \sin(2pft/n + q) \qquad (5.22)$$

A is the fraction of the inlet velocity, $V(r)$ is the inlet velocity as a function of radius, f is the frequency constant, t is the time, and q is the angle from the centre of the source. They find the transition is not helped significantly if the azimuthal factor, q, is not used.

The effect of the sinusoidal forcing can be seen in the following:

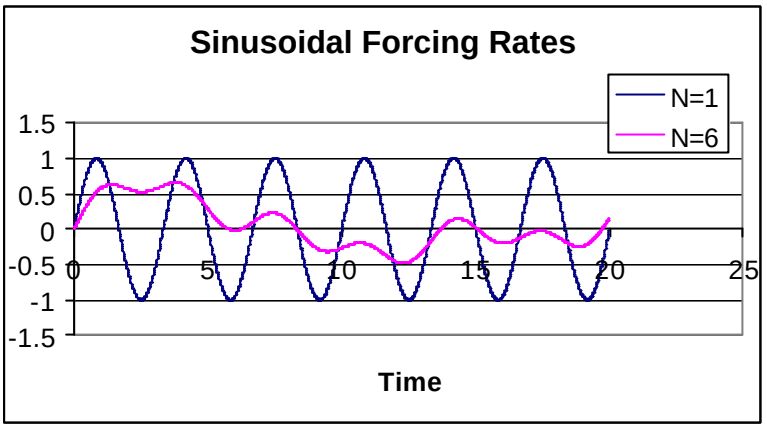

Figure 5.1 Forcing magnitude at the inlet.

This shows one full cycle for $\Delta t = 0.008$ and $f = 0.3$. Obviously the extra nodes reduce the time for one cycle proportionally, but there is also a significant reduction in the level of forcing that accompanies this. Zhou et al. (2001) use N=6. For the coarser grid used in this work a higher forcing rate was needed which is produced with N=2.

Random frequency noise can be used to introduce low frequency disturbances, without introducing any underlying structure to the flow. Using random fluctuations of the velocity component and temperature fields can be given random frequency by randomly determining the duration of each fluctuation. Every 200 time steps, the duration of the subsequent fluctuations is thus evaluated for each velocity and temperature fluctuation for each grid point across the inflow.

5.3.3 Outflow Boundary (Top)

The main problem with the top boundary is that it should not be there, i.e. there is no physically prescribed boundary condition. In the case of the entrainment boundary, more below, this is less of a problem since we know to a certain extent how it should

behave and can make use of that. We cannot predict the turbulent fluctuations of the flow at the top boundary, and there are no mathematical models to represent this. However, regardless of the accuracy of the boundary conditions they still have to be well-posed and stable. A number of schemes cause diverging oscillations which must not be allowed.

Research in the 1970's started resolving the latter issue. Non-reflecting boundary conditions were initially developed for hyperbolic systems in which all system variables can be described by propagating characteristic waves. The essence of the method is to identify outgoing and incoming characteristics at the bound and to stop all incoming waves. This means no information can come into the domain from outside, which is obviously not always a true representation, but does stop unstable oscillations. Givoli (1989) gives a review of the early works in this area. This method is typically not used with the incompressible N-S equations since the pressure term is elliptic and cannot be bounded with this method. Nevertheless Jin and Brava (1993) do develop these for the incompressible N-S momentum equations.

An alternative approach is the absorbing boundary condition. This is more often used for incompressible flows, although Hu (1996) develops them for the Euler (hyperbolic) equations. The main aspect of this method is to have a number of extra cells inside the boundary. In these cells, a damping function is used, so that the flow (or whichever variable in whichever system) has reached a condition (i.e. laminarised) that the traditional boundary conditions can accurately (and stably) treat. Oscillations are by definition reduced, but there is the extra computation time. The number of extra cells needed is problem dependent. The more are used, the less harsh the damping function, and hence the more accurate the domain will be next to the absorbing boundary.

As well as these umbrella methods, simply more accurate boundary conditions are developed, Bruneau and Fabri (1994) giving particularly good results. Unfortunately the BCs are dependent on an average flow velocity. This cannot (certainly should not) be used in the plume simulation where prescribing the outflow velocity will implicitly prescribe the entrainment velocity, which is an unknown quantity.

Local continuity is ultimately used for the velocity boundary. This behaves as an adjusted gradient boundary and consequently requires a fixed pressure (zero) for

stability. This is the chosen method. The tangential components are given a zero gradient boundary.

The absorbing boundary techniques were implemented in the code but were not found to provide any significant improvement in the results, and were consequently abandoned.

No inflow is allowed at the top for stability. This can be viewed as a clumsy but very simple and efficient non-reflecting boundary condition. This is required for stability. Wherever the BC is constrained to zero it is essential for continuity for the pressure to take a zero gradient.

5.3.4 Entrainment Boundaries (Side)

These are essentially the same as the outflow boundaries except the constraint is that flow comes in, and the tangential components are fixed to zero.

5.4 Multigrid and Poisson Solvers

The choice of Poisson solver was critical to the efficiency of the code. There were three main options: Krylov methods, multigrid methods, and fast Fourier transform (FFT) methods. The first two are iterative. It is acknowledged that the multigrid methods are the fastest available when used with suitable grids and conditions (boundary conditions and source terms). However, the Krylov methods (including conjugate gradient methods and minimum residual methods) can provide better all round performance on all types of grid. The FFT methods take a fixed amount of time no matter what the source terms and give an exact solution. The type of boundary condition alters the number of computations, although the grids must be structured suitably for a Fourier transform.

Cartesian coordinates are used, although part of the motivation behind the work is to investigate schemes readily useable on more general grids. Hess and Joppich (1997) show the multigrid methods to be more amenable to parallelisation, and hence multigrid methods are used.

Briggs (1987) gives a formal analysis of multigrid methods. However, these are the most intuitive of the fast Poisson solver methods, and are easier to understand through consideration of the grid rather than matrix operations. For the standard iterative methods where the local cells are the basis for each iteration, such as SOR or Gauss-Seidel, clearly the more cells there are in the domain, the more iterations it will take for the solution to propagate through the domain. More precisely, there are low and high frequency errors, and a coarse grid is good at rapidly reducing the low frequency errors whilst the fine grids can rapidly reduce the high frequency errors. The notion of the frequency of errors can be understood by considering the Fourier expansion of the error. The tendency is for the component with wavelength closest to the grid width to decrease the fastest. Multigrid uses this to solve the different frequency of errors by using a different grid for each scale, going from the complete domain grid, to the smallest possible grid to rapidly solve the largest wavelengths.

The 'V-cycle' is the algorithm employed here and is roughly described as follows, before a more detailed presentation is given below.

1. Iterate top-level grid with solver such as Gauss-Seidel.
2. Evaluate residual error on grid.
3. Restrict residual error as source term onto coarser grid.
4. Iterate error on coarser grid. Go to 2 until on coarsest grid.
5. Solve coarsest grid exactly.
6. Interpolate coarse grid error onto finer grid error.
7. Iterate finer grid error. Go to 6 until top-level grid is reached.

The linearity of the approximation and the error term justifies this addition of the error term.

$$\nabla^2 P = \nabla^2 P^{approx} + \nabla^2 P^{err} = S \qquad (5.22)$$

$$\nabla^2 P^{err} = S - \nabla^2 P^{approx} \qquad (5.23)$$

Each level of the multigrid solves the subsequent error terms from the previous grid.

5.4.1 2d Multigrid Poisson Solvers

The multigrid methods are typically analysed when described in a matrix form Briggs (1987), although can be far more easily and intuitively understood when considering their physical grid representation. Finite difference solvers and finite volume solvers are presented here. This difference is not strict, and an alternative perspective is simply to consider the methods to solve for an odd number of grid nodes in each axis or an even number of nodes in each axis.

5.4.2 Odd Numbered Nodes

Consider fig. 5.2 below. The small dots show the fine grid, and the circles show the coarse grid. If the coarse grid covers the whole domain the boundary could be placed either on the outer grid points or between the two outermost grid point layers. In this work, using staggered grids for the velocities, it becomes appropriate to use the outer boundary. This does not affect the main scheme but will affect the boundary conditions. There is only a single non-boundary coarse grid cell in this illustration. The first task is to evaluate the residual on the fine grid, which provides a new Poisson equation to solve; the error of the current approximation. This error is approximated at zero initially for each iteration (letting the error remain between iterations can seriously degrade convergence, or worse cause divergence). The source term for this is given by the residual error.

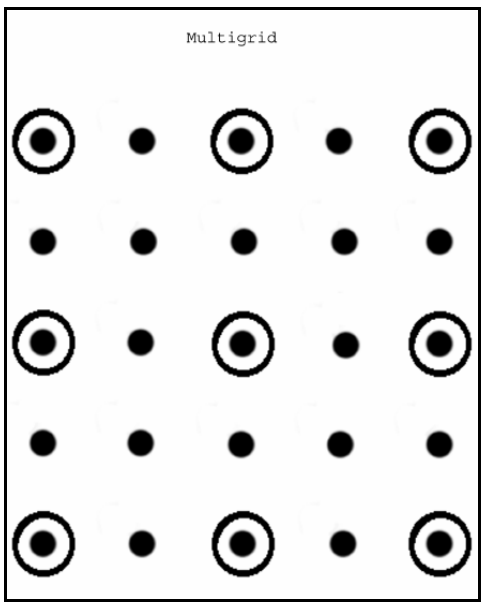

Figure 5.2 Fine and coarse grids for odd numbered multigrid. The fine grid is given by the small points and the coarse grid is given by the circles.

The key aspect of multigrid is here – in the transform of this discrete equation, into an equivalent discrete equation on a coarser grid. This is the restriction process. The most obvious method, from consideration of fig. 5.2 is to put the fine grid residual on to its respective coarse grid node. This is called an injection. This can cause stability issues if the errors are ill conditioned. In the buoyant jet flows simulated in this work, the inflow conditions cause this instability, and a higher order method is needed. This would be recommended anyway, since as well as giving stability, the convergence is significantly improved.

From a finite difference perspective, the idea is to take as much information from all the fine grid points. It can be seen that the following nine point stencil incorporates all the information from the fine grids, and spreads it evenly across the coarse grid points.

$$\begin{pmatrix} 1 & 2 & 1 \\ 2 & 4 & 2 \\ 1 & 2 & 1 \end{pmatrix} /16$$

The compound residual on the coarse grid becomes the source term. The application of this stencil is alternatively expressed in terms of a Fortran array, so the source term on the coarse grid is calculated in terms of the residuals on the fine gird.

$$\begin{aligned} source(I,J) = {} & (res(i-1,\, j+1) + 2*res(i,\, j+1) + res(i+1,\, j+1) \\ & + 2*res(i-1,\, j) + 4*res(i,\, j) + 2*res(i+1,\, j) \\ & + res(i-1,\, j-1) + 2*res(i-1,\, j) + res(i-1,\, j+1))/16 \end{aligned}$$

The upper case letters represent the coarse grid index, the lower case letters the fine grid index.

Other restriction routines can be developed somewhere between the injection and full weighted schemes. In 3d when the stencil becomes 27-point this would be a consideration, although the full weighted is used throughout this work.

The next grid is now prepared to be solved. In the illustration given, this is the coarsest grid, and should be solved exactly. Where this is not the coarsest grid, an

iterative solver should approximate the solution, before repeating the above procedure.

The inverse step of restriction is the interpolation or prolongation of the solved error back on to the fine grids. Injecting the coarse grid error back on to its fine grid counterpart, and then interpolating the error between the other grid points most easily does this. The interpolation used in this work is linear, although higher order methods could be appropriate on highly stretched grids. Here, the advantage of finite difference methods on odd numbered cells becomes apparent (if non-uniform grids are used). With a finite volume method, there becomes a question as to where the coarse cell error is being solved, since the coarse cell centre will no longer be exactly aligned with its respective fine cell centre, disallowing direct interpolation of the error onto the corresponding fine grid node. To interpolate the error using 3rd order polynomial curve fitting, a 5-point Gaussian elimination occurs for each cell. This is highly unstable when there is only very slight grid stretching since almost zero terms appear in the diagonal matrix. However, slight grid stretching becomes large stretching over a number of different grid sizes, and so can be an important factor.

After these errors are interpolated, they are added to the remaining error on the fine grid, and then further smoothed. This is repeated until the finest grid is reached, at which point the V-cycle begins again, until convergence is achieved.

5.4.3 Even Numbered Nodes

The alternative method, using an even number of nodes, works as follows. It is based on the finite volume perspective shown in fig. 5.2 below, although was developed in this work in a finite difference manner (only on a uniform grid).
The dots and circles mean as before. The first thing which is apparent is that the coarse grid cells shift their centre to the joining vertex of the four cells. The boundary cells do not move normal to the boundary, although they do move parallel to the boundary. These factors give it its advantages and disadvantages.

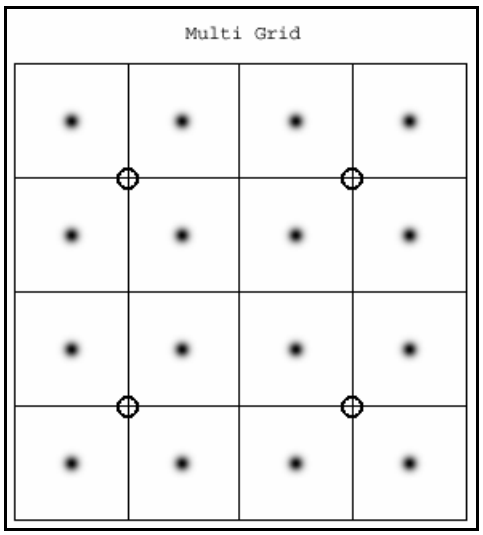

Figure 5.3 Multigrid fine and coarse cells and cell centres for even number grids.

The restriction routine can clearly be seen to simply require the average of the four surrounding fine cells. There are no (sensible) alternatives, and this is equivalent of the full-weighted restriction. In 3d this is an 8-point stencil rather than 27-point, a significant speedup. The smoothing routine is chosen and applied, in a similar manner to the odd numbered method, although in this method, the smoothing routine should be written in a manner suitable for non-uniform grids. This is due to the boundary conditions, where the width between any boundary point and the first central point is always half that of the distance between any two central points, and these distances, of course, are part of the discretisation[1]. This adds more or less time to the smoothing routine depending on its complexity.

The interpolation takes one of the following four stencils according to its location.

$$\begin{pmatrix} 9 & 3 \\ 3 & 1 \end{pmatrix}/16 \quad \begin{pmatrix} 3 & 9 \\ 1 & 3 \end{pmatrix}/16 \quad \begin{pmatrix} 1 & 3 \\ 3 & 9 \end{pmatrix}/16 \quad \begin{pmatrix} 3 & 1 \\ 9 & 3 \end{pmatrix}/16$$

These represent the bottom right, bottom left, top right, and top left fine cells within a coarse cell. These represent proportional areas, which become volumes in 3d.

The boundary cells must again be evaluated differently from the central cells. A bottom cell on the bottom edge uses the first stencil below, whilst the corner cells use the latter stencil.

[1] This is not strictly true. One can change the scheme at the boundaries but this is more cumbersome to code and restricts the compiler optimisers ability to optimise the array data retrieval from memory.

$$\begin{pmatrix} 3 & 3 \\ 1 & 1 \end{pmatrix} / 8 \quad \begin{pmatrix} 1 & 1 \\ 1 & 1 \end{pmatrix} / 4$$

These weightings are evaluated in accordance with the above method. It is *very important* that the boundary conditions on all grid levels are properly extrapolated into the corner and vertex cells before these schemes are used. Convergence for Neumann boundary condition problems is very significantly hindered without this. Accurate boundary conditions are essential for rapid convergence, and the corner and edge cells are used in the restriction and interpolation routines. For Dirichlet boundary conditions these are always zero, but can have significant non-zero values for Neumann boundaries.

5.4.4 Smoothing

As indicated above, smoothing is the name given to whichever iterative solver is used on each grid. The semi-implicit (but still explicitly calculated) Gauss-Seidel (G-S) method, where the points are successively updated using all the latest values is considerably faster than the Jacobi method, and also much more stable.

For Neumann boundary conditions, the order of sweeping with the Gauss-Seidel scheme directly affects the convergence rate. It is desirable for the Neumann boundaries to be at the end of the sweep, rather than the beginning. This is because there is zero error at the Dirichlet boundary conditions, and (without source terms) the neighbouring errors are guaranteed to reduce, with a zero initial approximation. This error reduction will then sweep across the domain. Starting with a Neumann boundary condition, there is no guarantee there will be a reduction in error, although (without source terms) it is guaranteed not to increase. So the error reduction coming from the Dirichlet boundary will take much longer to reach the Neumann boundary.

Inevitably, source terms can provide considerable problems, making the problem ill conditioned, and less stable. The G-S method must be used to overcome strong variations in the source terms, as the Jacobi method can rapidly oscillate and diverge.

5.5 Parallelisation

Large eddy simulations can require considerable computer power. The most powerful modern computers are parallel computers; that is a number of processing units working at the same time. There are two main types of parallel machine; the shared memory machine and the distributed memory machine. In addition to the usual programming language, Fortran 90 here, a parallel language must be used. Each type of machine has its own parallel languages, although codes written for the distributed memory machines can typically run on both. The Message Passing Interface (MPI) has become the most widely used language, due to its portability across machines, and its flexibility. The latest generation of parallel machines tend to be hybrid shared-distributed memory machines. Whilst shared memory languages have been extended to work on these machines, most notably OpenMP, MPI currently remains the language of choice.

Formally, two things are looked for in parallel codes, efficiency and scalability. Efficiency is the measure of how much of the processor resources are used. I.e. one wants each processor to be working to full capacity constantly. Low efficiency codes will have idle processors some of the time during execution. Scalability is a measure of whether the overall execution time remains the same if the job is doubled, and the number of processors used is doubled, and can be associated with the overheads of inter-process communication (assuming the code is otherwise efficient).

To achieve efficiency, good domain decomposition is required. This is straightforward on Cartesian grids. With explicit schemes, the work is evenly distributed with good decomposition. Implicit schemes depend on the solver, but are typically not 100% efficient. In the multigrid scheme, the smallest grids are constructed and iterated on a single processor. Due to the size of the grid this is not a time-consuming process, if it was the efficiency would be greatly reduced.

The question of scalability essentially requires communication costs to be linear with size of problem per processor. This is typically not the case. The more processors used, the greater the distance between processors, and hence the greater communication overheads. This is particularly true of ‘global’ communications; that is communication which is sent to or received by all the processors involved.

The usual method to get around these problems is to use non-blocking communication routines if the hardware supports this. These send and receive messages whilst the processor continues to process. In conjunction with large arrays this is very efficient, giving an effectively zero overhead for communication. However for small arrays the communication times are greater than the calculation times. There are also parts of the algorithm when there are no calculations to be done until the communications have been sent and received. The original MPI standard (there is MPI2 now) has no non-blocking global communication routines.

The domain decomposition should allocate an equal amount of work on each processor that also ensures a minimum of communication. In CFD the flow domain is split as equally as possible between the processors minimizing the surface area across which communication is necessary. Explicit methods are usual in LES, which makes it particularly suited to parallelisation. Each grid point only needs local values to march forward in time. At the boundaries, 'halo cells' are needed. These are the boundary cells on each processor (non-flow boundaries), which overlap with the domains of other processors. These halo cells must be kept updated through communication for the spatial discretisations to be accurate.
The objective for a good code is to keep the communication costs to a minimum.

By the late 1980's and early 1990's considerable research was going into parallel numerical algorithms. Serial algorithms are often not optimal on parallel machines. A good example of this, particularly relevant to the current work, is that of Lou and Ferraro (1996). They develop a numerical scheme similar to the one described above, and consider parallel issues, particularly that of the Helmholtz (generalized Poisson) solver. As indicated above non-blocking communication is the key to scalability. This is straightforward if the corner halo cells are not required. However, if they are, it must be sequential (blocking communication) which is detrimental to overheads. The alternative is to have explicit communication between diagonally local processors. This increases the complexity of the code considerably, and also increases the overheads. Nevertheless, scalability can be achieved, so long as the total number of grid nodes per processor is large enough. They find 16^3 grid nodes to be non-scalable, but 32^3 nodes and above to be reasonably scalable (using up to 256 processors on a Cray T3E does not go beyond approximately halving the time per processor).

Most LES simulations these days are run in parallel, and only a brief mention of the parallelisation is given. A number of these are reviewed in the next chapter.

5.6 3d Multigrid and Parallelisation Issues

The essence of 3d multigrid is, of course, identical to that of 2d. However, the coding complexity increases considerably, due to the increased number of boundary conditions. In 2d there are 4 edges, and 4 corners. In 3d this becomes 6 surface boundaries, 12 edges, and 8 vertices. All are straightforward in principle, but amount to rather messy and extensive coding. This is made much worse with the introduction of parallelism into the code.

Parallelisation requires domain decomposition, equivalent to that of the decomposition of the flow domain. A good balance is achieved, for both even and odd grid methods. However, the odd grid methods result in 8 different block sizes if the decomposition is in all three dimensions. This is required if the halo sizes are to be minimized. For example, on a 15^3 grid, the optimal (with regards to halo cell size) decomposition results in 8x8x8, 8x8x7, 8x7x8, 7x8x8, 8x7x7, 7x8x7, 7x7x8, and 7x7x7 grids on each processor respectively. The prolongation loops must be very carefully implemented to ensure the correct starting and stopping points. On an even grid, the decomposition would result in identically sized grids on each processor. Both methods require that that the starting loop has the correct boundary conditions, i.e. the left hand side of a right hand grid must not be wrongly bounded, just have the halo cells updated.

The communication costs, i.e. exchanging halo cells, can be detrimental to the cost of the overall scheme, and different parts of the multigrid scheme have different halo requirements. Starting with the smoother, the 2^{nd} order discretisation scheme used only requires the surface boundaries for its complete evaluation. This is achieved with a single halo swap, with the exchange occurring in all directions at the same time. This can be done in a non-blocking manner, so the smoothing subroutine can work on the inner part of the array, while the communication is processed. Then the boundary cells can be evaluated. This is advantageous in terms of there being essentially no

overhead for the communication, but damages the effectiveness of the G-S method, essentially making it a cross between the G-S method and the Jacobi method. Evaluation of the residual has the same halo requirements as the smoothing scheme.

The restriction scheme shows a difference in the odd and even schemes. The odd scheme requires all halo cells to be filled for its evaluation, including edge and vertex halo cells. There are two methods for a complete halo swap. The first is to have 26 separate communications, one from each of the potentially surrounding processors (in the virtual topology). This can be done, and will benefit from the non-blocking communication, but at considerable extra coding complexity. The evaluation of the residual is not affected by the order in which it is evaluated, and so does not suffer from problems similar to the smoothing scheme. The alternative is to use just 6 communications from the surface connected processors, i.e. those left, right, up, down, front and back processors, but not those diagonally linked. The halo swap must communicate the whole of the surface including the edge and vertex halo cells. However each dimension must be swapped in succession for all the halo cells to be correctly filled. This is due to after each dimensions halo swap, the next 'level' of halo cell is filled correctly; the surface first, followed by the edges, followed by the vertex cells. This can be made to be non-blocking but would increase the complexity of the coding considerably again. The array would need to be split into three components, ensuring each swap had been finished before beginning on the next. This is not too problematic on fine grids, but as further described below, does become problematic on coarse grids. The 6 communications, with 3 blocking procedures is used in this odd numbered code, after the first technique was dismissed. The odd scheme, by way of contrast, requires the correct halo cells for the restriction routine, as well as requiring more cells to restrict from.

For the interpolation routine the even cell method has advantages again, although the halo swapping requirements are the same. The complete halo is required for the boundaries. Emphasis is placed again here on the inclusion of the interpolation and extrapolation of the error on to domain edge and vertex boundaries as well before the interpolation is evaluated. For the odd numbered code, the placement of the interpolated error on the fine grid relative to the edge depends on the processors placement within the decomposition. Care must be taken in the subsequent interpolation. Some methods do not require interpolation between the halo cells first, although the trivially faster methods do.

The trickiest issue of the parallelisation of multigrid methods is how to deal with the coarse grids. In serial, the coarsest grid is naturally achieved using the main algorithm. This is not possible in parallel due to the distribution of the cells. Grids of unit width in at least one dimension are the coarsest grids available with the algorithm. This may (probably will) be prohibitively large for the total grids to solve exactly with an iterative solver, when the cost of communication is included. The two obvious approaches are to collect the remaining problem on a single node and solve that very quickly with a scalar multigrid code, or to gradually diminish the number of processors used. With a modest number of processors, the first method works well and sufficiently scales well (with memory caveats described later). Simulations with up to 16 processors have demonstrated this. The global communication required for this would ultimately destroy the scalability. The more processors are used the more time consuming the communication, but also the size of the serial problem would grow, potentially to a size larger than the fine, decomposed grids. The gradual diminishing of processors is much more complicated to code, and was only accomplished with a single dimension decomposition. The latter factor detracted from its speed, due to the increased communication overheads, although more significantly, the fact that the decomposition was in the Neumann boundary axis (the Y-axis, aligned with the gravity vector).

There are other multigrid schemes such as the full V-cycle and the W-cycle. Both use more coarse grid evaluations, which lead to lower parallel efficiency. Then there are options concerning the choice of the smoother, the restriction routine, and the interpolation. A Gauss-Seidel with over-and-under relaxation is used. Zhang (1996) shows that under-relaxation on the downwards part of the V-cycle and over-relaxation on the upwards part improves the convergence rate. A fully weighted restriction routine is used, and a linear interpolation scheme.

Dirichlet boundary conditions are the fastest to solve, and although well conditioned Neumann boundaries can be as fast, are not in fluid dynamic problems, particularly when the majority of boundaries become Neumann. Nevertheless good speeds can be achieved so long as the Neumann boundaries are represented on all grid levels. This can lead to instabilities however. Not putting the Neumann boundaries on the lower

grid levels is much more stable, although with considerable cost in convergence rate. However, the correlation between accuracy and convergence can be misleading in conjunction with Neumann conditions, particularly on large grids, since the convergence is evaluated locally only. It can be shown that multigrid techniques with a better convergence are less accurate in some situations.

The multigrid technique can either be used solely for the Poisson solver, or as a Helmholtz solver as would be required for the semi-implicit schemes of Kim and Moin, or can be used to solve the entire system on one grid. Ghia et al. (1982) introduce the final scheme for a steady-state vorticity equation solution.

5.7 Coding

Originally developed for non-uniform grids, low efficiency with the multigrid Poisson solver on stretched grids resulted in only uniform grids being used. The code is designed to be as modular as possible, and is written in Fortran 90 and MPI. The extra efficiency possible on uniform grids is exploited and the non-uniform characteristics were (mainly) removed. The use of modules (instead of common blocks in Fortran 77) greatly helps to accomplish this, making data very easy to pass between distant routines without having to be passed through every other routine on the way. Unfortunately, the use of modules appears to be slower than using automatic arrays, although there are more stringent memory restrictions on automatic arrays. Consequently, automatic arrays are used for the main flow variables u, v, w, T, and rho (but not the pressure term), and the rest are stored in modules.

The LMN fractional step method was developed in a 2d serial code initially, before being expanded to the parallel 3d code, which already had the Boussinesq equation solver on. The Poisson solver was developed independently so it could be used in different flow solvers, and also because it is the most complicated part of the code and required the most debugging.

A flow chart of the code is given in fig. 5.4 below. It follows the scheme of the predictor part of Najm et al. (1998) described earlier in the chapter. The MPI is initialised and the domain decomposition and virtual topology set up before the main

routine is entered. The random instabilities may need to be updated at each time step, and the sinusoidal forcing must be kept rotating. The turbulent stresses are calculated after the main component of the time derivative, R_i, is calculated. The regular and buoyant production terms for the subgrid kinetic energy equation require the stress and flux models to be already evaluated, and consequently must come at any point after this in the algorithm.

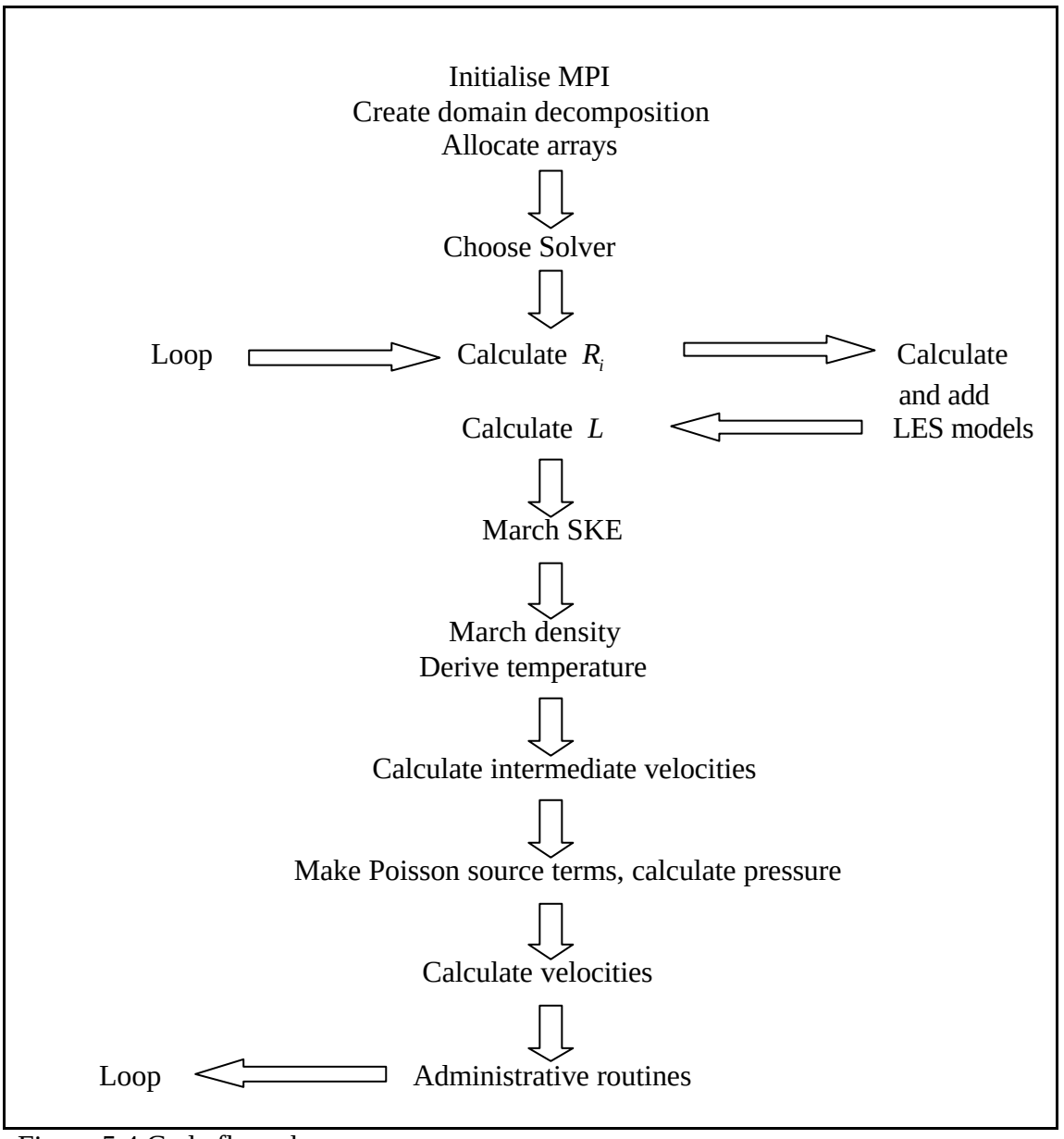

Figure 5.4 Code flow chart.

Subroutine	Multiplications	Additions	Arrays
Main	67	40	26
R123	288	255	7
Temp	44	37	6
Poisson	122	102	3

Table 5.1 Operation count for main routines.

The cost of the Poisson solver routine and others can be seen in table 5.1. This gives the approximate operation count for a single V-cycle (it varies with number of grids used). With 50 cycles per time-step approximately (see chapter 6), this very significantly requires the most computer time. The difference between routine R123 where R_i is made (eqn 5.7) and Temp, where L is made (eqn. 5.18) is approximately a factor of six rather than a factor of three, due to the staggered grid arrangement, and the conservative formulation of the momentum convection. The main subroutine includes the making of the pressure source terms, and the marching of the velocity and temperature fields after the derivatives are calculated in R123 and Temp.

Characteristics to note are the difference in arrays sizes used. The velocity components, temperature and subgrid kinetic energy all have double halos. The staggered arrangement of the velocities leads to different array sizes, and different halo-swapping routines need to be used accordingly. The bounding of the intermediate velocities only requires that the surface halo cells be filled, whereas the complete velocities (at the next time step) must be filled around the edges and vertices as well. This causes the same problems as for the multigrid solver, and different halo-swapping routines are for each case. The turbulent stresses only require a single halo, but this must be complete. The density array must have a triple halo – this is a requirement for a conservative formulation of the momentum convection discretisation if the stencil is 5-point – on a staggered grid this leads to a 6-point stencil for the density.
The arrays which need bounding, must be carefully bounded not using halo cell values before the halo-swapping occurs.

It is not sufficient to have a properly working code in which everything is calculated as it should be. The required information must also be extracted from the simulation. The memory requirements of the whole simulation go up proportionally to the amount

of desired information. In the case of the dynamic mixed models this adds a further 55 full arrays. Further large arrays are needed to work out the Reynolds averages. These could be evaluated using averages worked out in the first half of the simulation, as does Bastiaans (2000), or by taking full histories of chosen points in the domain. The latter is the methodology here.
The complexity of the code is also considerably increased, and the even distribution of the work-load can, in some cases, be affected.

Gathering data on to a single processor, during the simulation, in order to output it in a single file, can overload the memory, even on shared memory architectures where there is theoretically plenty of memory still available. This problem is reduced using dynamically allocated arrays for the total domain arrays rather than automatic, but the problem is not entirely eliminated. This leads to output files being written for each processor, and post-processing to be carried out to put the data back together.

5.7.1 LES Model Implementation

Ideally, the stress and flux models should be evaluated in a single routine, including all options and combinations for mixed models. This was expected to be too cumbersome and the task was split into smaller components. The static models were developed in independent routines. The disadvantages to this are slight. The efficient implementation of the eddy viscosity models, coupling it with the molecular viscosity is not taken advantage of, in order to keep the models as plug-in modules.
However, the dynamic models are all calculated in two routines, one for the stresses and one for the fluxes, and are implemented to allow the choice of any eddy or gradient model to be used in conjunction with either the Bardina or Leonard models. If these two routines were reduced to a single routine, no calculations would be performed twice unnecessarily.

Halo-swapping is not required for each stress or flux. For the static models, the halo sizes of the main arrays are sufficient to calculate the single halo of the stresses. In the dynamic models, this is not the case, but it is sufficient only to halo-swap the dynamic constant.

The transport of the subgrid kinetic energy uses a generic unsteady convection-diffusion equation with source terms evaluated elsewhere. A first-order Euler scheme only is used in time, with the 2nd order superbee TVD scheme used for convection, and 4th order central used for the diffusion term. The buoyancy term is not included in the calculation. The dynamic diffusion and dissipation terms require three point least squares, which can have the same numerical issues as the dynamic procedure applied to the stress or flux model constants.

In the dynamic mixed Smagorinsky/Bardina procedure for the calculation of the Smagorinsky constant the test level stresses and fluxes were calculated with the following formulas:

$$T_{ij} = \overline{\overline{\overline{u}_i \overline{u}_j}} - \overline{\overline{u}_i}\,\overline{\overline{u}_j} \tag{5.25}$$

$$Q_j = \overline{\overline{\overline{u}_j T}} - \overline{\overline{u}_j}\,\overline{\overline{T}} \tag{5.26}$$

This is a reasonable approximation, using the same approximation that the model is indirectly based upon, that $u_i \approx \overline{u}_i$ (note this is not the same assumption that the model uses, although it can be seen that this assumption is implicitly used, and also that this is the assumption under which most LES simulations are interpreted), and is a faster implementation (the final terms in each model would otherwise have a third filter on them, which is slow and would also increase communication overheads).

Table 5.2 below gives a rough operation count for the stress models. In the table the symbol X2 implies the operation count for whichever model is used in conjunction with the dynamic procedure doubles its static equivalent. The LDM count includes the transport equation (and direct evaluation of the test-grid kinetic energy), but not the dynamic evaluation of the source terms. These are counted in the listing for LDM-dyn.

	Multiplications	Additions	Arrays
Add Stress	27	21	12
Smag	51	29	11
Bsmag	61	35	11
StrucFunc	117	85	11
OneEq	41	21	10
Bardina	27	60	19
Leonard	41	27	10
Mixed SB	78	95	19

Mixed SL	92	52	11
Dynamic	X2+20	X2+58	30-50
LDM-fixed	101	89	14
LDM-dyn	+116	+218	+6

Table 5.2 Stress model operation count

Table 5.3 below shows similarly for the flux models.

	Multiplications	Additions	Arrays
Add Flux	3	9	4
SGDH	12	6	8
GGDH_1	37	17	14
GGDH_2	36	10	15
Bardina	13	33	14
Leonard	39	32	7
Mixed SB	25	42	14
Mixed SL	51	41	8
Dynamic	X2+10	X2+109	20-35

Table 5.3 Flux model operation count

These operation counts are rough and cannot exactly represent all the options available. Also there are further optimisation concerns not considered – do and if loops, function calls, and data rearrangement (particularly for administrative purposes), as well as the parallel overheads. These counts should illustrate the significance of the usage of cache memory. If the program can be run without exceeding this, the speedup benefits are very significant.

Of the static models, the Bardina has one of the lowest operation counts, but requires almost double the number of arrays. This change in memory requirements is the reason it is the slowest of the static models (mixed models excluded).

If the dynamic procedure is incorporated, the operation count and the array count goes up, more significantly the latter, and again very significant slow-down is found. The localised dynamic model is seen to require considerably more work than the other models.

The inclusion of the LES models, then, does not increase the operation count significantly. However, the number of arrays being operated on does increase very significantly, for the Bardina models and the dynamic models. This causes very significant slowdown, depending on the array size on each processor. Running a half million node job, with no subgrid model, on 16 processors on the Origin 2000, with

333MHz processors runs at approximately a third of the time of the same simulation on the same number of processors on a SUN 15k machine, with approximately 1000MHz processors, indicating good parallel efficiency. However, if a dynamic model is run with the same parameters, on the SUN 15k, it takes about twice as long to run. On the Origin 2000, it takes six times as long as on the SUN 15k. This gives super-linear speedup between the machines, and is directly attributable to the fast cache memory of the machines. If this is exceeded, the speed of the code is significantly reduced.

5.8 Simulation Review

Since the inception of LES with Smagorinsky's 1963 paper, the amount of research into LES has been steadily increasing, and more recently it has become more and more feasible to use it for practical simulations. The simulations particularly related to this work are presented here.

Boersma et al. (1998) in Delft develop a pressure-correction, finite volume incompressible code in spherical coordinates for the simulation of a turbulent jet. The coordinate system is ideal for this since there is very little wasted domain space. The domain boundaries are chosen to be a small distance from the edge of the plume entrainment. This method is clearly not very general though. A finite volume technique is used with second order spatial differences, and a second order Adams-Bashforth time discretisation. A fast Fourier transform strategy is used to solve the Poisson equation.

The traction-free boundary conditions described by Gresho (1991), and considered further elsewhere in this work, are used at the entrainment boundaries. These are suitable also for the outflow whilst the flow is laminar, but become unstable if turbulent. Hence, an advective boundary condition is used, similar to those sometimes used in channel flows, but where the average velocity of the outflow is evaluated each time-step. This method in conjunction with a number of absorbing boundary cells (described in the next chapter) is found to be stable. The usefulness of the advective boundary is questionable, since the outflow velocity clearly varies very significantly from the average.

They run a DNS of a jet with a Reynolds number of $2.4x10^3$, using a 450x80x64 cell grid reaching 45 inlet diameters downstream. Grid stretching is used in the direction of inflow in order to cover this distance. Running on a 10 processor CRAY-J90 and an 8 processor CRAY-C90 took approximately 5 seconds per time-step.

They investigate the effect of inflow conditions on the self-similar region of the jet. The profile of the inlet velocity is altered between simulations and they find, somewhat contrary to popular opinion, that the results are different. The similarity structures vary between the two test cases, leading them to support the assertion of George (1989), that there is no universal law for the similarity region of plumes. This would explain the great disparity between many experiments, and leads to the need to simulate truly representative experiments, rather than rely on the established theory. The state of plume theory needs to be reassessed in the wake of this, although in general the results will still hold, but not to arbitrary accuracy.

Starting with Boersma's code, Basu and Mansour (1999) in Stanford extend it to solve the Boussinesq equations and simulate the LES of the turbulent round plume. Implementing the dynamic Smagorinsky model and dynamic SGDH, and using a TVD scheme in order to stabilise the energy convective term, the simulation parallels the experiment of Shabbir and George (1994. Using $\mathrm{Re} = 3{,}500$, $Gr = 8{,}575{,}000$, and $\mathrm{Pr} = 0.7$, a domain 50 diameters downstream, with considerable grid stretching over a 128x40x32 cell grid, they found self-similar solutions for the velocity at x/D=6, and at x/D=15 for the temperature profile. The only turbulent inflow condition is the addition of random noise with a non-dimensionalised maximum of 0.02 to the inlet boundary. They find that the centreline values fit other experimental data (Rouse (1952) and Papanicolau and List (1989)) but not the data from the experiment it represented. They provide turbulence properties and mean values for comparative use. They run the simulation for 70,000 time-steps, providing 200 time cycles, where one time cycle is the time for something travelling at the inflow velocity to travel the inflow diameter. Simulation times take approximately 0.7 seconds per time-step using a 195MHz 8 processor SGI Origin 2000.

Webb and Mansour (2000) continue this work investigating the LES of jets and plumes, using the same parameters as Basu and Mansour (but with the Grashoff number set to zero for the jet). They consider their grid to be an order of magnitude smaller than the integral scale and an order of magnitude greater than the Kolmogorov

scale. This is a vague idea of what counts as true LES but they provide velocity and temperature spectra which fit the experimental expectations. Running 100,000 time steps, they again provide the turbulent stresses and the mean profile data. Overall they find the spread rates too low. Ultimately they cannot account for this, although they do demonstrate it is likely neither of the following: the traction-free boundary condition, or the Boussinesq assumption, which is broken near the inlet. They leave the LES model, particularly the turbulent Prandtl number as a possibility. In attempting to resolve the spread-rate problem they solve a line-sink analytic solution of irrotational laminar jets and plumes. They find the entrainment streamlines horizontal for the jet as expected, but for the plume there is curvature in the entrainment. This is contrary to other findings, including Zhou et al. (2001), Sanderson (2002), and the present work, which all solve numerically more general governing equations.

It is well established that the Smagorinsky model dissipates energy well, sometimes too much, but does not accurately represent the subgrid stresses. Liu et al. (1994) demonstrate this within a non-buoyant jet in particular. They find the dynamic model gives considerable improvement over the standard Smagorinsky.

Zhou et al. (2001) simulate the turbulent plume of Shabbir and George (1994), using the low Mach number formulation. The LES uses the Smagorinsky model, with the turbulent Prandtl number set at 0.3. They use the fractional step method proposed by Najm et al. (1998) with second order spatial and temporal discretisations. Rather than using a TVD scheme or an upwind scheme to ensure stability, they use the following form for the convective term in the energy equation, which naturally ensures continuity.

$$\left.\frac{\partial(ruh)}{\partial x}\right|_c = \frac{1}{2}\left[(ru)_e \left.\frac{\partial h}{\partial x}\right|_e + (ru)_w \left.\frac{\partial h}{\partial x}\right|_w\right] \tag{5.27}$$

The main simulation is run on a 128x256x128 grid on a domain of size 8x16x8 source diameters. Grid resolution effects are considered using a 4x8x4 domain with the same number of cells. Unlike steady state RANS simulations, grid independence cannot be achieved since the filter is typically defined by the grid width, and by definition different variables are being computed. However, a good measure of the accuracy of the simulation is achieved, and the relatively coarse grid is found to be sufficient. The

Reynolds number is 1300, and the Froude number is 1.54. The open boundary conditions allow entrainment through the use of fixed pressure and local continuity for the velocities. Luo and Zhou (2001) continue their work and show the large eddy successfully simulating a turbulent plume impinging on wall plates and in cavity enclosures.

Most experiments, particularly the more recent ones, take measurements a large number of diameters from the source, ranging up to 150 diameters in the case of Dai et al. (1994). This provides considerable computing issues in grid resolution requirements. Zhou et al.'s simulation can be shown to provide grid resolution at the Taylor microscale, if not exactly at the source, then fairly near it, it was run on 64 processors of a CRAY-T3E, being at the top end of the computer spectrum. Boersma's (1998) code goes some way to solving this issue, but spherical coordinates are widely applicable. Without the ability to simulate further downstream, there is then the problem of transition. Zhou et al. force the plume with a sinusoidal function of relatively low frequency, as well as adding random noise. A study into the stability of laminar plumes by Pera and Gebhart (1971) shows that high frequency disturbances are damped whilst low frequency disturbances rapidly propagate and grow. It can reasonably be assumed that the critical frequency beyond which the instabilities are damped increases with Rayleigh number.

These simulations are more about the flow being described then the turbulence model itself. Identical in spirit to this work it that of Bastiaans et al. (2000). A finite volume code is used. Treatment of convective terms is used for both the momentum equations and the temperature equation. They simulate 2d and 3d line plumes ($Ra = 10^{10}$) in a confined space with the purpose of investigating various LES models. The 2d plume is used to suggest the grid resolution required for a DNS against which to test the models. The DNS uses 195^3 cells and the LES uses 45^3. They consider the Smagorinsky, dynamic Smagorinsky, structure function, one-equation, and buoyancy modified-Smagorinsky model. The one equation model is altered for buoyancy, as is the formalism of the dynamic relations.

Essentially all but the buoyancy modified Smagorinsky are in good agreement with the LES. The dynamic model had to be clipped as expected, disallowing backscatter,

but this clipping occurred nearly everywhere, leaving the model negligible. They find the temporal spectra to be in good agreement, but the spatial spectra not in good agreement with the DNS. They find that the transition point is the most different between the DNS and LES.

Chapter 6

Validation and Simulation Issues

6.1 Introduction

It is essential to ensure that the code is working properly before full simulations are carried out. An appropriate validation technique must be applied to ensure that the code was correctly written – the numerical scheme, the parallelism, and the LES models each must be validated.

Initially a laminar plume was simulated. Chen and Rodi (1980) find no 3d laminar plume experiments (these are impractical to measure due to their sensitivity to the measuring devices), and no experiments have been carried out subsequently to the best of the author's knowledge. Comparison with other codes does provide confidence in the code, and there are properties of laminar plumes which can be exploited to demonstrate that the code works properly.

The numerical scheme in general is shown to be correctly implemented through correct qualitative results, and the parallelism is shown to be correct through the (near) perfect symmetry of the steady state solutions. The LES models are also validated in this manner. This does not perfectly validate the implementation, but is the best available method, and with faith that the implementation is correct, sheds light on an important aspect of LES modelling – behaviour in laminar regions.

Further validation on a turbulent plume highlights the difficulties and hurdles which must be resolved to result in a useful and informative simulation. This particularly concerns the boundary conditions.

Appendix C provides the simulation label listings.

6.2 Laminar Plume

An arbitrary laminar plume, accelerating all the way out of the domain, was simulated without using a subgrid model. A 31^3 grid covering a 7^3 non-dimensionalised domain was used, with 5 grid points across the inlet. The Reynolds number is 50, the Froude number 0.5, the temperature difference is 0.1, and the Prandtl number is 0.7. The time step is 0.05. This is simulation l1t. It was run for 1,000 time steps and reached a steady state.

Fig. 6.1 shows a smooth plot of the vertical velocity and temperature fields. The velocity increases continuously from the buoyancy effects (it would decrease eventually unlike a line plume), and the temperature decreases monotonically. These quantities are seen to be spreading as would be expected. The physical characteristics of the plume are shown to be properly captured. Fig. 6.2 shows the correct horizontal entrainment streamlines, and also the symmetry of those horizontal streamlines. This is a positive validation that the side boundary conditions can indeed entrain the ambient fluid properly, although an uneven entrainment rate is seen at the boundary (the entrainment must be perpendicular to the boundary, and the fixed pressure field should ideally be equidistant from the centre) it is cylindrically symmetric in from the boundaries.

The correctness of the decay was considered against other numerical schemes – the full (two-step) projection scheme, and a predictor-corrector scheme. The results were almost identical, suggesting the scheme is implemented correctly.

The validation of the models was carried out in a similar manner ensuring symmetry (where appropriate) for all the stresses and fluxes. l1t was chosen so that the flow is still accelerating at the top of the domain. This makes it easy to check the maximum velocity and the temperature difference (from the ambient) decay at the central top boundary point. Table 6.1 below shows these values when simulated by the different models. Symmetry was found in all models after debugging, apart from the Leonard model which causes a very slight (10^{-5} difference between the absolute values of the maximum and minimum horizontal velocities) push in the horizontal axial directions. ‘Mixed 1’ labels the static mixed model combining the Smagorinsky model and the Bardina models, ‘Mixed 2’ combines the Smagorinsky and the Leonard model, and

'Dmixed 1' labels the dynamic mixed model combining the Smagorinsky and Bardina models.

	V	dT(10e-2)	Stress	Flux
l1t	1.295	5.04	-	-
l2t	1.287	5.04	Smag	-
l3t	1.287	5.04	Bsmag	-
l4t	1.265	5.02	StrucFunc	-
l5t	1.278	5.04	One Eq	-
l6t	1.268	4.82	One Eq	SGDH
l7t	1.278	5.04	One Eq	GGDH_1
l8t	1.279	5.03	One Eq	GGDH_2
l9t	1.32	5.24	Bardina	Bardina
l1u	1.3	5.09	Leonard	Leonard
l2u	1.297	5.04	Mixed 1	Mixed 1
l3u	1.29	5.03	Mixed 2	Mixed 2
l4u	1.294	5.05	Dsmag	SGDH
l5u	1.293	5.05	Dsmag	DSGDH
l6u	1.295	5.04	LDM	SGDH
l7u	1.308	5.04	Dmixed 1	SGDH
l8u	1.305	4.94	Dmixed 1	Dmixed 1

Table 6.1 Laminar plume decay at top of domain. The velocity (which is maximum at this point) is given, as well as the temperature difference from the ambient at the same point.

The differences between the simulations are very slight, but the convergence of the scheme is good enough that these are still indicators of the behaviour. The eddy viscosity models, as expected, all dissipate momentum and temperature more quickly than the without a subgrid model. The structure function model dissipates the most and the Smagorinsky models dissipate the least. The Bardina and Leonard models are not dissipative, but rather the opposite, the Bardina model more strongly. These appear to act as an acceleration term. In the mixed Smagorinsky-Leonard model these effects seem to cancel each other out whereas for the Smagorinsky-Bardina, it is the Bardina terms which are stronger. The non-mixed dynamic models give almost identical results to using no subgrid model, whereas the dynamic mixed model simulations are affected the structural term.

These give a glimpse of the results to come.

6.3 Preliminary Turbulent Plume Simulations and Turbulent Plume Issues

A steady state laminar plume is much easier to simulate than a fully unsteady turbulent plume, and errors in the code are not necessarily found through their simulation. In particular, errors which grow and diverge (crash the simulation), which are stabilised in steady flow, can gradually increase in an unsteady flow over an arbitrary period of time. The slower the growth of the error, or the longer the error takes to emerge, the worse the problem is to find due to the amount of time required to find out if there is an error, and the large quantities of data which may be required to be tracked. During the debugging process, simulations were diverging after 50,000 time-steps, with the results unrecognisable as incorrect until approximately ten time steps before divergence. Test simulations were run to 100,000 time-steps, corresponding to a particle travelling 85 times through the domain at unit velocity. This was deemed sufficient to indicate that there were no unbounded errors, or that if there were they were negligible in this period. Simulations presented are not run for more than 50,000 time steps.

An image of a successfully simulated plume is given in fig. 6.3. This shows the isosurface of the vorticity magnitude. It is seen to breakdown gradually. The second image shows a lower vorticity magnitude isosurface, and also a contour plot of a slice in the X-axis. The contours can be seen to become tangential to the top domain. This is clearly wrong, but has to be considered an acceptable error. It is limited to very near the boundary, and assumed not to be consequential to the flow upstream.
The considerably worse boundary problem, which must be avoided is shown in fig. 6.4. Again, the isosurface is shown as well as an X-axis slice. The eddies get caught up in the corners of the domain and are not swept out of the domain. The results are un-useable. The problem arises from the (reduced) pressure boundary specification. Fixed zero pressure around the sides and the top is a suitable far field boundary. If the turbulent part of the flow interacts with these boundaries negatively then the assumptions are broken and high-pressure gradients will be created to enforce continuity. This negative pressure gradient is shown in fig. 6.5. This serves to disallow the eddies to flow out of the top of the domain, which is clearly unphysical.

A comparison of pressure isosurfaces is given in fig. 6.6. The difference is clear, with the expansion of l6o far more rapid than the expansion of l4o, resulting in these corner problems. It is essential for successful simulations to avoid these boundary problems.
Fig. 6.7 shows a snapshot of the pressure field, from one of the simulations presented in chapter 8, which is representative of all the simulations. The contours clearly show the high and low bubbles associated with swirling motions. The magnitude of the pressure contours are not adversely affected at the top boundary. In the same figure, the pressure averages are shown. The Dirichlet boundary conditions are clearly seen around the sides and top, but they are sufficiently far field for there to be space inside the domain for a stable smooth field to be established. These are sufficiently good boundary conditions for the pressure.

It is desirable to have transition as early as possible. This is affected a very great deal by the level of forcing utilised. A number of trial simulations indicated that the strength of the random instabilities was the more important forcing factor, although the sinusoidal forcing contributed as well. The problem with the high levels of forcing used, is that the convergence of the Poisson solver is very severely affected. From requiring approximately 20 cycles to achieve convergence, the ill-conditioned source terms at the boundary cause the use of 50 cycles to be required to almost achieve full convergence (normalised 10^{-6} residual error). The error is typically $5x10^{-6}$ after 50 cycles.

We can approximate the number of cells required for both a DNS and LES for a particular experiment by knowing the integral Reynolds number, which requires the integral length scale and the intensity of the fluctuating components.
The integral length scale of a plume can be estimated based on the half width of its spread rate, and the normalised fluctuations are found from the experiments. Shabbir and George (1994) suggest a turbulent Reynolds number of 1600 in the plume region, and the relation between the scales given in chapter 3, show that 40 cells across the integral length scale are required to capture the Taylor microscales. For a DNS the requirement would be 250 cells across that scale. Nevertheless, even on coarser grids the energy spectra can be captured which shows that true LES is carried out rather than VLES.

These plume simulations have a natural swirl, stemming from the sinusoidal instability, and exaggerated by the inlet conditions, which is present in all the results. The horizontal U in the Z-axis is shown in fig. 6.8. There is clearly some swirl going on, which is shown in more detail in fig. 6.9, in which the entrainment vectors are shown at a number of distances from the inlet. The sharp edges of the inflow boundaries (which are more square than round) can be seen to develop. These structures make the flow more complicated and the averaging process more time-consuming. Simulations take a long time to average completely. The plots, given in fig. 6.9, show that the plume core is not perfectly averaged. However, the horizontal velocities are small compared with the entrainment velocity, and small compared with the instantaneous velocities. Symmetry is not perfectly achieved which would be ideal, but the averages are good enough to extract significant information concerning the LES models. Averaging further over longer simulations was found to improve the averages very slowly, and so this duration of simulation was deemed acceptable for the purposes of this thesis, given the time constraints using computationally expensive methods.

Figs. 6.10 and 6.11 show the vertical momentum balance centrelines and profiles. These average each term in the momentum equation and relate their relative magnitude. These averages are qualitatively different to those from RANS balances, most notably the non-zero horizontal convection terms which show a correlation between the horizontal velocity and the horizontal velocity gradient, the effects of which are seen in the subgrid models. If there is a mean velocity gradient in the vertical velocity, which in this case is accelerating at the beginning and decelerating further downstream, this must be made to balance by the horizontal convection components, as the mean flow either sucks in the surrounding fluid in the case of accelerating mean flow or pushes away the fluid in the case of decelerating mean flow.

It can also be seen that near the source the total becomes non-zero. This is attributable to the high-pressure gradients from the forced instability fluctuations, which is required for this grid fineness.

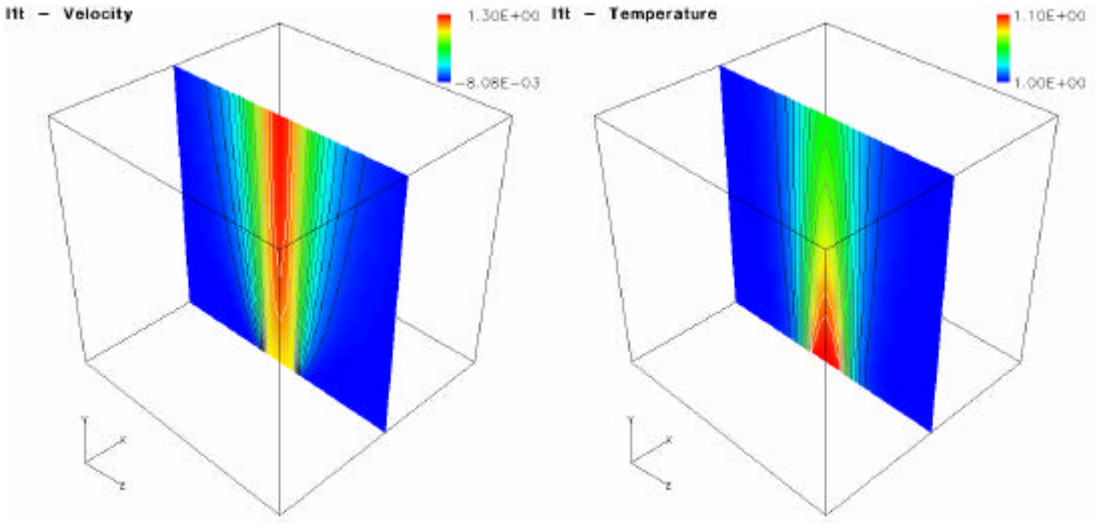

Figure 6.1 Velocity and temperature validation plots for l1t (no SGS model). Contour lines are plotted. The domain size is 7^3 and the inlet diameter is slightly over 1 ($1\frac{1}{31}$).

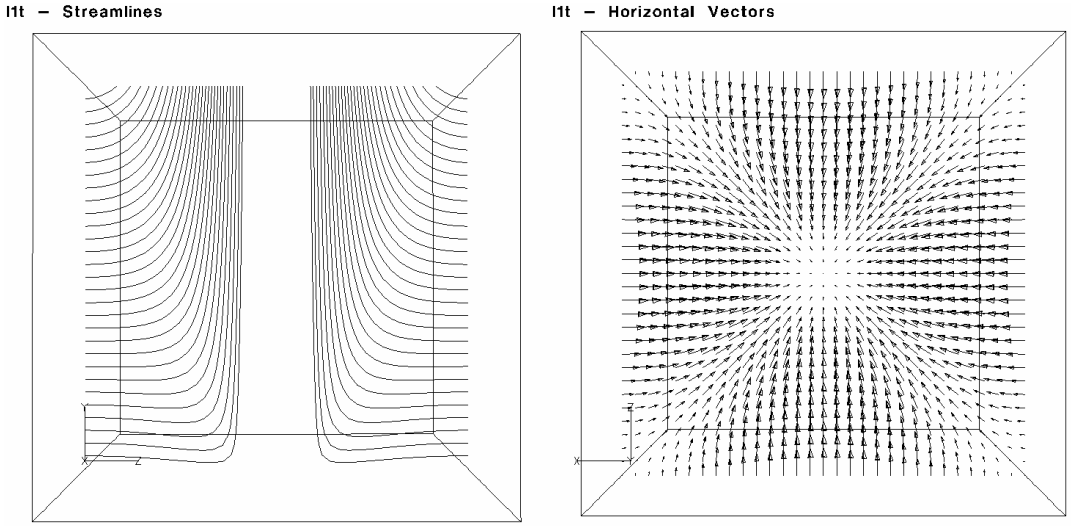

Figure 6.2 Streamlines and horizontal velocity vector components, y/D=5, for l1t.

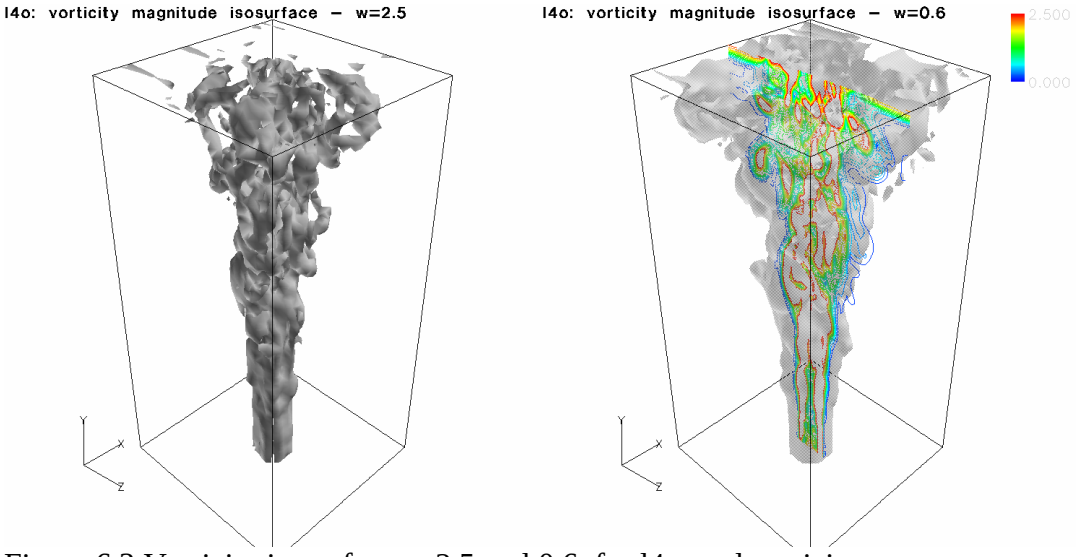

Figure 6.3 Vorticity isosurface at 2.5 and 0.6, for l4o, and vorticity contours.

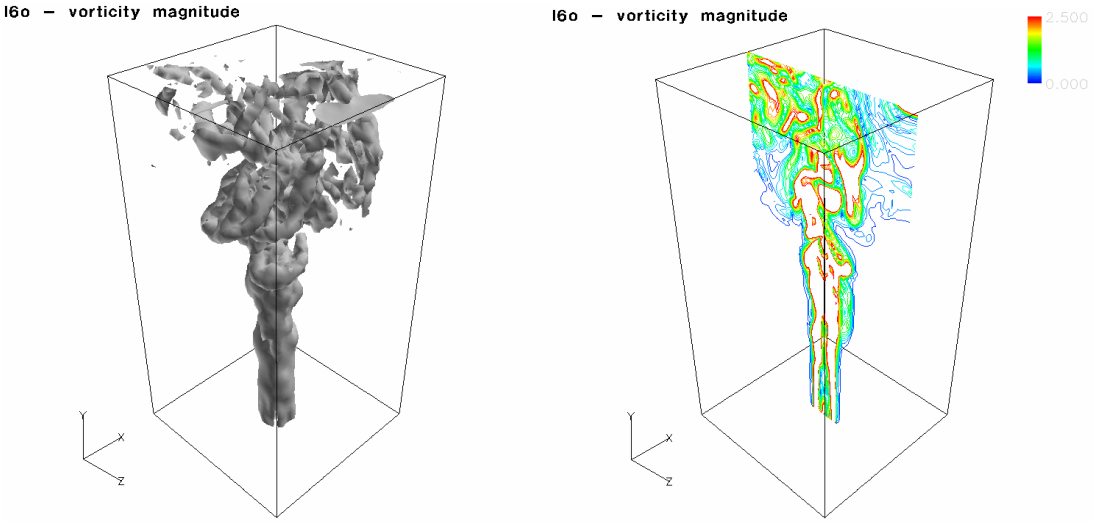

Figure 6.4 Vorticity magnitude isosurface and vorticity magnitude plot for l6o.

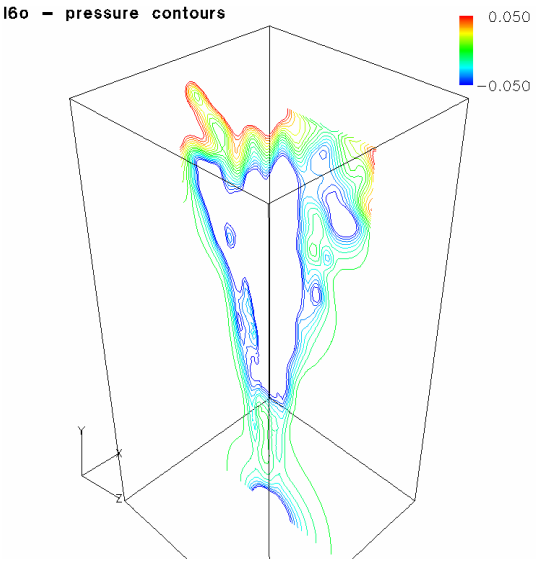

Figure 6.5 Instantaneous pressure plot for l6o.

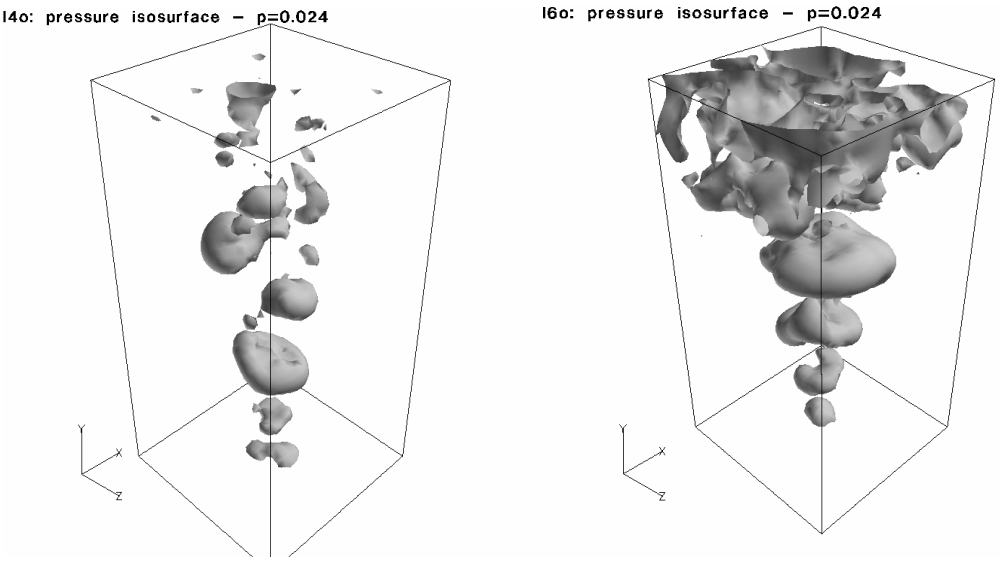

Figure 6.6 Pressure isosurfaces for l4o and l6o.

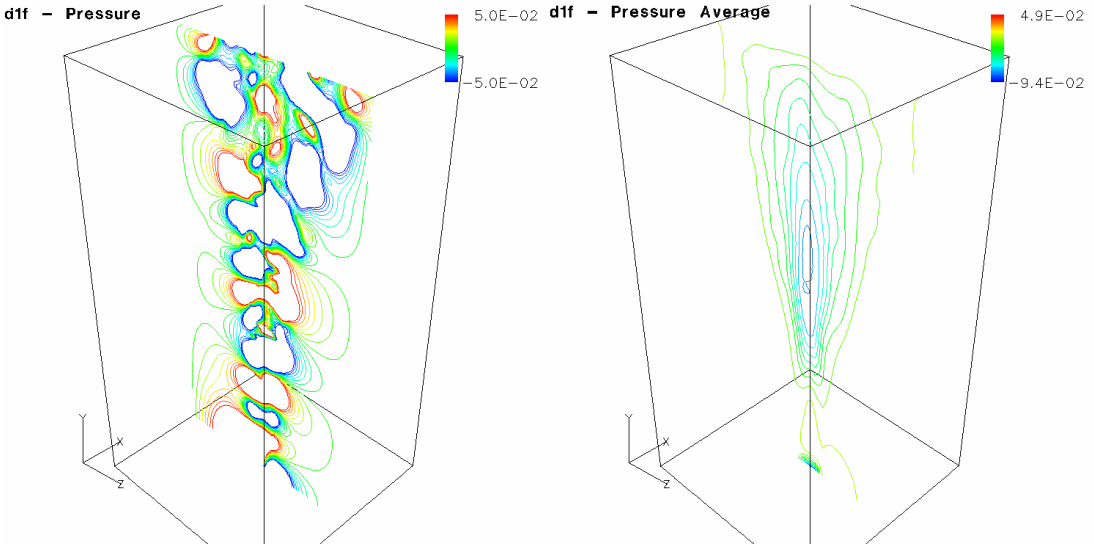

Figure 6.7. Instantaneous and average pressure plots for d1f.

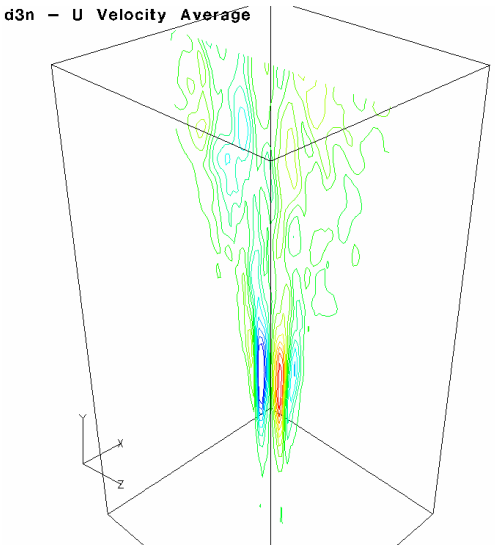

Figure 6.8 U velocity average plot highlighting the swirl in the plume for d3n.

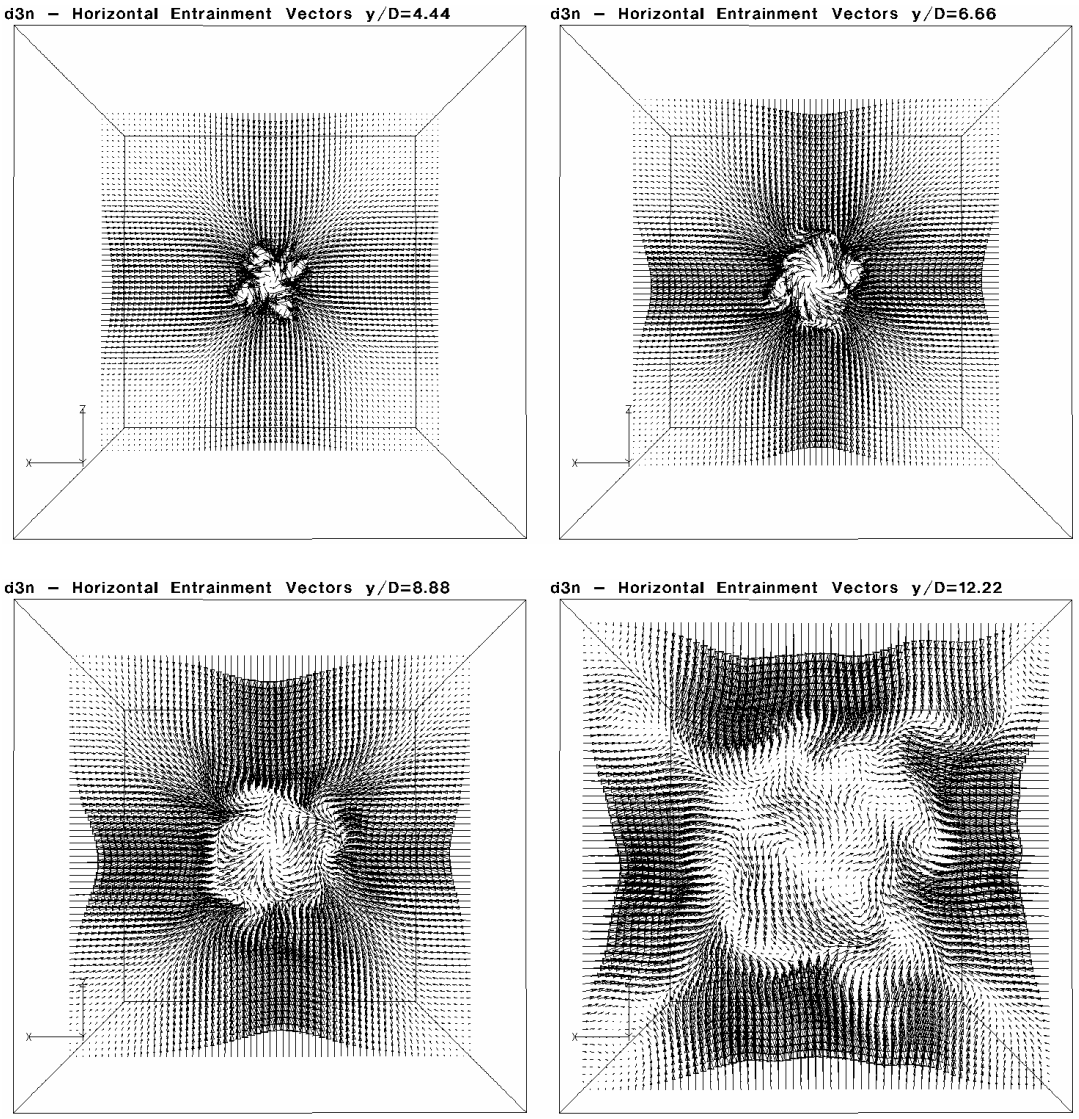

Figure 6.9 Horizontal entrainment vectors (not including vertical component).

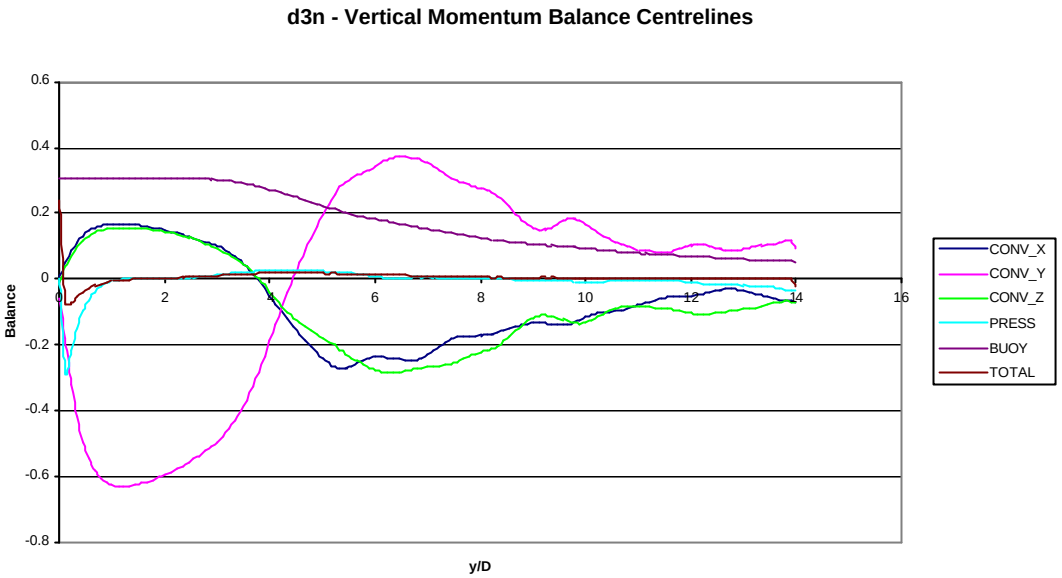

Figure 6.10 Vertical momentum equation balance centrelines for d3n.

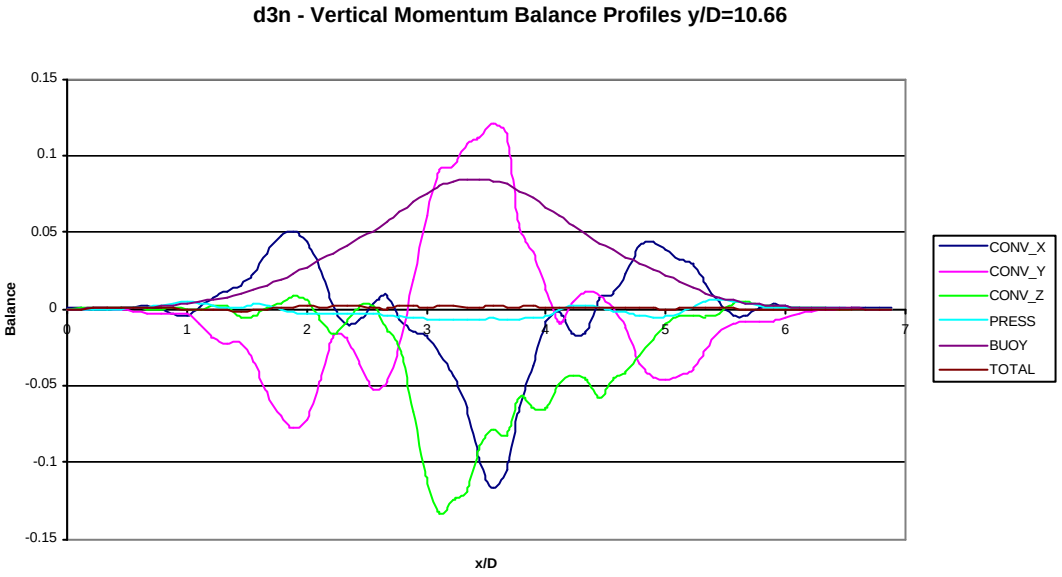

Figure 6.11 Vertical momentum balance profiles for d3n.

Chapter 7

Static Model Results

7.1 Introduction

The main results are broken into three chapters for ease of digestion. This chapter presents the results from simulations using the static models, chapter 8 presents the dynamic model results, and chapter 9 presents further simulations investigating further pertinent issues. Different data sets were retrieved from the simulations, with the administrative parts of the code being developed alongside the running of the simulations. More data was available from the later simulations, the dynamic model simulations and the further simulations.

The experiment of Shabbir and George (1994), with parameters chosen similarly to Zhou et al. (2001), was set up as the key simulation through which to study the models, details of which are given below. The expense of LES simulations is such that a parametric study of the different models necessitates coarser grids than those singular simulations more often published (see the review in chapter 5). Simulations on coarser grids should also highlight better the differences between models, since the finer the grid is the less significant the LES models become.

The first set of results focuses on the static eddy stress models, the second on the static gradient flux models, and lastly on the mixed models. A simulation without a subgrid model was also carried out for comparison. Centreline decay rates and radial profiles of the averaged velocity and temperature constitute the main analysis source, as well as similar plots of the turbulent stresses and fluxes. Illustrative snapshots of the instantaneous fields, isosurfaces, and averaged variables are also provided and discussed. These can highlight factors not observable in the graphs.

The stresses, t_{ij} are referred to as T11, T12, T13, T22, T23, and T33, and the fluxes, q_j, are referred to as EN1, EN2, and EN3.

7.2 Simulation Details

The following details provide the input conditions and simulation details for all the results, unless otherwise stated in this and the next chapter.

Shabbir and George (1994) follow up George et al's (1977) thermal plume experiment with a very similar experiment with better measuring equipment. A key issue in the plume experiments is the point at which the plume has become fully developed and it's characteristics are self-similar. That is the point beyond which the normalised radial profiles of the flow variables become constant. Shabbir and George find this early on, taking measurements 6.5 inlet diameters from the source through to 16 diameters from the source, 6.5<y/D<16. Other experimenters such as Dai et al. (1994) do not find self-similarity until y/D>40, making Shabbir and George the best experiment to simulate given the less extensive domain requirements.

A 6.35cm diameter nozzle allows a jet of heated air to enter a 2mx2mx5m high enclosure, at a velocity of 0.98ms^{-1}, and a temperature of 292C.

Approximately half a million grid points were used, on a uniform mesh of 63x127x63. The source width is 9 cells diameter. The non-dimensionalisation is based on the inflow velocity and the source width. The non-dimensionalised source is 1 unit diameter, and the inflow velocity is 1 unit. This results in a domain 7x14.11x7 units volume. The ambient temperature is assumed to be 300K and the jet 567K. This gives e, the temperature difference between the ambient and the inlet, a non-dimensional value of 0.893. The Reynolds number is 1300, and the Froude number is 1.54. Fixed zero pressure boundaries were used on the top and side boundaries, and zero gradient on the bottom. This is fine for the fully developed flow field, but continuity is broken where there is clipped outflow at sides and clipped inflow at the top, as the starting plume head moves out of the domain. The density was fixed at unity at the boundaries where there is inflow and a local gradient was used for the top outflow. The perpendicular velocities were fixed to zero on the side boundaries, and entrainment

was allowed ensuring local continuity for the normal velocity. For the top outflow boundary, local gradients were used for the perpendicular (to the boundary normal) velocities, and local continuity again for the normal velocity. The wall boundary at the bottom is no-slip and adiabatic.

The Low Mach Number formulation was used, using only the first step of the scheme of Najm et al. (1998), described in chapter 5. Since e is less than 2, this does not cause any stability difficulties, nor does it affect the formal accuracy, which is 2nd order in time. The 3rd order upwind scheme was used for momentum convection, and 2nd order central for the full molecular diffusion term. The temperature equation used the 2nd order 'superbee' TVD scheme for convection, given in appendix B, and a 2nd order central scheme for the diffusion. These schemes allow the simulations to be compared with simulations with no subgrid model.

The pressure term was also discretised with a 2nd order central scheme. A maximum of 50 V-cycles were allowed per time step, or until a normalised convergence of 10^{-6} was reached. The forced instabilities resulted in the maximum number of cycles usually being used, although the order of convergence reached was usually the same order of magnitude.

The non-dimensionalised cell widths are 0.111, and the maximum velocity of the flow is approximately 2.5, giving an optimal (CFL number of 1) time step of 0.0444. This limit is reduced in three dimensions by a third for explicit TVD schemes if they are to be guaranteed to remain TVD, before other source terms are considered, and a time step of 0.012 was utilised.

The forcing at the inflow was as follows. The sinusoidal instabilities (section 5.3.2) were applied with two modes, and strong random fluctuations were used also. 0.35 and 0.1 were the maximum strengths of the random frequency fluctuations for each momentum equation and the temperature equation respectively.

The simulations were run for 50,000 time steps. The averages were taken every 25 time steps between 5,000 and 49,000 time steps. Balances were averaged similarly. In the profile plots the centreline is at x/D=3.44.

Quick reference for simulation labels can be found in appendix C.

7.3 Static Eddy Stress Models

The four eddy model simulations are compared against each other, and a subgrid-less simulation. The labels for the simulations are as follows:
d1n: no subgrid model
s1t: Smagorinsky stress model and SGDH flux model
s2t: Buoyancy modified Smagorinsky stress model and SGDH flux model
s1f: Structure function stress model and SGDH flux model
o1e: One equation stress model and SGDH flux model
The model constants were those normally used, 0.01 for the Smagorinsky model and buoyancy-modified Smagorinsky model, 0.0634 for the structure function model, and 0.07 for the one equation model. The turbulent Prandtl number was fixed at 0.4 following Zhou et al. (2001).

This section shows the varyingly increased dissipation caused by the eddy models, and the delay in transition that is a consequence, and shows the results to vary strongly with the choice of model, although the buoyancy-modified Smagorinsky model is shown to give essentially identical results to the Smagorinsky model. The one equation model is shown to have a more complex behaviour than the other eddy models, which is examined. All the eddy models are shown to break the realizability conditions, and the mechanics of the models are discussed.

Fig. 7.3.1 gives snapshots of the vertical velocity and temperature distributions of simulation s1t, in order to illustrate the transient nature of the flow. They are taken at the end of the simulation, after 50,000 time steps, corresponding to 38.1 seconds. The contour-maximums are reduced from the variable maximums in both cases to make the flow characteristics clearer. The velocity fluctuations in the flow can be clearly seen, with the velocity surging upwards in parts and moving more slowly, corresponding to the downward parts of an eddy, in other parts. The temperature plot also shows the turbulent nature, but also more clearly shows the effects of intermittency. The large scale of cold air entrained near the top has not yet been mixed with the hot air of the plume core.
Fig. 7.3.2 gives the average fields of the vertical velocity and temperature. The contours are mainly straight and smooth respectively, with only the mildest kinks in

the velocity plot. This, combined with the average streamlines given in fig. 8.3.3, which have converged to the horizontal entrainment anticipated by theory and experiment, indicate a good and sufficient number of time-steps have been used for the averaging.

Figs. 7.3.4 and 7.3.5 show the velocity and temperature centreline decays of the above models. It is immediately clear that the choice of LES model does make a significant difference to the results. The notion that the choice of turbulence model does not make a difference is dispelled. Considering the velocity plot first, it is apparent that that the subgrid models significantly delay transition; the structure function model the most, followed closely by the one equation model, followed by both Smagorinsky models. Transition is roughly indicated by the peak velocity. Subsequently there is a rapid decay, after which the decay appears linear, before the bound of the domain is reached. Plume theory, Turner (1973), developed for non-Boussinesq plumes by Rooney and Linden (1996) and Woods (1997) for non-Boussinesq plumes, shows that the velocity should decay as $\bar{y}^{1/3}$ in the fully developed plume region, starting from a theoretical point source. The decays here are larger indicating the self-similar region has not been reached, or only just. The buoyancy modification to the Smagorinsky model is clearly shown to have very little effect in this simulation. This is contrary to the findings of Bastiaans (2000), who found it to be detrimental to the simulation of a confined plume.

Even though the spread rates cannot be directly calculated from these simulations, due to self-similarity concerns and a strong sensitivity to the averaging process, the strength of the decays indicate the spread rates qualitatively; the more dissipative the model, the greater the spread rate, and hence the swifter the decay. Likewise the greater the dissipation, the greater the delay in transition will be. The decay rates do behave as expected in this relation to their transition. The Smagorinsky models cause faster decay than no subgrid model and the structure function and one equation models decay faster still.

An instantaneous and an average plot of the subgrid kinetic energy are given in fig. 7.3.6. This shows the subgrid kinetic energy transport to recognise the intermittency. Both images show the lack of subgrid energy near the inlet along the centreline, although it takes significant non-zero values before transition has occurred. (This suggests better turbulent inflow conditions should be found. Possibilities include

recycling the outflow turbulence into the inflow. This has not been tried, although improvements here would considerably improve the effectiveness of the simulation.) Nevertheless, the average plot is good, and finds the peak subgrid energy somewhat downstream of transition at approximately 8 diameters from the inlet.

Figs. 7.3.7 and 7.3.8 show the centrelines and profiles of the individual stress components, taken from s1t, the Smagorinsky model simulation. The plots are much less smooth that those for the velocity and temperature plots. The terms have a higher variance (since they are the multiple of two variables), requiring longer simulations for smoother averaging. The behaviour is clear however. The normal stresses break the realizability conditions. In the laminar region the vertical normal stress, T22, is negative, whereas the others, T11 and T33, are negative in the turbulent region. Chapter 6 illustrated the momentum balances and showed the correlation between the horizontal velocity and horizontal velocity gradient in the presence of a vertical mean gradient. Similar considerations lead to the negative horizontal normal stresses on the centreline, breaking the realizability conditions. The acceleration of velocity in the laminar region leads to the vertical stress breaking the realizability condition, and correspondingly the horizontal stresses are 'legal' with regards to the condition in this region.

The expectation that the horizontal velocities are zero along the centreline is not fully achieved. There are slight large scale structures which have not been fully averaged out, and are in the T12 and T23 stresses, which should be zero on the centreline. Instead they are positive while the plume goes through transition, and then fall in value afterwards. This occurs at y/D=8, and shows it is not from the plume tilting to one side. The magnitude is small but not negligible in the plot, although the T13 stress is negligible. The vertical normal stress, T22, has the greatest magnitude on the centreline. These components are well enough averaged to show their general behaviour, although it is unlikely that further averaging would yield similar decay rates near the exit of the domain. It is well documented (for example Chen and Rodi, 1980) that the stresses reach their self-similar state further down-stream than the velocity and temperature fields.

In fig. 7.3.8 it can be seen that it is the radial stress, T12, which is the most significant (correspondingly T23 in the Z-axis), with a peak slightly over twice the magnitude of the peak of T22. Here, both normal stresses are non-zero, and are not negligible. Both,

considered in the X-axis with the plot, have their component based on the negative velocity gradient, decelerating at their respective central slices of the domain. However, the X-axis normal stress, T11, also has a positive component to be added from the mean entrainment velocity. U is non-zero on the X-axis profile line. At the plume edge this makes T11 positive but is not as strong as the deceleration at the centre where it is still negative.

The T22 centreline plots are presented for each model in fig. 7.3.9. The behaviour clearly reflects the velocity decay. The delayed transition leads to greater initial acceleration of the plume in the laminar region, leading to different peaks of the stress after transition. The one equation model does not have the immediate dissipation of the other models at the inlet, where the transport equation is bounded with low turbulence, but soon reaches a similar magnitude to the structure function model. It predicts T22 to be weaker through transition, and continues to be the lesser term through the decay, although both the one equation and the structure function models have larger stresses than the two Smagorinsky models, which have virtually identical stresses. The peak of the structure function model causes the slightly greater delay in transition, and will be slightly more dissipative.

The tail end of the plots show no decay but horizontal distributions. This is a difficult region due to the boundary conditions. However, an extension of the domain would be expected to show these as slight curves, corresponding to the decay of the velocity, and also that these regions are the start of fully developed plume turbulence in which the plume laws are applicable. The larger gradients after the peak are in the main transitional region.

The two most significant stress profiles of T22 and the radial stress, T12 in the X-axis, are shown in figs. 7.3.10 and 7.3.11. Given the limited region of self-similarity, it is inappropriate to normalise the plots. Here, the plot of T22 does show that all models reflect a negative correlation in the entrainment region at the edge of the plume, even though the mean vertical velocity is zero or positive. The plot of T12 also shows the relative magnitudes at 10.66 diameters away from the source (y/D=10.66). All of these plots maintain the clear similarity between the Smagorinsky and the buoyancy modified Smagorinsky models. The magnitude of the T22 stress is larger for s1f, the structure function model, than for o1e, the one equation model, whereas the radial stress is similar, representative of a slightly higher mean vertical velocity,

which has spread slightly less at this point, as well as again suggesting that the structure function model is the more dissipative.

Some spectra plots are given from s1f, the structure function simulation. Time spectra are used since spatial spectra are not possible to calculate in this simulation, given it has no homogeneous directions. The turbulent kinetic energy is plotted in wave space alongside each axial component, at three points along the centreline. Fig.7.3.12 plots them at y/D=7.11, fig. 7.3.13 at y/D=10.66, and fig. 7.3.14 at y/D=14. The first shows the vertical small-scale fluctuations to be much stronger than the horizontal components. The plot doesn't show the negative values, stemming from the structures of transition. This region is not fully turbulent.

The second plot is fully developed turbulence although it is not entirely isotropic. The vertical component is larger than the others, but not significantly. The expected –5/3 gradient is also plotted. This distribution predicts a slightly stronger gradient. The most interesting plot is at y/D=14. This is taken a single cell away from the boundary. The problems at the boundary have been discussed earlier. It is surprising to see such good spectra so close to the boundary. The turbulence has continued to develop and is here completely isotropic. This in part justifies the use of the boundary conditions, but does not imply other errors are not introduced, however.

The temperature fluctuation spectra is given in fig. 7.3.15. It has been found experimentally (for example Dai et al., 1994) that the spectra has two ranges, and Zhou et al's (2001) simulation finds the same behaviour. The first takes the –5/3 law, and becomes a –3 law closer to the dissipation range. Both gradients are plotted and show the spectra to lie in between them. It could be argued that at the top the gradient is closer to –5/3, and at the bottom it is nearer –3, but consideration of fig. 7.3.16 refutes this. The latter plot at the boundary, y/D=14, shows the –5/3 gradient to be well captured, but not the –3. This can be seen as either a positive or a negative. LES modelling should work so long as the inertial subrange is caught, which is well demonstrated from these plots, and capturing greater detail than is required represents wasted computational expense.

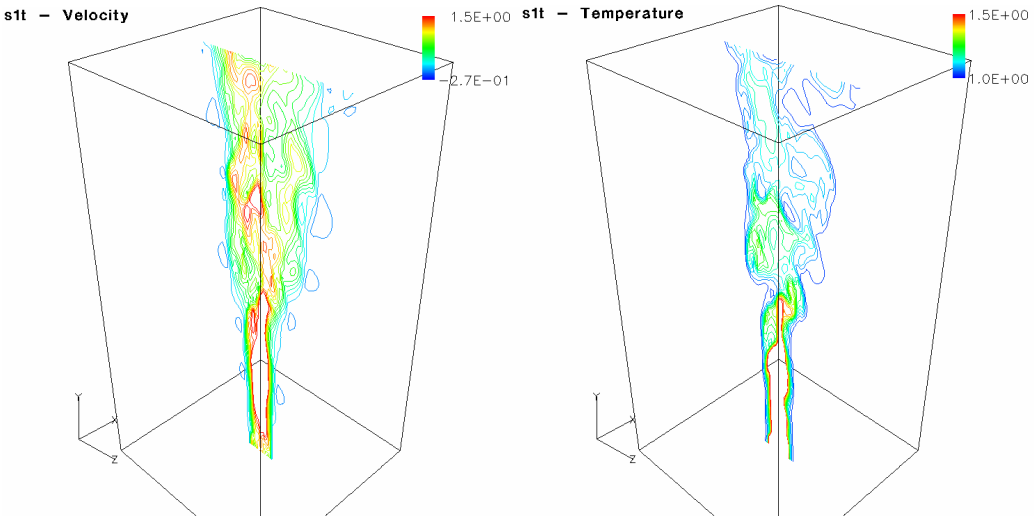

Figure 7.3.1 Instantaneous vertical velocity and temperature snapshots, from the Smagorinsky model simulation, s1t.

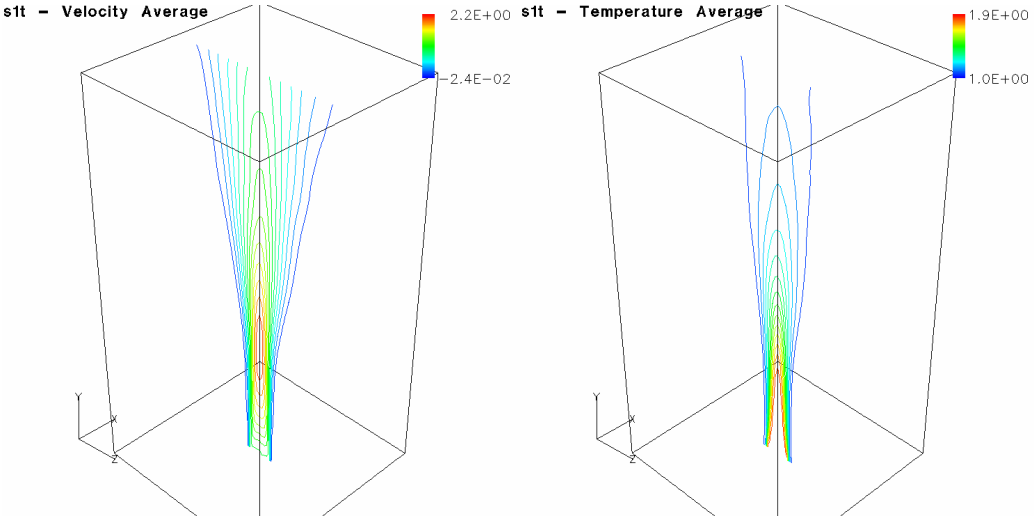

Figure 7.3.2 Vertical velocity and temperature averages, s1t.

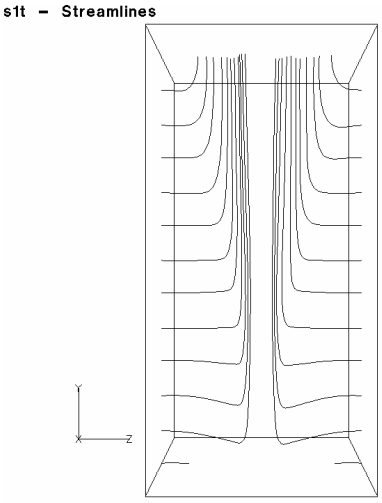

Figure 7.3.3 Average streamlines plot, s1t.

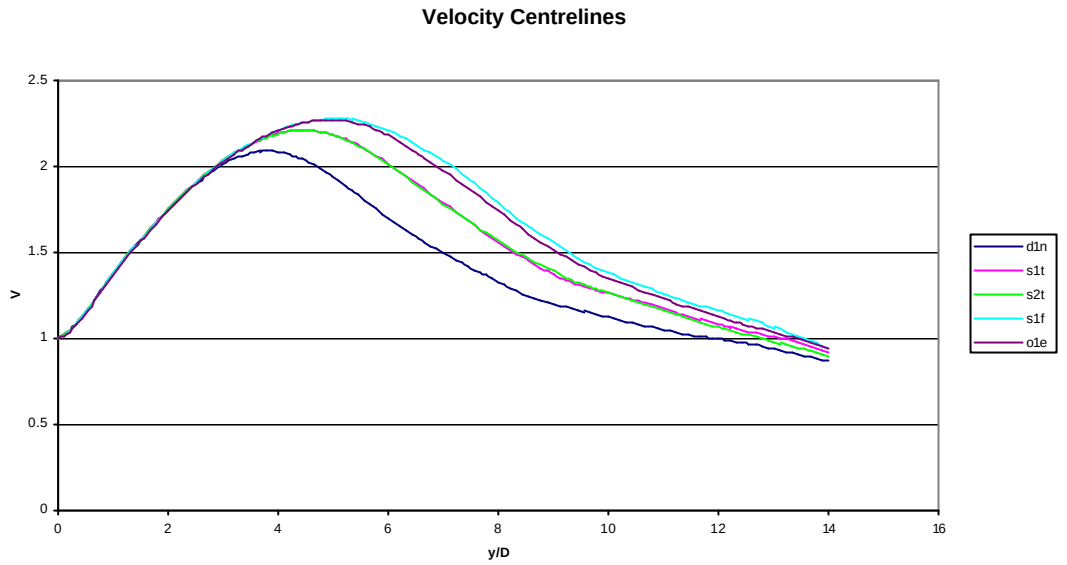

Figure 7.3.4. Velocity centrelines for d1n, no subgrid model, s1t, Smagorinsky model, s2t, buoyancy-modified Smagorinsky model, s1f, structure function model, o1e, one equation model.

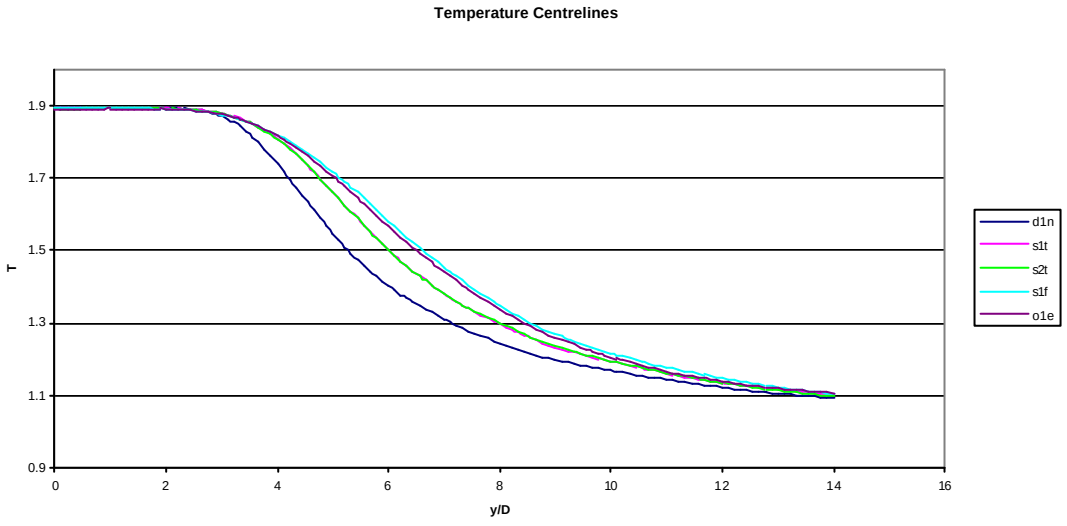

Figure 7.3.5. Temperature centrelines for d1n, no subgrid model, s1t, Smagorinsky model, s2t, buoyancy-modified Smagorinsky model, s1f, structure function model, o1e, one equation model.

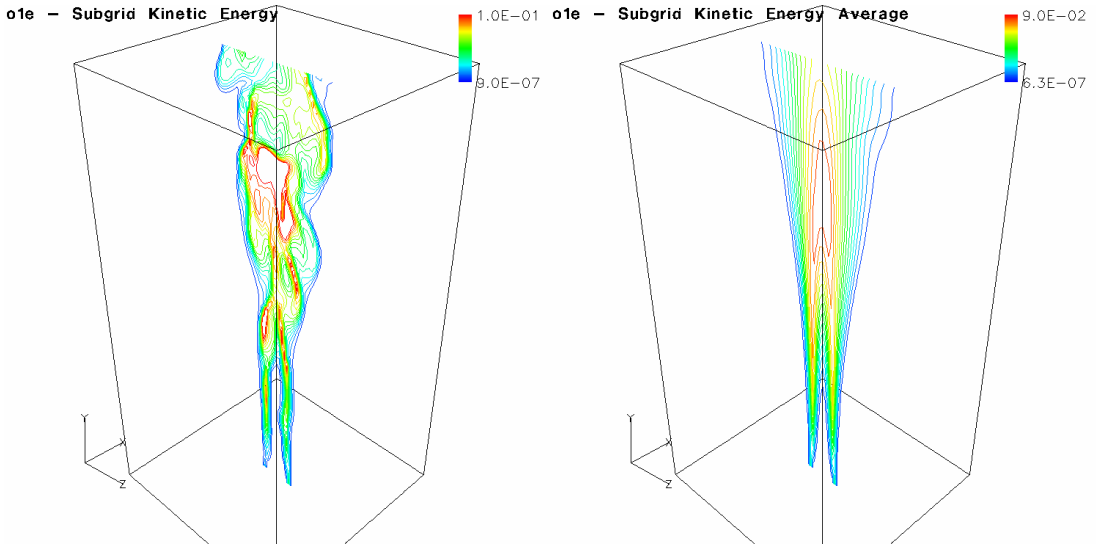

Figure 7.3.6 Instantaneous and averaged subgrid kinetic energy plots for the one equation model, o1e.

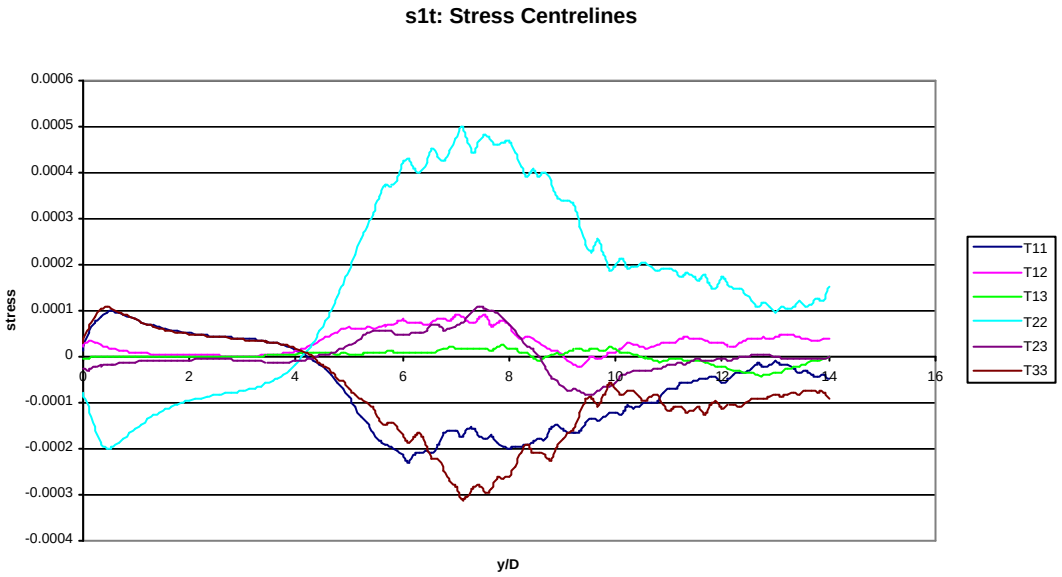

Figure 7.3.7 Stress centrelines for the Smagorinsky model, s1t, with Tij labelling the individual stresses.

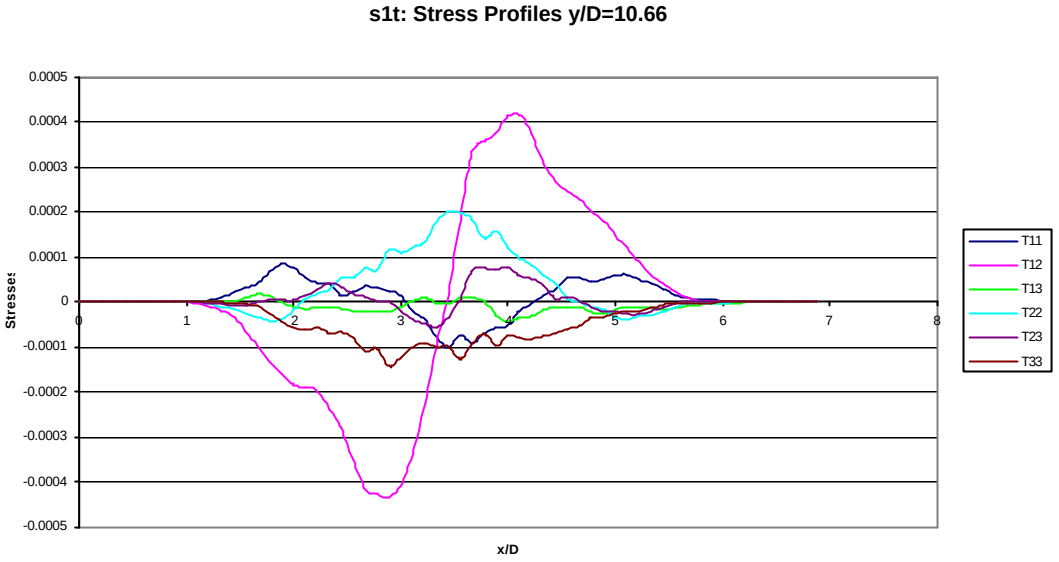

Figure 7.3.8 Stress profiles for Smagorinsky model, s1t, 10.66 diameters from the source, with Tij labelling the individual stresses.

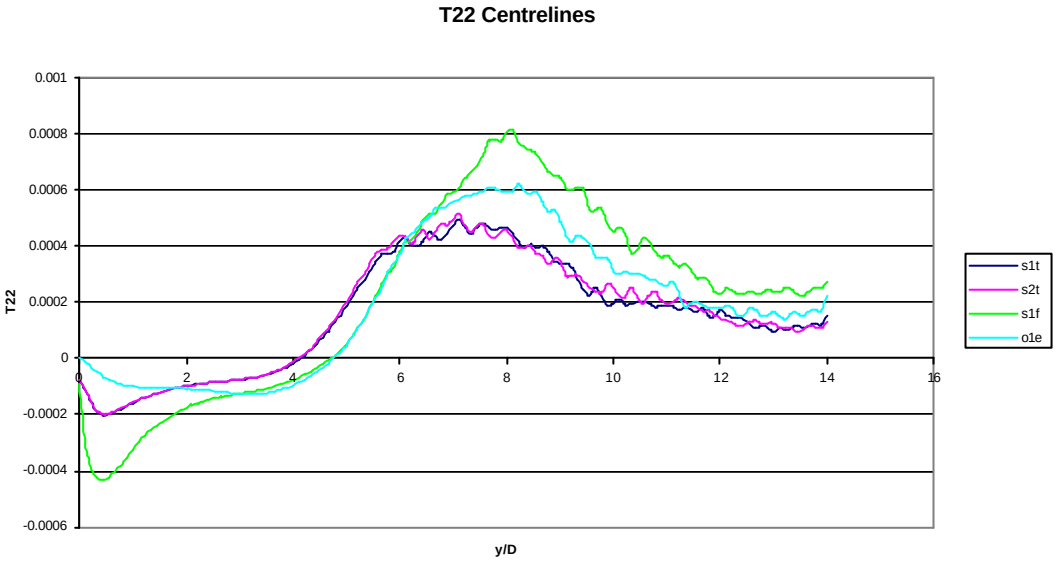

Figure 7.3.9 T22 centrelines for s1t, Smagorinsky model, s2t, buoyancy-modified Smagorinsky model, s1f, structure function model, o1e, one equation model.

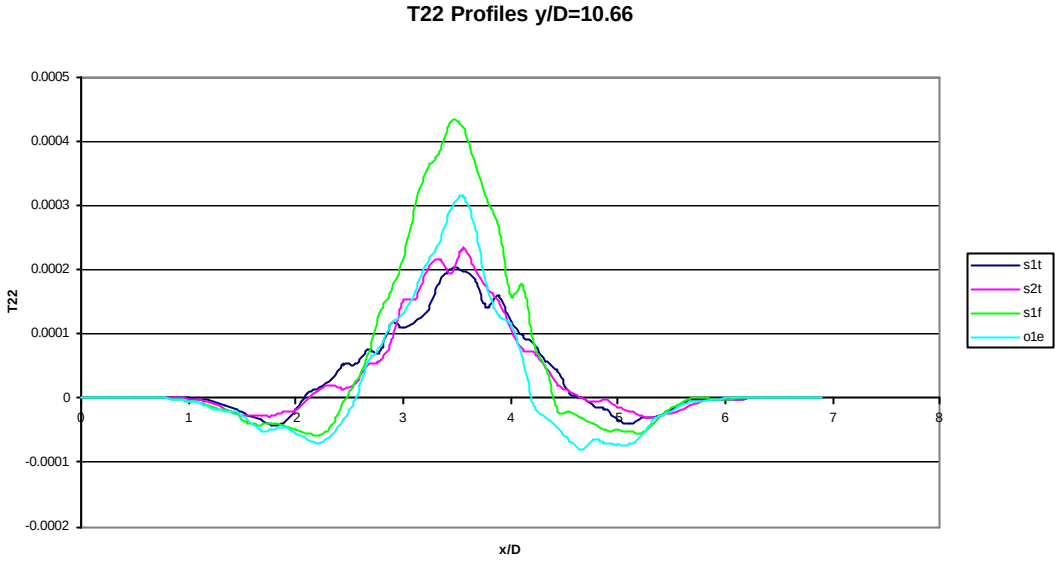

Figure 7.3.10 T22 Profiles for s1t, Smagorinsky model, s2t, buoyancy-modified Smagorinsky model, s1f, structure function model, o1e, one equation model.

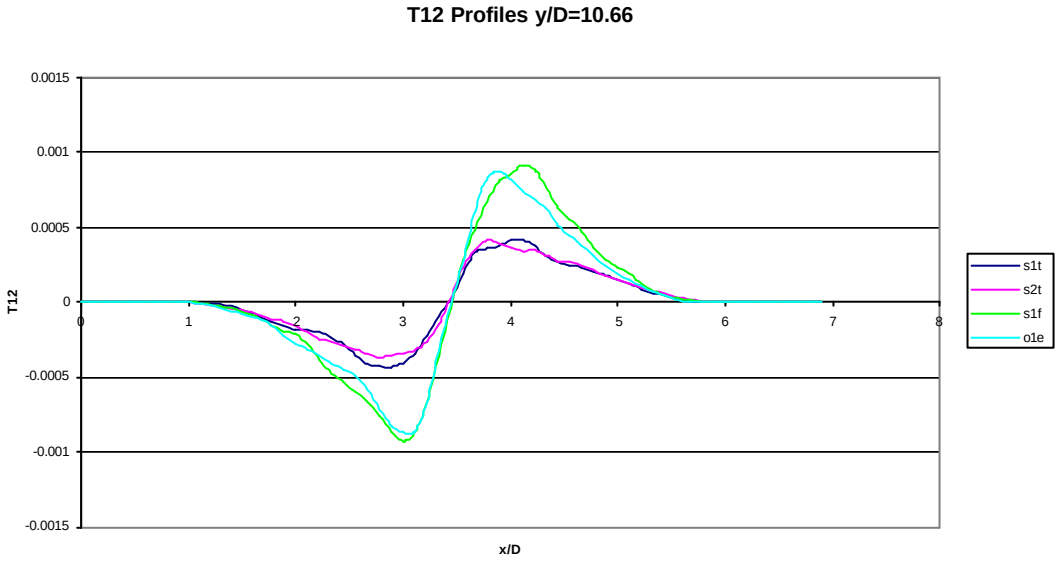

Figure 7.3.11 T12 profiles for s1t, Smagorinsky model, s2t, buoyancy-modified Smagorinsky model, s1f, structure function model, o1e, one equation model.

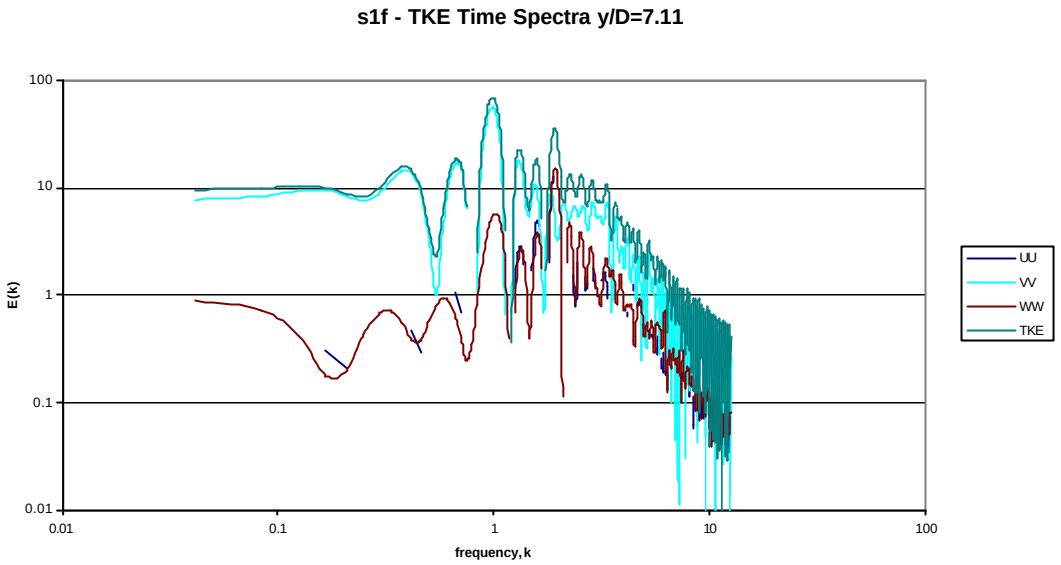

Figure 7.3.12 Turbulent kinetic energy spectra plot for structure function model simulation, s1f, at y/D=7.11.

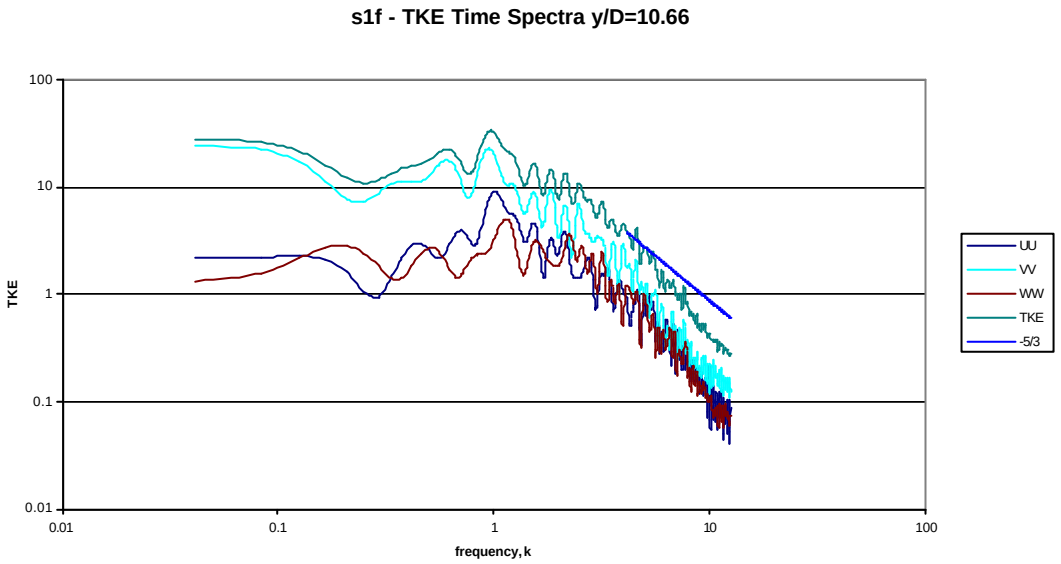

Figure 7.3.13 Turbulent kinetic energy spectra plot for structure function model simulation, s1f, at y/D=10.66.

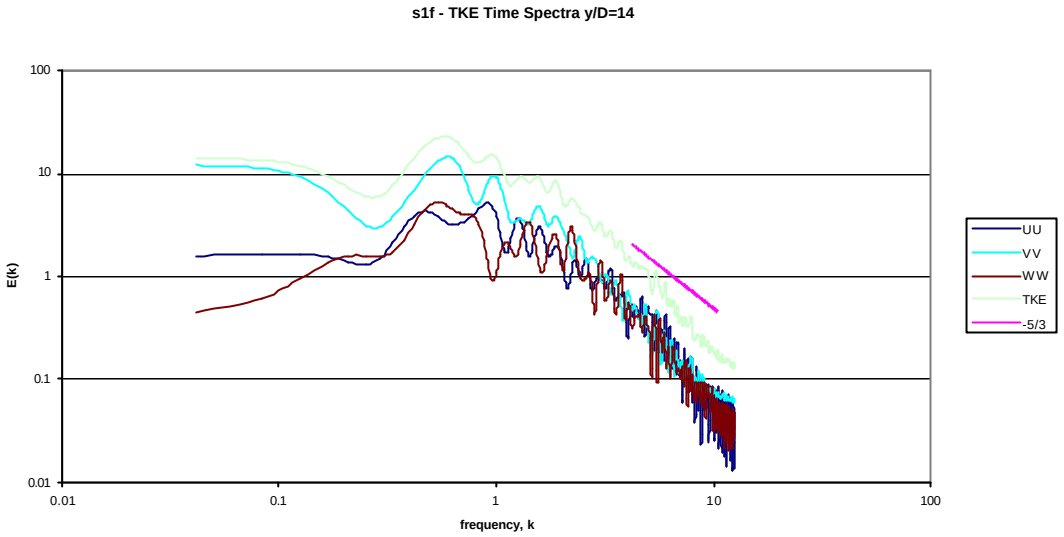

Figure 7.3.14 Turbulent kinetic energy spectra plot for structure functions model simulation, s1f, at y/D=14.

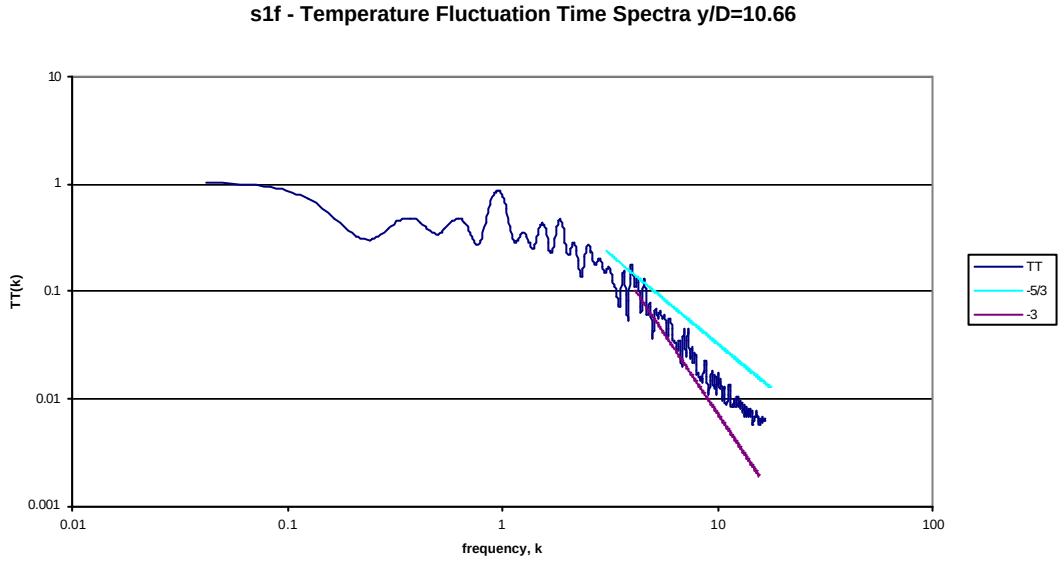

Figure 7.3.15 Temperature fluctuations spectra, TT(k), for structure function model simulation, s1f, using SGDH for the fluxes, at y/D=10.66.

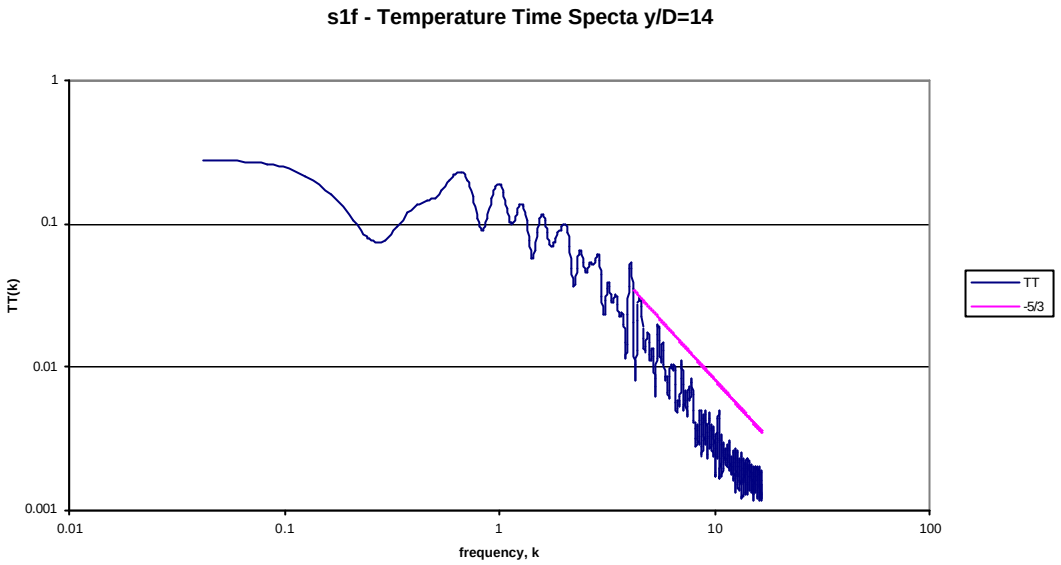

Figure 7.3.16 Temperature fluctuation spectrum, TT(k), for structure function model simulation, s1f, with SGDH model for fluxes, at y/D=14.

7.4 Gradient Flux Models

This section describes and compares the gradient flux models behaviour. It is essential that these models be tested in conjunction with the one-equation model since the second formulation explicitly requires the subgrid kinetic energy from the equation. The simulation labels are:

d1n: no subgrid models

o1e: one equation model for stresses and SDDH model for the fluxes

o2e: one equation model for stresses and no flux model

f1c: one equation model for stresses and GGDH_1 for the fluxes

f2c: one equation model for the stresses and GGDH_2 for the fluxes

Recall that the first formulation substitutes the modelled subgrid stresses directly into the subgrid kinetic energy term. The model constant for the GGDH models, after initial runs, was set to 5, an order of magnitude larger than the RANS model suggestion of Jones and Musange (1988).

It is shown that the GGDH models have a better behaviour in laminar regions than the SGDH model, due to a different qualitative behaviour, and consequently better handles transition. The constant for the two GGDH models should not be the same if they are to be equivalent. The importance of the flux model in general is shown.

Looking at the velocity and temperature decays in figs. 7.4.1 and 7.4.2, the most apparent feature is the very strong effect on transition the SGDH model has. The one equation model by itself, o2e, delays transition marginally and then has a higher dissipation. The two GGDH models contribute further to this effect, but the SGDH model contributes the most. The GGDH models are a significant improvement on the SGDH model.

A closer investigation of the temperature decay plot around the transition point, highlights the very close relationship between the temperature and velocity coupling. Fig. 7.4.3 plots the temperatures in the range 2<y/D>4. It can be seen that the temperature has already started decaying when the SGDH model is used. This is due to its high gradients across the jet/ambient fluid boundary near the inlet. The SGDH model lets each flux component be proportional to a temperature gradient in a single

dimension, whereas the more detailed GGDH models are based on mean composition of gradients related to the appropriate stresses in all dimensions. Near the inlet, the SGDH model recognises this uni-directional gradient as turbulence, while the GGDH models do not dissipate from a similar false recognition.

As the temperature decay is damped the transition process is slowed a lot. On the other hand, the GGDH models, which do not have negative diffusivity, maintain their initial inflow value longer than for d1n, without a subgrid model. The coupling between the velocity and the temperature is, of course, not linear. Here we see the effect of the subgrid stresses damping the velocity fluctuations, which in turn, dampen the temperature decay. i.e. it is in the initial transitional fluctuations that cause the extra spread and the swifter decay in d1n over o2e, f1c and f2c. After the transition occurs, these four simulations rapidly overtake o1e in decay, although further downstream o1e has the greater decay after transition has been achieved.

It can also be seen in this region that f1c goes through transition first, but is quickly caught up by f2c.

The EN2 flux centreline is given in fig. 7.4.4. The earlier temperature decay for o1e is reflected in the magnitude of EN2 increasing earlier, although this is a by-product of the increased earlier spread. It is the radial flux which causes the spread.

It is seen that the second formulation of the GGDH model has a magnitude larger than the SGDH model, and that the first formulation is somewhat less than a half of that, although the difference in magnitude between the two models decreases the further through transition is gone.

The formulation of the GGDH models is such that it behaves as a non-isotropic Prandtl number, and the turbulent stresses of the eddy models incline the vertical flux, EN2, to be the dominant term in the plume core, which has less effect on the overall flow than the radial flux, EN1 (in the X-axis). Fig. 7.4.5 shows a plot of the fluxes (EN1 is left out for f1c and f2c as it is a negligible term, but it is a key component of the consideration of the plot). The difference in magnitude between EN2 terms of the GGDH models and the SGDH model is not a reasonable reflection, due to the difference of their centreline values, but it does show the qualitative difference between them – that the radial term is larger for the SGDH whereas it is the axial term for the GGDH models.

Figs. 7.4.6 and 7.4.7 show the centrelines of the subgrid kinetic energy and the turbulent viscosity. There is only a marginal difference (between f1c and f2c) induced by the two GGDH models, although f1c, with the weaker fluxes, reaches the higher value in both cases even though o2e, without a flux model is lower. This highlights the non-linearity and the subtlety of the way in which the terms can interact.

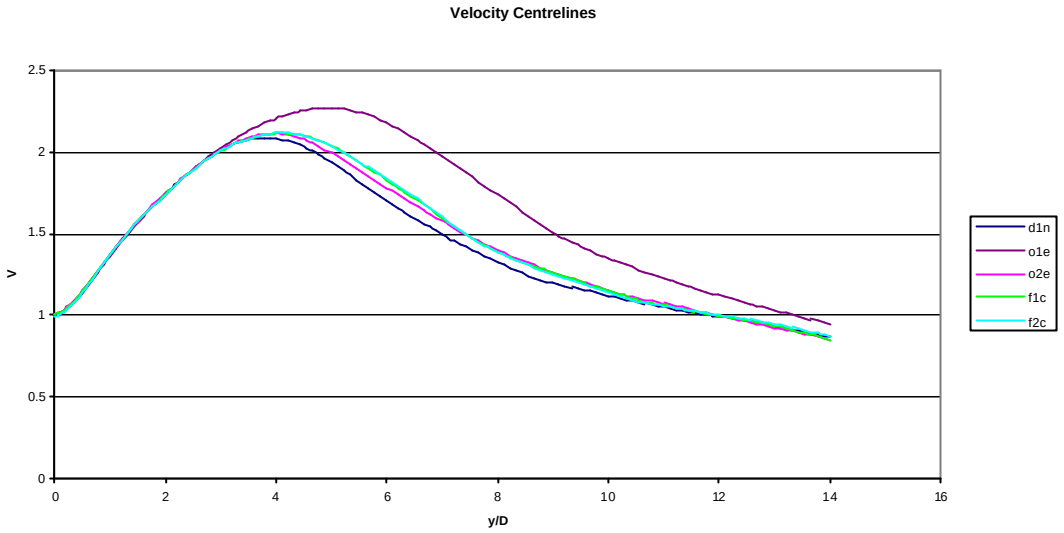

Figure 7.4.1 Vertical velocity centrelines for d1n, no subgrid model, o1e, one equation model with SGDH flux, o2e, one equation stress model, no flux model, f1c, one equation model with first formulation of the GGDH model, GGDH_1, f2c, one equation model with second formulation of the GGDH model, GGDH_2.

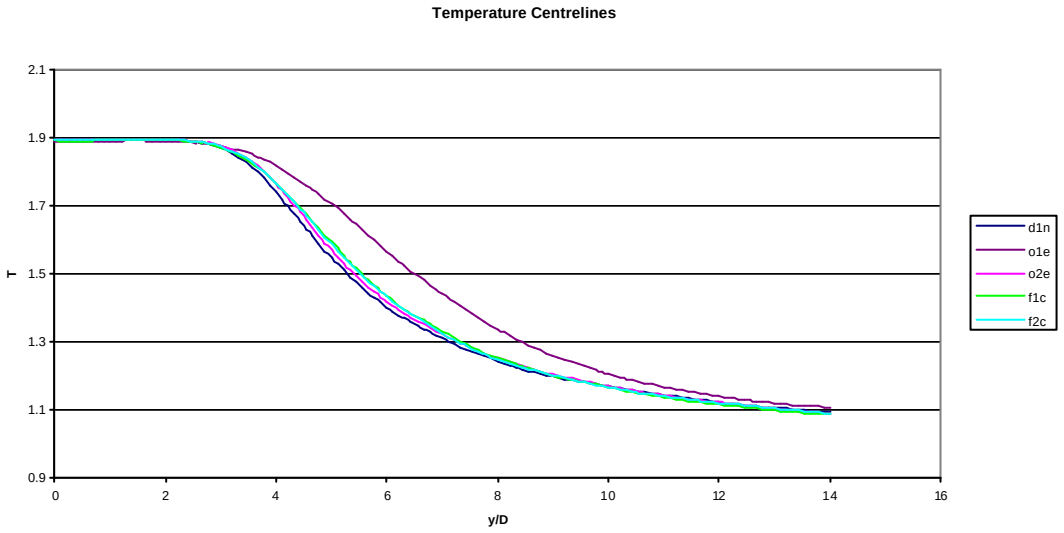

Figure 7.4.2 Temperature centrelines for d1n, no subgrid model, o1e, one equation model with SGDH flux, o2e, one equation stress model, no flux model, f1c, one equation model with first formulation of the GGDH model, GGDH_1, f2c, one equation model with second formulation of the GGDH model, GGDH_2.

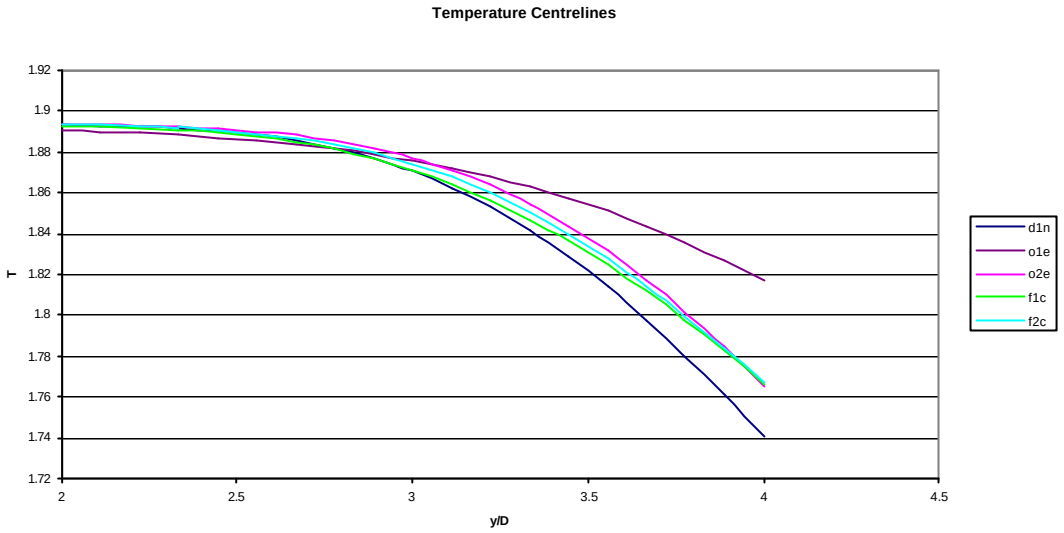

Figure 7.4.3 Temperature centrelines in the range 2<y/D<4 for d1n, no subgrid model, o1e, one equation model with SGDH flux, o2e, one equation model, no flux model, f1c, one equation model with first formulation of the GGDH model, GGDH_1, f2c, one equation model with second formulation of the GGDH model, GGDH_2.

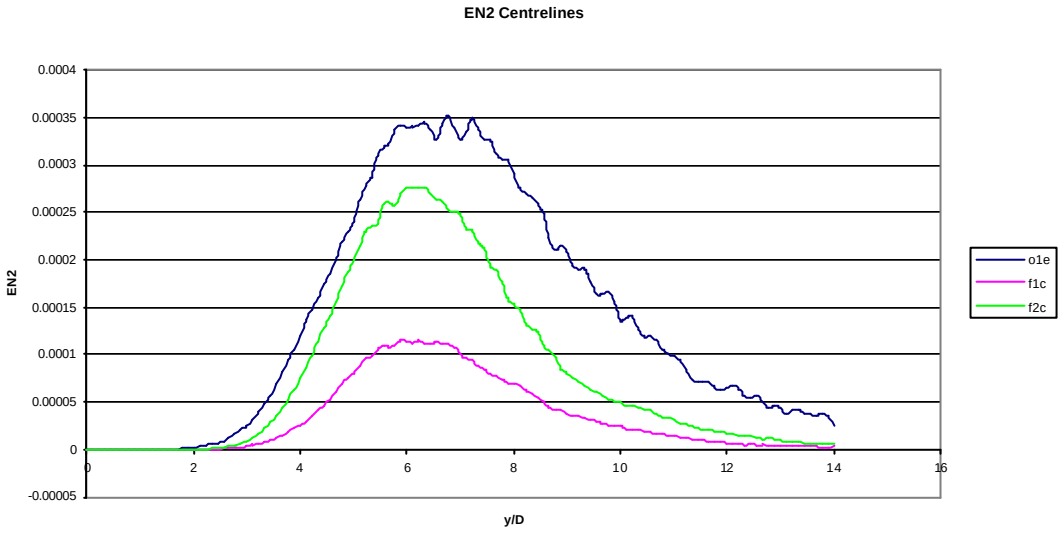

Figure 7.4.4 Vertical temperature flux, EN2, centrelines for o1e, one equation model with SGDH flux, f1c, one equation model with first formulation of the GGDH model, GGDH_1, f2c, one equation model with second formulation of the GGDH model, GGDH_2.

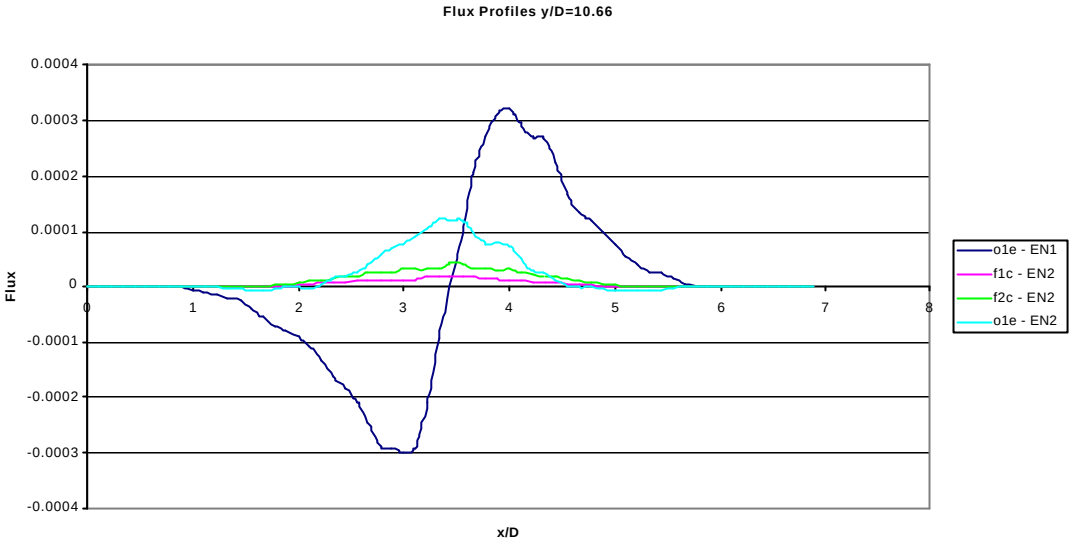

Figure 7.4.5 Profiles for the vertical flux, EN2, and radial flux, EN1 for o1e, one equation model with SGDH flux, f1c, one equation model with first formulation of the GGDH model, GGDH_1, f2c, one equation model with second formulation of the GGDH model, GGDH_2.

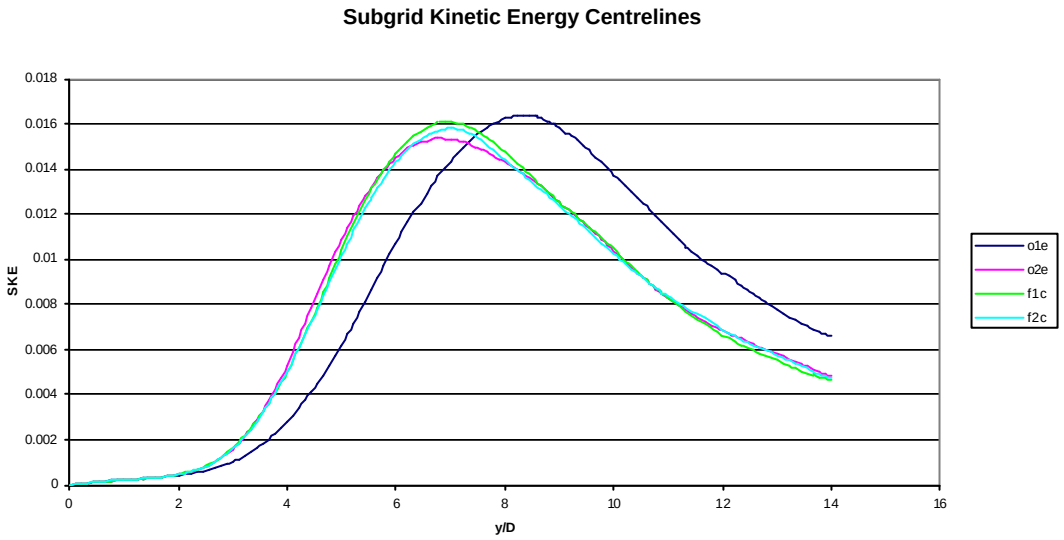

Figure 7.4.6 Subgrid kinetic energy centrelines for o1e, one equation model with SGDH flux, o2e, one equation model, no flux model, f1c, one equation model with first formulation of the GGDH model, GGDH_1, f2c, one equation model with second formulation of the GGDH model, GGDH_2.

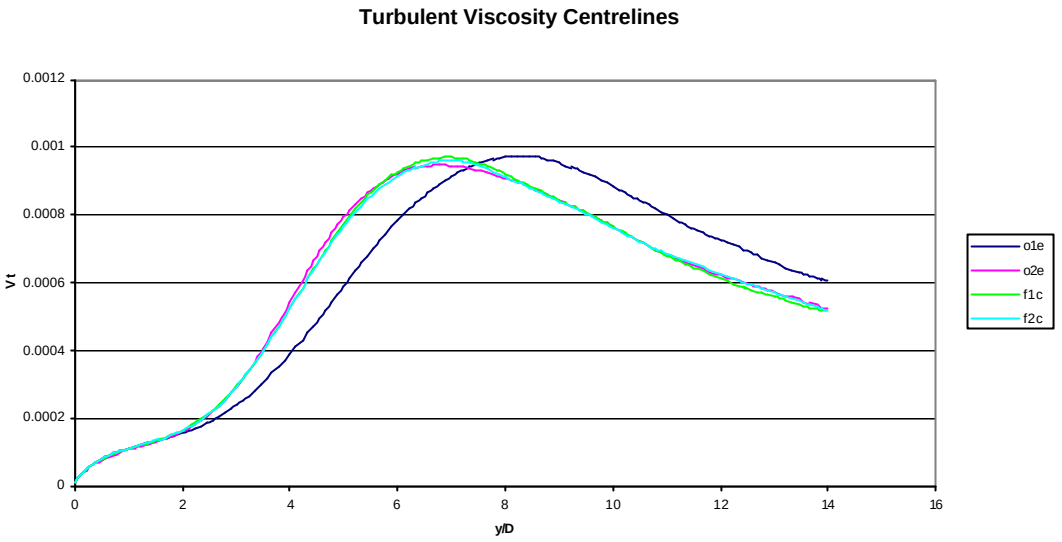

Figure 7.4.7 Turbulent viscosity centrelines for the eddy viscosity models for o1e, one equation model with SGDH flux, o2e, one equation model, no flux model, f1c, one equation model with first formulation of the GGDH model, GGDH_1, f2c, one equation model with second formulation of the GGDH model, GGDH_2.

7.5 Mixed Models

The mixed models are considered alongside d1n and s1t. The labels for the two static mixed models are

d1n: no subgrid model

s1t: Smagorinsky stress model and SGDH flux model

m1x: mixed Smagorinsky and Bardina stress model and mixed SGDH and Bardina flux model.

m2x: mixed Smagorinsky and Leonard stress model and no subgrid flux model.

Both models use the type B mixed formulation, halving each component. For both the stress and the flux models the Smagorinsky or SGDH components are referred to as the eddy components and the Bardina or Leonard components are referred to as the structure components. These two simulations were run for less time than other simulations, for 40,000 time-steps, averaging over 35,000, again every 25 time-steps.

The mixed models are shown to be very beneficial, with the structural terms generally much stronger than the eddy terms. The two components have a balancing effect on the transition point, as well as the decay rates.

The velocity and temperature decays are plotted in figs. 7.5.1 and 7.5.2. The results are strikingly close to the d1n results. Transition occurs at the same point, and slightly sooner in the case of m2x. However, the decay rate is very slightly less for m1x initially although it increases later. M2x, however, appears to have a slower decay all the way down the centreline. Note that this is not a direct indictor of the spread rate as it was for the eddy and gradient models. The validation on laminar plumes indicated that the Leonard and Bardina models can provide an acceleration term rather than a purely diffusive term.

The main centreline stress, T22, is plotted for both cases against the Smagorinsky model simulation s1t in fig. 7.5.3. The main point is the very significant difference in magnitude of the stresses between all three models, with the Bardina model the largest, followed by the Leonard, followed by the eddy viscosity, which is relatively enhanced from the effects of its later transition. Fig. 7.5.4 shows the T12 profiles and although m1x has strongly the larger value the difference is not as much as for T22.

The stress centrelines and profiles of m1x and m2x are given in figs 7.5.5-7.5.8. The plots are qualitatively different to the eddy viscosity models. The horizontal normal stresses, T11 and T33 are positive, adhering to the realizability conditions. All the normal stresses, including T22, are much larger than the eddy model stresses. Counter-intuitively, given the increased magnitude of the model averages, the mixed models have far less effect on the flow than the pure eddy models. This is due to the fact that the two components have opposite effects on the plume, which to a certain extent cancel each other out. This is only half of the situation however. It is worth pointing out that whatever the magnitude of the stresses, if they have a certain relation with their respective transport equations, the resulting flow will not be affected. This occurs when the stresses or fluxes for each equation scale up the time-derivative by the same factor, effectively only changing the time step. This shows that finally it is the relative magnitude between the stresses which governs the behaviour, more than the difference in magnitude of the stresses. The vertical normal stress stretches the plume (vertically) as the decreasing velocity makes it a positive source term, and the horizontal normal stresses constrain the spread of the horizontal momentum acting as an acceleration towards the plume centreline.

Qualitatively m1x and m2x are similar, although the m1x stresses are larger, by approximately a factor of two. The stresses show the normal stresses to be the dominant terms, with the radial T12 stress in the X-axis, correspondingly T23 in the Z-axis, a significant but smaller term. This is dissimilar to the eddy models, in which the radial stress is the most significant term of the model. With the above considerations explains the lack of increased spread.
The magnitude of the structure components are generally much larger than those of the eddy models, even though their values have been halved for the mixed model formulation.

The non-normal stresses for m2x in figs. 7.5.7 and 7.5.8 are less than zero, and the stress profiles for m2x show a one-sided nature in the distribution, tending to the right-hand side. Velocity profiles are shown in figs. 7.5.9 and 7.5.10, of both mixed models and the eddy models from section 8.3, at y/D=10.66. It can be seen that there is a very slight tendency for the plume to drift. However, the one-sided distribution of

the mixed Leonard model has not caused any more drift than the Bardina model, which has a more even distribution. It is suggested that the non-linearity of the Leonard model exaggerates the imperfections of the averaging process, whereas the Bardina model, filtering its non-linear components and taking the difference of them, reduces this effect.

The flux centrelines are shown in figs. 7.5.11 and 7.5.12. Again, the Bardina mixed model has the significantly stronger EN2 term. Also, the radial flux, EN1 in the X-axis, is stronger for the mixed Bardina model, although the difference is much less than for EN2. The mean velocity at y/D=10.66 is lower for m1x but the radial flux is greater than the for the SGDH model. The difference between the normalised fluxes would be slightly increased.

The models have a number of mechanisms working on them which interact in different ways. In the eddy stress model the horizontal normal stresses, T11 and T33, are the terms which spread the horizontal momentum components. Breaking realizability conditions, the eddy models dissipate this momentum outwards. The Leonard and Bardina components of these two terms are much stronger, and work to confine the momentum rather than spread it, with the opposite sign. Of course, it is much more difficult to confine than to expand, and the larger magnitudes have less effect on the decay rates. For the spread of the vertical momentum, the T12 (or T23) and T22 stresses are the key components, the latter counterbalancing the former. The eddy models here have a stronger relative magnitude in T12, and correspondingly a greater impact on the resulting flow.
For the flux models the mixed models are stronger, and qualitatively the same as the eddy models, but the relative magnitude between the EN1 or EN3 and EN2 is different. The combination of these terms result in the mixed Bardina model having a slightly lower decay rate than no subgrid model, whereas the similar, but weaker mixed Leonard model overall has a marginally greater decay rate.
The temperature profiles, fig. 7.5.13, show the greater spread and slight tilt to the right of m1x. The further spread is caused at least partially by the flux model.

A number of images relating the mixed model components are shown. Fig, 7.5.14 shows axial slices of the normal stress components for m2x. The averaging is

reasonable, and certain trends become apparent. The dominance of the structural terms is clearly shown, with the minimum difference, for the T33 stress, being a single order of magnitude. The structure component of T11 is seen to be somewhat lopsided at around y/D=4, reflecting the imperfections of the averaging more strongly then the Bardina component does in m1x.

The ratio's are also interesting to consider, and are given in fig. 7.5.15, in which the eddy component is the denominator, and the structure component the numerator. The three main stresses are considered as well as the non-radial normal stress. The difference between the components of the T12 and T23 stresses is confirmed to be less than for the normal stresses. The radial stress, T23, however shows a moderate ratio in the turbulent region, indicating that the eddy component has a non-negligible role in this stress. The centre and edges are large where averages tend to zero.

T22 and T33 are almost inverted plots of each other. T22 has a very high ratio down the centreline which very sharply at the edges becomes very strongly negative, as the eddy component turns negative, due to the very slightly negative average vertical velocity there. T33, for which the eddy component breaks the realisation rules, is negative along the centre, becoming slightly positive at the edges and inverting the sign of the ratio.

Plots from the m1x flux models of EN2 and EN3 are given in fig. 7.5.16. Positive correlations are seen for both components in the plume core. However, in the entrainment region there is acceleration in the velocity and a positive gradient in the temperature before they both decline once fully entrained, and the correlation of these two gradients changes the sign of the flux component.

The T22 eddy component centrelines, plotted in fig. 7.5.17, show that the eddy structure component is not greatly affected by the inclusion of the structure component, and that the magnitudes are half of the normal eddy component, as the model formulation prescribes. Fig. 7.5.18 further highlights the difference in magnitude between the eddy and structural components, giving the T22 component profiles. The EN2 eddy component centrelines are also shown to be half of their non-mixed value, also unaffected by the structural component, in fig. 7.5.19.

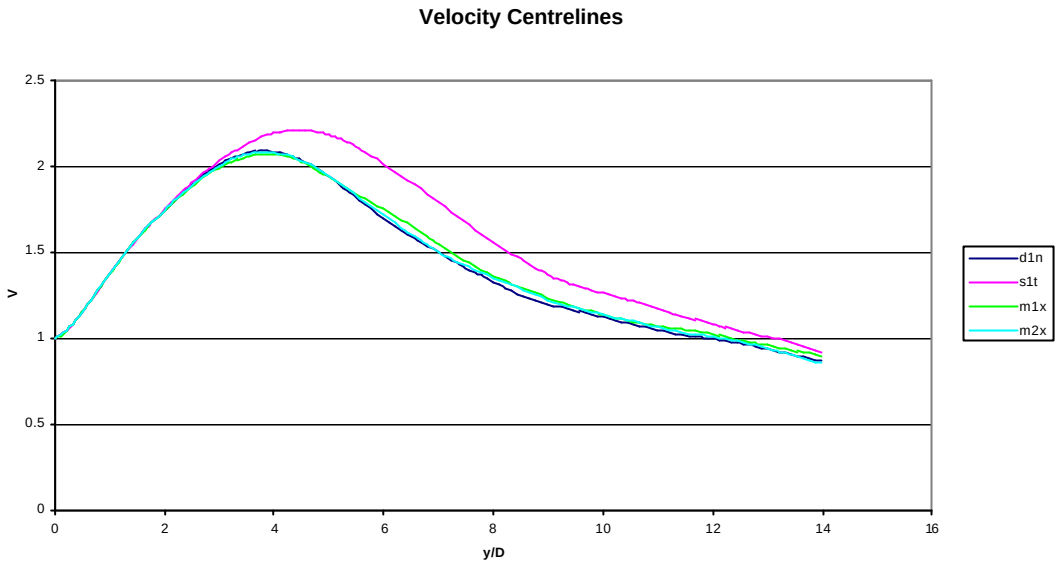

Figure 7.5.1 Velocity centrelines for d1n, no subgrid model, s1t, Smagorinsky model and SGDH flux, m1x, mixed Smagorinsky/Bardina stress model, mixed SGDH Bardina flux model, m2x, mixed Smagorinsky/Leonard stress model, no flux model.

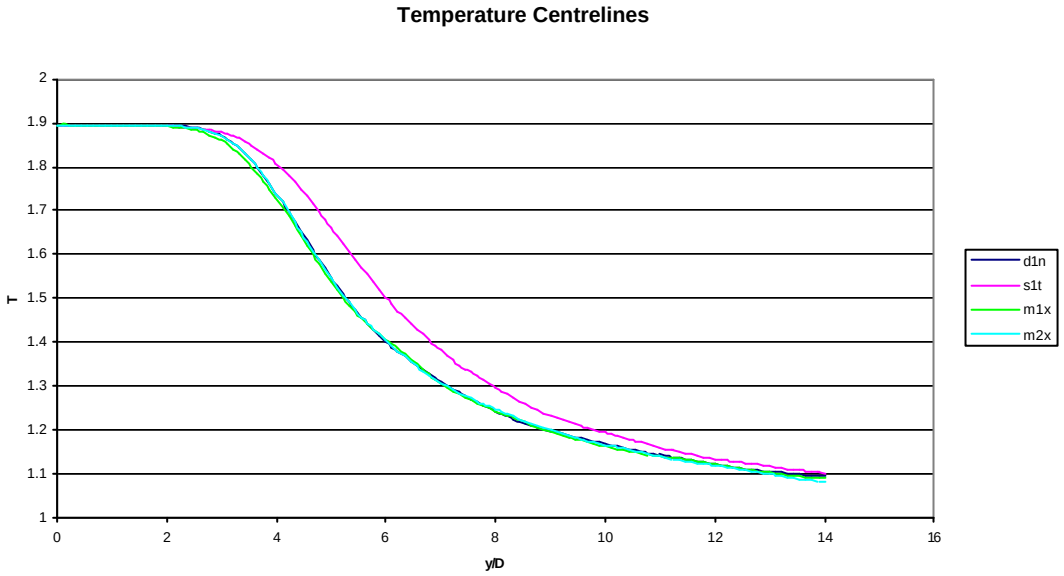

Figure 7.5.2 Temperature centrelines for d1n, no subgrid model, s1t, Smagorinsky model and SGDH flux, m1x, mixed Smagorinsky/Bardina stress model, mixed SGDH Bardina flux model, m2x, mixed Smagorinsky/Leonard stress model, no flux model.

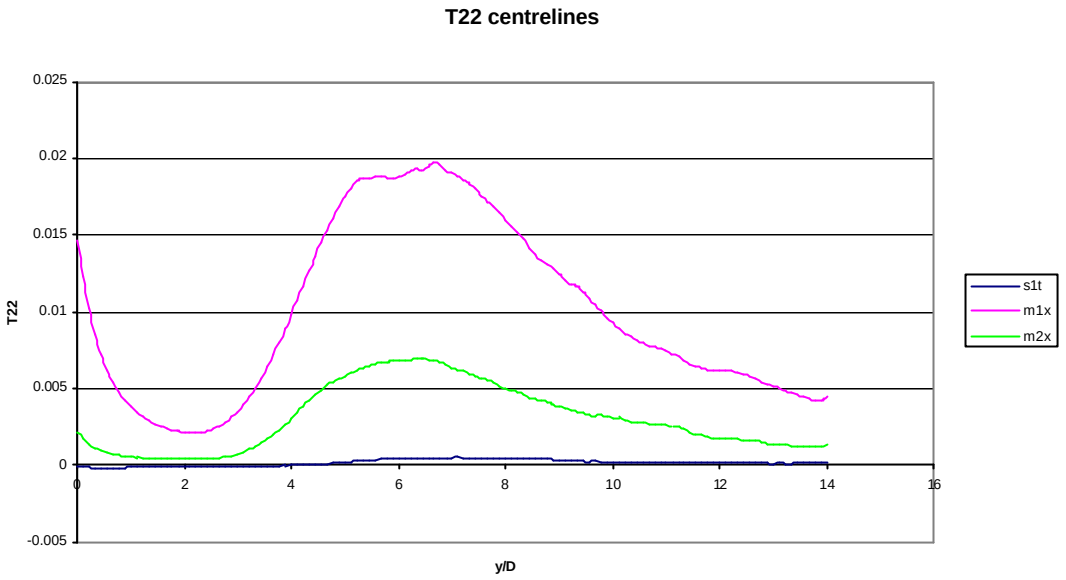

Figure 7.5.3 Vertical normal stress, T22, centrelines for s1t, Smagorinsky model and SGDH flux, m1x, mixed Smagorinsky/Bardina stress model, mixed SGDH Bardina flux model, m2x, mixed Smagorinsky/Leonard stress model, no flux model.

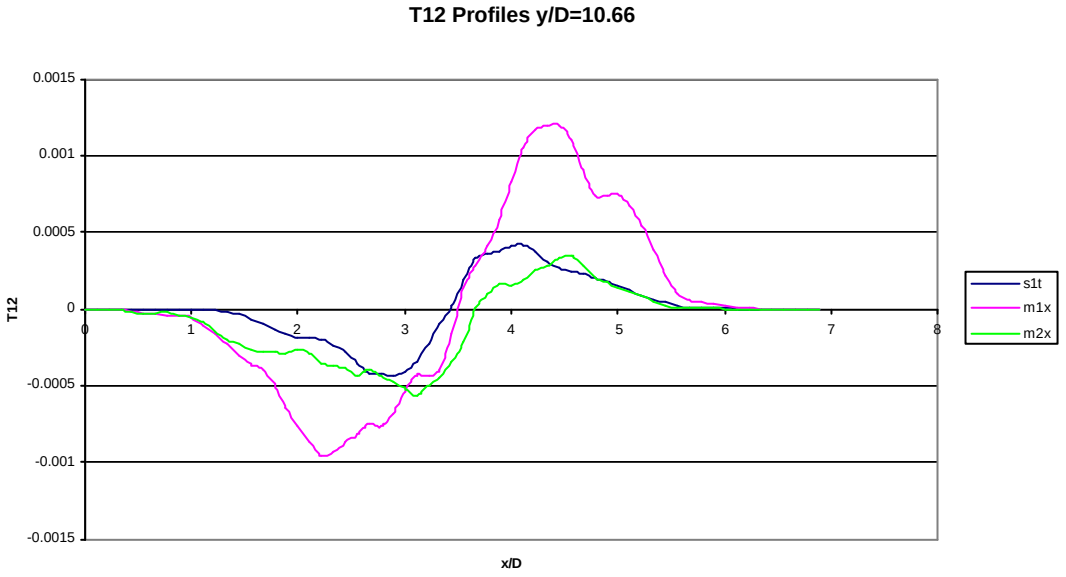

Figure 7.5.4 Vertical radial stress, T12, profiles at y/D=10.66 for s1t, Smagorinsky model and SGDH flux, m1x, mixed Smagorinsky/Bardina stress model, mixed SGDH Bardina flux model, m2x, mixed Smagorinsky/Leonard stress model, no flux model.

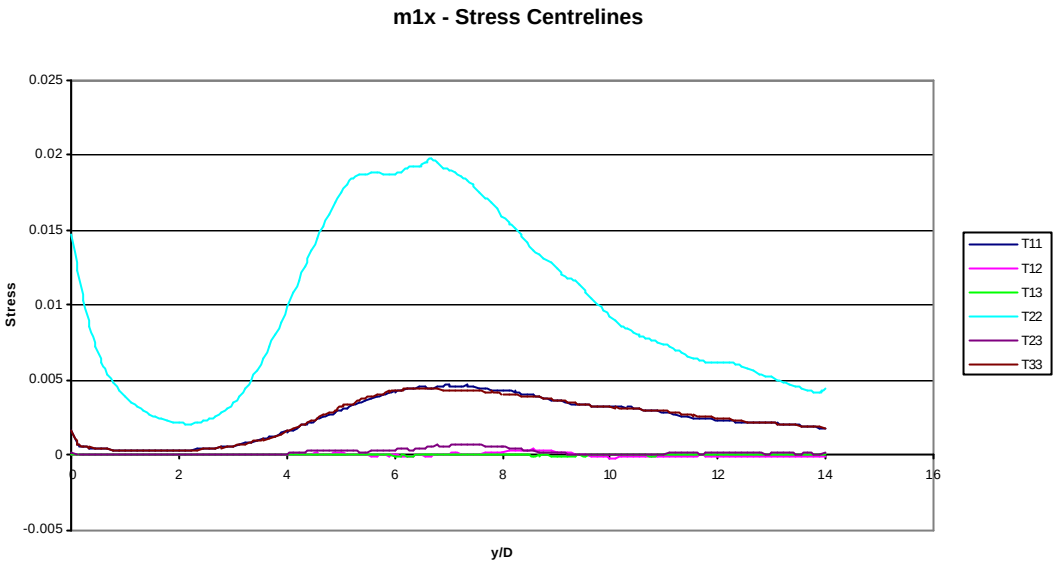

Figure 7.5.5 Stress centrelines for m1x, mixed Smagorinsky/Bardina stress model, mixed SGDH/Bardina flux model.

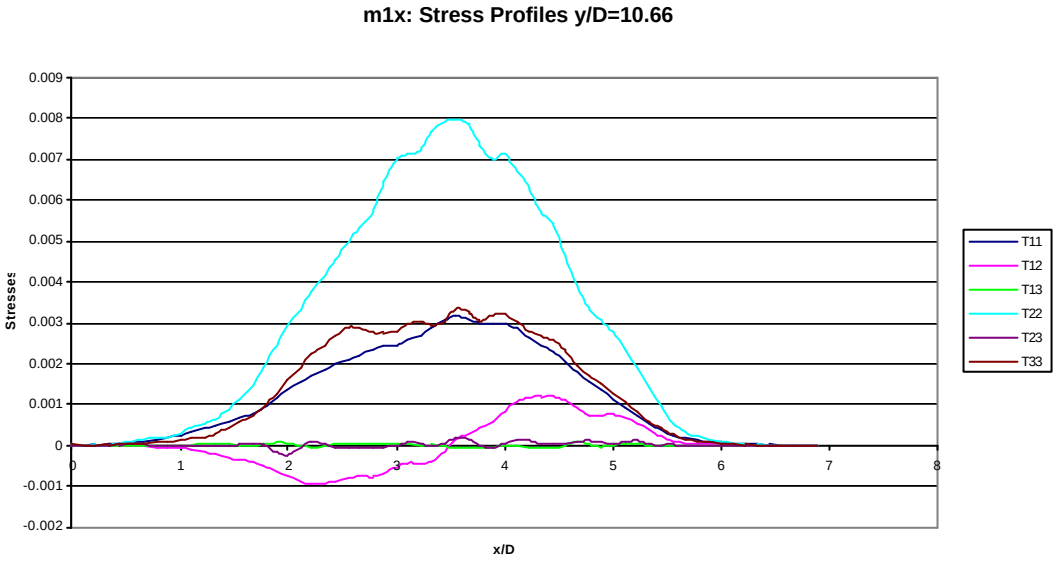

Figure 7.5.6 Stress profiles for m1x, mixed Smagorinsky/Bardina stress model, mixed SGDH/Bardina flux model, at y/D=10.66.

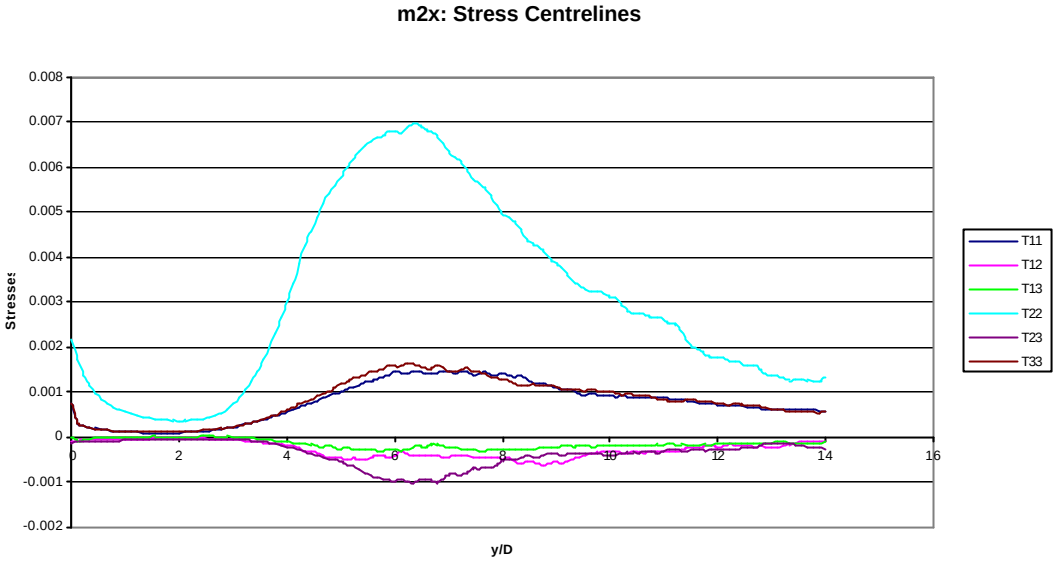

Figure 7.5.7 Stress centrelines for m2x, mixed Smagorinsky/Leonard stress model, no flux model.

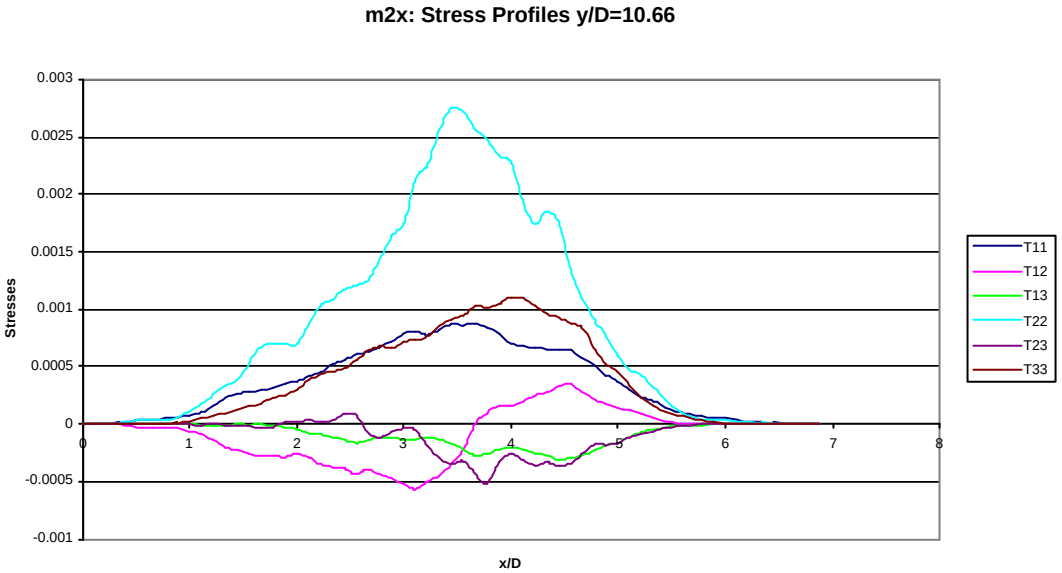

Figure 7.5.8 Stress profiles for m2x, mixed Smagorinsky/Leonard stress model, no flux model, at y/D=10.66.

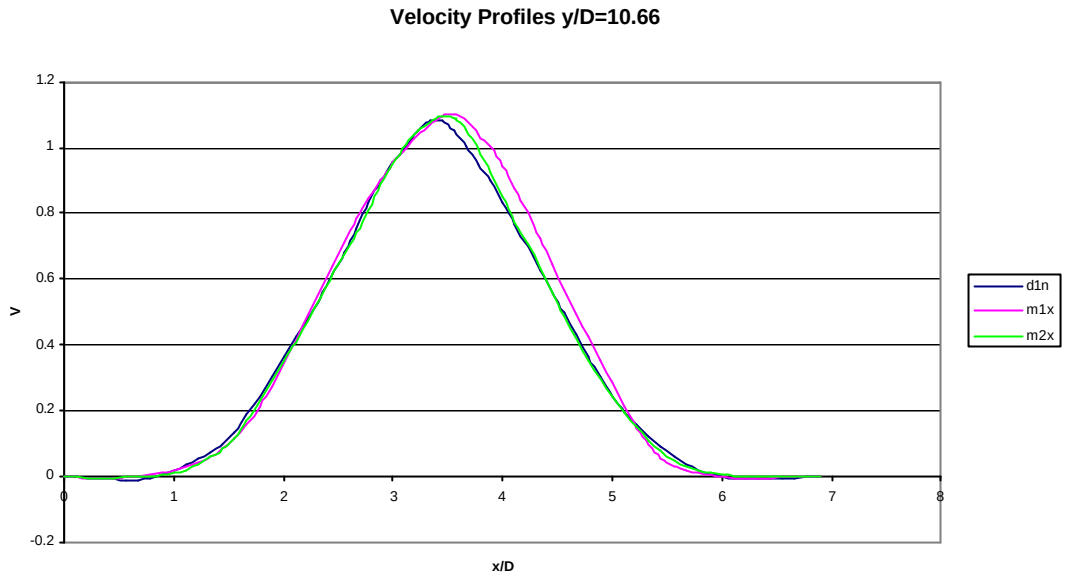

Figure 7.5.9 Vertical velocity profiles at y/D=10.66 for d1n, no subgrid model, m1x, mixed Smagorinsky/Bardina stress model, mixed SGDH Bardina flux model, m2x, mixed Smagorinsky/Leonard stress model, no flux model.

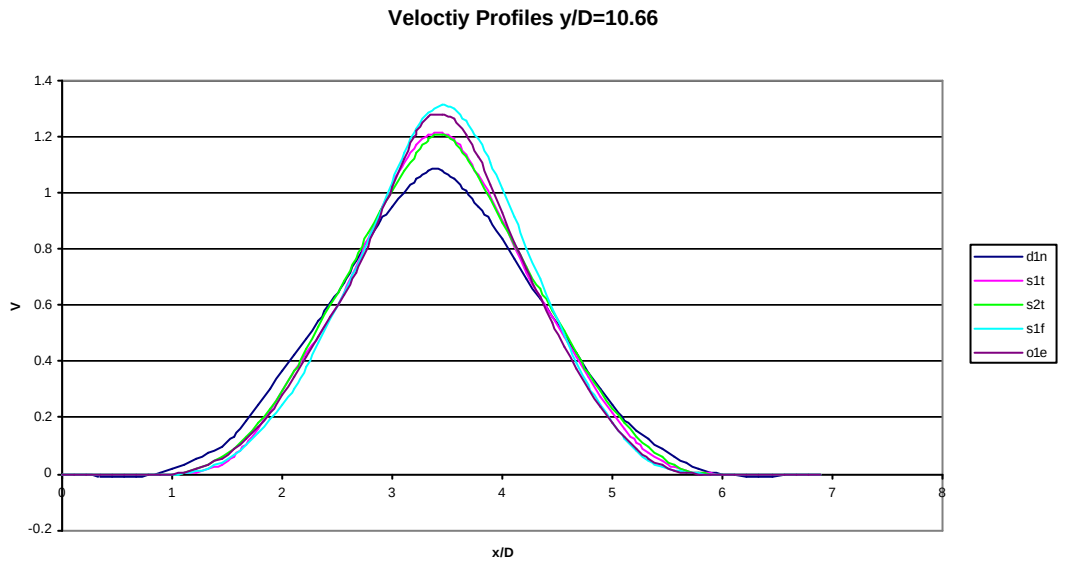

Figure 7.5.10 Vertical velocity profiles at y/D=10.66 for static model simulations from section 7.3, d1n, no subgrid model, s1t, Smagorinsky model, s2t, buoyancy-modified Smagorinsky model, s1f, structure function model, o1e, one equation model.

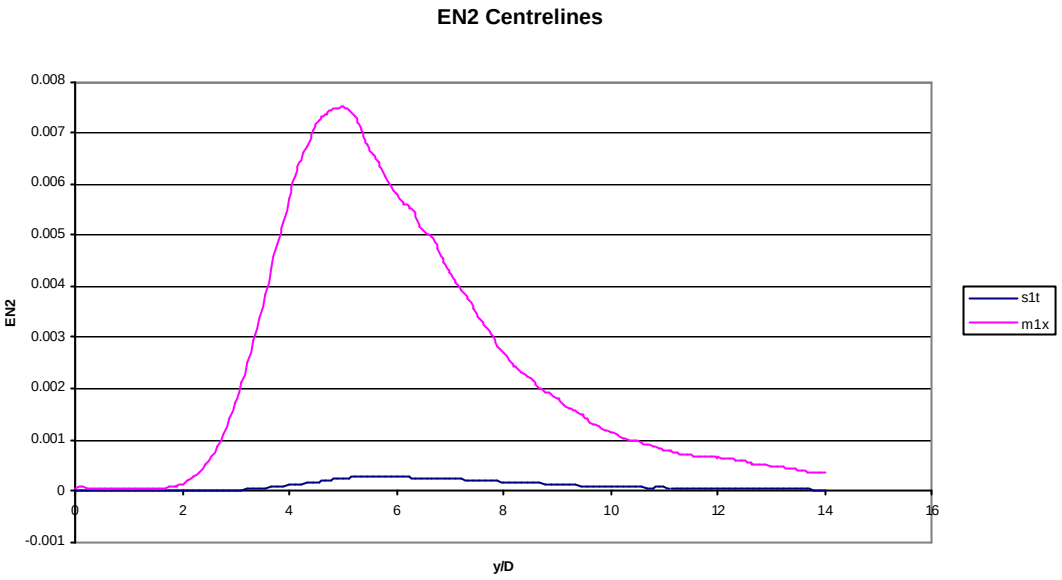

Figure 7.5.11 Vertical flux, EN2, centrelines for s1t, Smagorinsky model and SGDH flux, m1x, mixed Smagorinsky/Bardina stress model.

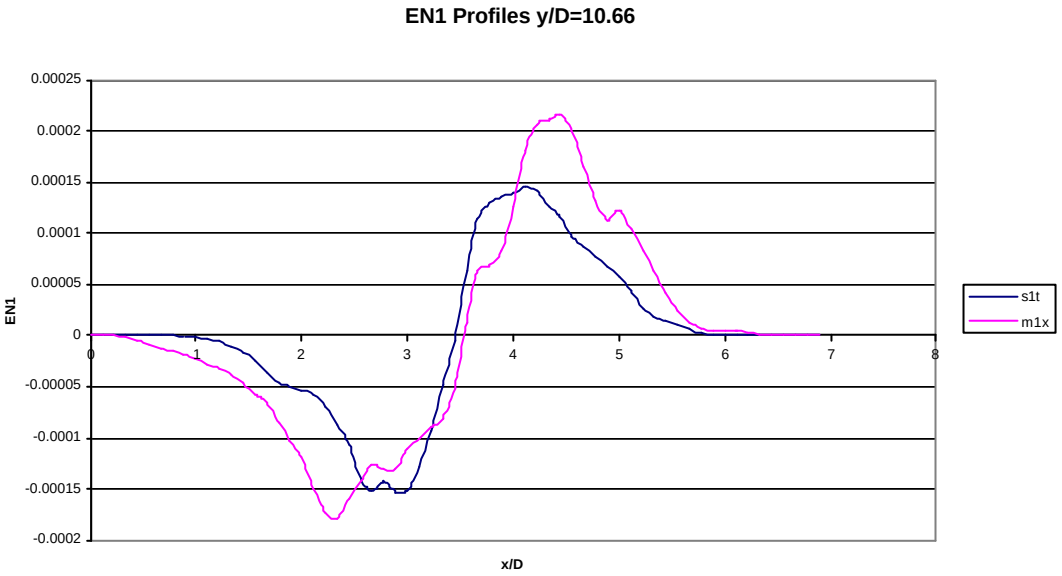

Figure 7.5.12 Radial flux, EN1 in X-axis, profiles for s1t, Smagorinsky model and SGDH flux, m1x, mixed Smagorinsky/Bardina stress model.

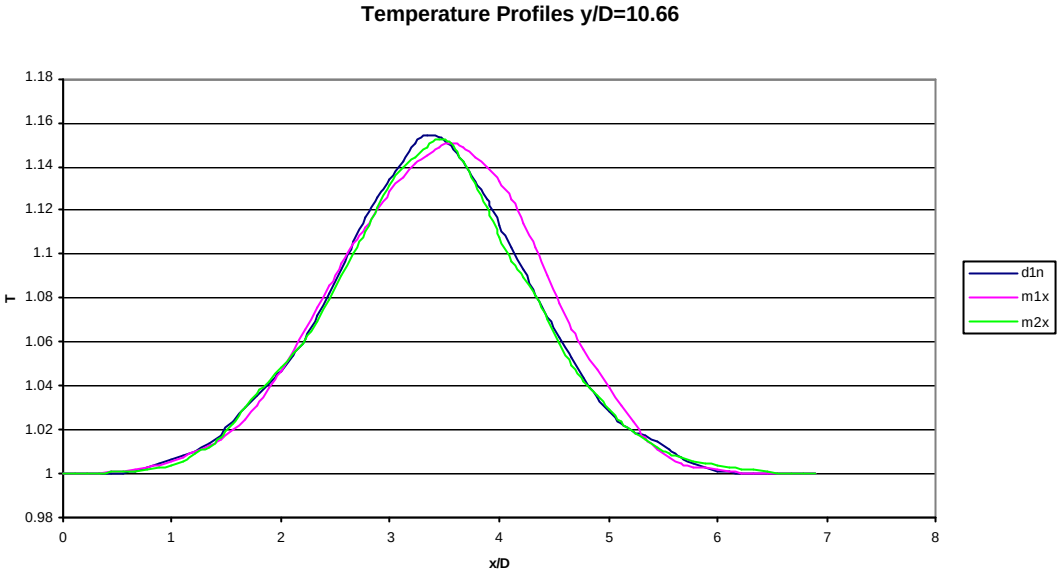

Figure 7.5.13 Temperature profiles at y/D=10.66 for d1n, no subgrid model, m1x, mixed Smagorinsky/Bardina stress model, mixed SGDH Bardina flux model, m2x, mixed Smagorinsky/Leonard stress model, no flux model.

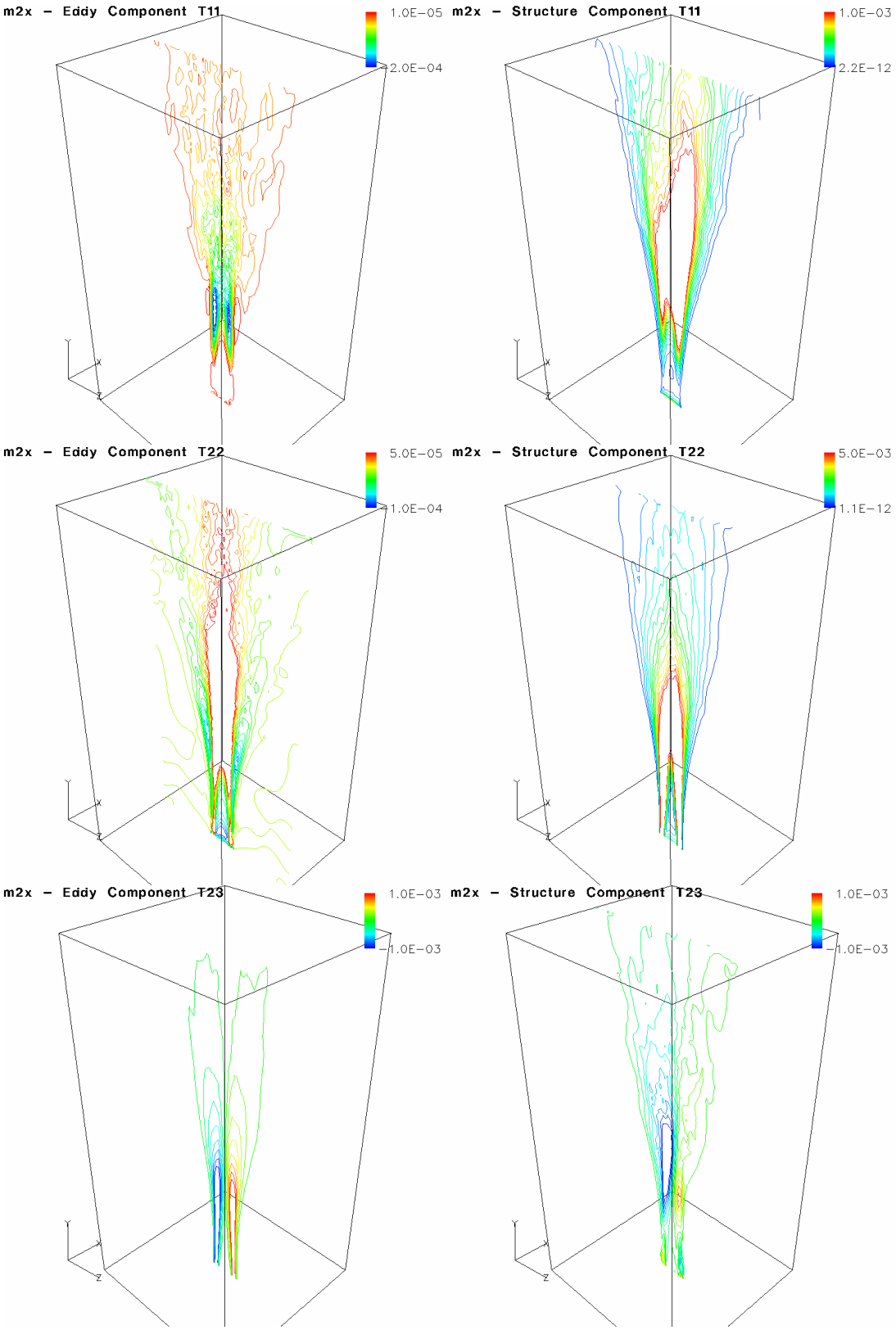

Figure 7.5.14a Mixed model stress component contributions for m2x, mixed Smagorinsky/Leonard stress model, no flux model.

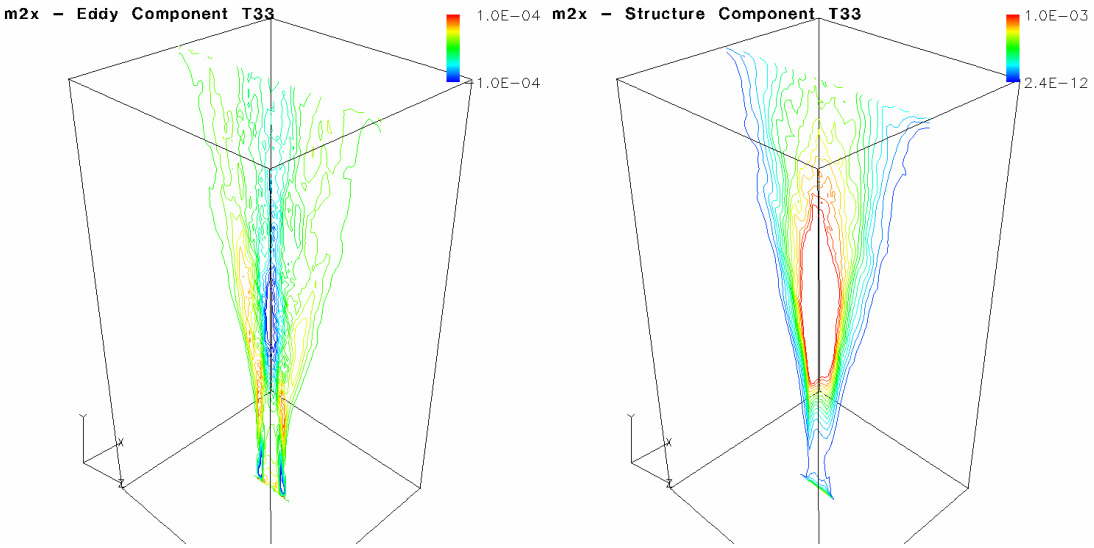

Figure 7.5.14b Mixed model component contributions for m2x, mixed Smagorinsky/Leonard stress model, no flux model.

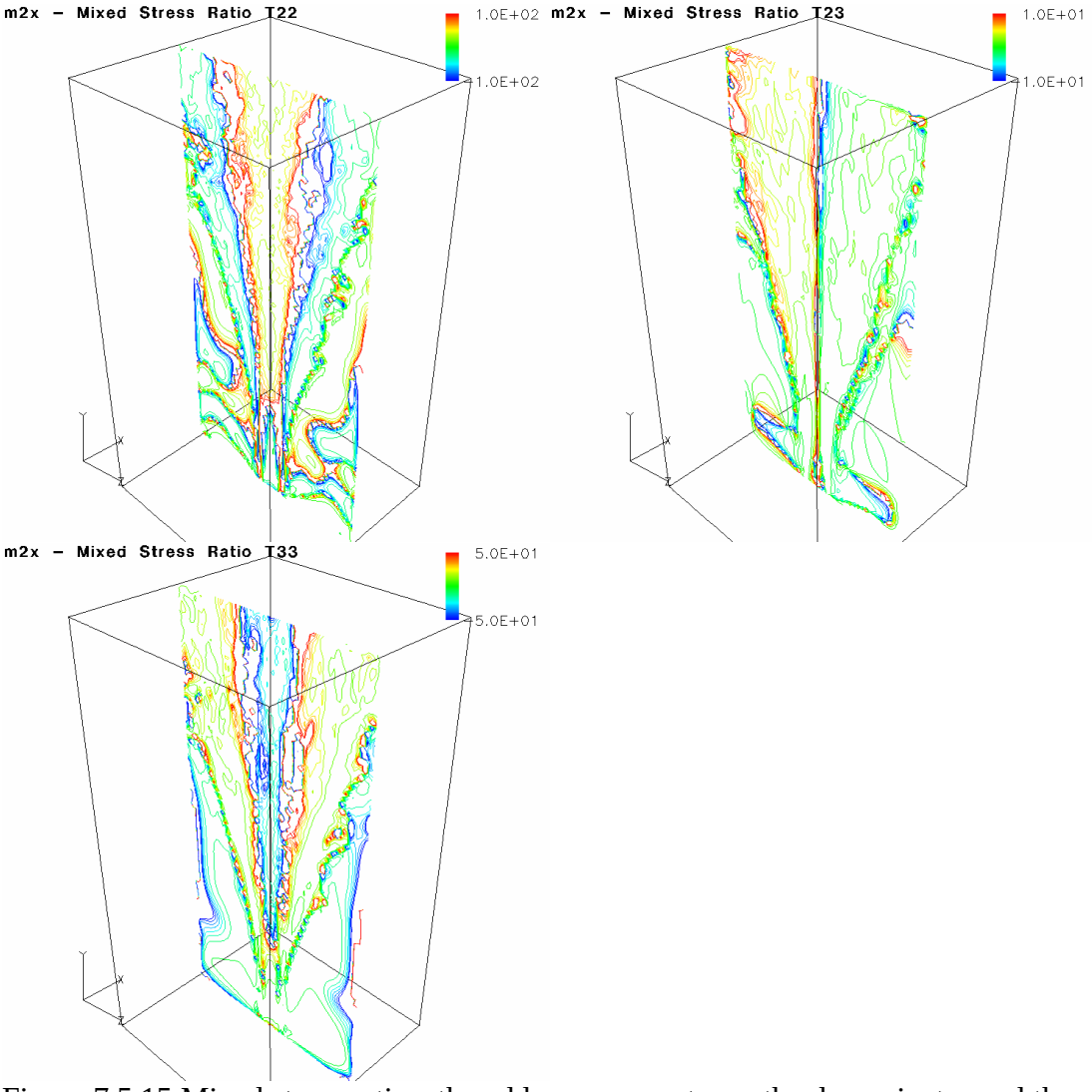

Figure 7.5.15 Mixed stress ratios, the eddy components are the denominator and the structure components are the numerator, for m2x, mixed Smagorinsky/Leonard stress model, no flux model.

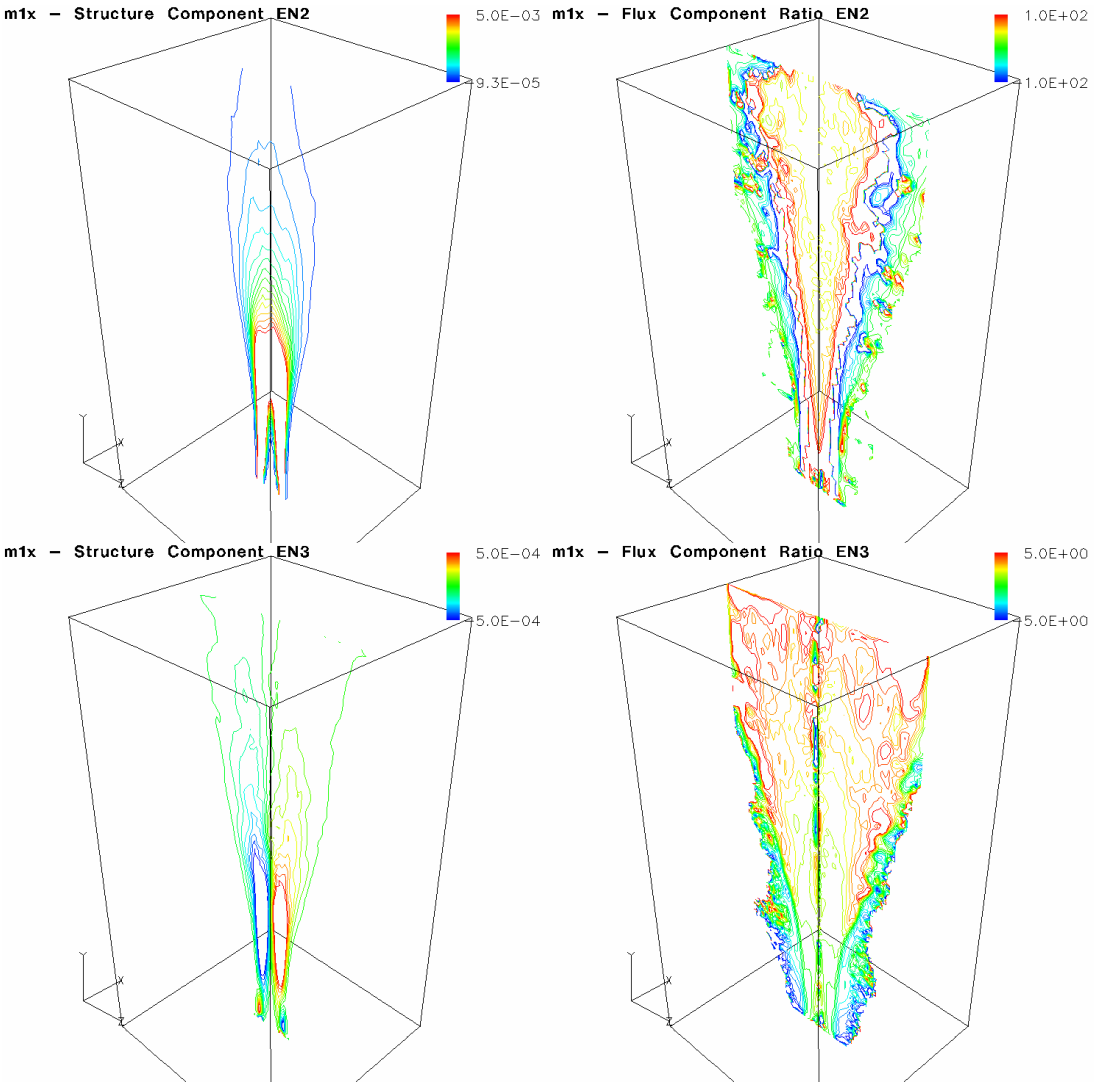

Figure 7.5.16 Structure flux components and flux component ratios for m1x, mixed Smagorinsky/Bardina stress model, mixed SGDH Bardina flux model. The denominators are the eddy components and the structure components are the numerator.

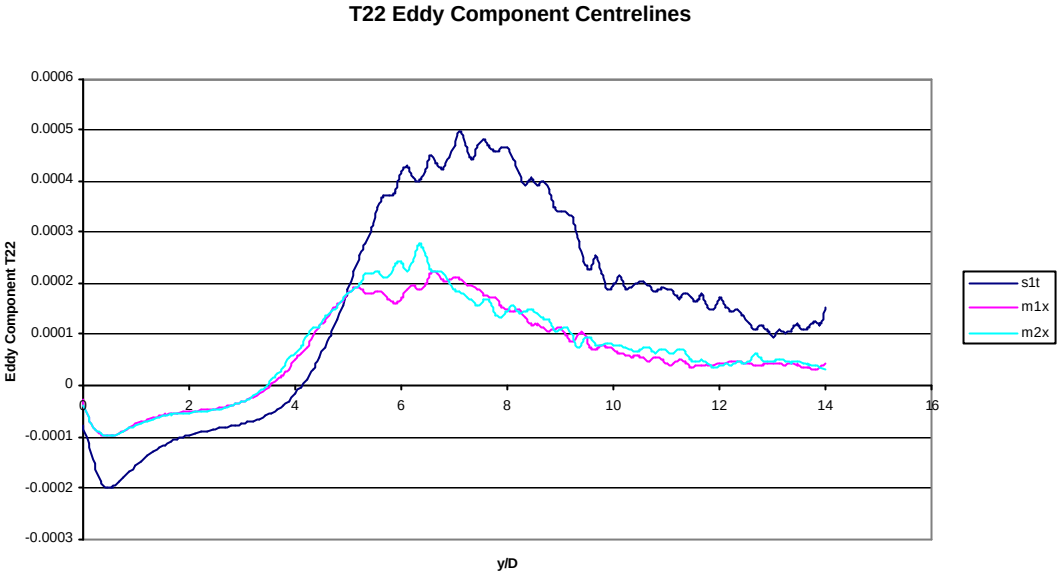

Figure 7.5.17 T22 Eddy component centrelines for s1t, Smagorinsky model and SGDH flux, m1x, mixed Smagorinsky/Bardina stress model, mixed SGDH Bardina flux model, m2x, mixed Smagorinsky/Leonard stress model, no flux model.

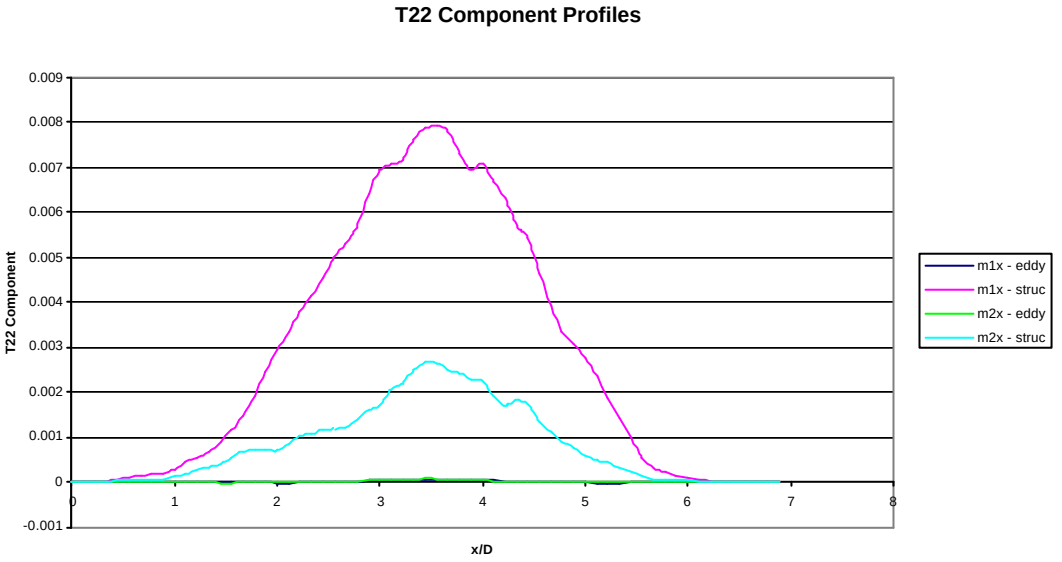

Figure 7.5.18 Eddy and structure component profiles for m1x, mixed Smagorinsky/Bardina stress model, mixed SGDH Bardina flux model, m2x, mixed Smagorinsky/Leonard stress model, no flux model.

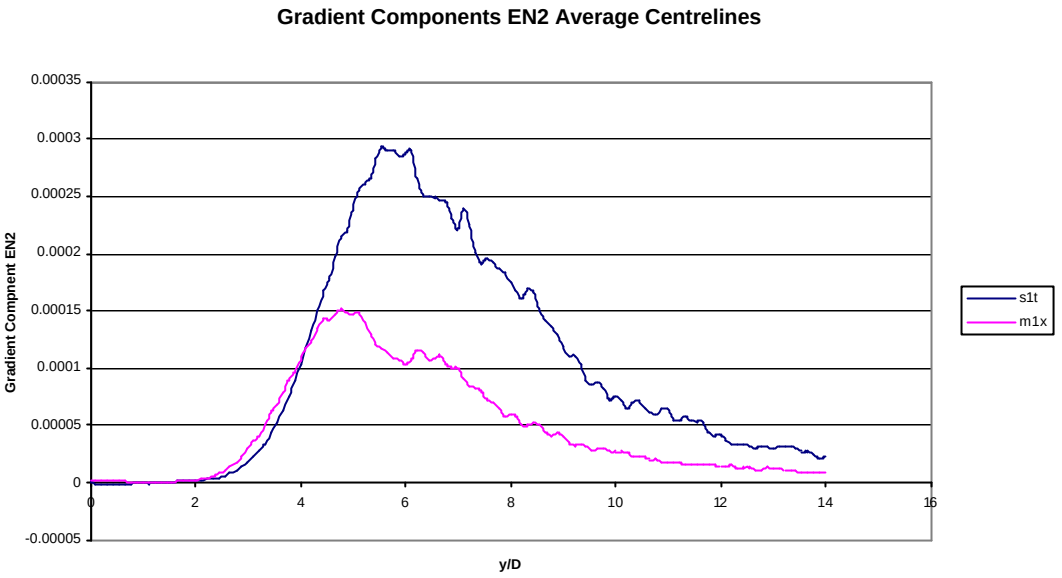

Figure 7.5.19 Gradient component centrelines for s1t, Smagorinsky model and SGDH flux, m1x, mixed Smagorinsky/Bardina stress model, mixed SGDH Bardina flux.

7.6 Summary

The static eddy stress models behave similarly. It is clear that they are dissipative and that the level of dissipation is a direct consequence of the model constant. With the recommended constants for each model the structure function and one equation models are significantly more dissipative than the Smagorinsky models which are themselves more dissipative than the numerical scheme alone. The constants could be chosen to make the dissipation equivalent in the developed turbulent region.

The subgrid fluxes are shown to play a very significant role also in section 7.4. The SGDH model has a large radial flux component which considerably delays the transition point, through the more rapid spread of the temperature. The GGDH models radial fluxes are significantly lower and consequently do not delay transition as much. The vertical fluxes are the dominant term for the GGDH models, as opposed to the radial fluxes for the SGDH model. The second formulation gives greater magnitudes for the fluxes. Ideally, these models would be equivalent, so that $\frac{1}{2}t_{ii} = SGE$ holds true, where SGE is the subgrid energy. The difference between the two models shows this is not the case, although it is impossible to determine whether the models are not aligned with the subgrid energy, or vice versa.

The mixed model simulations show that, on these coarse grid simulations, the structural components are the larger components, qualitatively and quantitatively different, such that better transition is achieved. The greater magnitude of the structural components is expected, as found by Piomelli et al. (1991), since they represent the largest of the subgrid scales, whereas the dissipative scales are smaller.

The mechanics of the models have been considered, and it can be seen that even though the GGDH models are purely dissipative, they are closer to the structure models qualitatively.

Chapter 8

Dynamic Model Results

8.1 Introduction

This chapter addresses the dynamic models. Similarly to chapter 7 the models are considered in subsections. The Smagorinsky models are presented first, followed the localised dynamic model (LDM) simulations, and latterly by the mixed model simulations. The dynamic constants are considered, and their impact assessed. When the turbulent Prandtl number is evaluated with the dynamic procedure, it's inverse is considered to be the model constant, since this is the most straightforward implementation. The simulations have the same details described in section 7.2. Average plots of the centreline values and profiles are given. Momentum balances are considered as well as the Reynolds stresses (time averaged fluctuations of the filtered variables). The energy spectra are considered. Also, the histories of the constants are considered at various points in the profile to examine the models ability to handle intermittency.

8.2 Dynamic Smagorinsky Models

The dynamic Smagorinsky simulations are compared against the static Smagorinsky simulation, and the test case without a subgrid model d1n. The labels are below.
d1n: no subgrid models
s1t: static Smagorinsky stress model and static SGDH flux model
d1f: dynamic Smagorinsky stress model and static SGDH flux model
d2f: dynamic Smagorinsky stress model and dynamic SGDH flux model

In the static cases, the turbulent Prandtl number was 0.4, corresponding to an SGDH constant of 2.5. Preliminary results suggested bounding the evaluation of the Smagorinsky constant was helpful to stability, and Davidson (1997a) finds similarly. Consequently, the Smagorinsky model was bounded by 1, two orders of magnitude greater than the static recommendation of 0.01. It is shown this is a satisfactory bound; fig. 9.5 shows the instantaneous plots of the constant distribution, within two ranges. There are very few points which go above 0.05, and those that do are caused by numerical difficulties with the denominator in laminar flow. The SGDH constant is also bounded. A value of 100 is used, and is again shown to be sufficient; fig 8.2.8 shows the instantaneous values of the flux model constants for d2f.

The dynamic eddy models are shown to be a significant improvement over the static eddy models, particularly with regards to transition. The model constant varies in intermittent regions, and does provide overall dissipation. The dynamic flux models, SGDH and GDDH, are shown to be negligible in conjunction with a dynamic eddy model, and is ultimately thought to be due to the correlation between the turbulent viscosity and the temperature fluctuations.

Simulation d1f is considered in some detail, and properties of the plume are considered in greater detail than in chapter 7. Some issues presented in chapter 7 are also reconsidered. Fig. 8.2.1 shows instantaneous snapshots of the velocity and temperature fields. The four plots give a good impression of the turbulence. The temperature plot shows a good turbulent distribution, with the contour range up to 1.5 (instead of the maximum of 1.89). This is, again, done to highlight the turbulent characteristics. The horizontal velocities show the structured breakdown into turbulence. Layers can be seen in the U velocity showing X-axis oscillations, while the W velocity plot shows the fluctuations growing until the flow breaks down. The average plots for these variables are very similar to those for the static eddy models and are not repeated.

A snapshot of each of the subgrid stresses is shown in fig. 8.2.2. The effect of the clipping of the dynamic constant can be seen here. The distribution of stresses is limited to a certain amount of the domain. Within this range all the stresses are of a similar magnitude, with the vertical normal stress, T22, marginally larger. The realizability conditions are broken again, with T11, T22, and T33 taking negative

values. T11 and T33 are roughly equally distributed between the positive and negative (although the averages are non-zero), although T22 is weighted with more values on the positive side. This is due to having a mean vertical flow. It is noted here that the eddy viscosity model was not designed to adhere to the realizability conditions, and it is worth remembering that only certain filters have this requirement. The other stresses are seen to behave as would be expected, with T23 notably negative of the one side of the domain and positive on the other.

Fig. 8.2.3 shows the average normal stresses. T22 is mainly positive, although T11 and T33 give mainly negative results (T33 is positive at the edge of the plume). This negative value was unexpected, although in hindsight was inevitable. This was explained in section 7.3.

Fig. 8.2.4 also shows the temperature fluxes. These have no equivalent realizability requirements, and so their eddy assumption breaks no formal rules. The same behaviour can be seen as the stresses. EN1 appears evenly distributed, between positive and negative, EN2 has more positive, and EN3 splits positively and negatively between the two halves of the domain. The important point here is that for all the points in the domain that have non-clipped turbulent stresses, there is a temperature flux evaluated. This is in contrast to the fluxes calculated with the dynamic model.

The instantaneous and average distribution of the Smagorinsky constant is shown in fig. 8.2.5. In homogeneous, isotropic turbulence, Piomelli et al. (1991) show that up to 50% of the points can be clipped at any given instance, depending on the filter. In a combined laminar/turbulent flow, such as a thermal plume, it is difficult to distinguish between whether the constant is the result of numerical error, or from the correct calculation in a turbulent region. The lower right hand side and upper left hand side of the instantaneous plots in fig. 8.2.5 show this kind of numerical error where laminar flow is entrained. The instantaneous turbulent viscosity (fig. 8.2.6) shows this error to be insignificant, since the vorticity is sufficiently small to quash the effect of the erroneously large constant. If the constant was not bounded, then the vorticity may not be sufficiently small to stop the significant impact of a potentially vast constant. The constant varies across the flow, with values up to approximately 50% larger than the prescribed constant being fairly typical. Values higher than this are attributed to

numerical error. The difficulty of knowing whether the constant is evaluated correctly is further hindered if it is a region where intermittency occurs.

Plots from d2f, the dynamic Smagorinsky stress model with the dynamic SGDH flux model are now considered, although simulations using the dynamic GGDH models were also carried out and showed the same negative conclusions, for the same reasons, and are not presented. The flux models turn out to be negligible in these simulations, and have no impact on the resulting flow. This is in contrast with their static model counterparts which do strongly affect the flow. Fig. 8.2.7 shows the distribution of the Smagorinsky constant, and the turbulent viscosity beside shows where the significant stresses are. The non-clipped areas of the SGDH model, appear to cover a greatly reduced area in fig. 8.2.8 The model constant is also evaluated to be two orders of magnitude smaller than expected (a turbulent Prandtl number of 0.4 corresponds to a SGDH constant of 2.5. The constants returned are maximum $O(10^{-1})$. This combination of small constants, and clipping apparently in most areas leads to negligible flux terms. Fig. 8.2.9 shows a snapshot of the fluxes, and their limited spread and magnitude. Qualitatively however, the behaviour is correct.

Figs. 8.2.10 and 8.2.11 show the velocity and temperature centrelines of the above models, respectively. It is apparent that the dynamic models provide results very similar to d1n. Transition is not delayed at all, and in the case of d1f transition is slightly accelerated. Speculatively, this is to do with the clipping or erratically large constants of the SGDH model, providing an extra mechanism to create instability. It would be expected that the decay would be higher than for d1n. While this is necessarily the case, being a purely diffusive term, it is not clear from the velocity plot. The temperature plot shows this more clearly, however, with both d1f and d2f marginally faster to decay.

The similarity between these results does not support the argument that choice of LES model is unimportant, but goes further suggesting that choosing a LES model is unnecessary. Nevertheless, it is still important to investigate the behaviour of the models.

The T22 stresses and turbulent viscosity are plotted in figs 8.2.12 and 8.2.13. The initial instabilities are quickly damped, shown by the high initial values, which rapidly

fall to almost zero. The static eddy models do not do this, and the plot of s1t, fig 8.2.13, shows the turbulent viscosity to start lower and to dissipate less before transition occurs. A surprising consequence is the difference in sign of T22 in this region, slightly positive for the dynamic models, and negative for s1t and the other static eddy models. This appears to be a result of clipping – looking back at figs. 8.2.5 and 8.2.7 the initial regions have few positive constants.

The strong initial damping of the oscillations would suggest that transition would be delayed. It could be speculated, however, that it is only the high frequency oscillations which are immediately damped, and the low frequency instabilities remain into the region where the turbulent viscosity has been reduced, whereas the static models dissipate oscillations of all frequencies without discretion.

The magnitude of the dynamically modelled stresses are higher even though their eddy viscosities are lower and the constant is lower on average (the eddy model is $-2u_t S_{ij}$). This would appear to imply that S_{ij} is larger on average for the dynamic models, which in turn would indicate that the dynamic models allow more grid scale turbulence than the static models. Energy spectra (not plotted here) show that this is not the case, and in fact the energy in the eddy scales is larger at each scale for the static model, showing the small scales energy is more dependent on the mean velocity than the action of the subgrid model in this case. The alternative explanation, believed to be the correct one, is to do with clipping again. T22 is shown to have negative components in fig. 8.2.2. If the constant is clipped more often when S_{ij} is negative then the higher average is explained. The profiles of T22 and the turbulent viscosity are plotted in 8.2.14 and 8.2.15. The same pattern is seen, that the dynamic eddy stresses are larger than the static, even though the constant is less, and the turbulent viscosity is less.

Further in fig. 8.2.12, the d2f T22 plot peaks before d1f, but appears to have the slower transition from fig. 8.2.10. From the static eddy model results, it was observed that the larger the fluxes, the slower the transition and the greater the dissipation. D2f, shown to have negligible temperature fluxes below, would be expected to have faster transition and slower decay than d1f, but this is not the case. However, the temperature decay is marginally less, as would be predicted. The faster transition for d1f than d1n, however, is difficult to explain. Speculatively, the dynamic procedure

itself with widely varying values adds to the instabilities, with a balance between the level of instability added and the dissipation added.

Figs. 8.2.16 and 8.2.17 show the T12 and T11 profiles respectively. The T11 plot shows a similar trend to T22, with the dynamic models giving larger magnitudes. T12, however, bucks this trend and the static model has a larger magnitude, although this would be diminished or reversed by normalisation. Figs. 8.2.18 to 8.2.20 give plots of the fluxes. All show the dynamic SGDH model to have negligible values.

The Smagorinsky constant averages are plotted in fig. 8.2.21. These show the same properties, suggesting minimal impact of the flux model on the constant. After transition the model seems to level out at approximately 0.08, slightly less than the recommended value of 0.01.
The SGDH model constant, for which the average is not plotted, does not reach a maximum of a hundredth of the recommended value. The temperature centreline decay can be seen to be marginally greater for the more diffusive d1f simulation.

The balances of the vertical momentum equation and the temperature equation are now considered. Fig. 8.2.22 gives the vertical momentum balance for d1f. The stresses are not included as they appear negligible next to the other components. The total is close to zero, but is slightly off around the transition region. The total shows it to be better averaged than individually considered components suggest; they are slightly non-smooth, and indicate that erroneous large-scale structures have been well averaged. The trends of the behaviour are still clear, however. In this region the vertical momentum is seen to be the dominant term, although downstream it is equal to the buoyancy term. The pressure term is small, and the horizontal convection components show the negative correlated behaviour discussed in chapter 6, that emerges in any flow with a decelerating mean direction. The vertical component is quite strongly negative in the initial region, corresponding to the region of flow acceleration and becomes positive as the plume decelerates into the plume core.
Fig. 8.2.23 shows the profiles of the vertical momentum balance at y/D=10.66. The vertical convection at the edge does not reflect an average negative velocity there. Instead it shows the deceleration of the plume along the centreline, and the acceleration of the fluid at the edges of the plume, where entrainment is occurring.

This is an inevitable characteristic of plumes, not reported on in experiments or other simulations, and is information RANS models cannot capture (assuming they are steady state). The buoyancy is a strong term and takes the Gaussian distribution expected from theory. It is a very smooth plot, highlighting the difficulties of averaging higher order moment terms – the greater the variance of the averaged term, the more points it will need to average properly. The buoyancy term has one component, whereas the rest multiply two. The problem increases as the number of multiplied components increases. The horizontal components behave as expected from the balance shown in chapter 6, with the U-component positive and negative, and the W-component purely negative (these are shown in the X-axis).
The temperature balances are displayed in figs. 8.2.24 and 8.2.25. These are similar to the momentum balances, without the pressure or buoyancy terms. Again the averages are good; the total is almost zero. These also show the inevitability of the negative horizontal convection terms, since to balance the equation they must be opposite in sign to the vertical component.

The TKE spectra are not presented for d1f and d2f. They are similar. However the temperature spectra of both simulations are given in fig. 8.2.26. The large scales are the same, and the beginning of the inertial range is the same. Tentatively, it appears as though the dynamic SGDH model does result in there being more energy in its smallest scales (unlike the un-plotted comparisons of spectra with strongly different centreline values in which all the scales are different, these are similar in the mid-range). The impact on the overall flow is limited given the proportion of energy contained in these. This slight difference would be expected, however, since the fluxes were shown to be negligible, whereas using the static SGDH model should dissipate these small scales. It is equally possibly numerical error at the bottom of the spectra.

Plots of the (filtered) vertical Reynolds stress and (filtered) TKE profiles are given in fig. 8.2.27. These are taken early in the transition region at y/D=7.11. The plot is rather busy, but it is apparent from the Reynolds stress term that the d1f model has a wider spread than d1n and d2f. The TKE plots do not show this difference. Fig. 8.2.28 shows the horizontal components, which confirm the increased spread of the d1f

simulation. A less busy plot of just d1n and d1f is given further downstream, at y/D=12.44, in fig. 8.2.29 for further clarity.

The dynamic models ability to handle intermittency is assessed following the histories of the vertical velocity and temperature at fixed points across the plume, as well as the model constant histories. These are presented from d2f. The Smagorinsky constant history is similar for both d1f and d2f. The histories show 800 time-steps totalling 10 non-dimensionalised time units.

Figs. 8.2.30 and 8.2.31 show the vertical velocity and temperature at 7.11 diameters from the source. A correlation can be made out at times along the plots between the plot at x/D=0 and x/D=0.44. The structure of one plot is shortly after reproduced by the other, or vice versa. At points the correlation is broken altogether. The correlation is more clearly seen in the temperature histories.

Further out the effects of intermittency and entrainment can be observed. At x/D=1.33 there are virtually no effects of the temperature. One 'temperature-difference-containing' eddy can be seen, which is already highly diffused. The velocity component is constantly fluctuating but only slightly. Although there is no strict physical definition of the edge of a plume, this region can be considered to be just outside the edge. Slightly inside the edge, at x/D=0.88, the behaviour is opposite to the behaviour outside. The point is mainly passed by 'temperature-difference-containing' eddies, but the entrainment of a 'gust' of cold air can be clearly seen.

Figs. 8.2.32 and 8.2.33 show the model constants over the same period of time. The centreline constant has the highest peaks. These correspond with the peaks of the velocity history, but fall off very quickly afterwards as the velocity slows down without a significant gradient, suggesting a mainly laminar eddy. These peaks have a value much higher than the recommended constant because of the problems in a laminar region. At times 1 and 6, where the velocity fluctuation is relatively rapid, the constant takes more expected values – a strong dissipation constant of 0.02 at 1, and a fluctuation between 0 and 0.02 at 6 time units. At x/D=0.44 the turbulence fluctuations are weaker. The further out along a radial spoke, the more damped these fluctuations are, reducing the peak constant value. The plot inside the plume edge shows the model constant accommodating itself to the eddies, from which much of the small-scale turbulence has already been diffused. The constant varies much more slowly. Outside the plume the constant varies more than the vertical velocity and

temperature plots would suggest. Consideration of the radial velocity history, in fig. 8.2.30, shows that the entrainment rate varies as the eddies sweep by, without causing significant vertical or perpendicular fluctuations. This small one-dimensional oscillation causes the constant to take a value up to 0.005, half the specified amount. This is not turbulence.

The SGDH constant history shows similarly that the constant peak decreases away from the centreline, although there are fewer positive values. At the point outside the plume, the model takes a positive value before the temperature-difference bubble passes. This has no effect due to the lack of temperature gradient. By the time the bubble has arrived the constant is in decline but is zero again when there is a temperature gradient.

The constant never goes as high as given in the static model (con=2.5). This was initially thought to be due to the very diffusive TVD scheme, although it is likely related to the lack of correlation of the temperature fluctuations with the turbulent viscosity (see section 9.3). The histories are shown further downstream also in figs. 8.2.34 and 8.2.35. These give a similar picture, but in this more developed turbulence, the SGDH constant now takes more peaks of a similar order of magnitude to the suggested value, although still smaller.

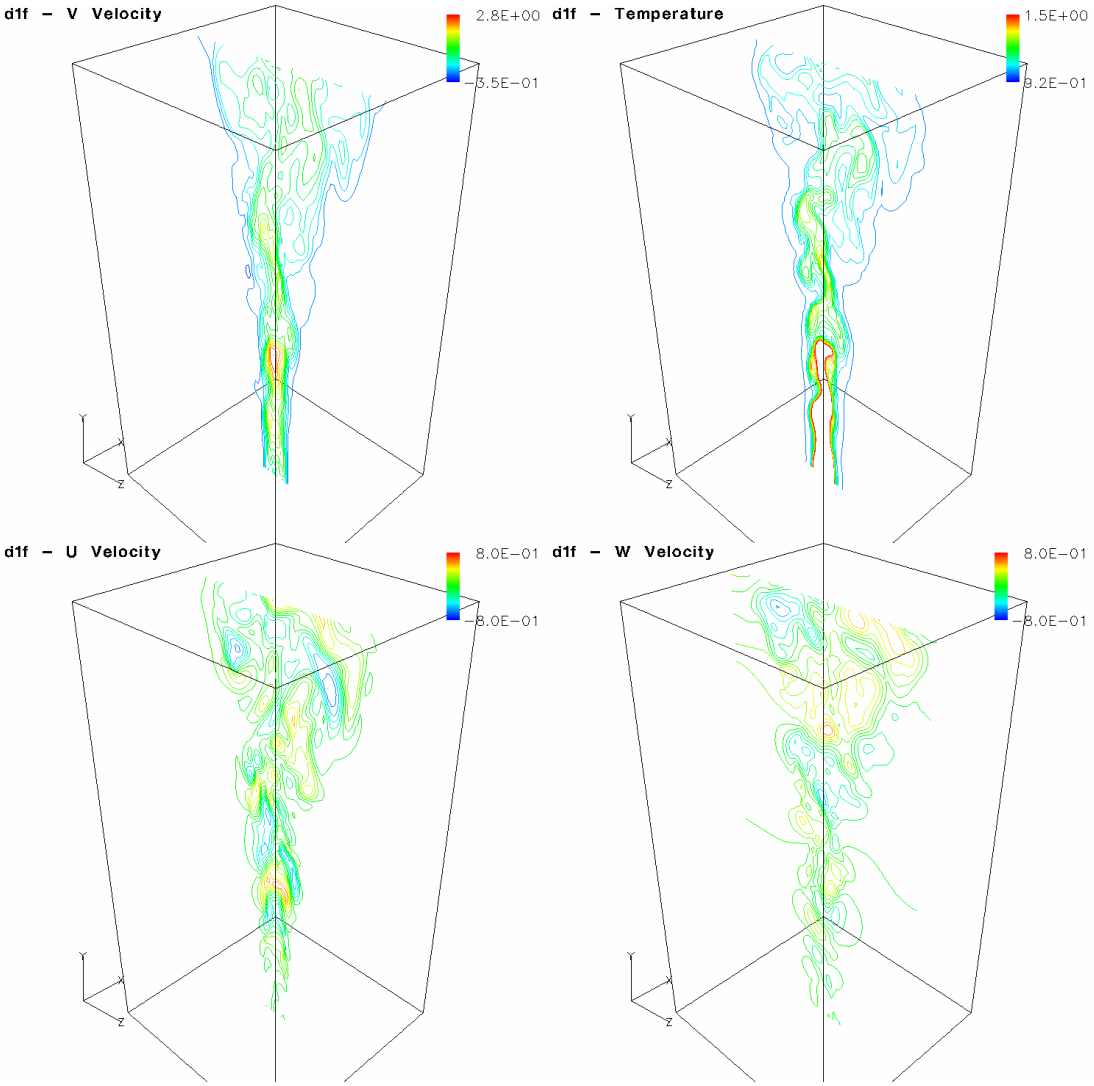

Figure 8.2.1 Instantaneous velocity and temperature snapshots for d1f, the dynamic Smagorinsky stress model and static SGDH flux model.

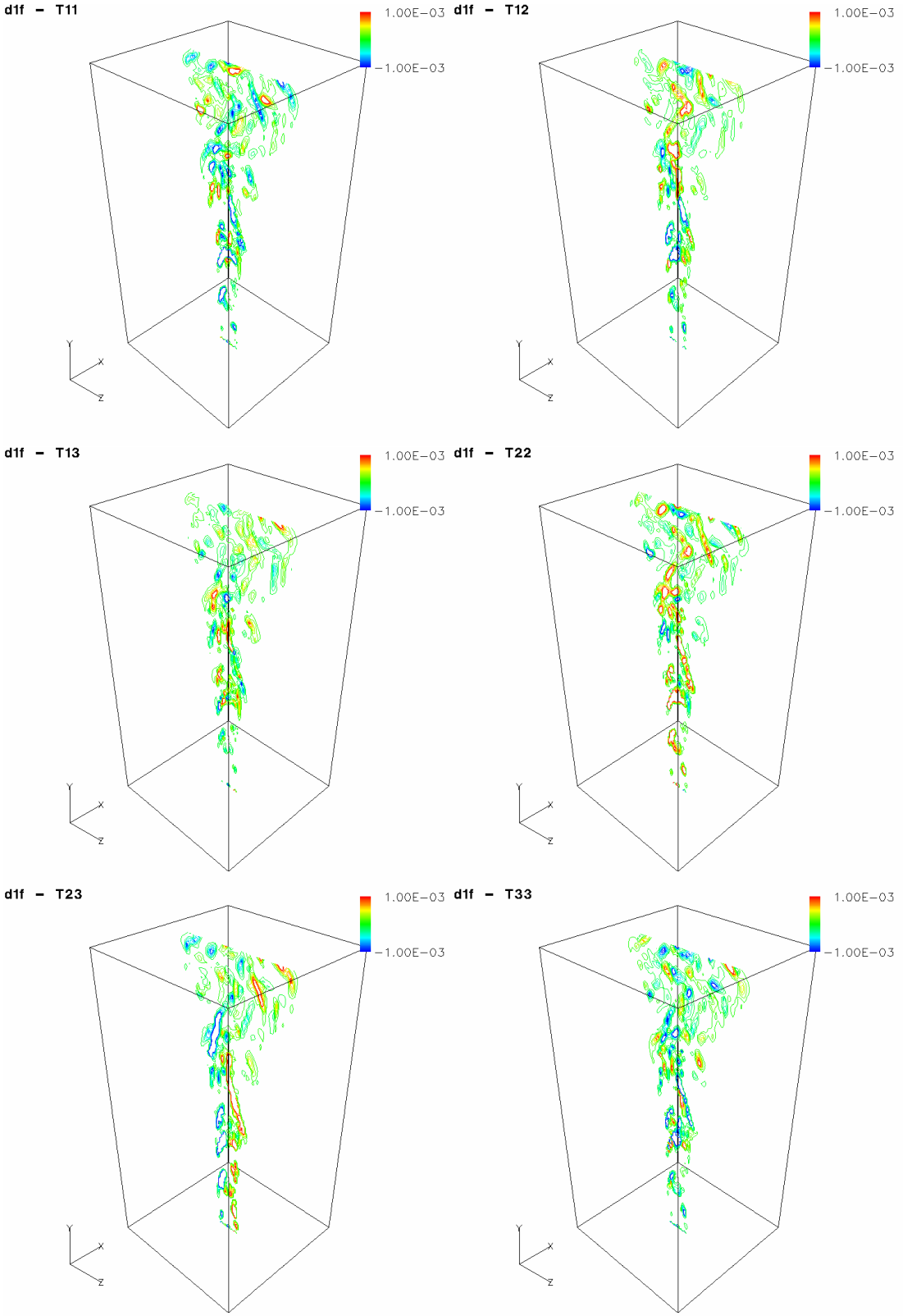

Figure 8.2.2 Instantaneous subgrid stress snapshots for d1f, the dynamic Smagorinsky stress model and static SGDH flux model.

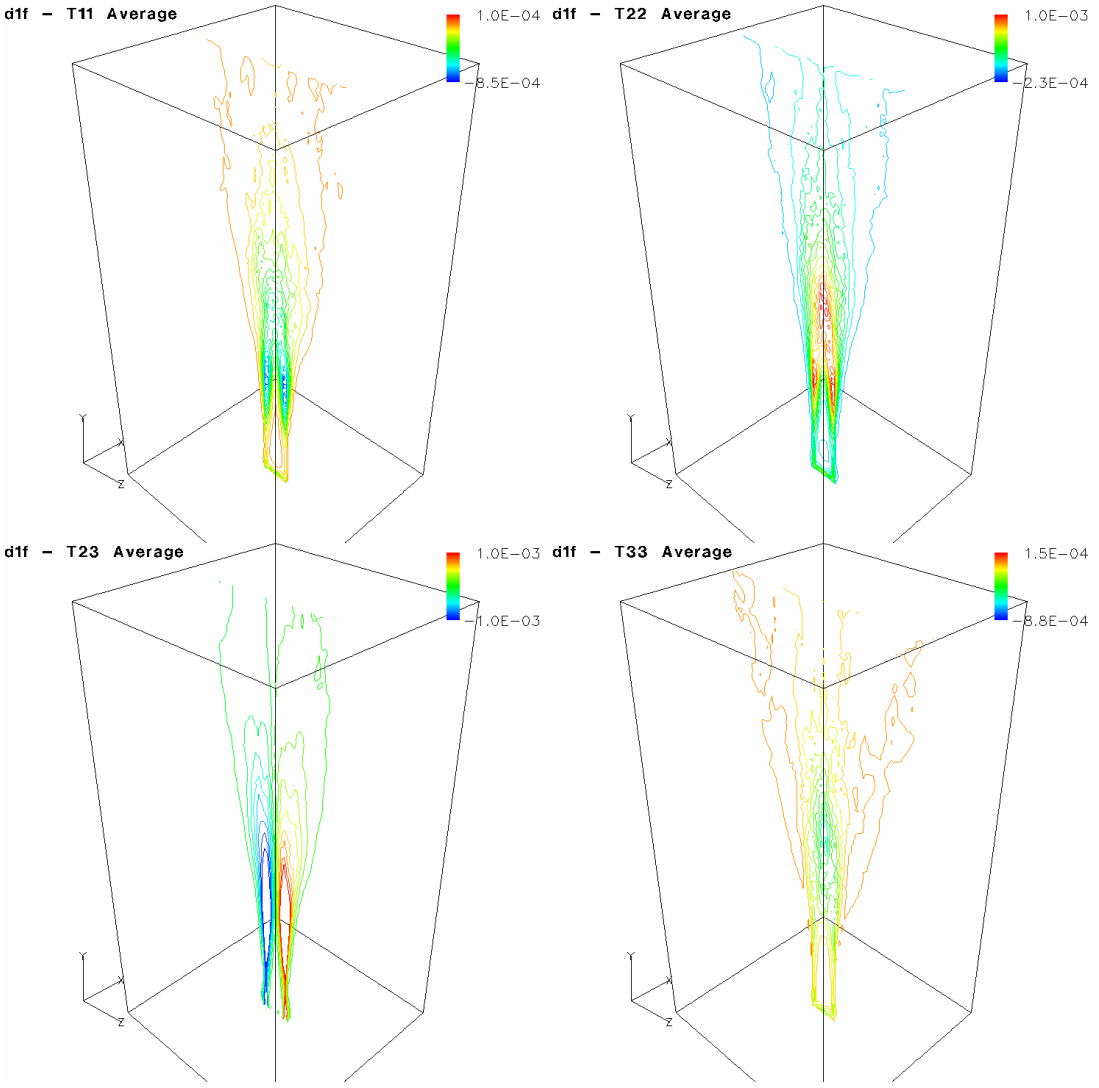

Figure 8.2.3 Stress averages for d1f, the dynamic Smagorinsky stress model and static SGDH flux model.

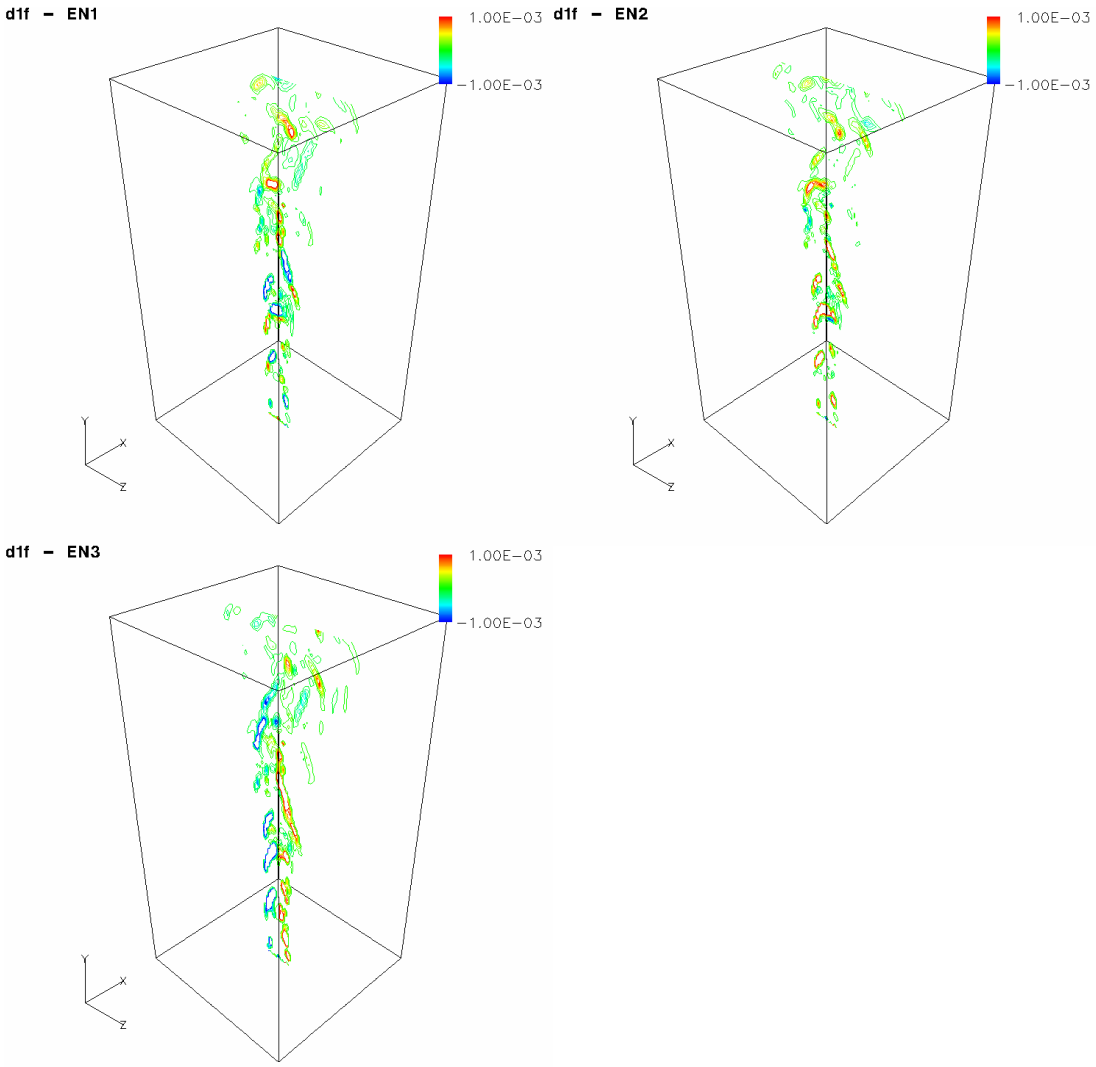

Figure 8.2.4 Instantaneous fluxes for d1f, the dynamic Smagorinsky stress model and static SGDH flux model.

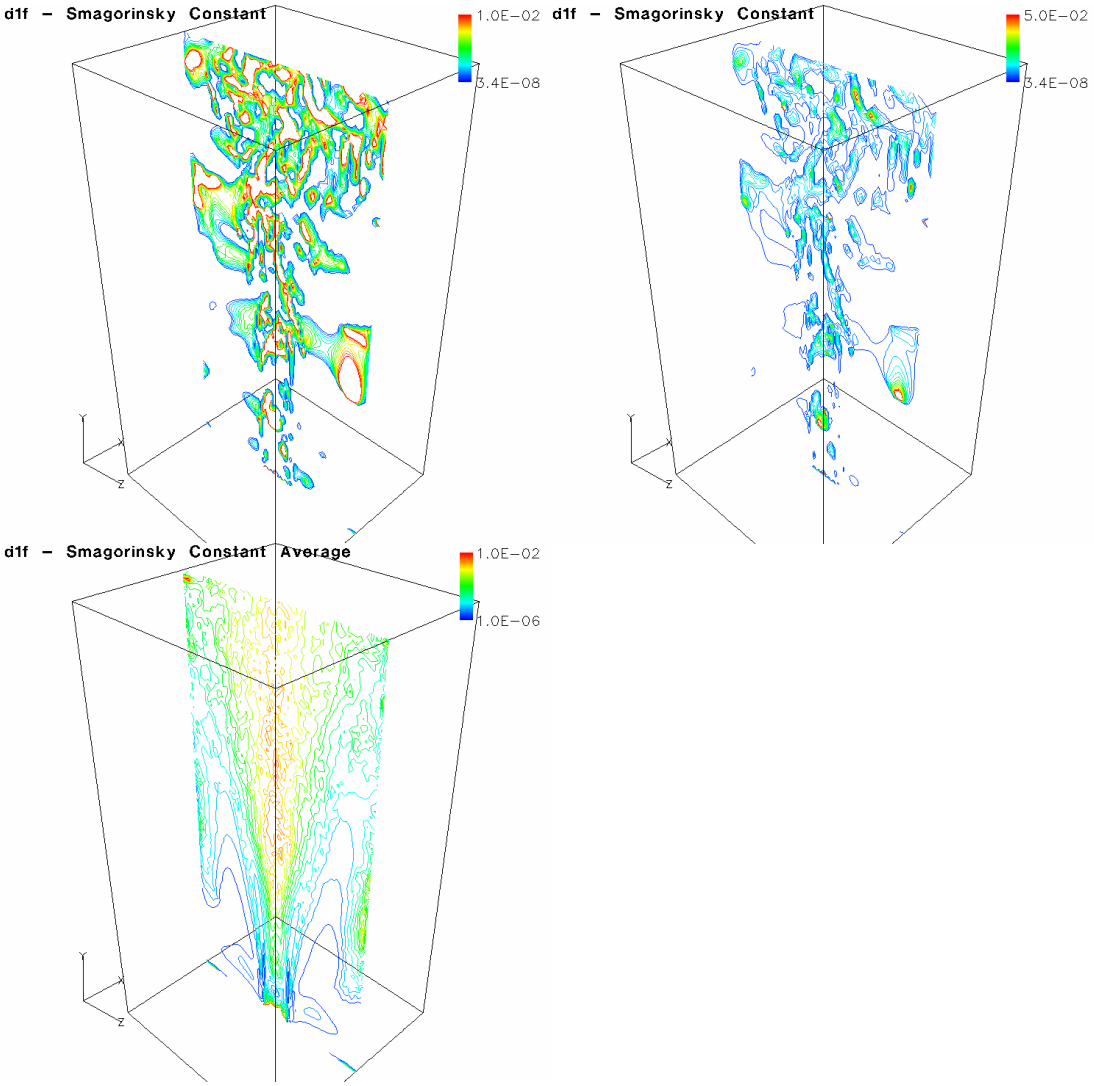

Figure 8.2.5 Instantaneous Smagorinsky constant with different contour ranges, and average constant value, for d1f, the dynamic Smagorinsky stress model and static SGDH flux model.

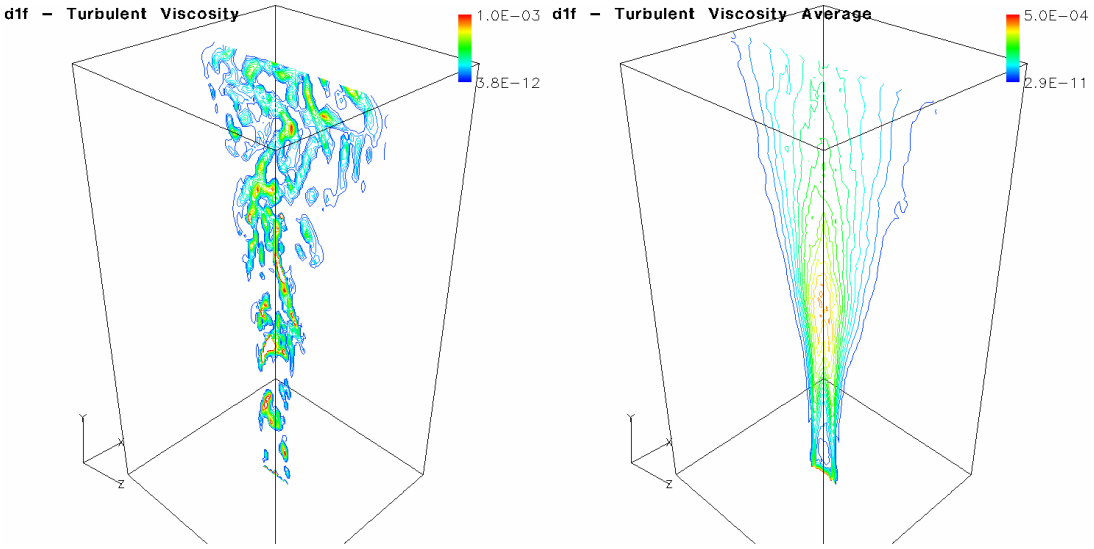

Figure 8.2.6 Instantaneous and averaged turbulent viscosity for d1f, the dynamic Smagorinsky stress model and static SGDH flux model.

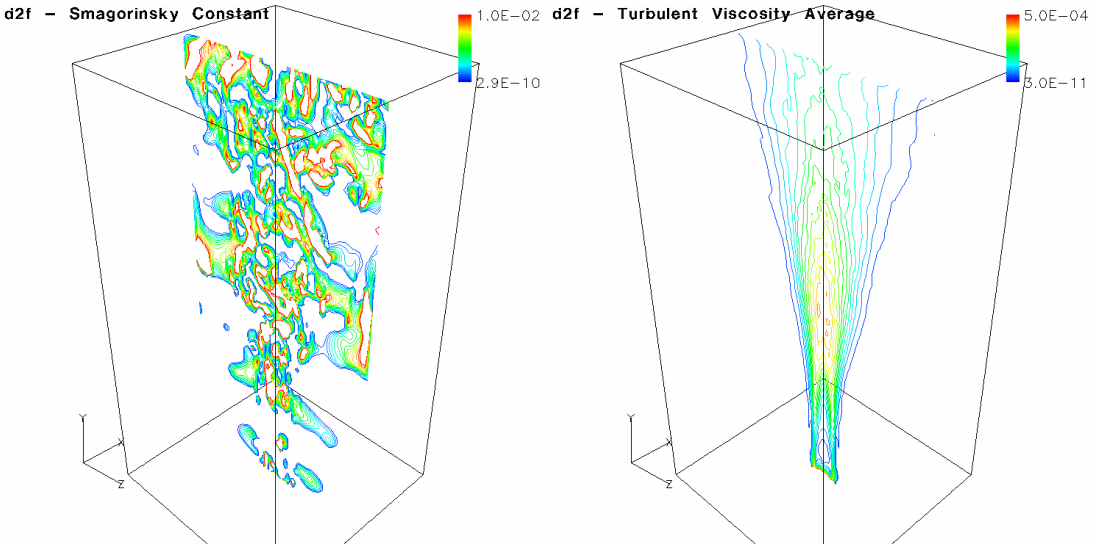

Fig. 8.2.7 Instantaneous Smagorinsky constant and average turbulent viscosity for d2f, the dynamic Smagorinsky stress model and dynamic SGDH flux model.

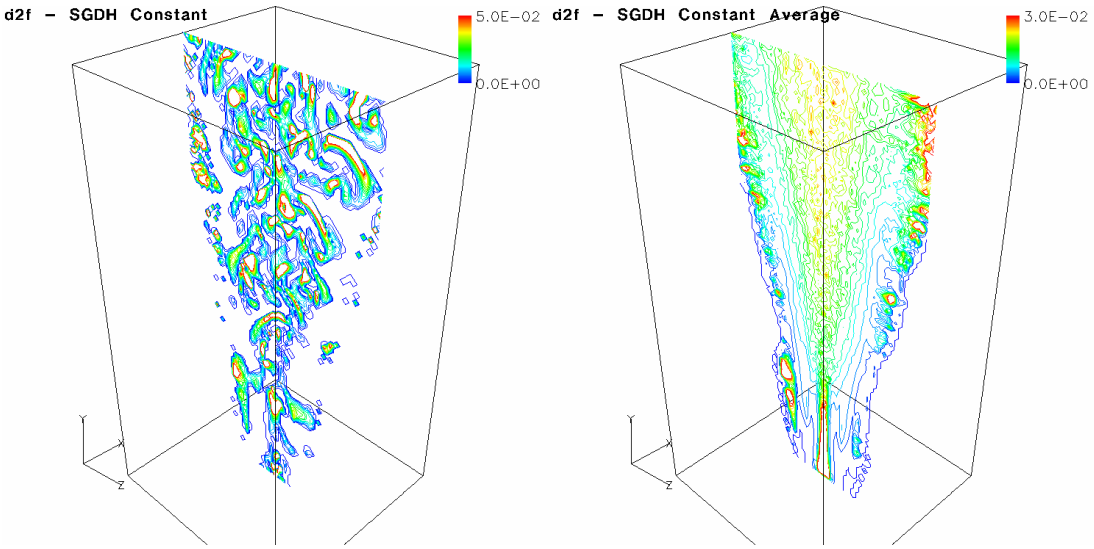

Figure 8.2.8 Instantaneous and average SGDH constant for d2f, the dynamic Smagorinsky stress model and dynamic SGDH flux model.

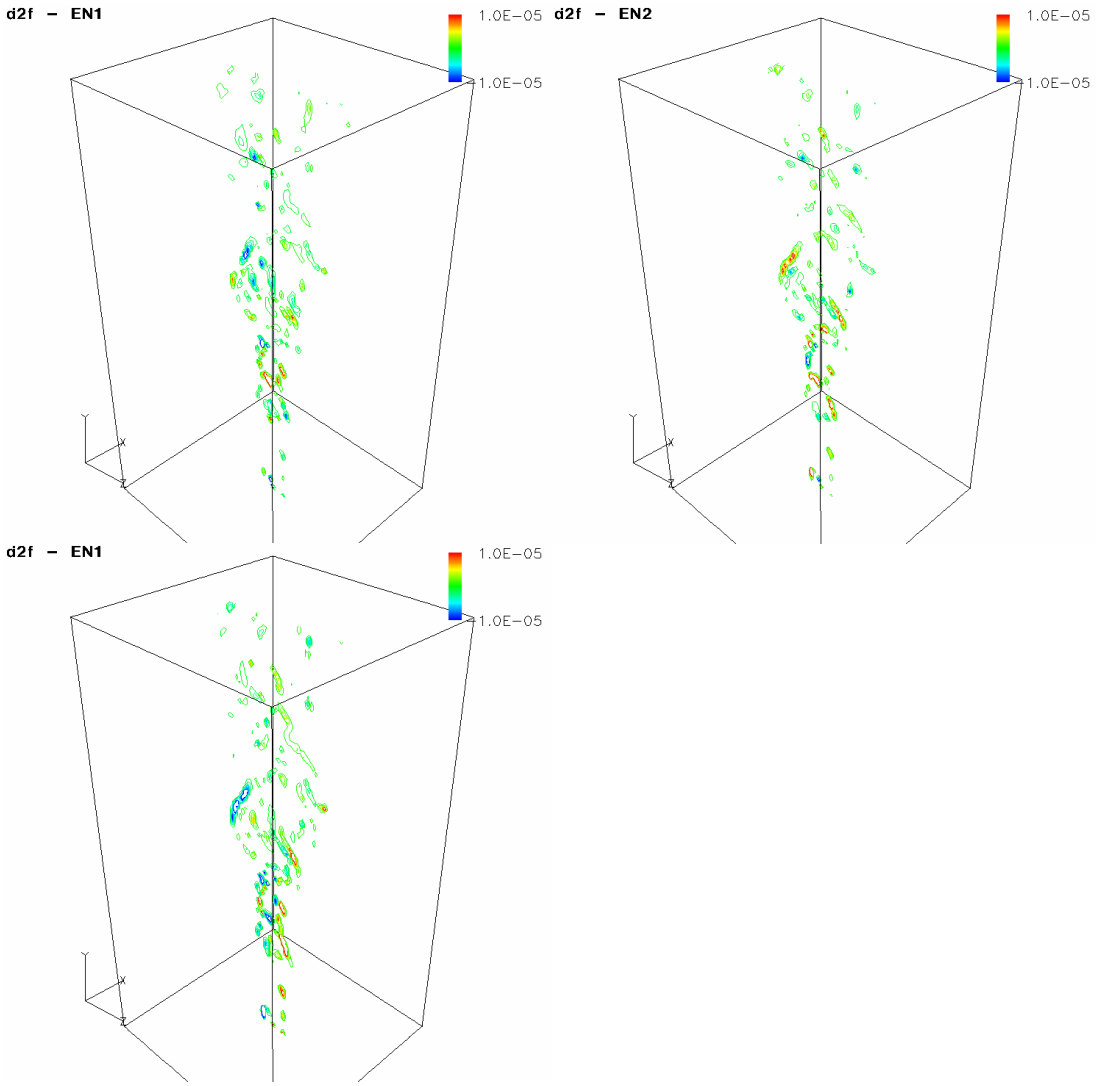

Figure 8.2.9 Instantaneous flux values for d2f, the dynamic Smagorinsky stress model and dynamic SGDH flux model.

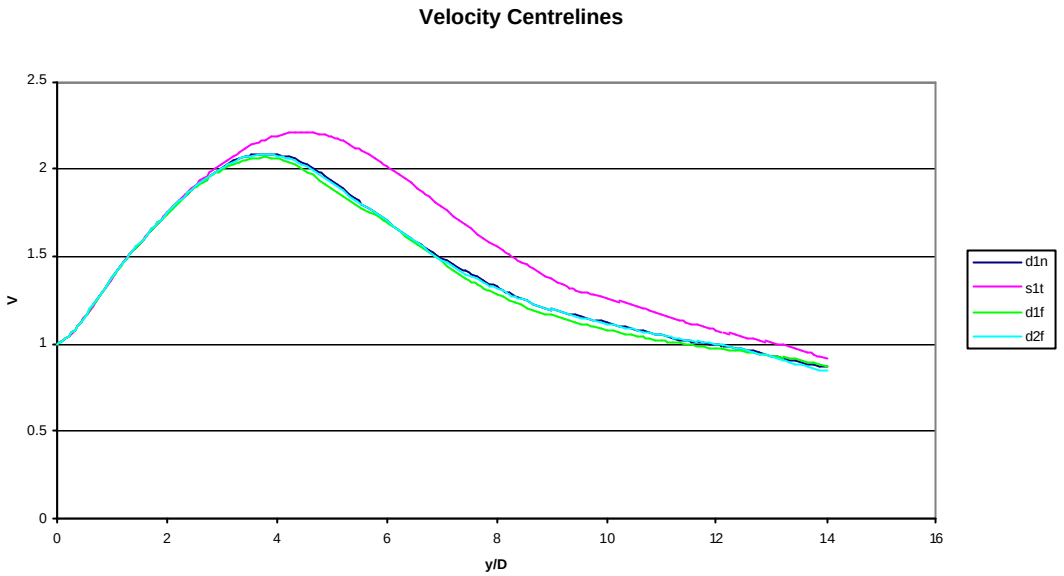

Figure 8.2.10 Velocity centrelines for d1n, no subgrid models, s1t, static Smagorinsky stress and static SGDH flux models, d1f, dynamic Smagorinsky stress, static SGDH flux models, d2f, the dynamic Smagorinsky stress and dynamic SGDH flux models.

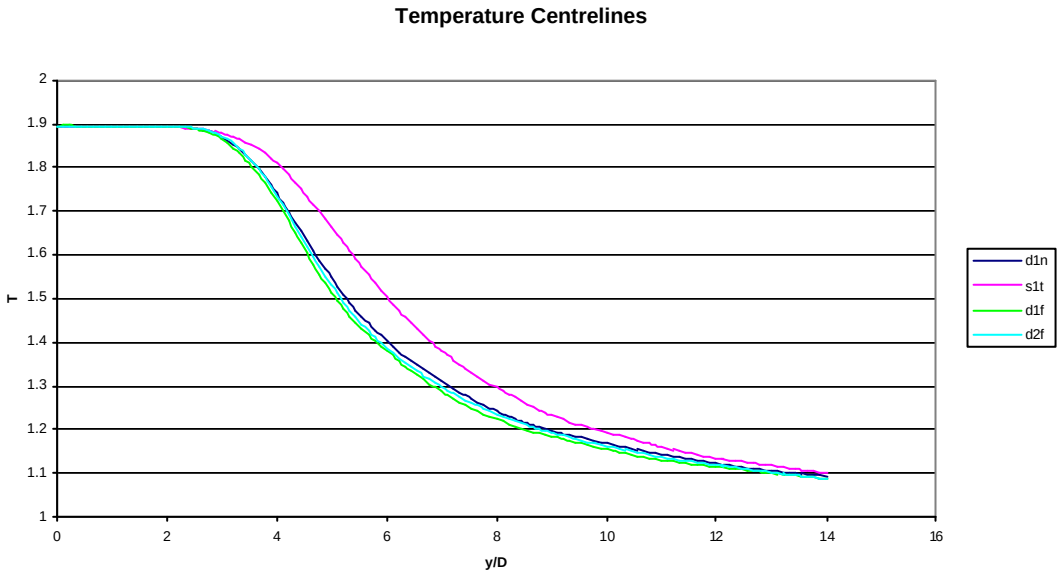

Figure 8.2.11 Temperature centrelines for d1n, no subgrid models, s1t, static Smagorinsky stress and static SGDH flux models, d1f, dynamic Smagorinsky stress, static SGDH flux models, d2f, the dynamic Smagorinsky stress and dynamic SGDH flux models.

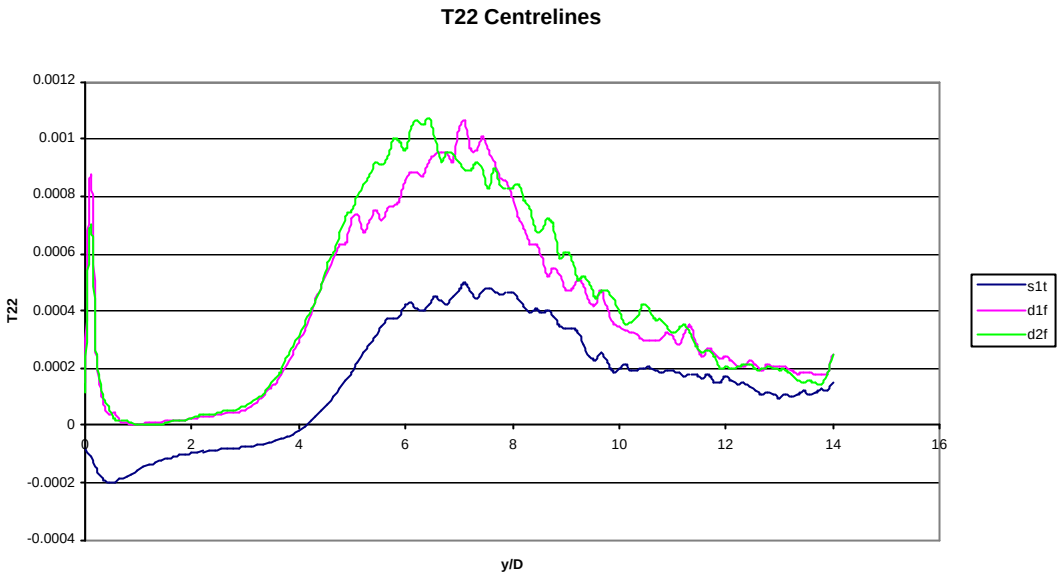

Figure 8.2.12 T22 centrelines for s1t, static Smagorinsky stress and static SGDH flux models, d1f, dynamic Smagorinsky stress, static SGDH flux models, d2f, the dynamic Smagorinsky stress and dynamic SGDH flux models.

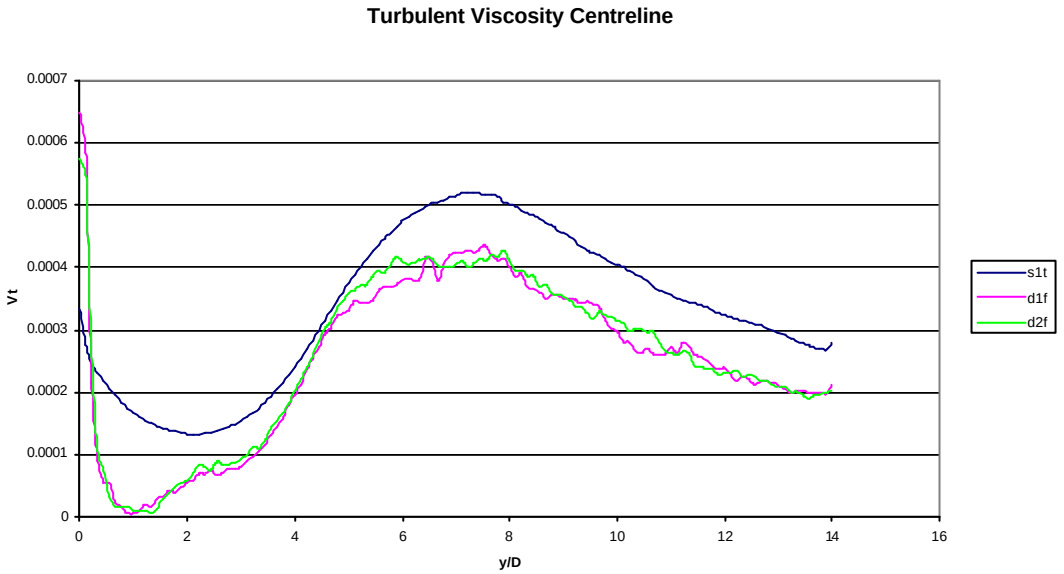

Figure 8.2.13 Turbulent viscosity centrelines for s1t, static Smagorinsky stress and static SGDH flux models, d1f, dynamic Smagorinsky stress, static SGDH flux models, d2f, the dynamic Smagorinsky stress and dynamic SGDH flux models.

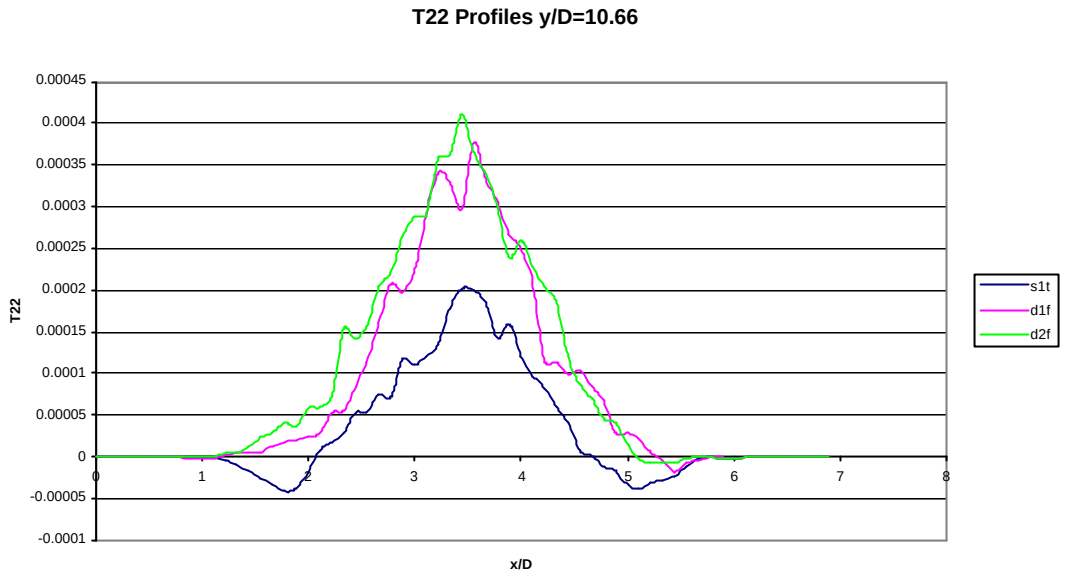

Figure 8.2.14 T22 profiles for s1t, static Smagorinsky stress and static SGDH flux models, d1f, dynamic Smagorinsky stress, static SGDH flux models, d2f, the dynamic Smagorinsky stress and dynamic SGDH flux models.

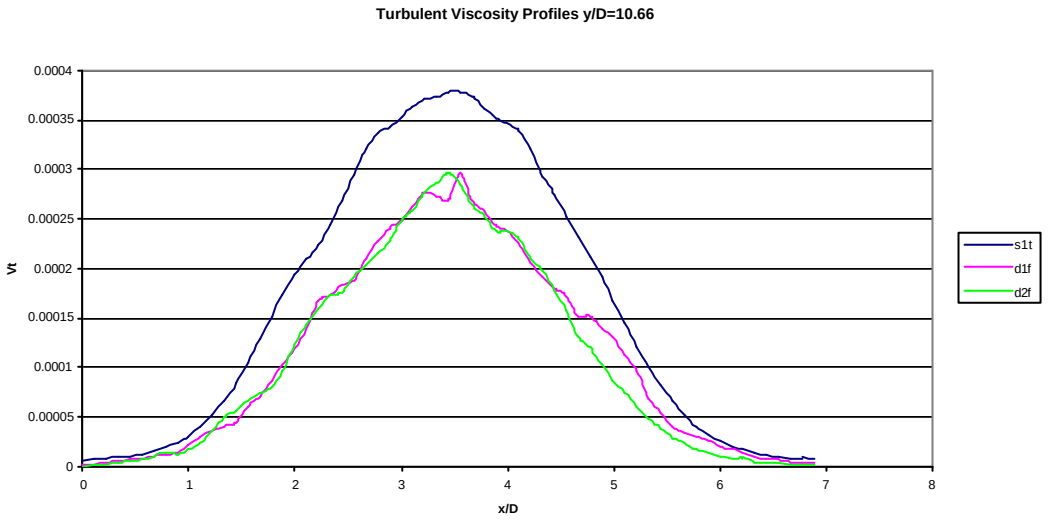

Figure 8.2.15 Turbulent viscosity profiles for s1t, static Smagorinsky stress and static SGDH flux models, d1f, dynamic Smagorinsky stress, static SGDH flux models, d2f, the dynamic Smagorinsky stress and dynamic SGDH flux models.

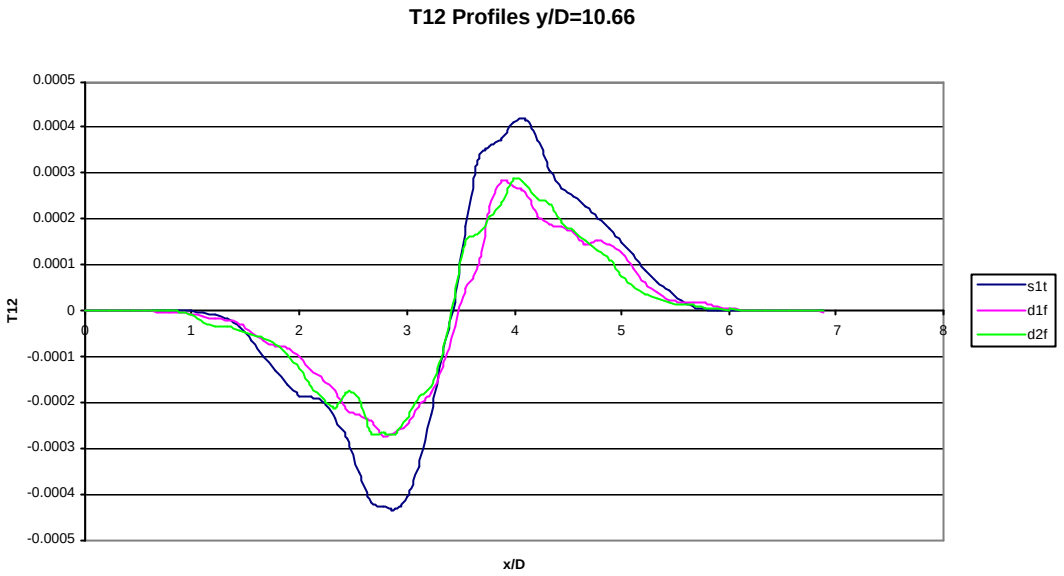

Figure 8.2.16 T12 profiles for s1t, static Smagorinsky stress and static SGDH flux models, d1f, dynamic Smagorinsky stress, static SGDH flux models, d2f, the dynamic Smagorinsky stress and dynamic SGDH flux models.

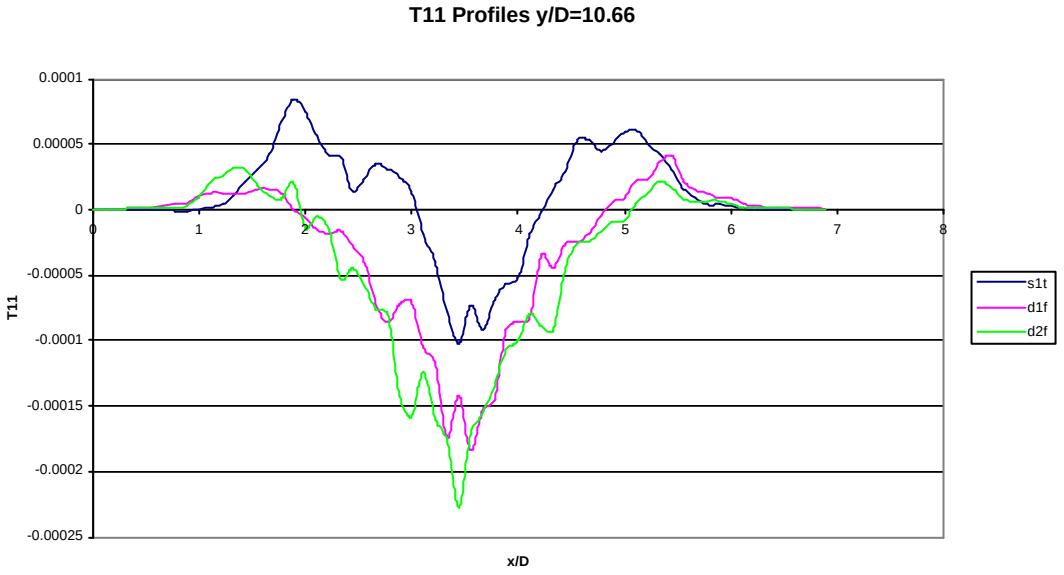

Figure 8.2.17 T11 profiles for s1t, static Smagorinsky stress and static SGDH flux models, d1f, dynamic Smagorinsky stress, static SGDH flux models, d2f, the dynamic Smagorinsky stress and dynamic SGDH flux models.

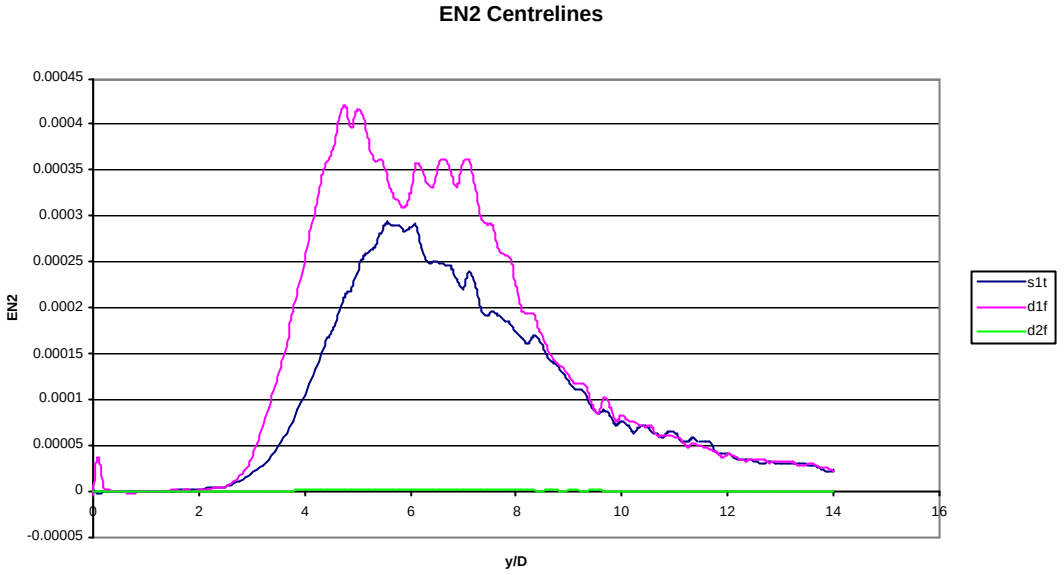

Figure 8.2.18 Vertical flux, EN2, centrelines for s1t, static Smagorinsky stress and static SGDH flux models, d1f, dynamic Smagorinsky stress, static SGDH flux models, d2f, the dynamic Smagorinsky stress and dynamic SGDH flux models.

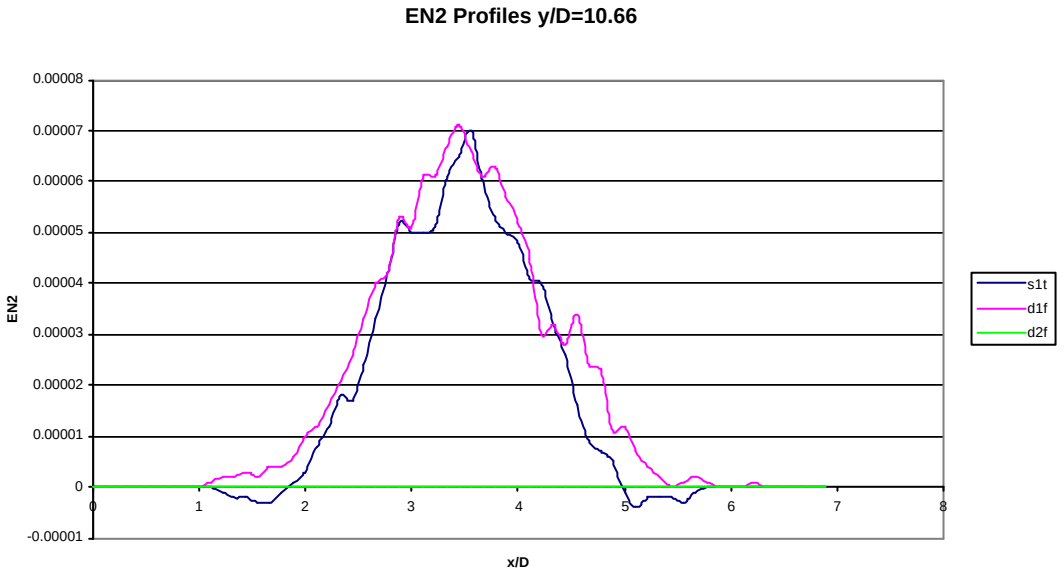

Figure 8.2.19 Vertical flux, EN2, profiles for s1t, static Smagorinsky stress and static SGDH flux models, d1f, dynamic Smagorinsky stress, static SGDH flux models, d2f, the dynamic Smagorinsky stress and dynamic SGDH flux models.

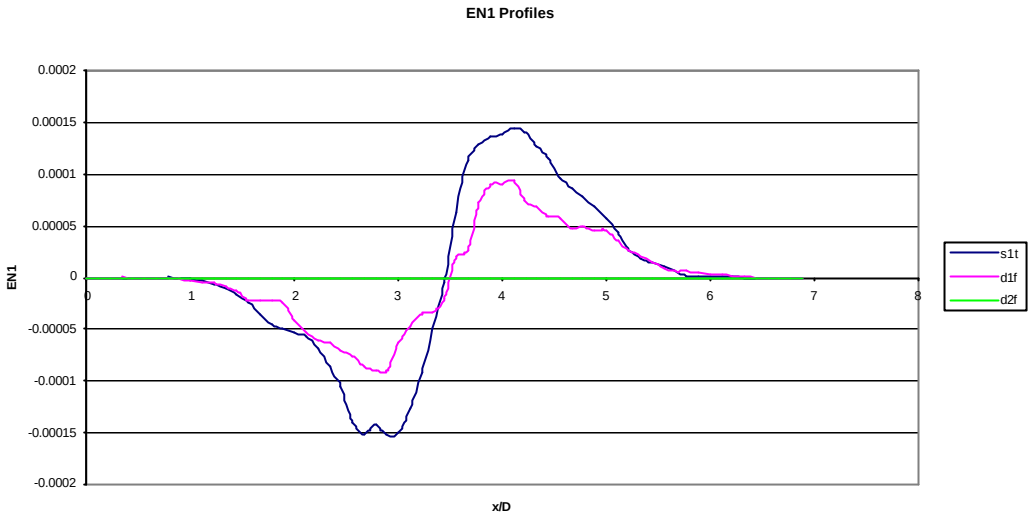

Figure 8.2.20 Radial flux, EN1 in X-axis, profiles for s1t, static Smagorinsky stress and static SGDH flux models, d1f, dynamic Smagorinsky stress, static SGDH flux models, d2f, the dynamic Smagorinsky stress and dynamic SGDH flux models.

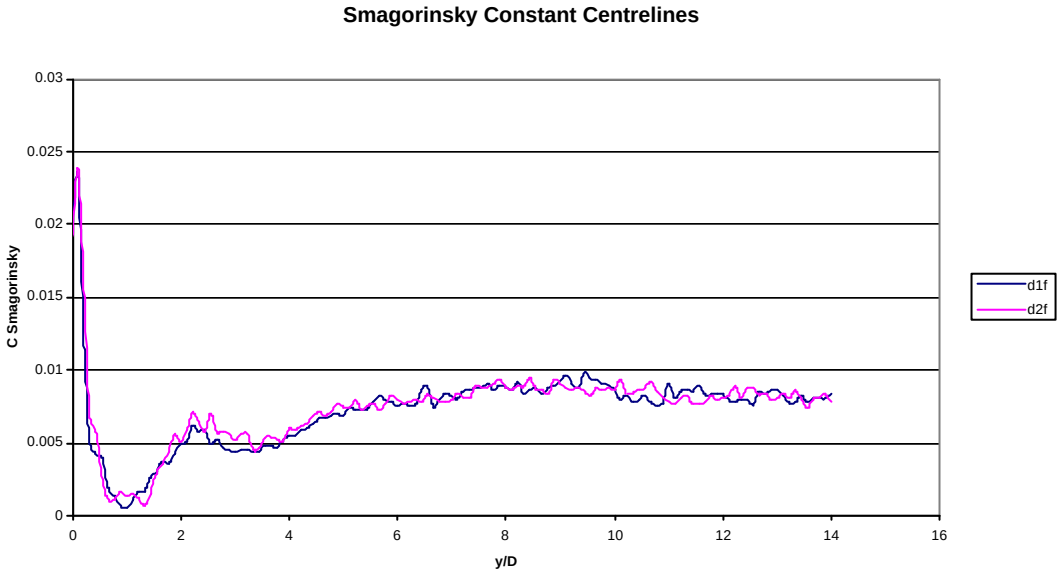

Figure 8.2.21 Smagorinsky constant centrelines for d1f, dynamic Smagorinsky stress, static SGDH flux models, d2f, the dynamic Smagorinsky stress and dynamic SGDH flux models.

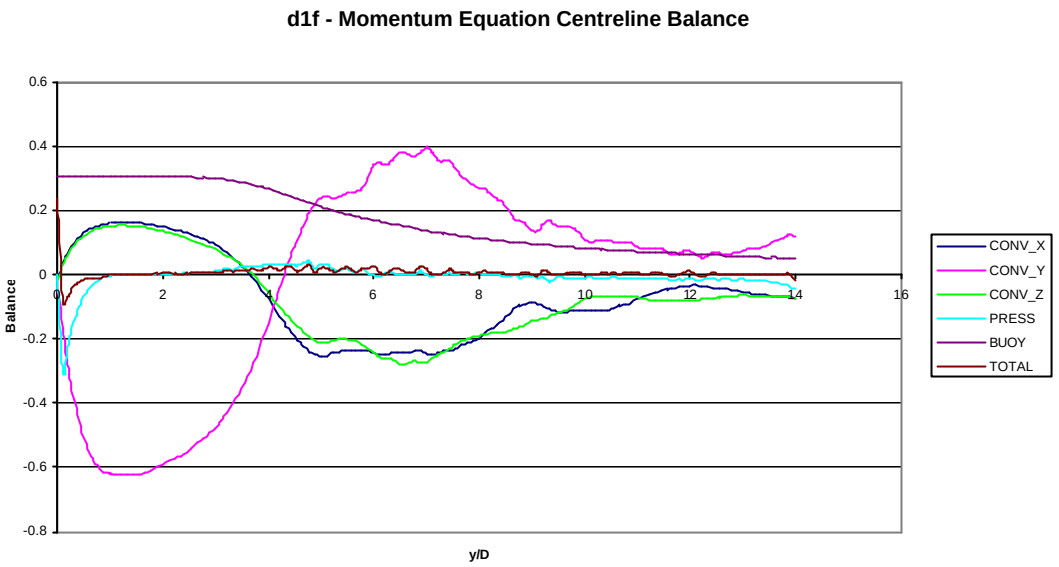

Figure 8.2.22 Vertical momentum equation centreline balance for d1f, dynamic Smagorinsky stress, static SGDH flux models.

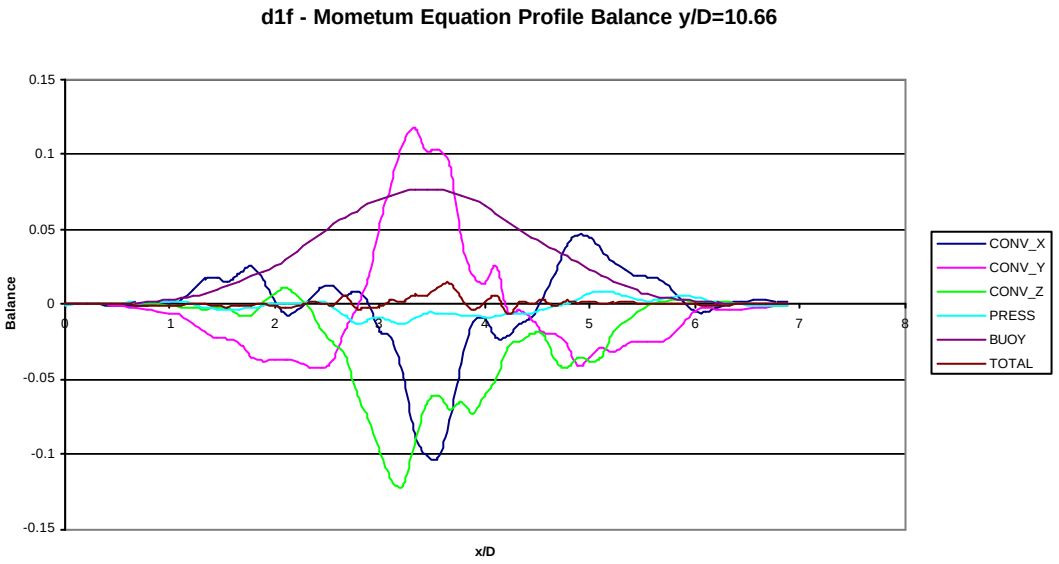

Figure 8.2.23 Vertical momentum equation profile balance, at y/D=10.66, for d1f, dynamic Smagorinsky stress, static SGDH flux models.

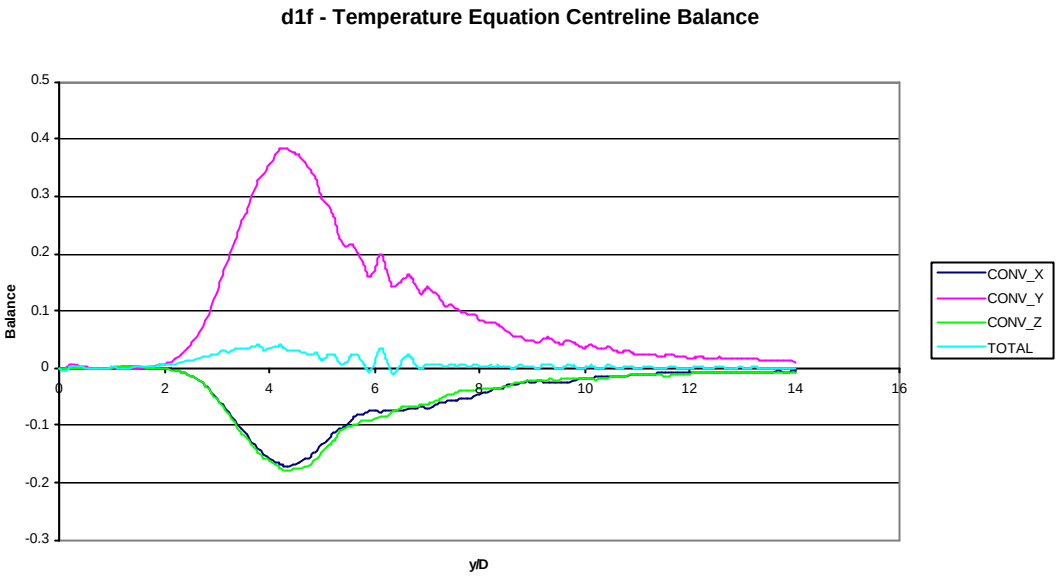

Figure 8.2.24 Temperature equation centreline balance for d1f, dynamic Smagorinsky stress, static SGDH flux models.

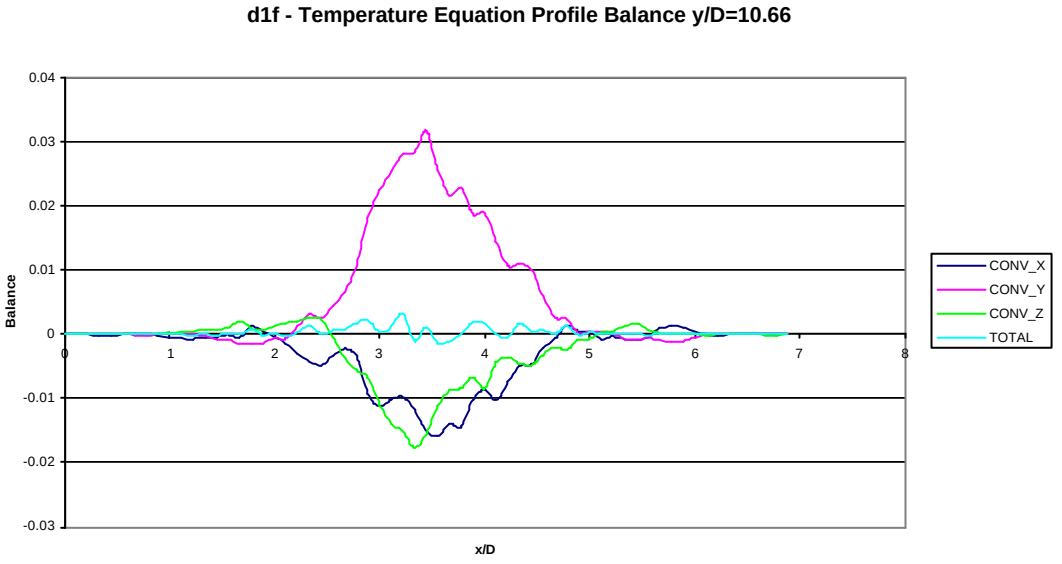

Figure 8.2.25 Temperature equation profile balance at y/D=10.66 for d1f, dynamic Smagorinsky stress, static SGDH flux models.

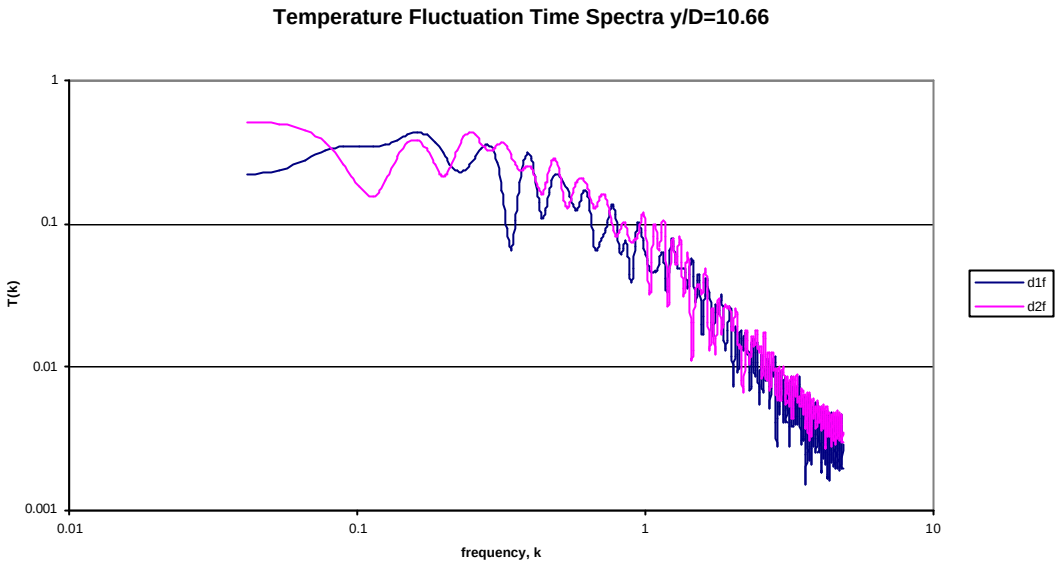

Figure 8.2.26 Temperature fluctuation, TT, time spectra, for d1f, dynamic Smagorinsky stress, static SGDH flux models, d2f, dynamic Smagorinsky stress, dynamic SGDH flux models.

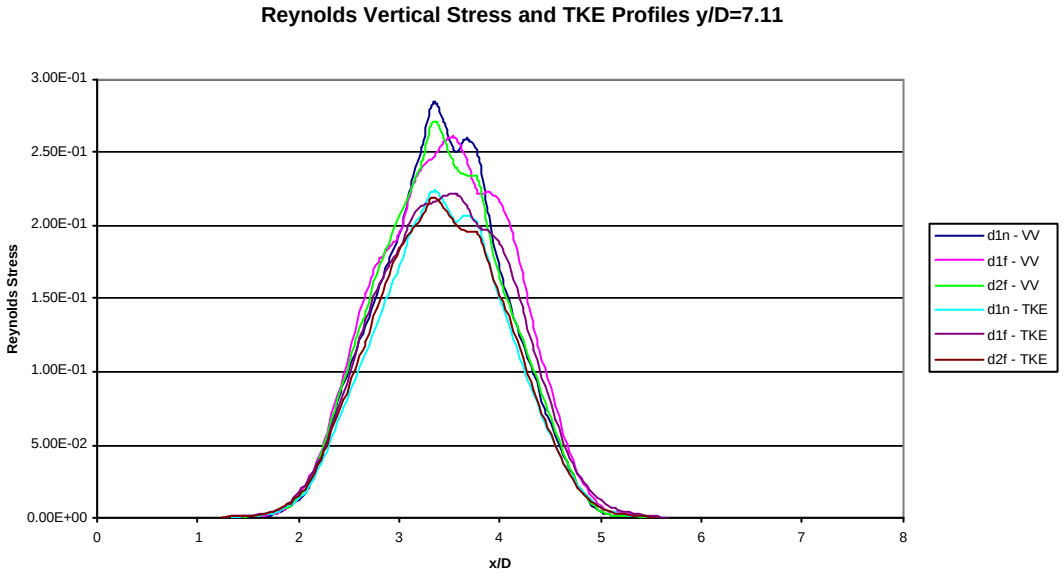

Figure 8.2.27 Vertical Reynolds stresses and turbulent kinetic energy profiles for d1n, no subgrid models, d1f, dynamic Smagorinsky stress, static SGDH flux models, d2f, dynamic Smagorinsky stress, dynamic SGDH flux models.

.

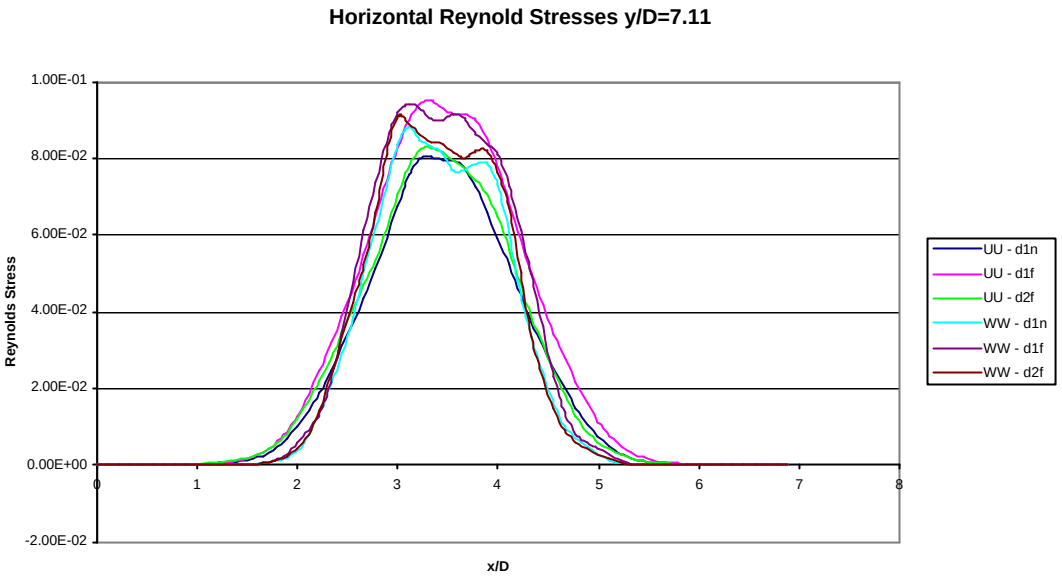

Figure 8.2.28 Horizontal Reynolds stress profiles for d1n, no subgrid models, d1f, dynamic Smagorinsky stress, static SGDH flux models, d2f, dynamic Smagorinsky stress, dynamic SGDH flux models.

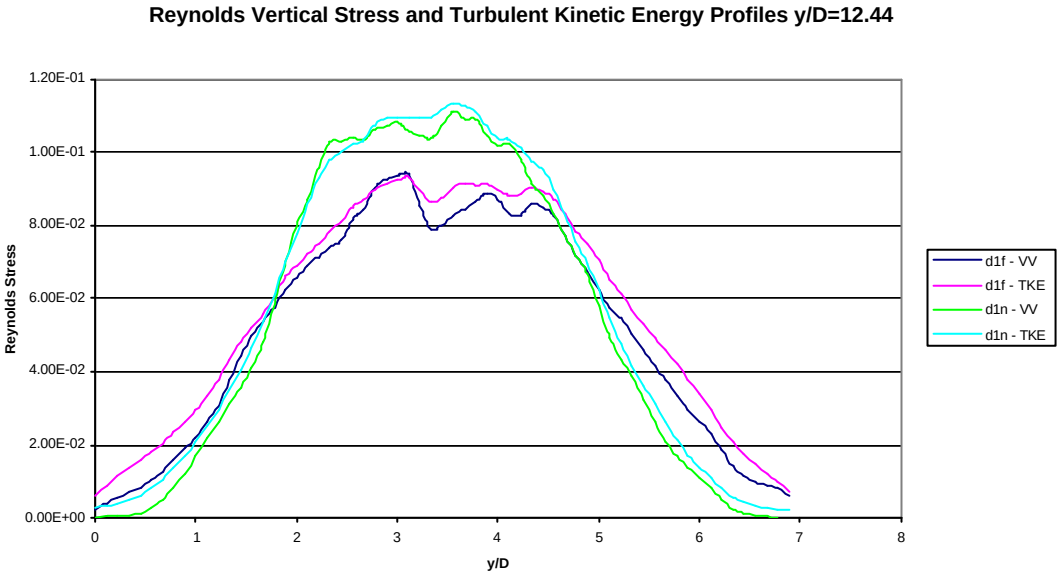

Figure 8.2.29 Reynolds stress and turbulent kinetic energy profiles for d1n, no subgrid models, d1f, dynamic Smagorinsky stress, static SGDH flux models.

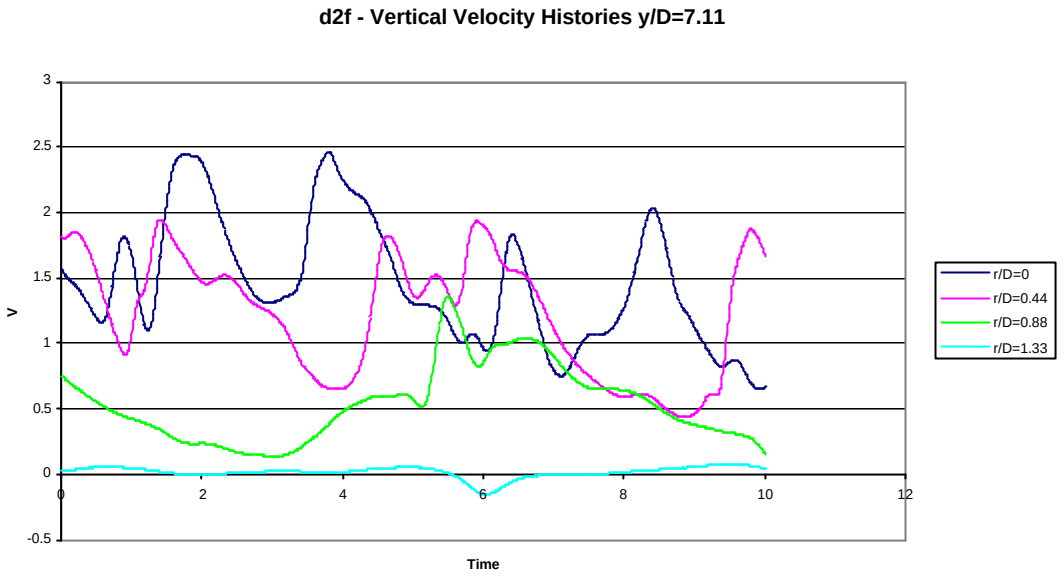

Figure 8.2.30 Vertical velocity histories at different radii from the centreline, at y/D=7.11 for d2f, dynamic Smagorinsky stress, dynamic SGDH flux models.

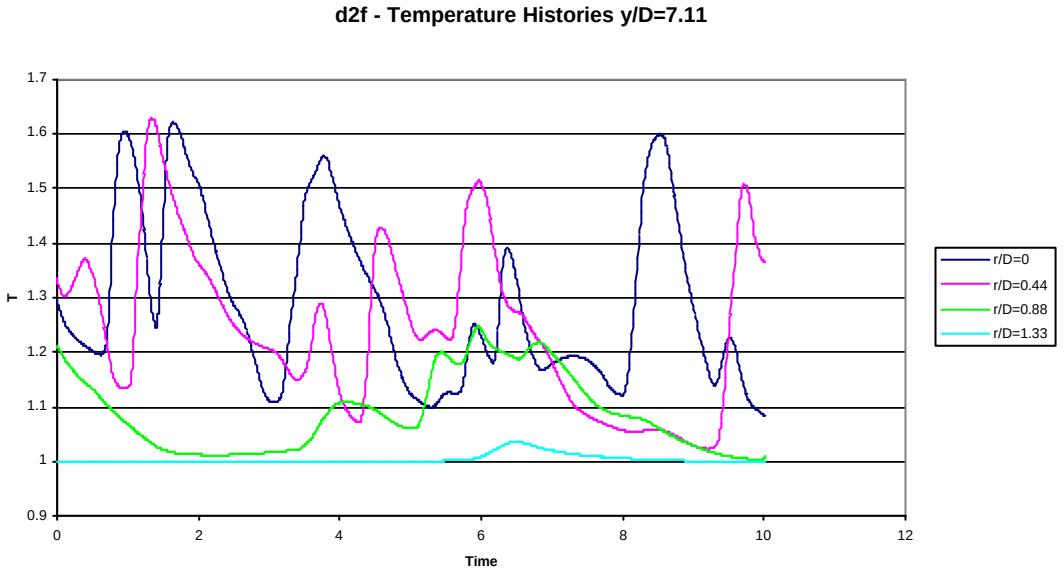

Figure 8.2.31 Temperature histories at different radii from the centreline at y/D=7.11 for d2f, dynamic Smagorinsky stress, dynamic SGDH flux models.

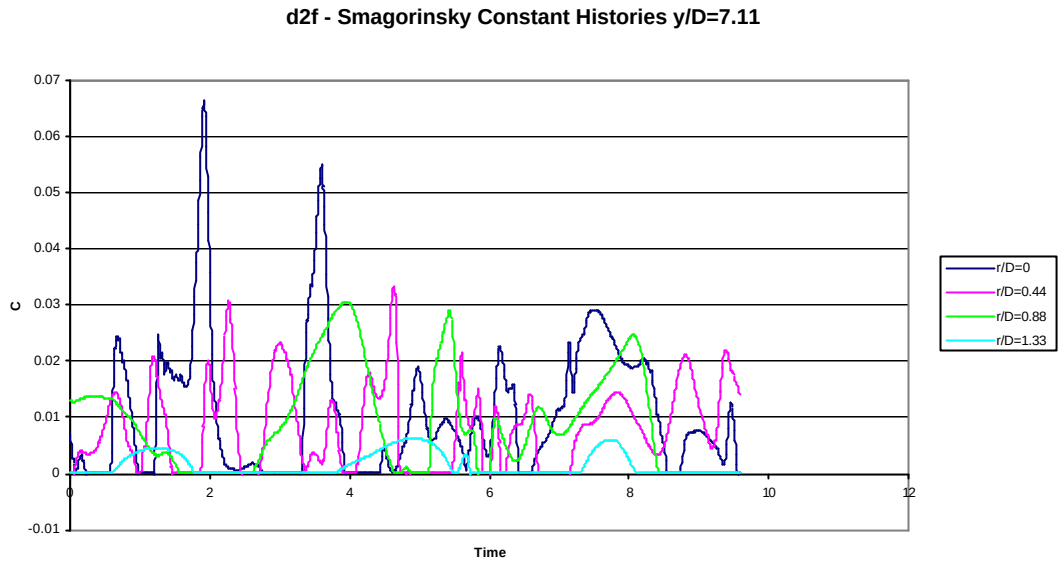

Figure 8.2.32 Smagorinsky constant histories at different radii from the centreline at y/D=7.11 for d2f, dynamic Smagorinsky stress, dynamic SGDH flux models.

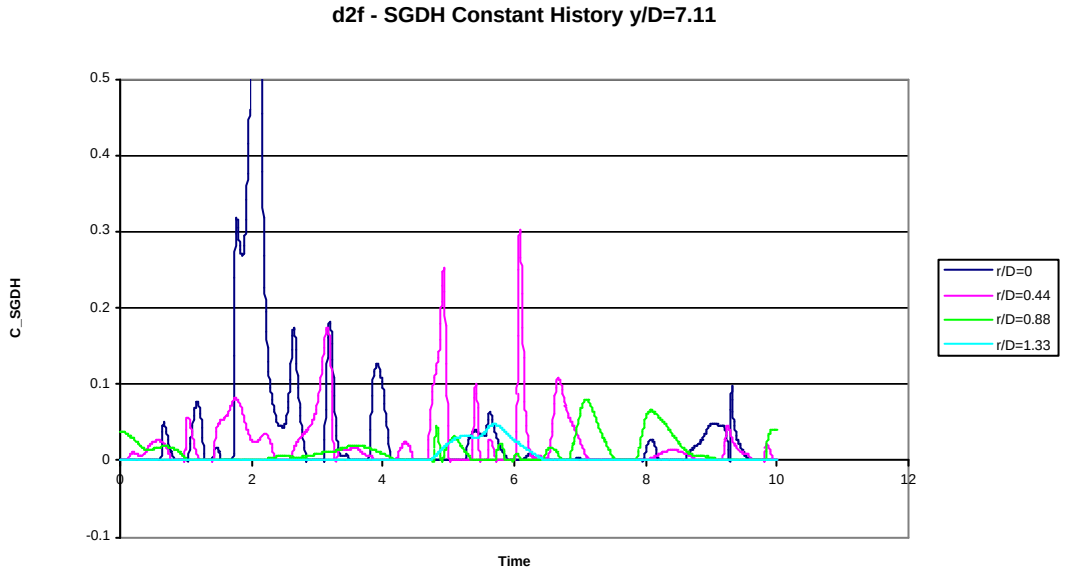

Figure 8.2.33 SGDH constant histories at different radii from the centreline, at y/D=7.11 for d2f, dynamic Smagorinsky stress, dynamic SGDH flux models.

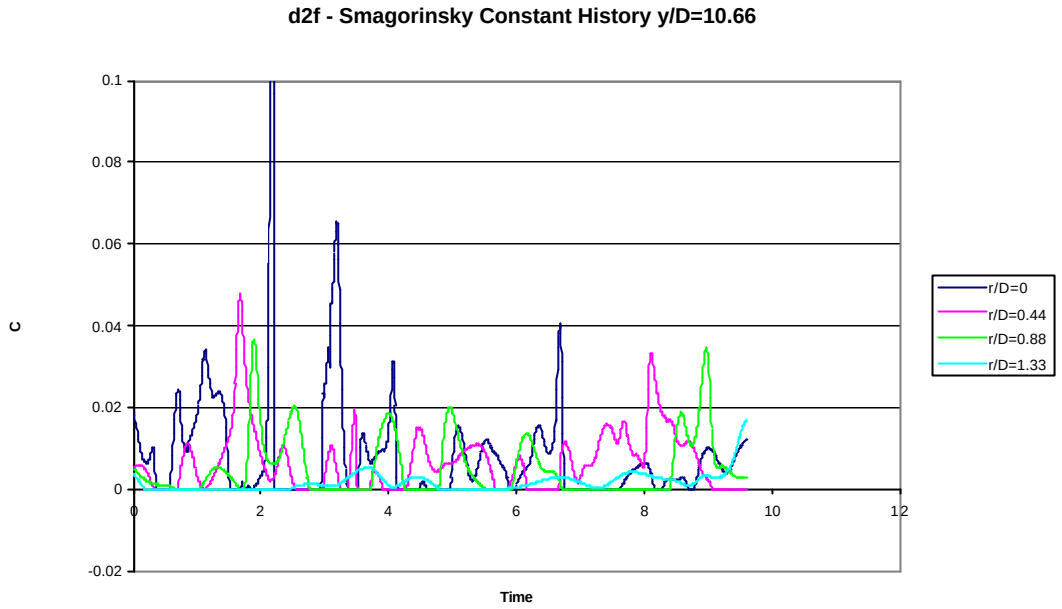

Figure 8.2.34 Smagorinsky constant histories at different radii from the centreline, at y/D=10.66, for d2f, dynamic Smagorinsky stress, dynamic SGDH flux models.

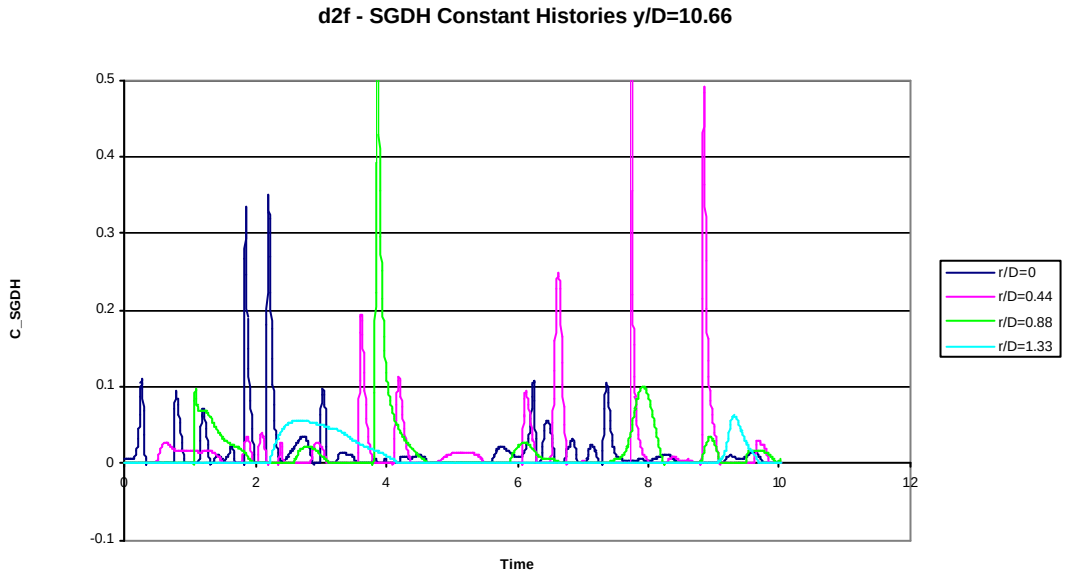

Figure 8.2.35 SGDH constant histories at different radii from the centreline, at y/D=10.66 for d2f, dynamic Smagorinsky stress, dynamic SGDH flux models.

8.3 Localised Dynamic Model Simulations

Two simulations have been carried out with the localised dynamic model. The simulations are labelled as follows:
d1n: no subgrid model
d1f: dynamic Smagorinsky stress model and static SGDH flux model
l1d: localised dynamic model with dynamic modelling of subgrid energy transport terms (see section 5.7) and with static SGDH model.
l2d: localised dynamic model with static modelling of subgrid energy transport terms and static SGDH model for fluxes.
In both cases the test-grid scale kinetic energy was evaluated directly, using 4.77, rather than with a transport equation. This is a faster and equally effective method according to Davidson (1997a, 1997b).

The dynamic procedure for the models in the SKE equation are concluded to be more accurate than their fixed model counterparts and that the resulting stresses are somewhat different in magnitude as a consequence. However, the differences between the dynamic eddy stress models, including the dynamic Smagorinsky are slight in these simulations, for the flow characteristics observed, and these differences are lessened by the diffusive numerical scheme.
The dynamic dissipation model in the SKE transport equation is well calculated in the plume core, but the dynamic diffusion term is numerically erratic. The stress model constant is found to be lower than the theoretical value (more so than the dynamic Smagorinsky model).

Plots for the main flow variables remain similar to those gone before, and are not reproduced. Fig 8.3.1 shows the instantaneous subgrid kinetic energy and test-grid kinetic energy for l1d. The significant difference from the static model is the lack of subgrid energy at the edges of the jet inflow where there are high horizontal gradients. The test-grid plot is plotted with the same contour distribution and shows it's greater magnitude everywhere over the subgrid plot. This must be the case: the sub-test-grid scales must contain more energy than the subgrid scales due to the larger filter width. However, using the direct evaluation method, the gradients at the jet edge at the inlet

are still reflected. This does not affect the development of the subgrid energy as the LDM stress constant is still calculated to be small.

The instantaneous and averaged eddy model constant are printed in fig. 8.3.2. The constant can be seen to achieve its recommended value of 0.07. Even though this is achieved instantaneously, the average shows the centreline to be a greatly reduced 0.02.

Fig. 8.3.3 shows the averaged constants for the dissipation (c1) and diffusion (c2) terms in the SKE equation, described by equations 4.51 and 4.52 respectively. Both constants are clipped to be positive. This is a physically necessary requirement as well as necessary for stability in the latter case. Backscatter should not occur in either the dissipation or diffusion terms. The production terms should represent this.
C1 has reasonable central values (the contour limit is 5, and the recommended value is 1). The diffusion term, on the other hand, gives values two orders of magnitude greater than that expected along the centreline, and reduces to zero at the edges symmetrically.

Figs. 8.3.4 and 8.3.5 show the velocity and temperature centrelines respectively, again with d1n and d1f. The values are virtually identical from the plot, with the two localised dynamic models even closer to d1n, the simulation without a subgrid model, than d1f.
The turbulent viscosity graph, fig. 8.3.6, shows the Smagorinsky model to give significantly larger values than both LDM models. The qualitative behaviour is, in a sense, better for the LDM models since they do not recognise as much turbulence as the velocity fluctuations are developing, although the effect on transition by the dynamic Smagorinsky model is beneficial in this case. The fixed model LDM simulation has higher magnitudes than the dynamically modelled LDM simulation, which can also be seen in the T22 centreline graph in fig. 8.3.7.
The profiles of the vertical velocity and the T12 stress (taken in the X-axis), figs. 8.3.8 and 8.3.9 respectively, show that the velocity spread rates are very similar indicating that the difference in magnitude between the l1d and l2d T22 stresses is not sufficient to make a strong difference between their results.

The eddy constant is much lower than the predicted 0.07, and is quantified in figure 8.3.10, and plotted with the d1f (dynamic Smagorinsky) constant. The d1f constant was only slightly less than the usual prescribed value, and is easily accounted for with the dissipative discretisation used. However, the LDM constant has gone to less than a third of the given value for both l1d and l2d regardless of the difference in the magnitude of the subgrid kinetic energy. This indicates the significant over-dissipation of the standard static one-equation model induced by the constant.
This plot also shows very clearly the breakdown into chaos of the flow.

The SKE centrelines are plotted for l1d and l2d in fig. 8.3.11, and are very different. The static model generates more subgrid energy early on and maintains a significantly higher value, more than the difference in the centreline stresses would suggest. However the square root in the model (eqn. 4.19) explains this difference.
The temperature fluxes are shown in figs 8.3.12, 8.3.13 and reflect the differences in magnitude of the turbulent viscosity, again showing the behaviour of the SGDH model.

The dynamic SKE equation dissipation constant is about three times as large as the static value constant, and is the cause for the difference in magnitude of the subgrid kinetic energy between l1d and l12. The centrelines are shown in fig. 8.3.14. The diffusion constant also converges to a much higher value than its static constant (10 rather than 0.1), and is shown in fig. 8.3.15, although the dissipation term is the stronger of the two.

The TKE and temperature spectra, given in figs. 8.3.16 and 8.3.17, are very similar for the LDM model simulations, the dynamic Smagorinsky simulation, and d1n, the simulation without a subgrid model.
The Reynolds stresses are plotted in figs. 8.3.18 and 8.3.19 for the momentum and temperature equations respectively. They show that the vertical fluctuations are the largest as expected, but also show the magnitude of the horizontal normal fluctuations, which do not occur in the vertical momentum balance, but which also have a significant magnitude. This is a significant term in the behaviour of plumes which is usually overlooked.

The Shabbir and George (1994) experiment shows constant centreline intensities for the normalised axial, radial, and temperature turbulent intensities. The other correlations do not asymptote and so cannot be assessed without a full centreline plot, which was not retained from the simulations. Table 8.1 below gives the intensities of these values at four points for d1n, d1f, and l1d.

	d1n			d1f		
y/D	UU	VV	TT	UU	VV	TT
7.11	19%	35%	49%	21%	34%	52%
10.66	24%	35%	54%	25%	34%	54%
12.44	24%	33%	54%	24%	32%	52%
14	26%	33%	55%	25%	32%	51%
	l1d			Exp.		
y/D	UU	VV	TT	UU	VV	TT
7.11	18%	34%	49%			
10.66	23%	36%	53%	0.19%	0.32%	0.40%
12.44	23%	35%	55%	0.19%	0.32%	0.40%
14	26%	35%	51%	0.19%	0.32%	0.40%

Table 8.3.1 2nd Moment Intensities

The three simulations show similar enough results that, again, further averaging could yield different conclusions. The trend for all the models is clear, however, in that all the turbulent intensities are over-predicted, particularly the temperature fluctuations, although the dynamic Smagorinsky model has the vertical velocity components correct by the end of the flow. Flow further downstream would also be expected to improve this.

Self-similarity is considered for l1d, and is representative of the other dynamic model simulations. The assumption that the flow has fully gone through transition, and that the self-similar region of the plume has been achieved is shown to be nearly established, although the convergence of the plots is still a problem, and exacerbated by the fact that the stresses take a longer time for the averages to converge fully than for the velocity and temperature fields, due to the square having a larger variance. It has been found (Dai et al., 1994) that the Reynolds stresses take a longer distance from the source to become self-similar than the velocities and temperatures. If these are found to be self-similar it can be assumed that the whole flow is self-similar.

The self-similarity plots in figs. 8.3.20-8.3.22 are rather rough, but indicate that these stresses have almost achieved similarity. The normalisation process is with the maximum value of the respective stress, and the half-width, which according to the theory given by Chen and Rodi (1980), must be equal for each stress. The half-width is accordingly evaluated for the first stress given, UU, and used for the subsequent stresses UV and VV. Earlier plots, including the spectra, show that the simulations are in an almost fully turbulent region by y/D=10.66. The second point is taken only a single cell away from the boundary, and is affected by the boundary conditions.

Figs. 8.3.23 and 8.3.24 show the time histories, of dissipation and diffusion coefficients over 10 time units. The dissipation constant, c1, was bounded by 100 and the latter, c2, is unbounded from above. Both were bounded from below by 0. This is sufficient.

The dissipation constant remains within the bounds and has few clipped points. The further from the centreline, the greater the magnitude of the constants, indicating numerical problems with intermittency or that the energy is already well dissipated. The diffusion constant is much more erratic with a considerable amount of clipping and numerical difficulties. While the centreline constant for the dissipation seems to be reasonably evaluated, and the constant of approximately 3 would be recommended, the diffusion constant is left uncertain. However, the small value of the diffusion, and the results of l1d, show this numerical fluctuation not to be damaging to the simulation. Davidson, 1999 does not incorporate the diffusion term at all, assuming it to be negligible.

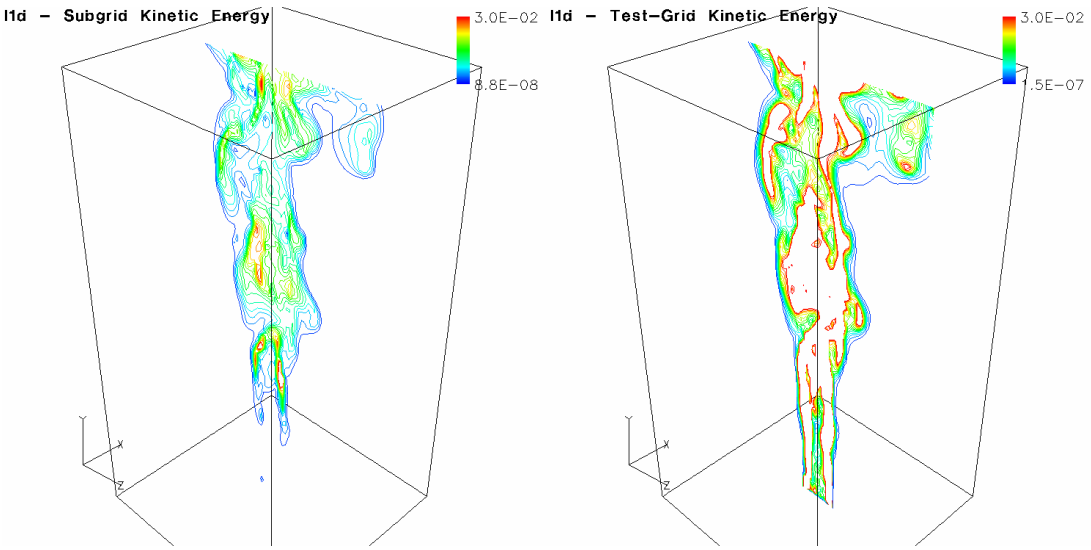

Fig. 8.3.1 Instantaneous subgrid and test-grid kinetic energy plots.

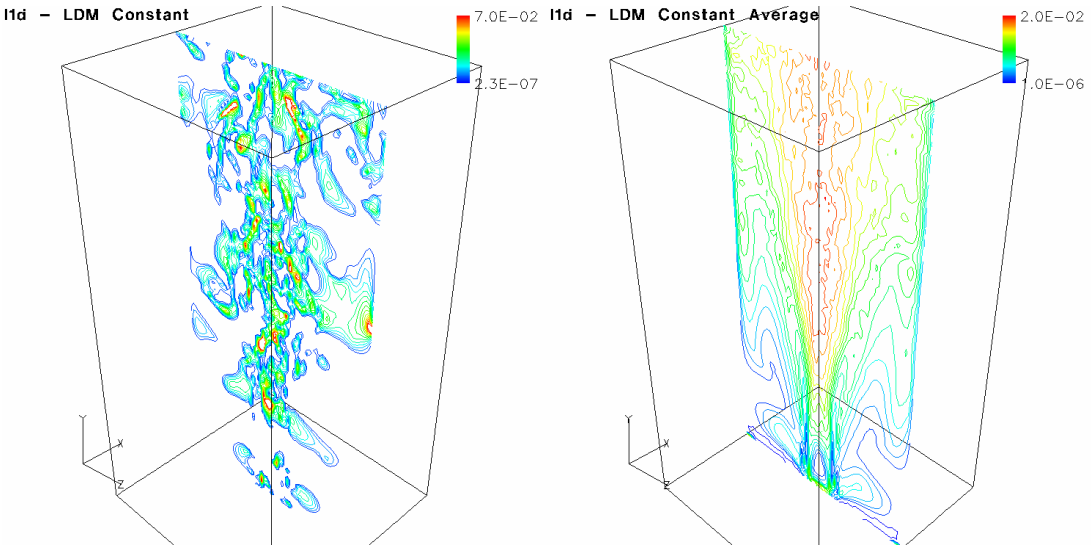

Fig. 8.3.2 Instantaneous and averaged eddy constant values.

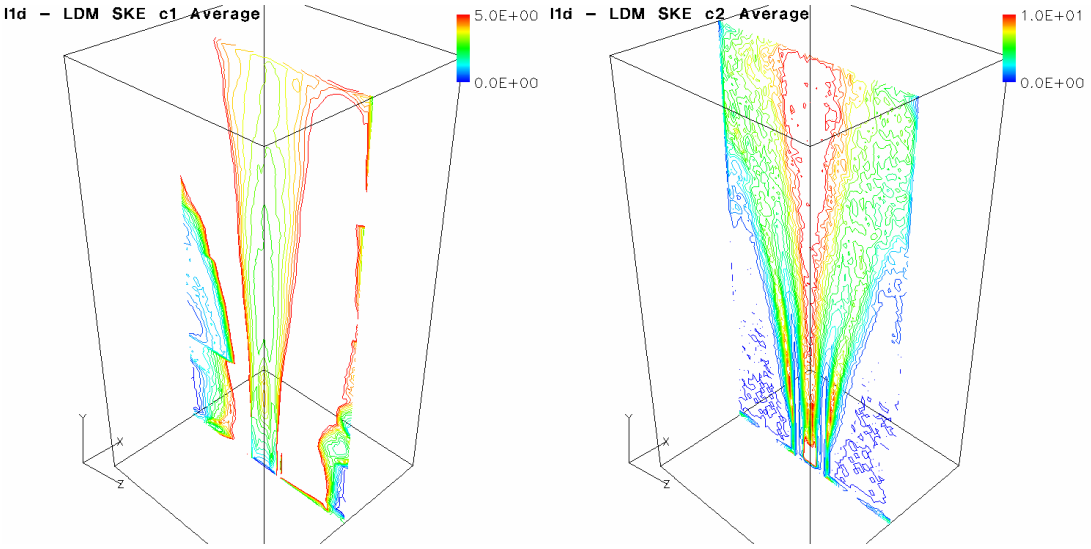

Fig. 8.3.3 Dissipation and diffusion constant averages for subgrid kinetic energy.

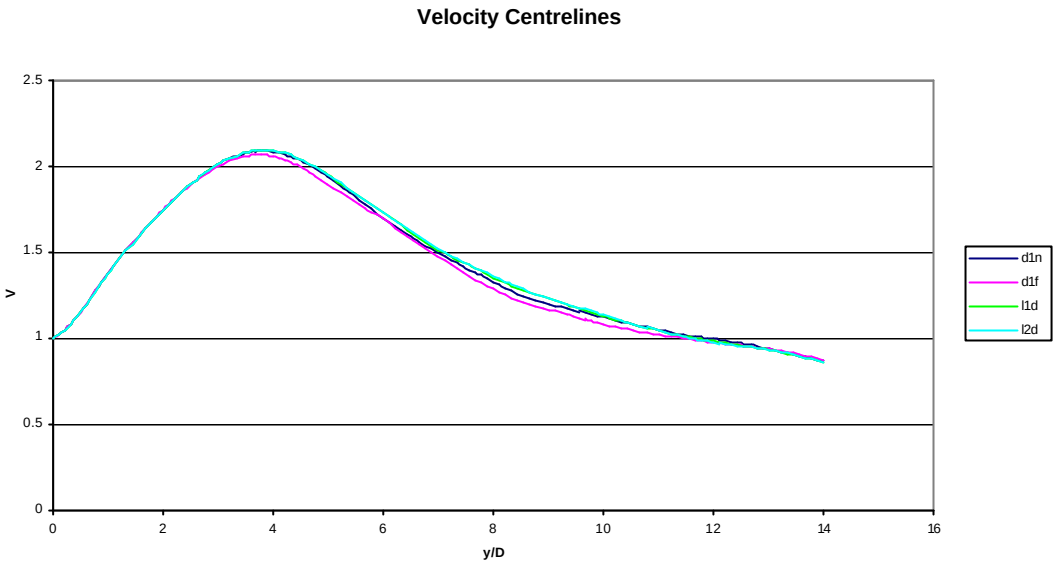

Figure 8.3.4 Vertical velocity centrelines for d1n, no subgrid models, d1f, dynamic Smagorinsky stress, static SGDH flux models, l1d, LDM with dynamic SKE constants stress, static SGDH flux models, l2d LDM with static SKE constants stress, static SGDH flux models.

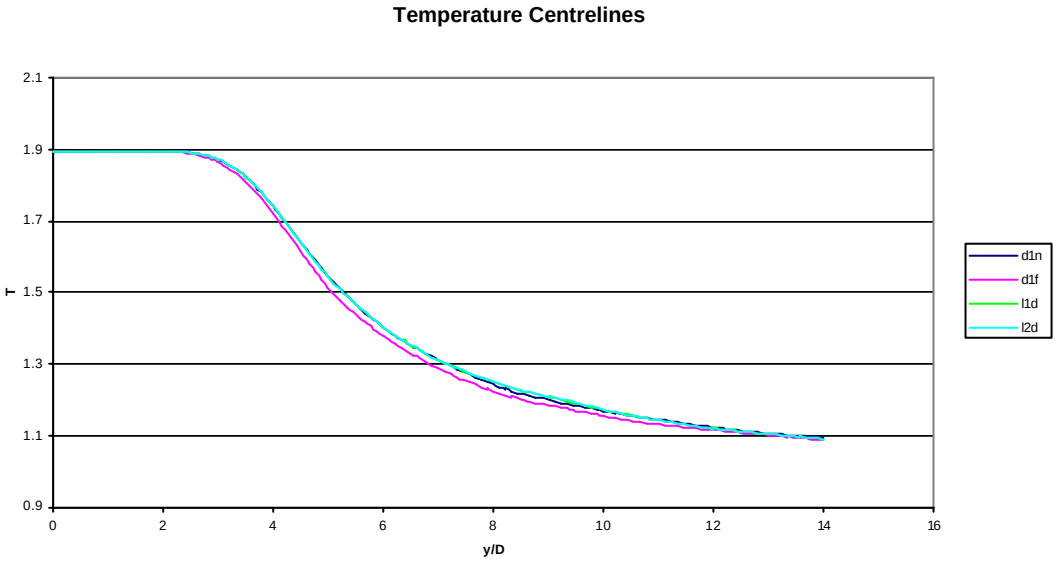

Figure 8.3.5 Temperature centrelines for d1n, no subgrid models, d1f, dynamic Smagorinsky stress, static SGDH flux models, l1d, LDM with dynamic SKE constants stress, static SGDH flux models, l2d LDM with static SKE constants stress, static SGDH flux models.

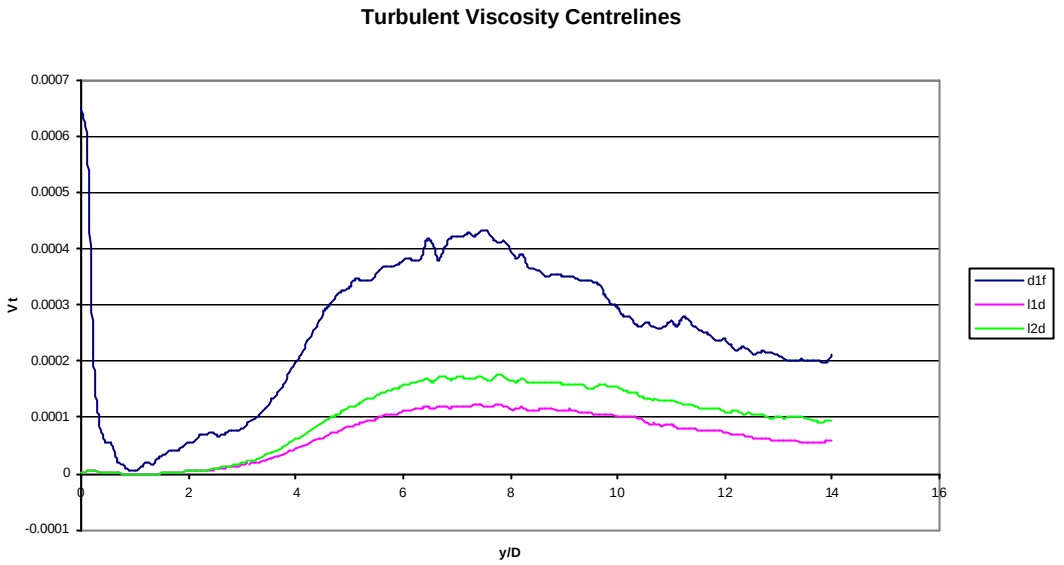

Figure 8.3.6 Turbulent viscosity centrelines for d1f, dynamic Smagorinsky stress, static SGDH flux models, l1d, LDM with dynamic SKE constants stress, static SGDH flux models, l2d LDM with static SKE constants stress, static SGDH flux models.

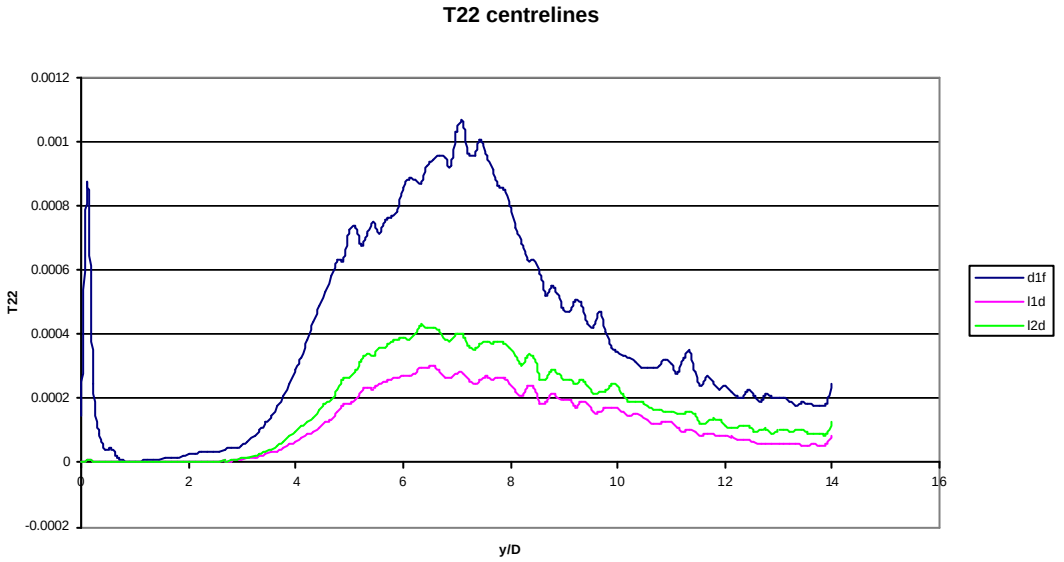

Figure 8.3.7 T22 centrelines for d1f, dynamic Smagorinsky stress, static SGDH flux models, l1d, LDM with dynamic SKE constants stress, static SGDH flux models, l2d LDM with static SKE constants stress, static SGDH flux models.

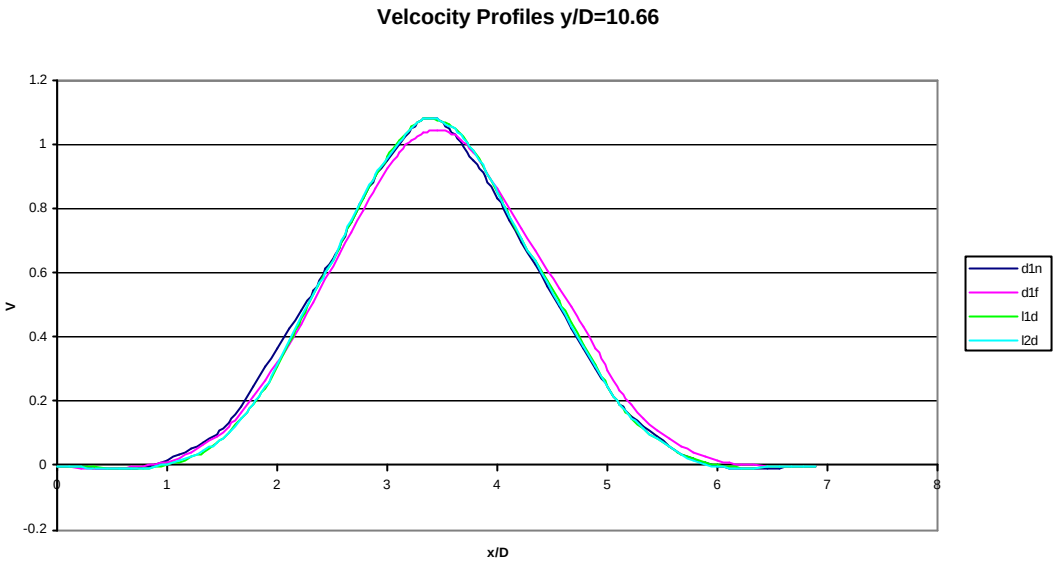

Figure 8.3.8 Velocity profiles for d1n, no subgrid models, d1f, dynamic Smagorinsky stress, static SGDH flux models, l1d, LDM with dynamic SKE constants stress, static SGDH flux models, l2d LDM with static SKE constants stress, static SGDH flux models.

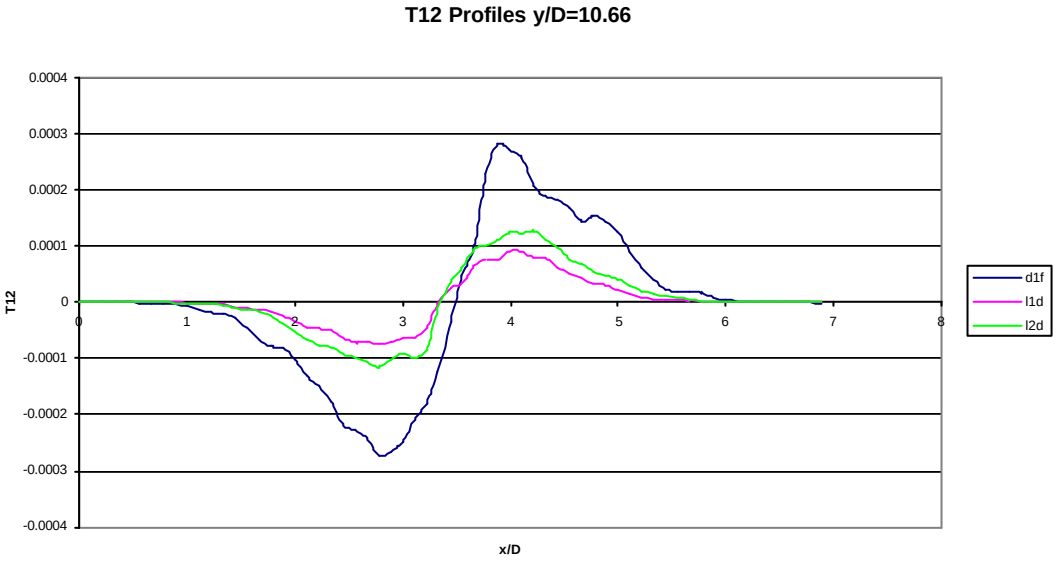

Figure 8.3.9 T12 Profiles for d1f, dynamic Smagorinsky stress, static SGDH flux models, l1d, LDM with dynamic SKE constants stress, static SGDH flux models, l2d LDM with static SKE constants stress, static SGDH flux models.

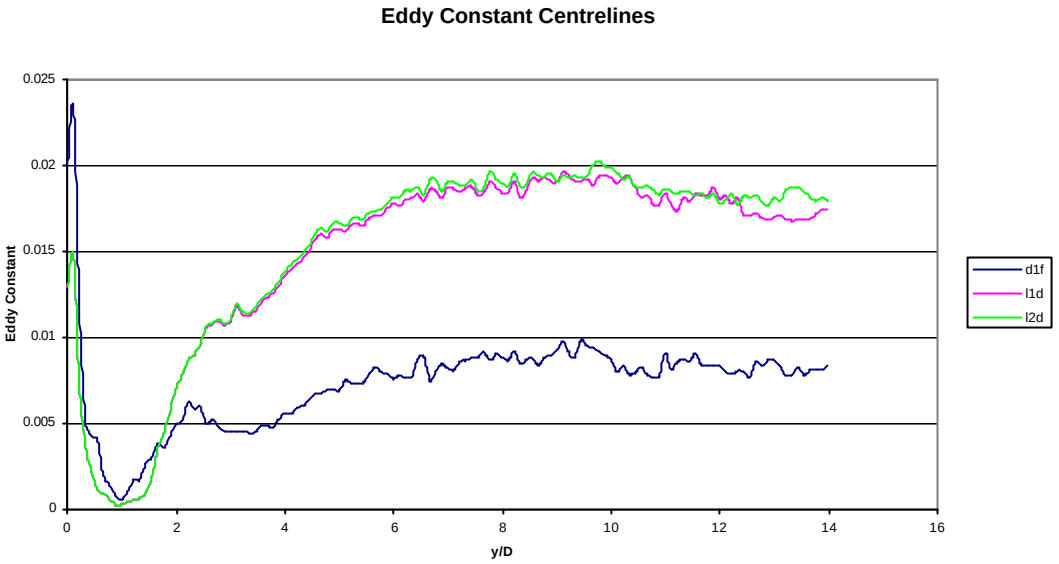

Figure 8.3.10 Eddy constant centrelines for d1f, dynamic Smagorinsky stress, static SGDH flux models, l1d, LDM with dynamic SKE constants stress, static SGDH flux models, l2d LDM with static SKE constants stress, static SGDH flux models.

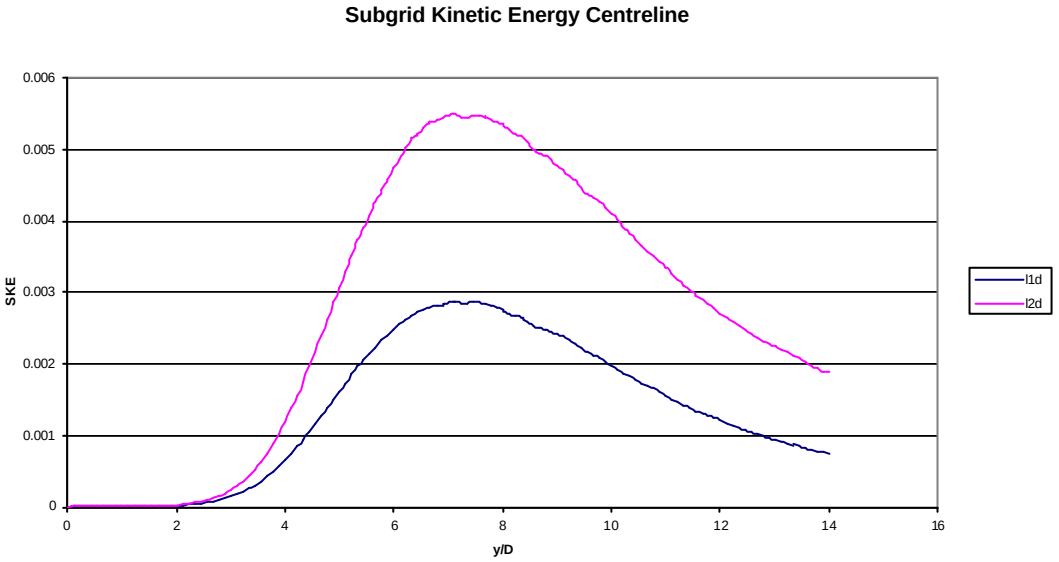

Figure 8.3.11 Subgrid kinetic energy centrelines for l1d, LDM with dynamic SKE constants stress, static SGDH flux models, l2d LDM with static SKE constants stress, static SGDH flux models.

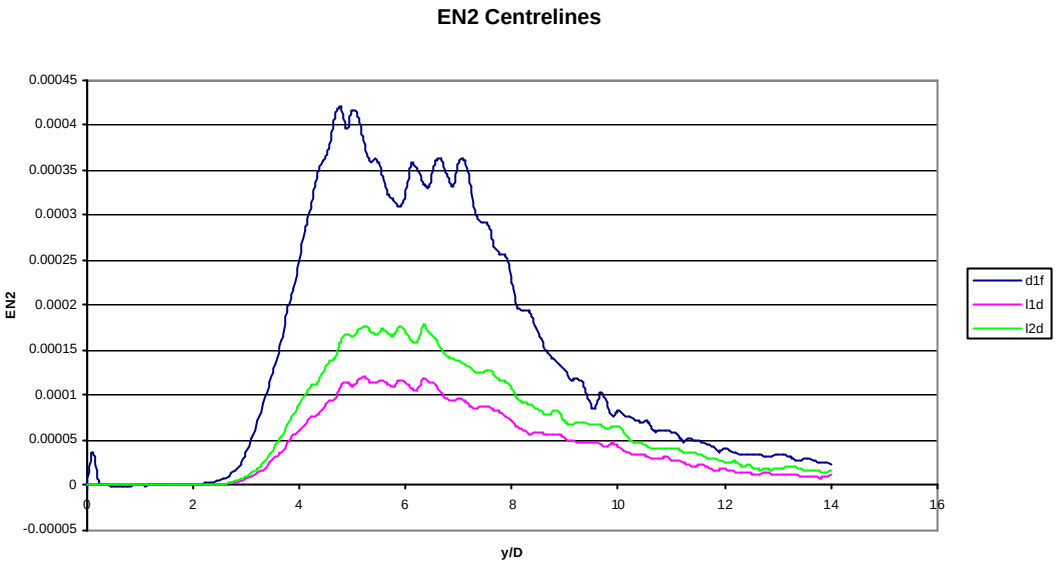

Figure 8.3.12 EN2 centrelines for d1f, dynamic Smagorinsky stress, static SGDH flux models, l1d, LDM with dynamic SKE constants stress, static SGDH flux models, l2d LDM with static SKE constants stress, static SGDH flux models.

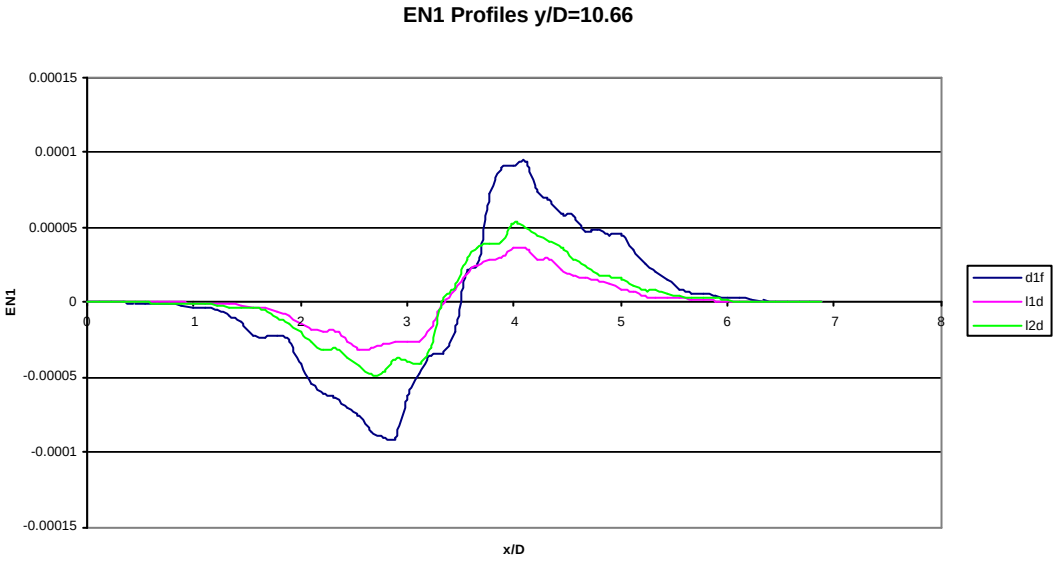

Figure 8.3.14 EN1 profiles for d1f, dynamic Smagorinsky stress, static SGDH flux models, l1d, LDM with dynamic SKE constants stress, static SGDH flux models, l2d LDM with static SKE constants stress, static SGDH flux models.

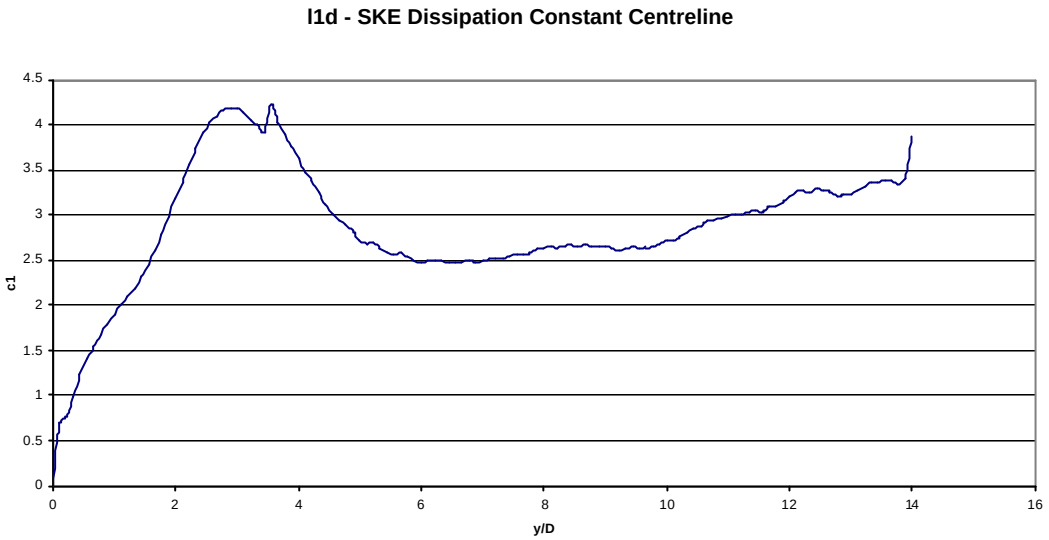

Figure 8.3.14 Subgrid kinetic energy dissipation constant centreline for l1d, LDM with dynamic SKE constants stress, static SGDH flux models.

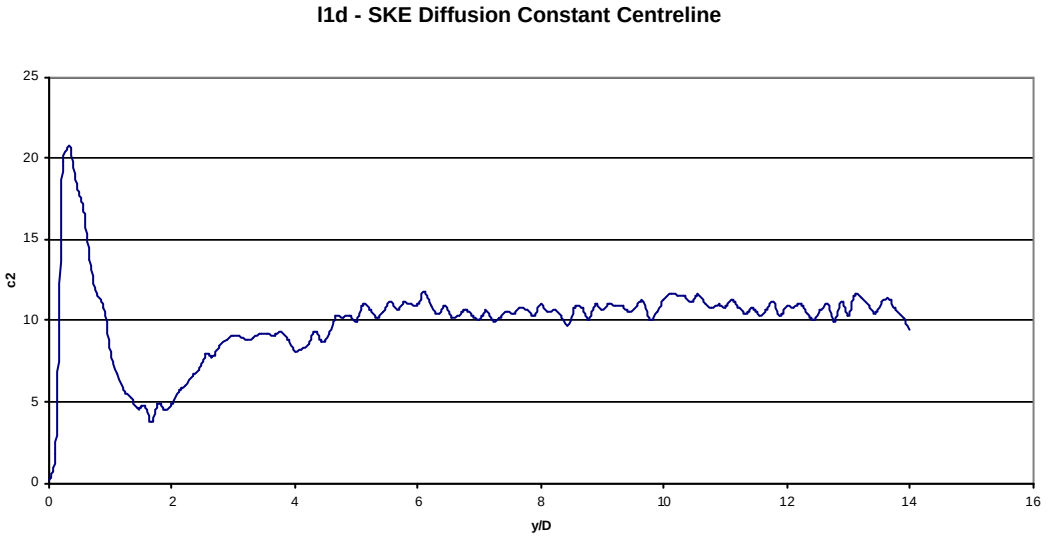

Figure 8.3.15 Subgrid kinetic energy diffusion constant centreline for l1d, LDM with dynamic SKE constants stress, static SGDH flux models.

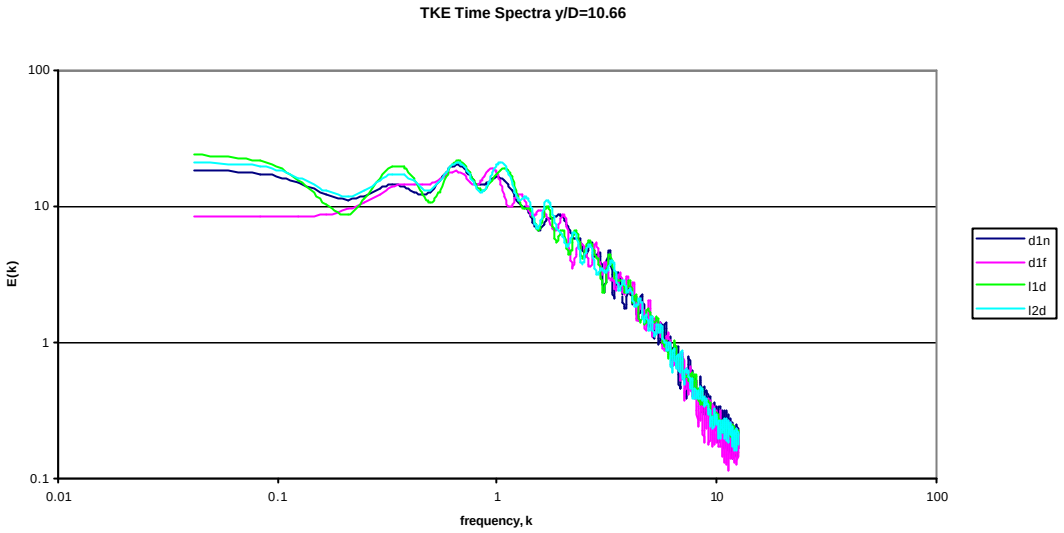

Figure 8.3.16. Turbulent kinetic energy spectra for d1n, no subgrid models, d1f, dynamic Smagorinsky stress, static SGDH flux models, l1d, LDM with dynamic SKE constants stress, static SGDH flux models, l2d LDM with static SKE constants stress, static SGDH flux models.

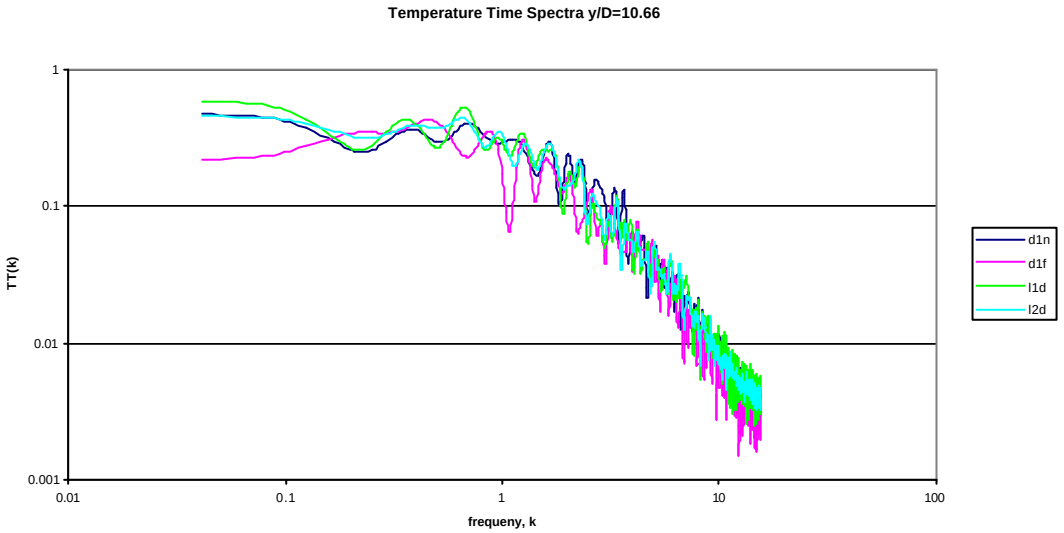

Figure 8.3.17 Temperature time spectra for d1n, no subgrid models, d1f, dynamic Smagorinsky stress, static SGDH flux models, l1d, LDM with dynamic SKE constants stress, static SGDH flux models, l2d LDM with static SKE constants stress, static SGDH flux models.

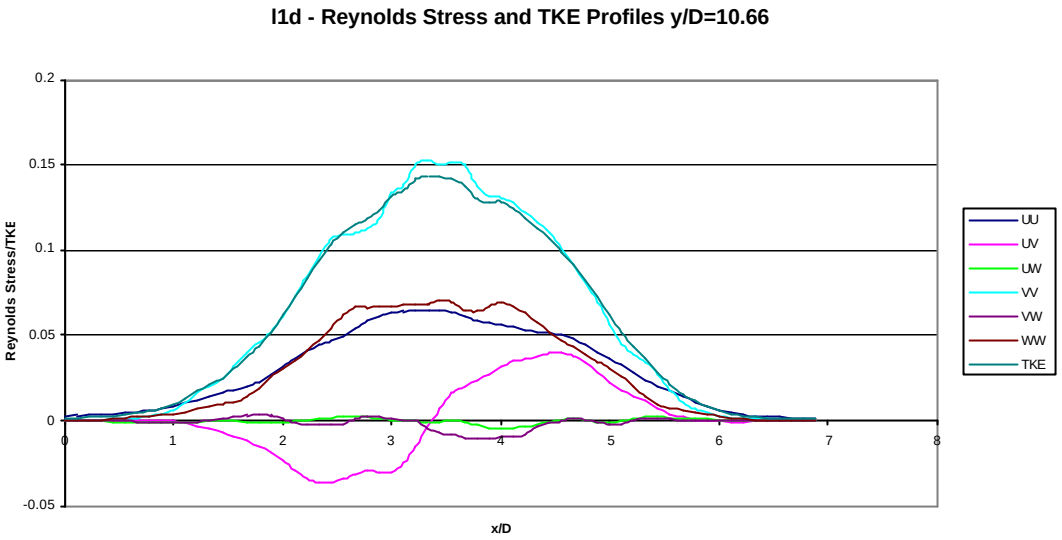

Figure 8.3.18 Reynolds stress and TKE profiles for l1d, LDM with dynamic SKE constants stress, static SGDH flux models.

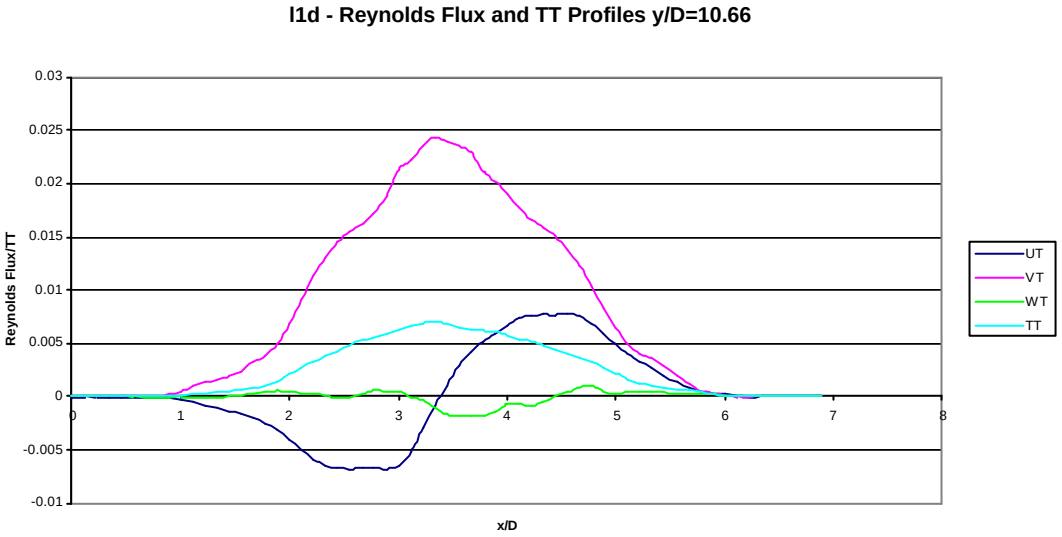

Figure 8.3.19 Reynolds Flux and TT Profiles for l1d, LDM with dynamic SKE constants stress, static SGDH flux models.

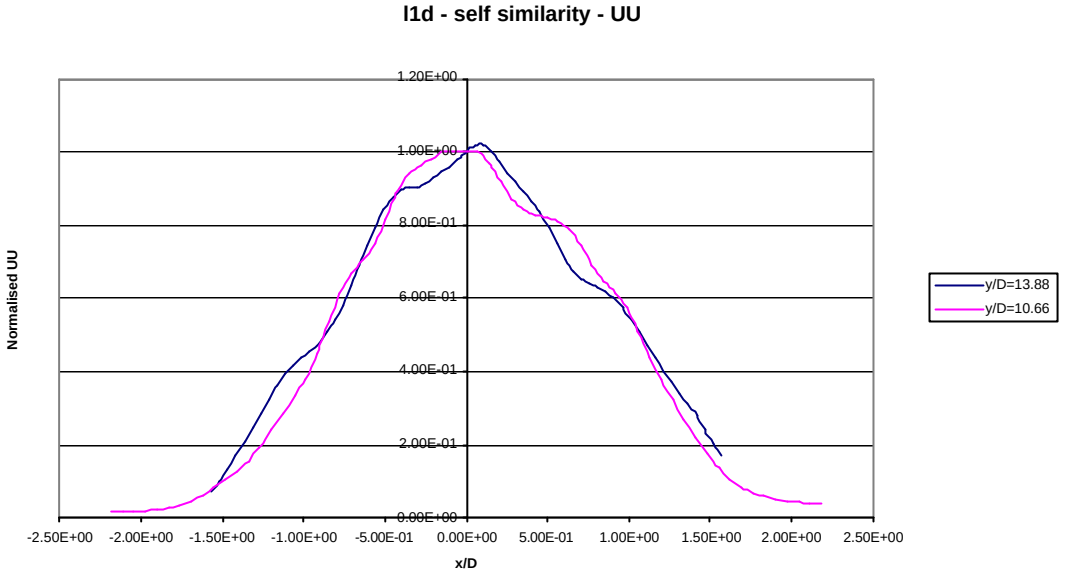

Figure 8.3.20 Self-similarity for UU Reynolds stress for l1d, LDM with dynamic SKE constants stress, static SGDH flux models.

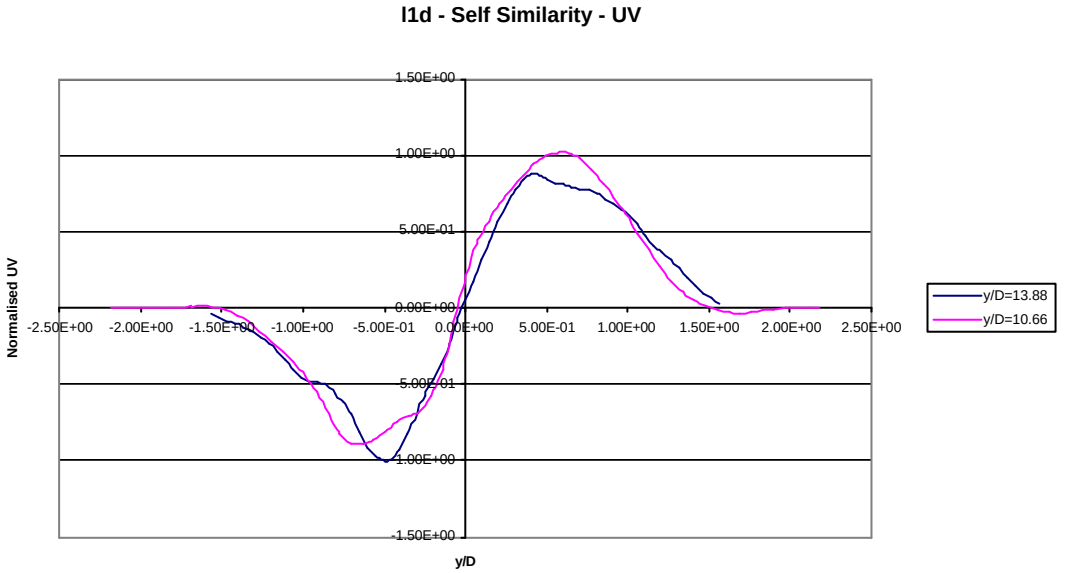

Figure 8.3.21 Self-similarity for UV Reynolds stress for l1d, LDM with dynamic SKE constants stress, static SGDH flux models.

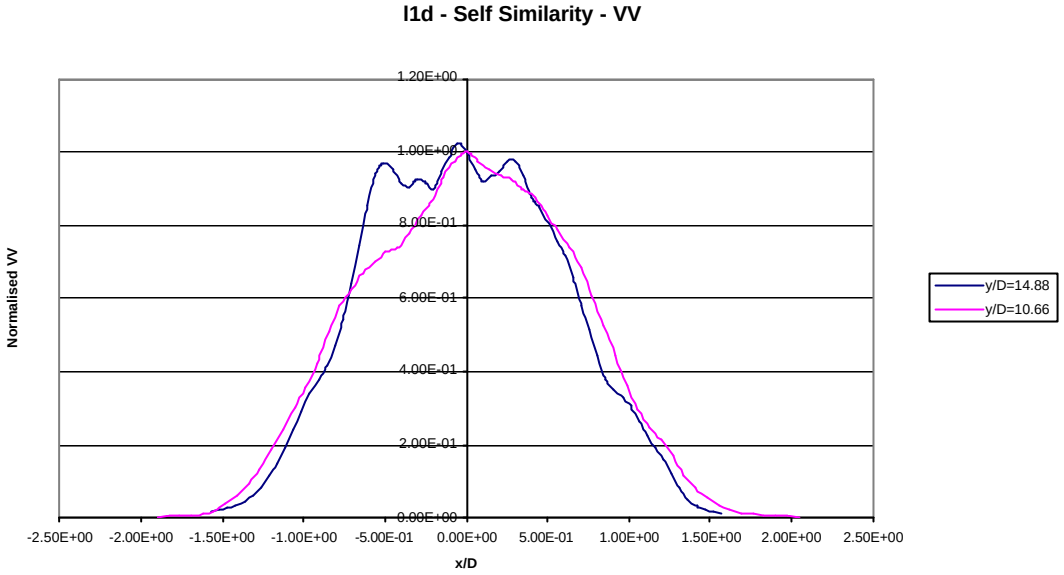

Figure 8.3.22 Self-similarity for VV Reynolds stress for l1d, LDM with dynamic SKE constants stress, static SGDH flux models.

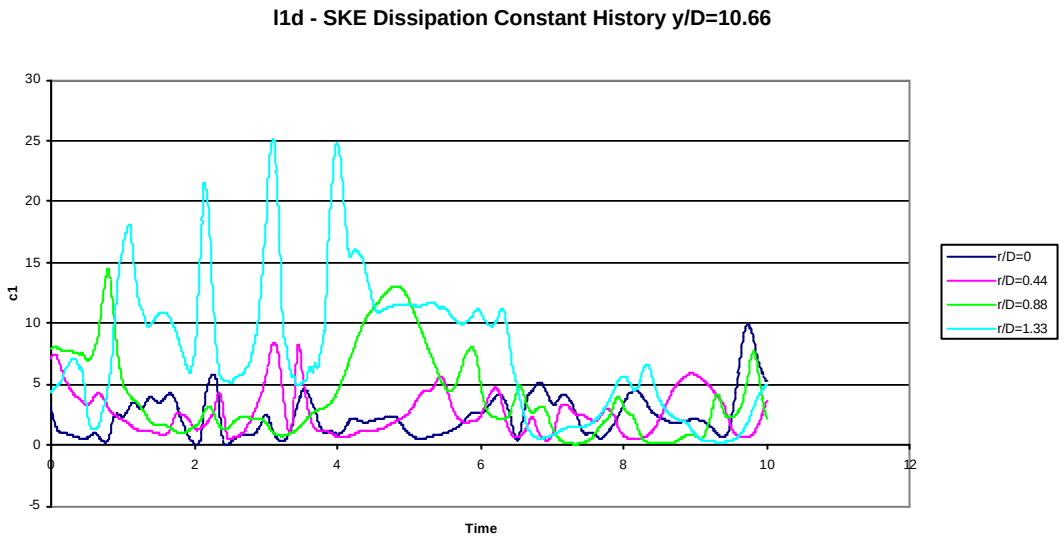

Figure 8.3.23 Subgrid kinetic energy equation dissipatio n constant time histories at different radii for l1d, LDM with dynamic SKE constants stress, static SGDH flux models.

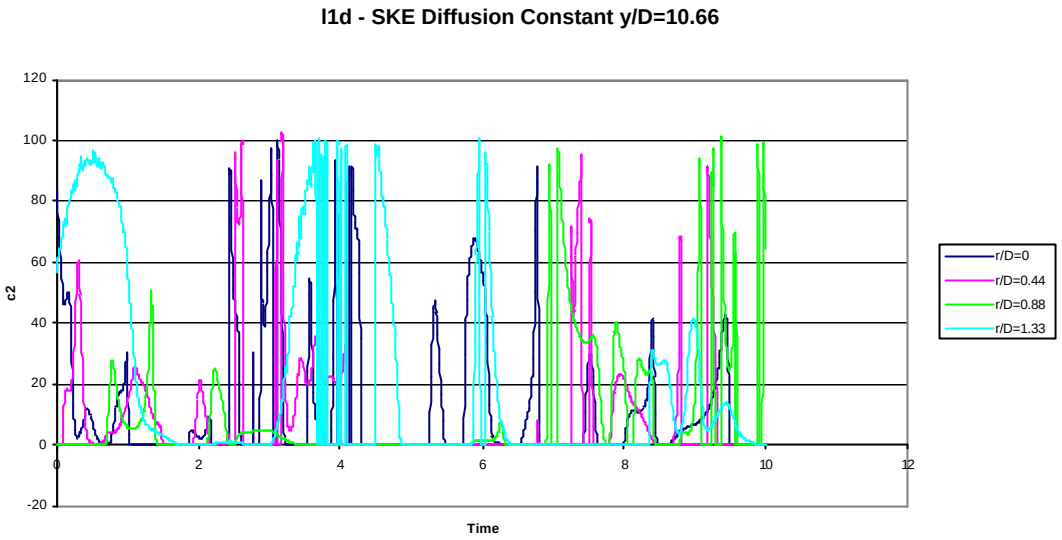

Figure 8.3.24 Subgrid kinetic energy equation diffusion constant time histories at different radii for l1d, LDM with dynamic SKE constants stress, static SGDH flux models.

8.4 Dynamic Mixed Models

Two simulations have been carried out with dynamic mixed models. The simulations are labelled:
d1n: no subgrid models
d1f: dynamic Smagorinsky stress model and static SGDH flux model
d1m: dynamic mixed Smagorinsky and Bardina stress model and SGDH flux model
d2m: dynamic mixed Smagorinsky and Bardina stress model and dynamic mixed SGDH and Bardina flux model
Similarly to the static mixed model simulations, the second formulations were used, halving each models contribution to the mix. The whole turbulent viscosity is passed to the flux routine in order to evaluate the SGDH component wholly for d1m or in half for d2m.

The dynamic mixed models are shown to be the best models for this test domain and parameters. The transition rate is improved and the eddy component maintains a significant value. The eddy component in the flux model also has a significant value also, which it does not in the dynamic Smagorinsky/dynamic SGDH case, d2f. The structure components are still found to be the dominant terms, however.

The velocity profiles are plotted in fig. 8.4.1, against d1n, without a subgrid model, and d1f, the dynamic Smagorinsky, static SGDH simulation. The static mixed model simulations showed very similar decays for both the velocity and temperature decays when plotted against d1n. Earlier transition is shown for both the d1m and d2m simulations. This transition occurs at the same point, although d1m is then more dissipative. In the static model simulations the effects of the eddy and structure components on transition counterbalanced each other, whereas the dynamic procedure has reduced the eddy components contribution in the laminar region, as it does for the dynamic Smagorinsky model in d1f. Fig. 8.4.2 gives the temperature centrelines, which also show the early transition of the mixed model simulations followed by less dissipation.
Fig. 8.4.3 shows plots from d1m of the main stress averages in the vertical momentum equation in the X-axis – T22 and T23. The eddy components and structure

components are also plotted, and show that in both cases the eddy and structure components follow the same qualitative behaviour. Fig. 8.4.4 shows the T33 plot, which, similarly to the static mixed models, gives opposite signs for the eddy and structure components. The eddy component (still) breaks the realizability conditions.

A snapshot of the Smagorinsky component constant and the average are given in fig. 8.4.5. With the Bardina model representing the Leonard and Cross terms, those where backscatter mainly occurs, the expectation is that there will be less clipped values for the Smagorinsky component which only represents the Reynolds terms in the mixed model. The average is qualitatively the same as it is for d1f, with the same erratic values at the boundaries which do not affect the flow, but the magnitude is higher. This suggests either higher values when the constant is not clipped, or that the expectation of fewer clipped points is validated. The dynamic SGDH model constant, fig. 8.4.6, is much more clipped than the stress model. Table 8.4.1 below shows the percentages of the points not clipped along the centreline (percentages evaluated over 10,000 time steps). The proportion of non-clipped stress model constants is not significantly affected by the inclusion of the Bardina component in the turbulent region, although it is reduced in the transient region. The inclusion of the Bardina model in the flux model has significantly reduced the number of non-clipped values, but manages to maintain significant average values for the eddy component of the fluxes.

	d2f		d1m	d2m	
y/D	C	C_SGDH	C	C	C_SGDH
7.11	66%	50%	63%	61%	36%
10.66	68%	57%	72%	68%	30%

Table 8.4.1 Percentage of dynamically evaluated constants not clipped.

The temperature fluxes, EN2, and EN3, with their component parts are shown in fig. 8.4.7. The separate components are shown to be qualitatively the same.

Figs. 8.4.8-8.4.10 show the turbulent viscosity centrelines, the Smagorinsky component constant centrelines, and the T22 eddy component centrelines respectively. The turbulent viscosities can be seen to be almost double, for the mixed model simulations, what they are for the dynamic Smagorinsky. This is due to an

almost doubled constant. The T22 eddy centreline shows the eddy components to be almost equal in the fully developed turbulent region. This indicates that the dynamic procedure has 'overridden' the halving of the eddy component, and ensured that the dissipation is at that magnitude. This also indicates that the Bardina model is not dissipative, even though most of the models averages are qualitatively the same and of a similar or greater magnitude than the dissipative part. However, during transition, d1f has a larger peak value, even though this is not the case for the constant or the turbulent viscosity. The effect of the Bardina components on the flow field could be the explanation for this.

The T22 centrelines are shown in fig. 8.4.11, and show the mixed models to be significantly larger. Fig. 8.4.12 shows the profiles of T22 and its components, from d1m, and shows that the structure component is the dominant term. The T11 component profiles are shown in fig. 8.4.13, showing these terms to be opposite in sign, and again that the structure component is much larger. In T12, fig. 8.4.14, the eddy and structure components are less dissimilar in magnitude, although the structure term is still the greater. This is the contributing term to the momentum spread, and is much less than the Bardina components contribution to the normal component, T22, in which the effect is to stretch the plume, which lessens the spread. The Bardina model stretches the plume more than it spreads the plume.

The EN2 centrelines are plotted in fig. 8.4.15, and show that the Bardina component term is again much stronger. Also though, the increase in static SGDH model value can be seen, between d1m and d1f, to be related to the increased turbulent viscosity. The components are shown for d2m in fig. 8.4.16, and confirm that the Bardina component is the dominant term. Fig. 8.4.17 shows the profiles.

An interesting aside demonstrating the sensitivity of the formulation of the Bardina model is added here relating to the EN2 centreline plot. A simulation was accidentally run with the Bardina model calculated as

$$q_j = \overline{\overline{u}_j \overline{\overline{T}}} - \overline{\overline{u}}_j \overline{\overline{T}} \qquad (8.4.1)$$

Including the extra filter for the temperature multiple in the first term on the rhs of 8.4.1 changed the large positive Bardina component in the transition region of EN2,

fig. 8.4.15, to a large negative component, although in the developed flow region it was still positive. The two radial fluxes retained their qualitative behaviour.
This suggests that the choice of filter and formulation could have significant consequences on the model, in certain regions of the flow.

Finally, fig. 8.4.18 shows the radial flux, EN1, and shows that the magnitudes of the eddy and structure components are equal. More strongly than for the momentum this indicates that the stretching induced by the structure term of EN2 is greater than the spread caused by the structure term of EN1.

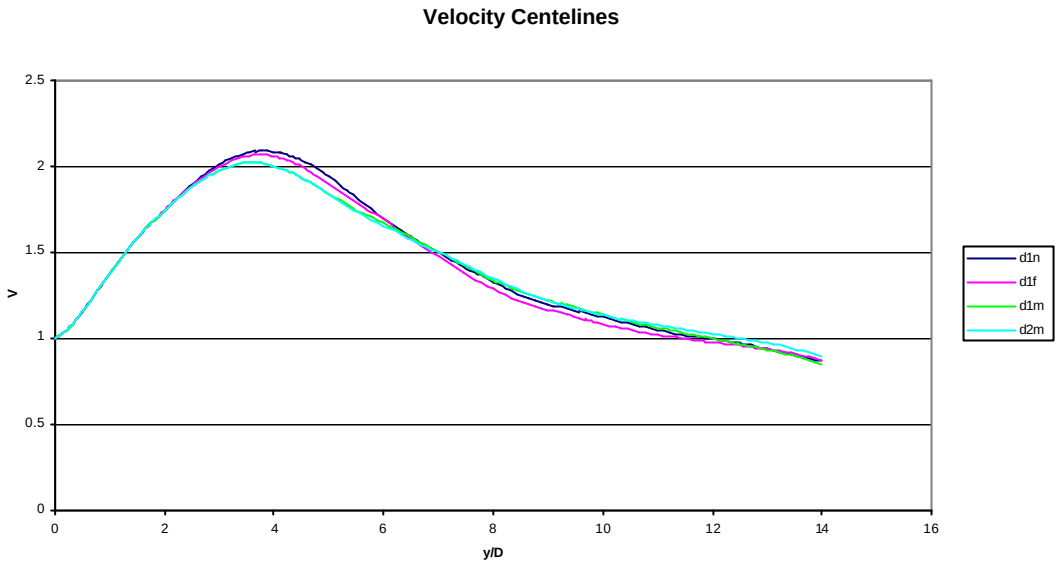

Figure 8.4.1 Velocity centrelines for d1n, no subgrid models, d1f, dynamic Smagorinsky stress and static SGDH flux models, d1m, dynamic Smagorinsky/ Bardina stress and static SGDH flux models, d2m, dynamic Smagorinsky/ Bardina stress and dynamic SGDH/ Bardina flux models.

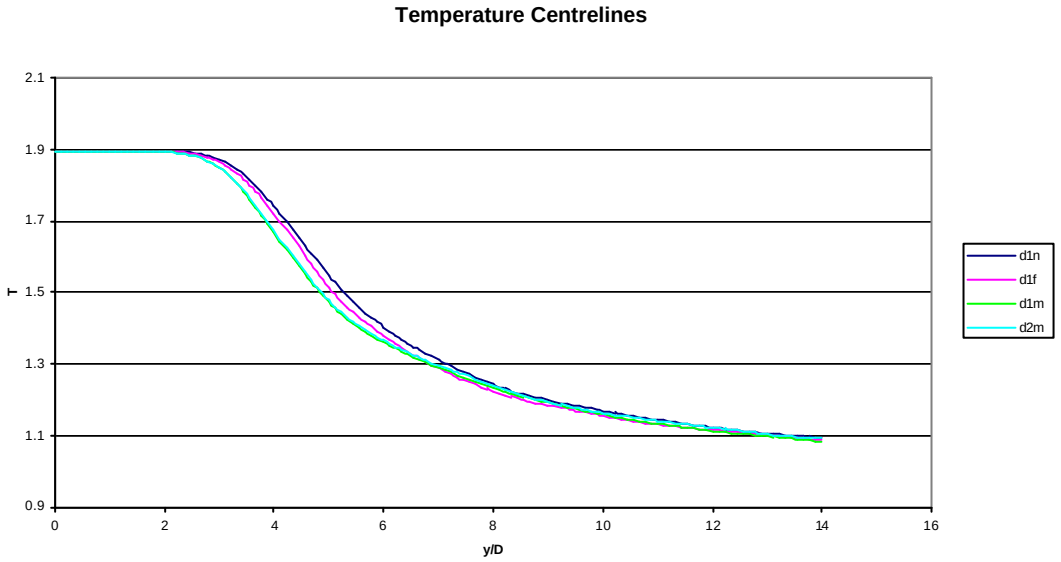

Figure 8.4.2 Temperature centrelines for d1n, no subgrid models, d1f, dynamic Smagorinsky stress and static SGDH flux models, d1m, dynamic Smagorinsky/ Bardina stress and static SGDH flux models, d2m, dynamic Smagorinsky/ Bardina stress and dynamic SGDH/ Bardina flux models.

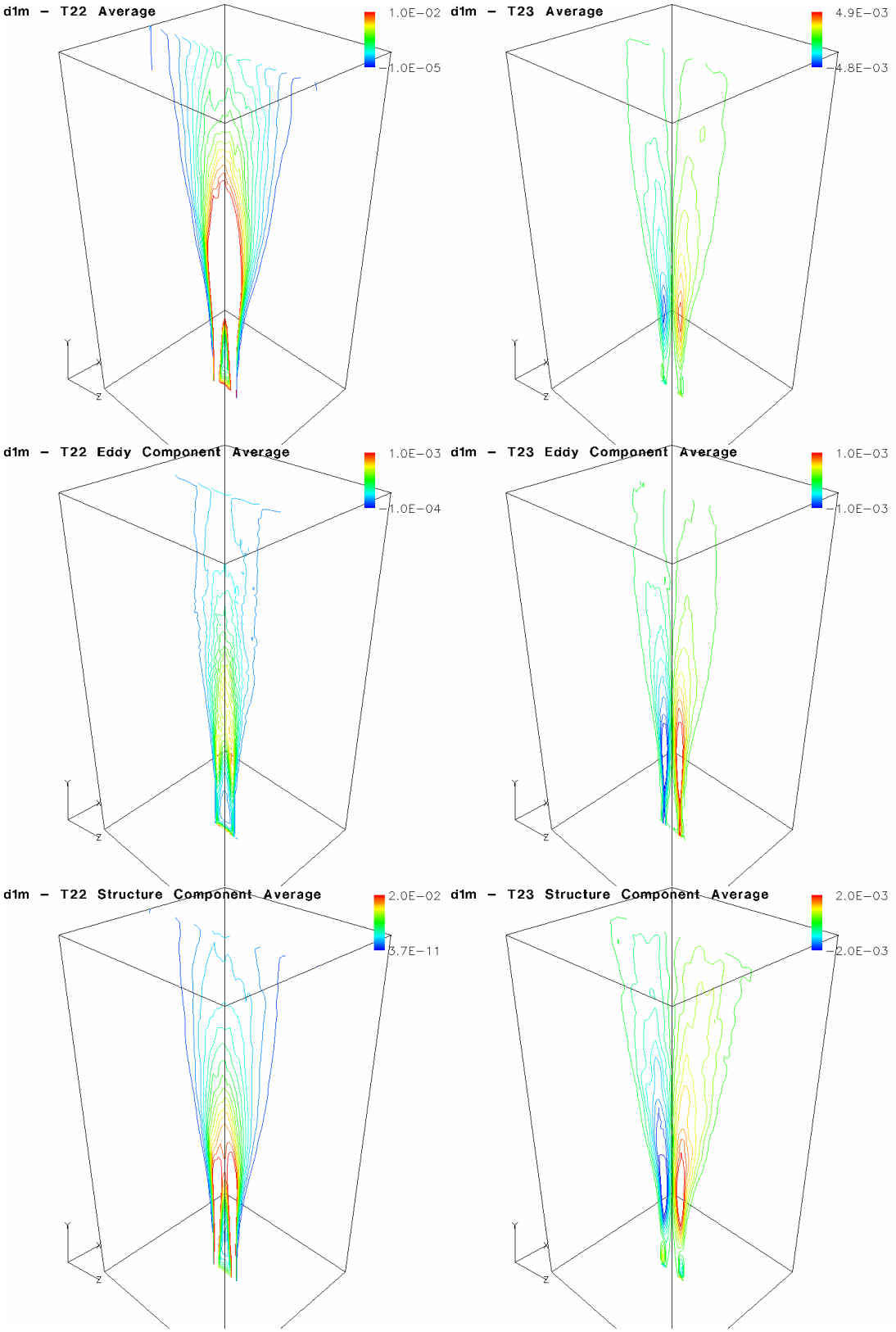

Fig. 8.4.3 Stress and component averages for T22 and T23 for d1m, dynamic Smagorinsky/ Bardina stress and static SGDH flux models.

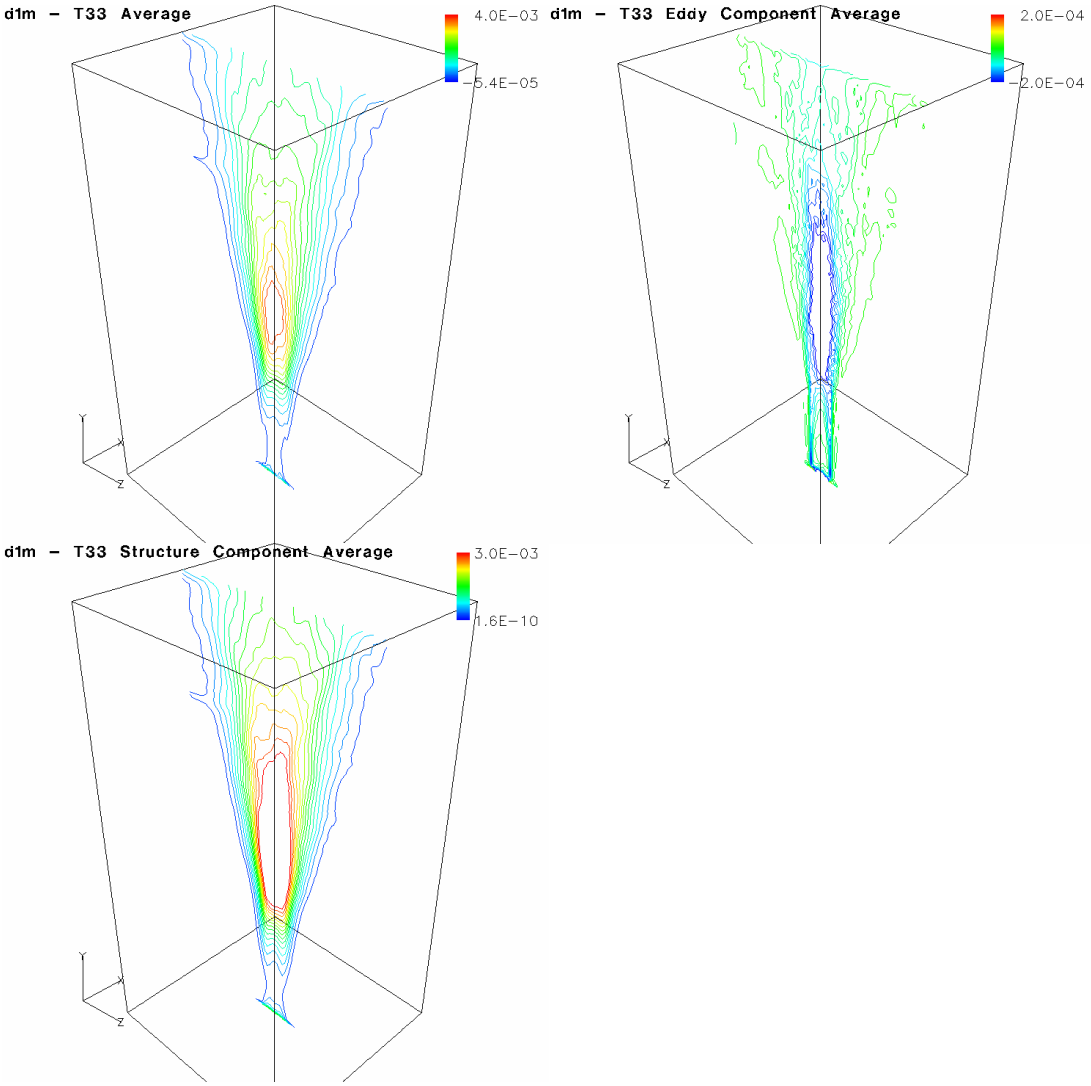

Fig. 8.4.4 Stress and component averages for T33 for d1m, dynamic Smagorinsky/ Bardina stress and static SGDH flux models.

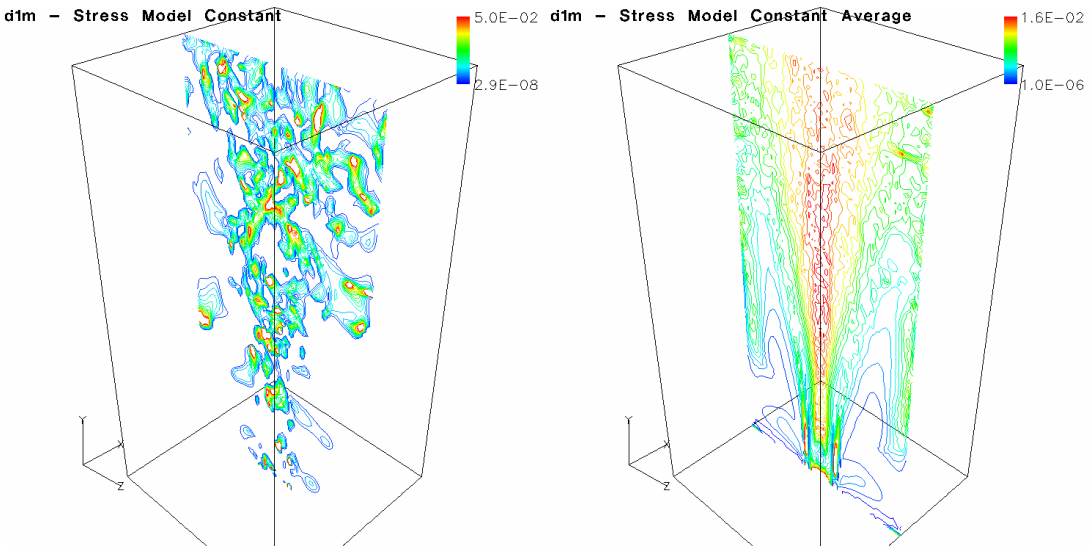

Figure 8.4.5 Instantaneous and average stress constant, for d1m, dynamic Smagorinsky/ Bardina stress and static SGDH flux models.

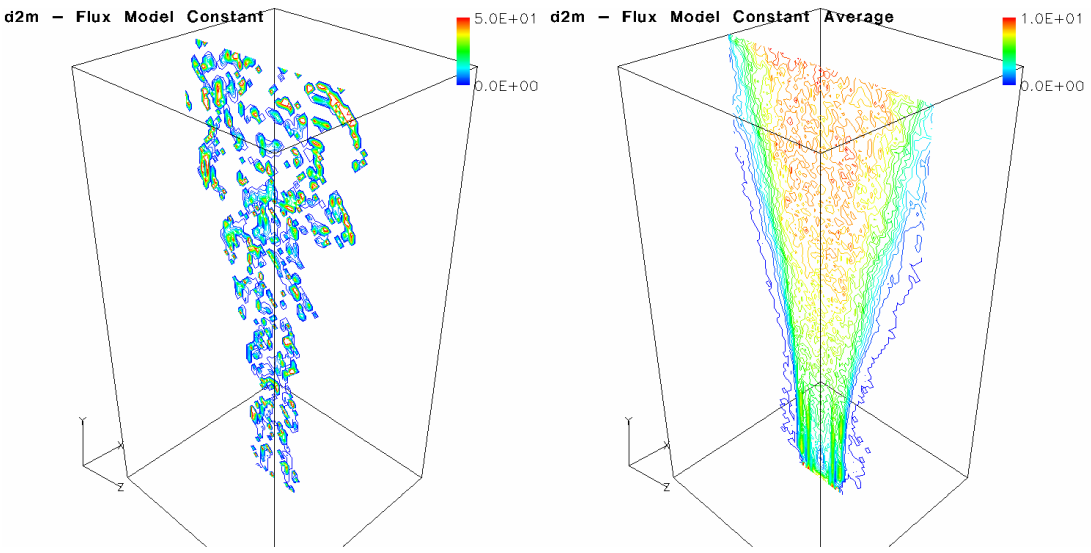

Figure 8.4.6 Instantaneous and average stress constant, for d2m, dynamic Smagorinsky/ Bardina stress and dynamic SGDH/Bardina flux models.

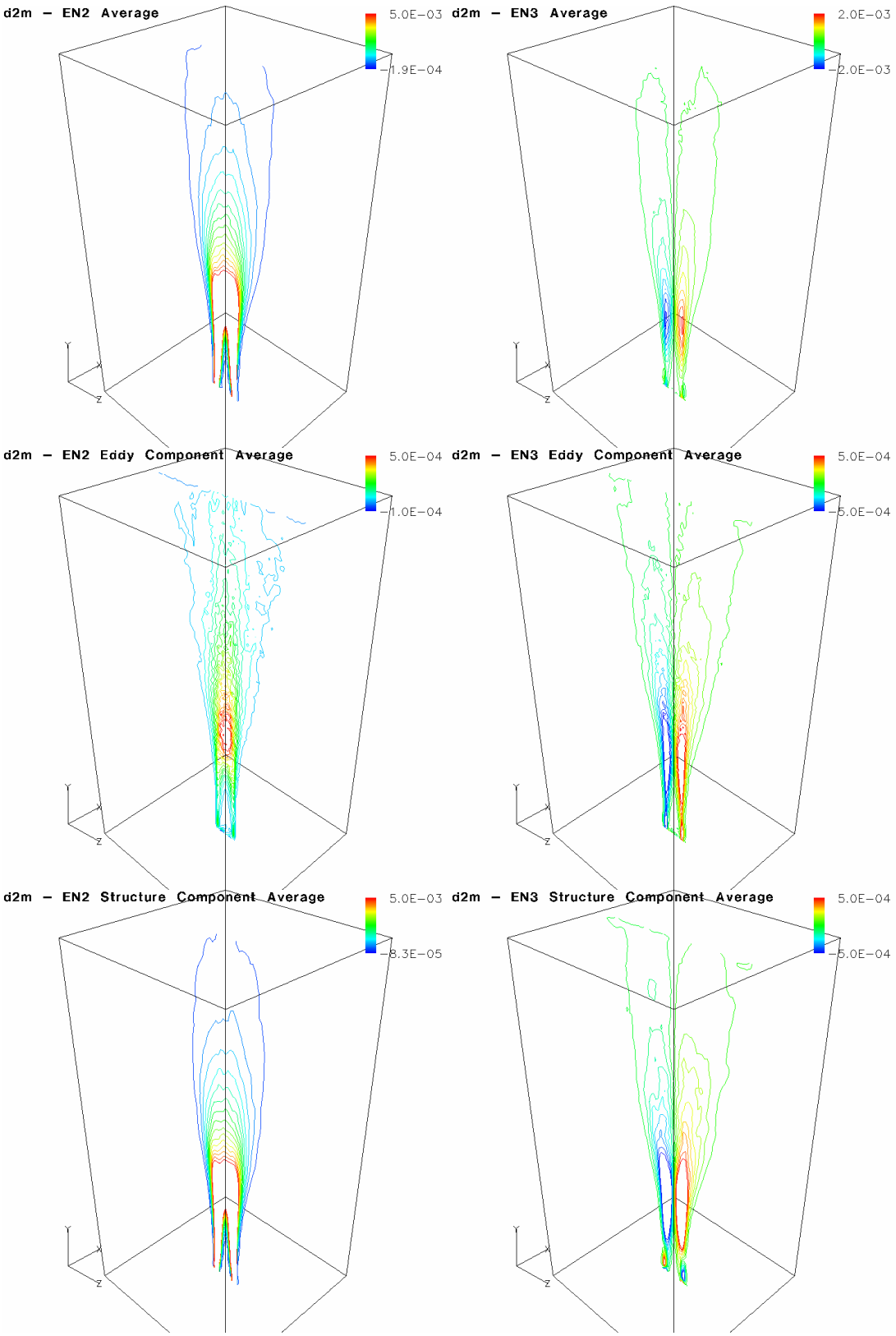

Fig. 8.4.7 Flux model and component averages for EN2, EN3, for d1m, dynamic Smagorinsky/ Bardina stress and static SGDH flux models

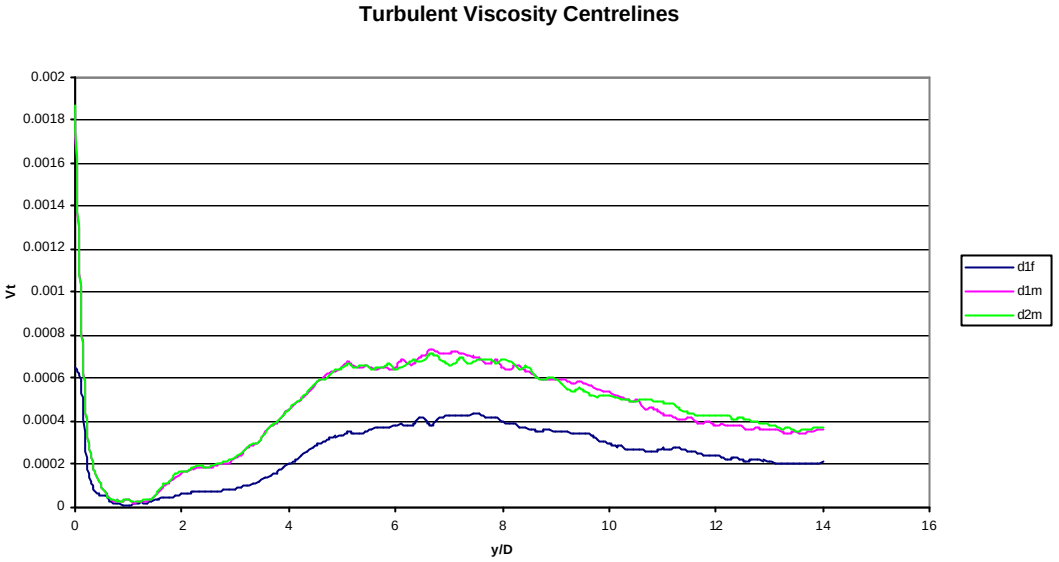

Figure 8.4.8 Turbulent viscosity centrelines d1f, dynamic Smagorinsky stress and static SGDH flux models, d1m, dynamic Smagorinsky/ Bardina stress and static SGDH flux models, d2m, dynamic Smagorinsky/ Bardina stress and dynamic SGDH/ Bardina flux models.

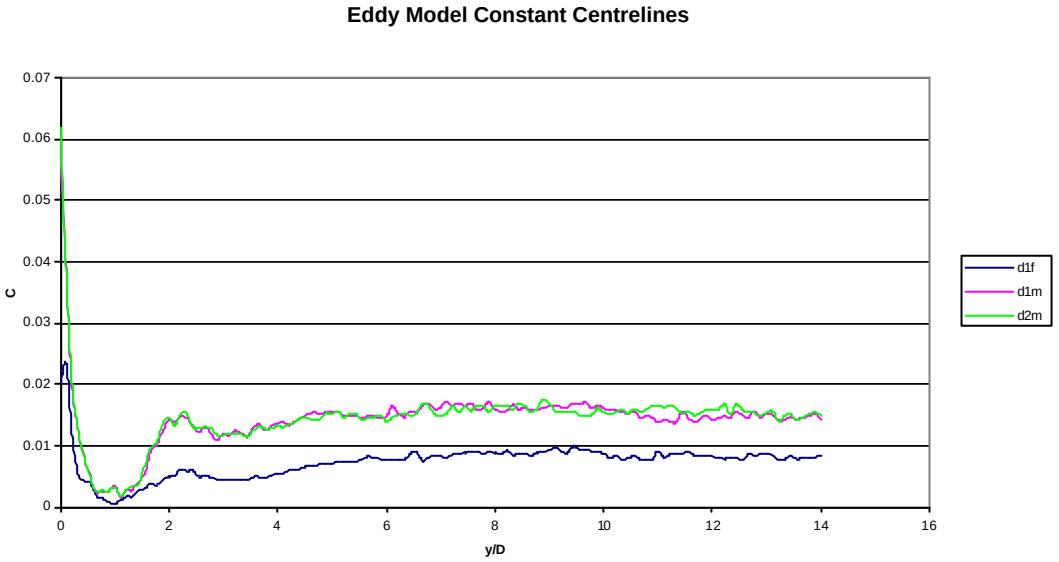

Figure 8.4.9 Eddy model constant centrelines for d1f, dynamic Smagorinsky stress and static SGDH flux models, d1m, dynamic Smagorinsky/ Bardina stress and static SGDH flux models, d2m, dynamic Smagorinsky/ Bardina stress and dynamic SGDH/ Bardina flux models.

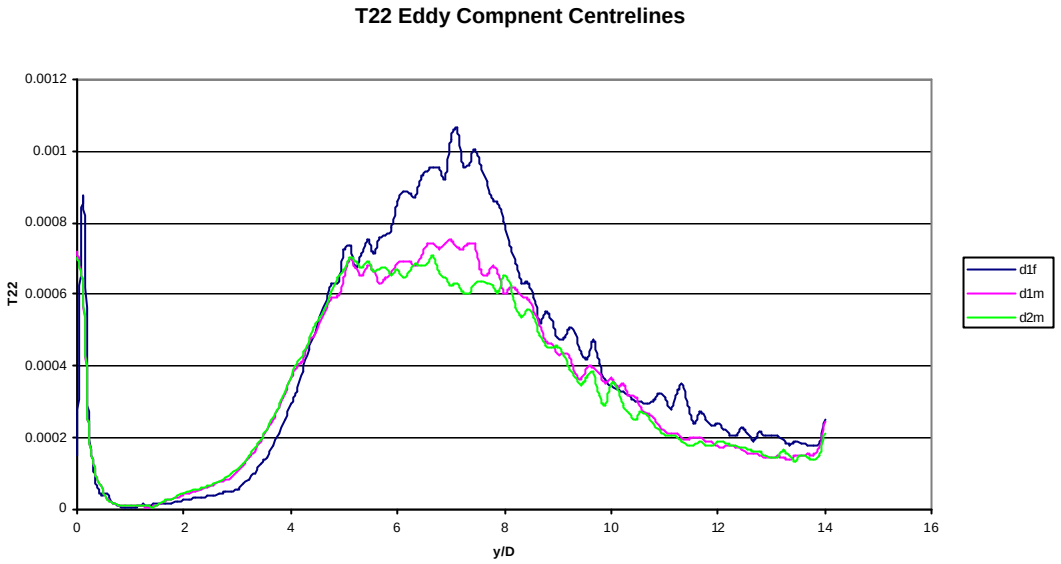

Figure 8.4.10 T22 Eddy Components for d1f, dynamic Smagorinsky stress and static SGDH flux models, d1m, dynamic Smagorinsky/ Bardina stress and static SGDH flux models, d2m, dynamic Smagorinsky/ Bardina stress and dynamic SGDH/ Bardina flux models.

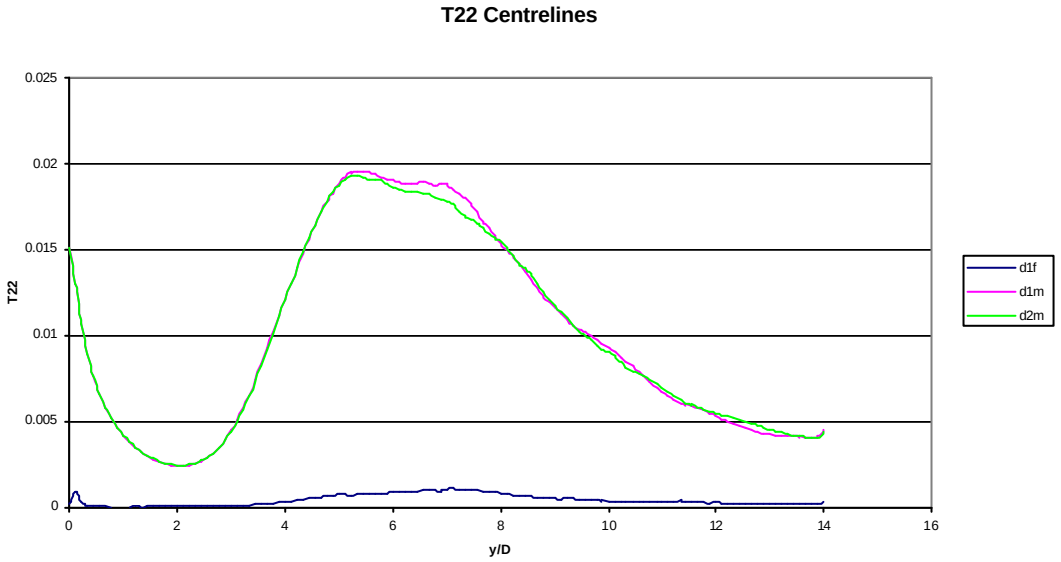

Figure 8.4.11 T22 centrelines d1f, dynamic Smagorinsky stress and static SGDH flux models, d1m, dynamic Smagorinsky/ Bardina stress and static SGDH flux models, d2m, dynamic Smagorinsky/ Bardina stress and dynamic SGDH/ Bardina flux models.

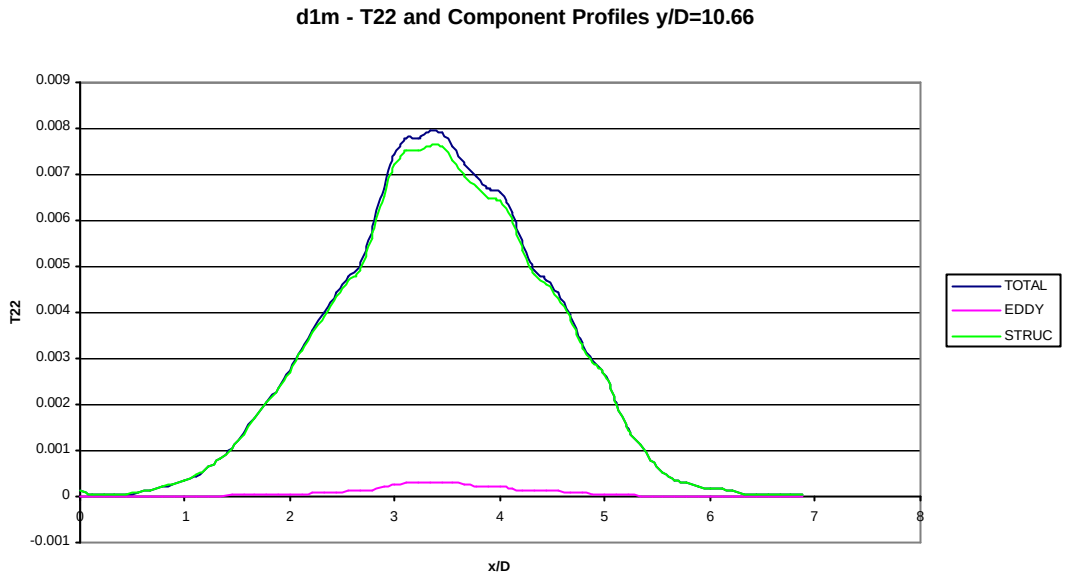

Figure 8.4.12 T22 and component profiles, y/D=10.66, for d1m, dynamic Smagorinsky/ Bardina stress and static SGDH flux models.

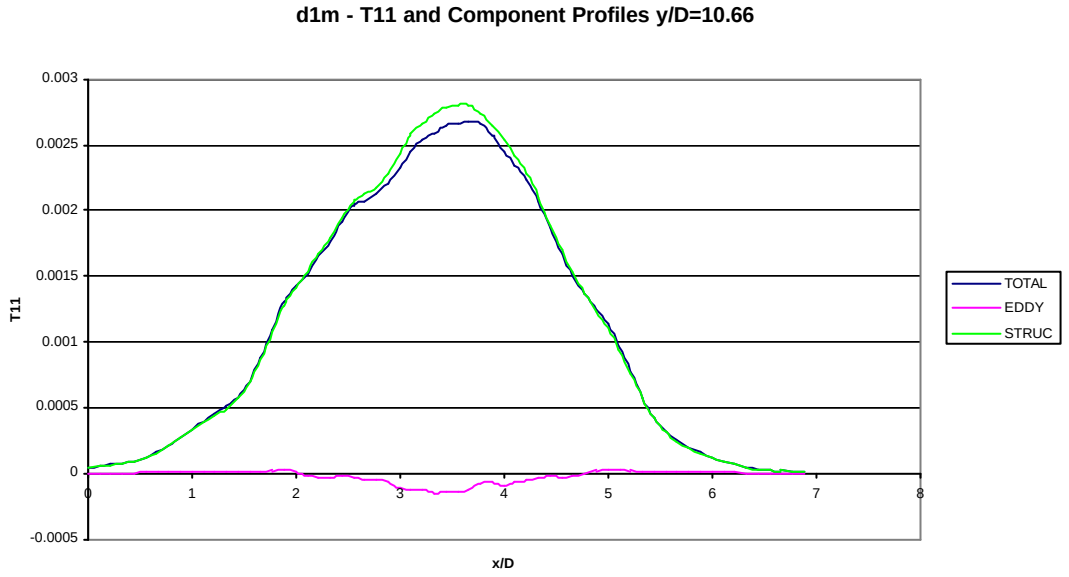

Figure 8.4.13 T11 and component profiles, y/D=10.66, d1m, dynamic Smagorinsky/ Bardina stress and static SGDH flux models.

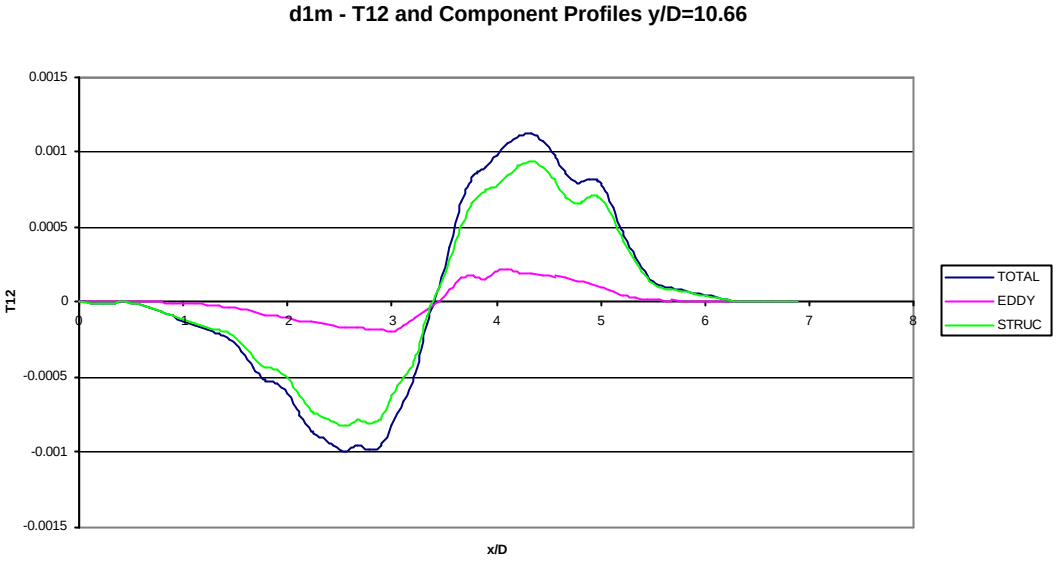

Figure 8.4.14 T12 and component profiles, y/D=10.66, d1m, dynamic Smagorinsky/ Bardina stress and static SGDH flux models.

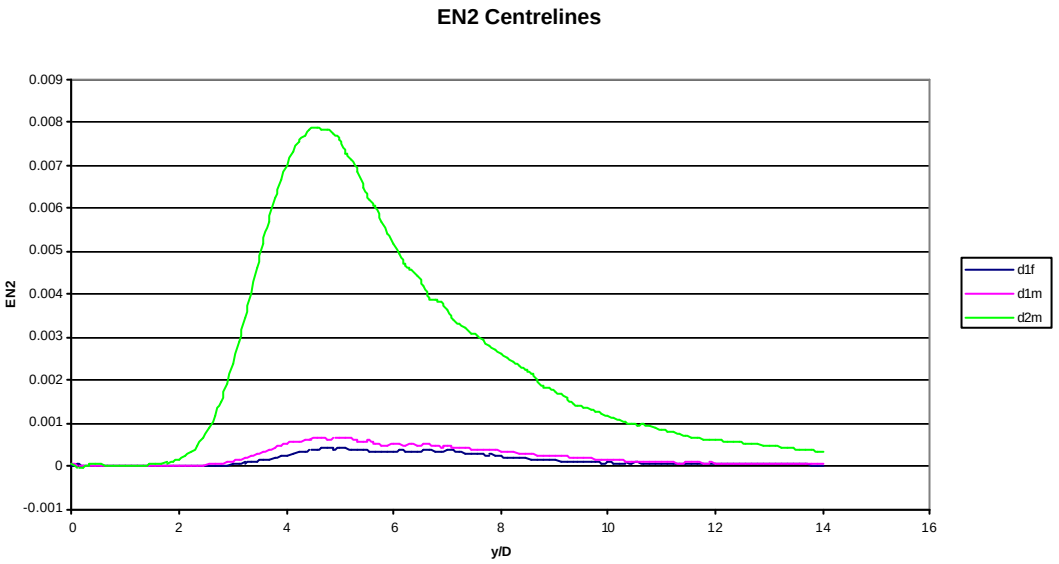

Figure 8.4.15 EN2 centrelines for d1f, dynamic Smagorinsky stress and static SGDH flux models, d1m, dynamic Smagorinsky/ Bardina stress and static SGDH flux models, d2m, dynamic Smagorinsky/ Bardina stress and dynamic SGDH/ Bardina flux models.

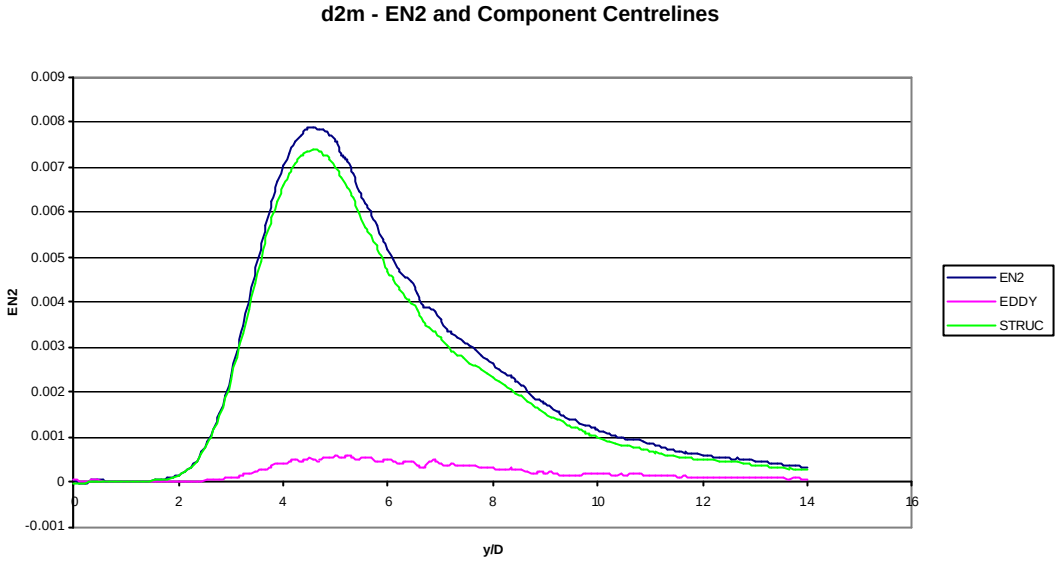

Figure 8.4.16 EN2 and component centrelines for d2m, dynamic Smagorinsky/ Bardina stress and dynamic SGDH/ Bardina flux models.

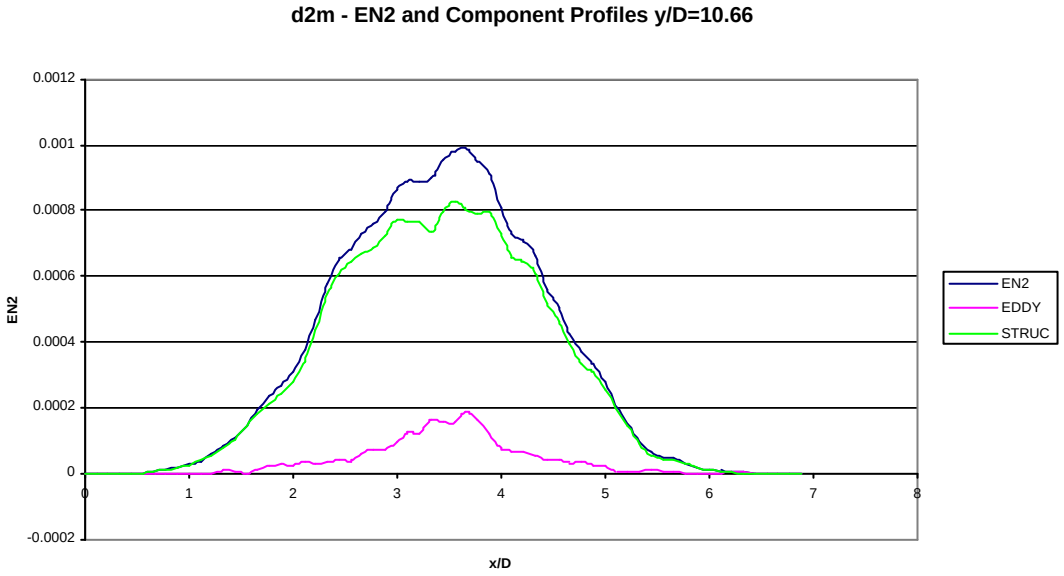

Figure 8.4.17 EN2 and component profiles, y/D=10.66, d2m, dynamic Smagorinsky/ Bardina stress and dynamic SGDH/ Bardina flux models.

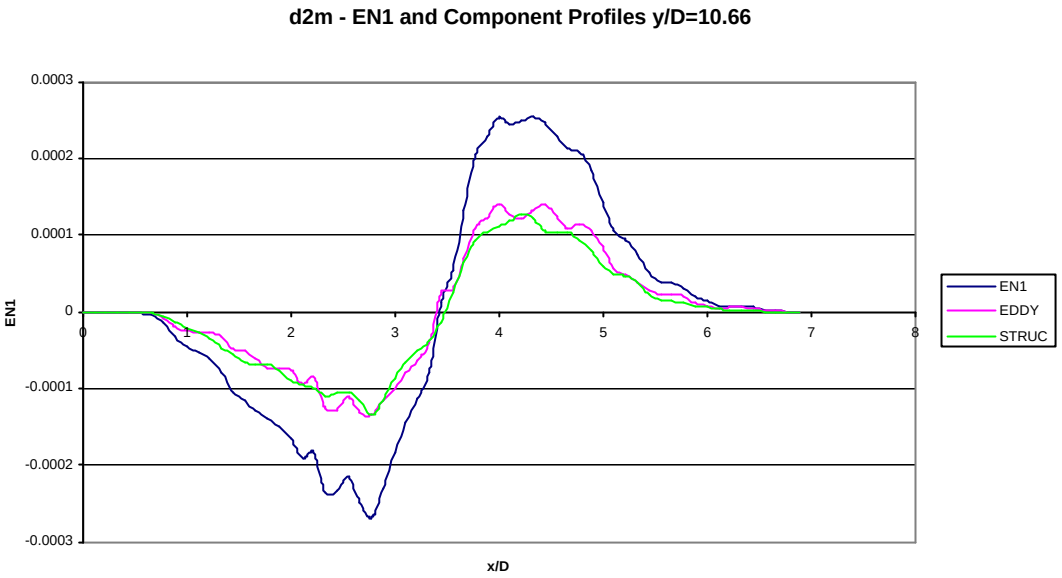

Figure 8.4.18 EN1 and component profiles, y/D=10.66, for d2m, dynamic Smagorinsky/ Bardina stress and dynamic SGDH/ Bardina flux models.

8.5 Summary

The differences between the dynamic model simulation results are much less than for the static models, and are closer to the simulation without a subgrid model, d1n, although there are still discernable and significant differences, mainly concerning transition and the characteristics of the models themselves.

The dynamic Smagorinsky models were shown to be effectively dissipative, although less so than their static counterparts. Behaviour in laminar regions was good; the turbulent viscosity average was low, even though the constant average was high at the boundaries. Importantly, the transition, however inaccurately captured by the scheme as a whole, was not detrimentally affected by the models, unlike the static models, and even aided by the instability caused by clipping and the numerics of the dynamic procedure. Backscatter is not resolved due to the clipping and approximately 30% of the points were clipped for the stress model in the turbulent region. The dynamic flux models gave negligible results. This was not related to the clipping, which had 50% of the points clipped in the turbulent region, but probably connected to the turbulent viscosity being out of synchronisation with the temperature fluctuation levels.

The localised dynamic models are given increased accuracy by the dynamic modelling of the SKE transport terms, but the difference is not sufficient to alter the main flow averages, but this situation is expected to change with non-diffusive numerical schemes. The stress model average constant was found to be 0.02 rather than the theoretical 0.07, and the dynamic modelling of the dissipation constant was well evaluated and found the constant average to be higher than the recommended value. The diffusion term constant was not well described by the dynamic procedure because of numerical sensitivity, and the average is not useful. Again the transition is not adversely affected.

It was shown self-similarity was almost achieved but not entirely, and the large turbulent intensities (the horizontal normal Reynolds stress, and the Reynolds temperature fluctuation) could reflect this, although the dynamic Smagorinsky model simulation gave marginally better values.

Dynamic mixed models with half of each component summed were simulated, and showed the same mixture of behaviour as the static mixed models. The structure components do increase the transition rate, while the dynamic procedure keeps the

eddy component low in the laminar and initially transient regions. The expectation that the dynamic mixed model would decrease the number of clipped points was not achieved, and for the fluxes increased the amount of clipping. Nevertheless, for the stress model, the constant average almost doubles effectively cancelling the halving of the eddy component contrary to Zang et al. (1993) who find the constant reduced, and the average of the eddy component in the flux model becomes a non-negligible value, making the dynamic mixed flux model a considerable improvement over the other dynamic non-mixed flux models.

Chapter 9

Further Simulations

9.1 Introduction

This chapter considers further issues. The simulations in the previous two chapters have been carried out under identical circumstances, including the random noise. The only differences have been in the duration of the averaging process for the static mixed model simulations. Here, simulations are carried out which investigate the effect of the grid coarseness, the numerical scheme, and the Boussinesq assumption in the governing equations, which all impact directly on the results, most surprisingly for the Boussinesq assumption.

9.2 Dynamic Smagorinsky on Coarse Grid Simulation

A coarse grid simulation was carried out to further investigate the dynamic Smagorinsky model model, and to see if the dynamic procedure will be able to handle a coarser grid. The results tell more about the nature of capturing transition numerically than they do about the dynamic Smagorinsky model, although there are still useful observations to be made.

The domain is almost twice the size of the previous domains. Five grid points cover the inlet diameter, again totalling one non-dimensional spatial unit. It is 25.4 units high and 12.6 units wide and deep. The grid size remains 63x127x63 points and has the same non-dimensional parameters as those given in chapter 7. The time-step was doubled to 0.024, keeping the CFL number almost the same. All other simulation details were kept the same. Importantly, the number of time-steps was kept the same, and the averaging process is carried out between the 5,000th time-step and the 49,000th

time-steps, again, doubling the physical time period over which the averaging was done.
This is labelled f1n. The earlier dynamic Smagorinsky model simulation with, d1f, and the static structure function model simulation, s1f, both with static SGDH flux models, are also plotted for comparison.

Fig. 9.2.1 shows the averaged velocity and temperature. The velocity reaches a higher peak than for d1f (and all the other simulations). Both plots are qualitatively the same, as is expected. Fig. 9.2.2 shows an instantaneous vorticity magnitude plot and an instantaneous temperature plot. These appear to show reduced spread rates, and less detail of the turbulence is captured. The size of the domain, however, is such that there appear to be no eddies which reach the corners of the top boundary. The plots of the instantaneous dynamic Smagorinsky constant in fig. 9.2.3 supports this, although there is still curvature in the flow resulting in some non-zero values outside of the plume core, but notably less than for d1f (fig. 8.2.5). The average plot in the same figure confirms this, showing a significantly reduced average value outside the plume. Inside the plume the distribution is well within the domain, and the edges are far from the corners.

Fig. 9.2.4 shows the velocity centrelines. The f1n simulation peaks at 2.5 at y/D=8, whereas d1f peaks at 2.1 at y/D=4. The maximum velocity found in the earlier simulations, was the static structure function simulation, s1f, which peaks at 2.3, at y/D=5. The decay for f1n appears to be an exaggerated and damped version of that for d1f. The delay in transition is not compensated by a sufficiently increased dissipation rate, which is the case for s1f. The temperature plot in fig. 9.2.5 shows the same relation. Similarly to the discussion in section 7.4, the temperature decay has started sooner for f1n, although it continues to decay much more slowly further on - it takes approximately twice the distance of d1f from the source to reach a magnitude of 1.1.

By the end of the domain, figs 9.2.6 and 9.2.7, show that the turbulent viscosity for f1n has reached a similar value as that of s1f, and that the magnitude of the turbulent stresses, represented by T22, are of a similar value for all three simulations, although somewhat larger for f1n, which should, of course, have more energy in its larger

subgrid scales. It is shown that this similarity only occurs by the end of the domain because the transition has been delayed until this point below.
The model constants are shown in fig. 9.2.8, and show that the coarse grid constant is much higher in the transitional period, but is converging to a value similar to that of d1f by the end of the domain (0.011 for f1n, 0.008 for d1f). This high value in the transition region also contributes to the dissipation, and also delays transition.
Fig. 9.2.9 shows that the EN2 value for f1n reaches a similar but larger value to the other models also by the end of the domain. This and the spectra below show that once transition has been achieved the coarse grid is sufficient for reasonable LES simulations, but that the effect on transition is very significantly detrimental. The normalised (by the centreline velocity) EN1 profiles are given in fig. 9.2.10, and show the magnitude of the f1n flux to be larger than that of d1f.

The TKE and temperature spectra are plotted for f1n in figs. 9.2.11 to 9.2.13 at points y/D=12.8, 19.2, and 25.1 respectively. These are the same number of grid points along the domain as those spectra plotted for the structure function model simulation, s1f in figs. 7.3.12-7.3.14. The breakdown into isotropic turbulence has taken a similar number of grid points. Initially, at y/D=12.8, the vertical fluctuations are much stronger. By y/D=19.2 they are only slightly stronger, and by the top of the domain, at y/D=25.1, isotropic turbulence has been achieved.

The main terms of the f1n vertical velocity centreline balance are plotted with the d1f centreline balances in fig. 9.2.14. The stress terms are still small and are not included. The f1n plot appears to be an elongated version of d1f, but is not. The buoyancy term exactly reflects the temperature distributions (which are not equal when stretched). The magnitudes of the convection components are larger for d1f even though the velocities are less. Again, the finer grid allows sharper gradients, which allow this difference. Even though the spectra were good at the boundary, the curling up of the vertical convection component in this plot and in the other balance plots clearly shows the error introduced by the boundary. This boundary error appears to be dependent on the physical distance from the boundary rather than the number of grid points away. The upturn occurs at about two diameters from the boundary in each case, suggesting that the grid resolution is not problematic at the boundary, although the boundary condition is.

The Smagorinsky constant histories are shown in figs. 9.2.15 and 9.2.16, at y/D=12.8 and y/D=19.2. The plots are taken at identical grid coordinates to the equivalent plots of the histories of the constant from the d2f simulation (for this comparison d2f can be considered the same as d1f) in figs. 8.2.32 and 8.2.34. The plots show the same trends of the magnitude, frequency decreasing further along the radius and the smoothness increasing.

The percentage of non-clipped values are taken along the centrelines and given in table 9.2.1 below. These are measured over 10,000 time steps. The energy spectra showed the corresponding points (f1n at 12.8 and d2f at 7.11, or f1n at 19.2 and d2f at 9.66) to be in a similar state of turbulence, although these results indicate that f1n is further behind with only 52% unclipped cells. It appears as though the centrelines are tending towards an approximately 70% average. Bastiaans (2000) found the constant to be clipped or a negligible quantity almost everywhere. These results indicate that the level of backscatter remains the same at different grid sizes (in the turbulent region).

y/D	f1n	y/D	d2f
12.8	52%	7.11	64%
19.2	66%	9.66	68%

Table 9.2.1 Percentage of non-clipped Smagorinsky constants

While the comparison between the effect of the models in d1f and s1f is direct, the comparison between d1f or s1f and f1n is not. The hope that the difference between the models would be highlighted from this simulation is not rewarded. The transition period has become the dominant period of the flow, and it has become apparent that the very major changes in quantitative behaviour, is less to do with the LES model and more to do with the grid spacing.

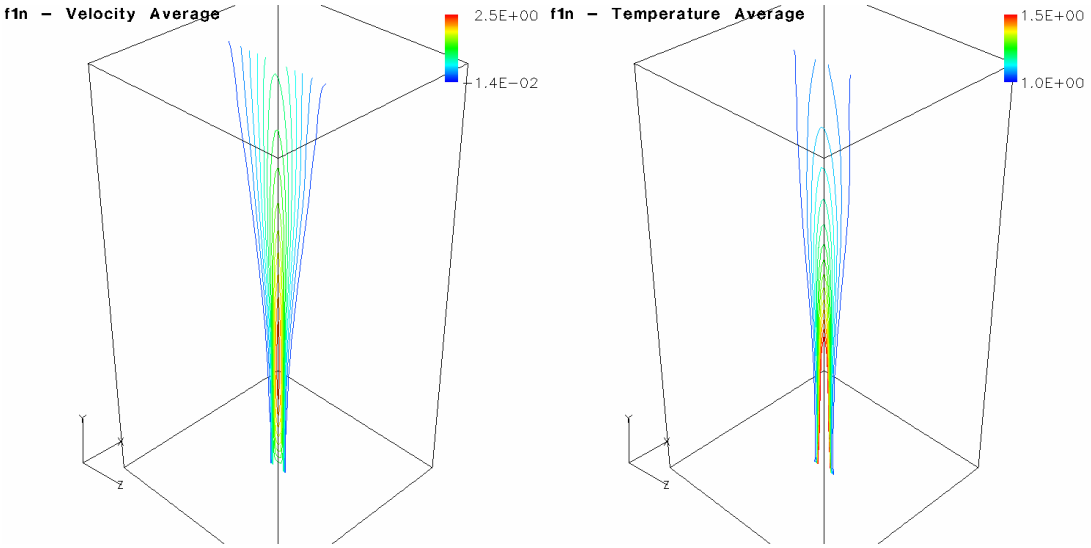

Figure 9.2.1 Vertical velocity and temperature averages for f1n.

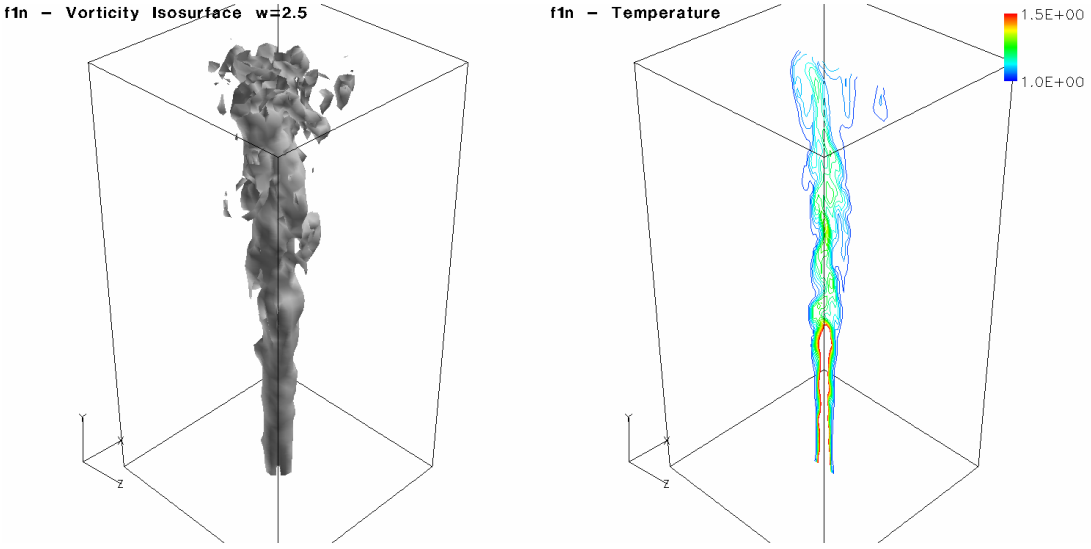

Figure 9.2.2 Instantaneous vorticity isosurface and temperature plots for f1n.

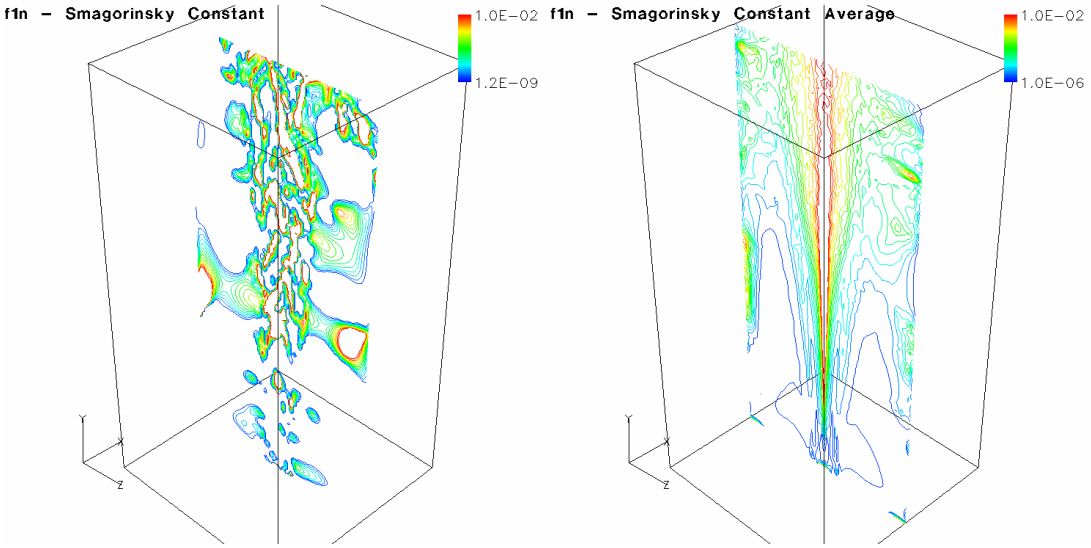

Figure 9.3.3 Instantaneous and average Smagorinsky constant averages for f1n.

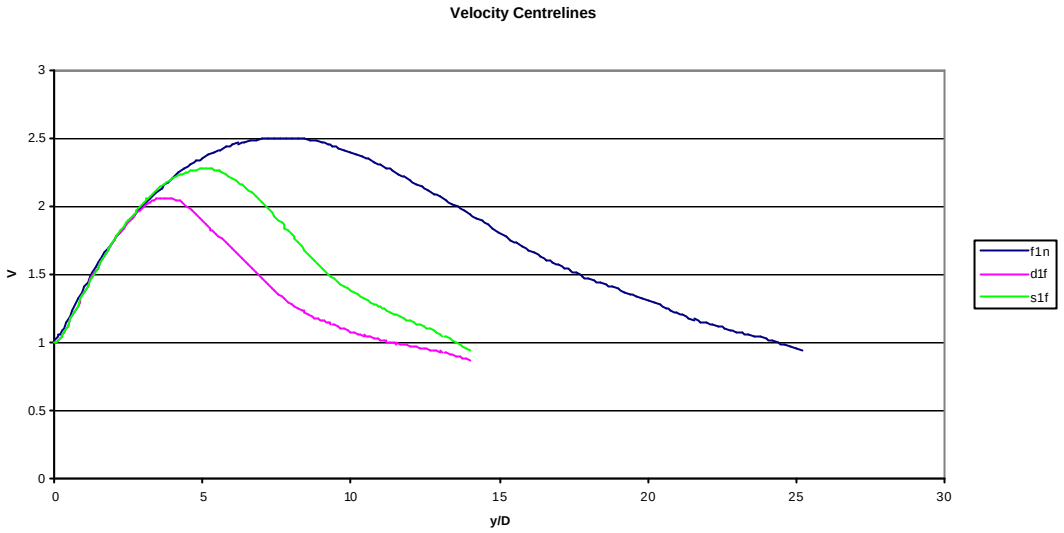

Figure 9.2.4 Vertical velocity centrelines for f1n, dynamic Smagorinsky stress and static SGDH flux models, d1f, dynamic Smagorinsky stress and static SGDH flux models, s1f, static structure function stress and static SGDH flux models.

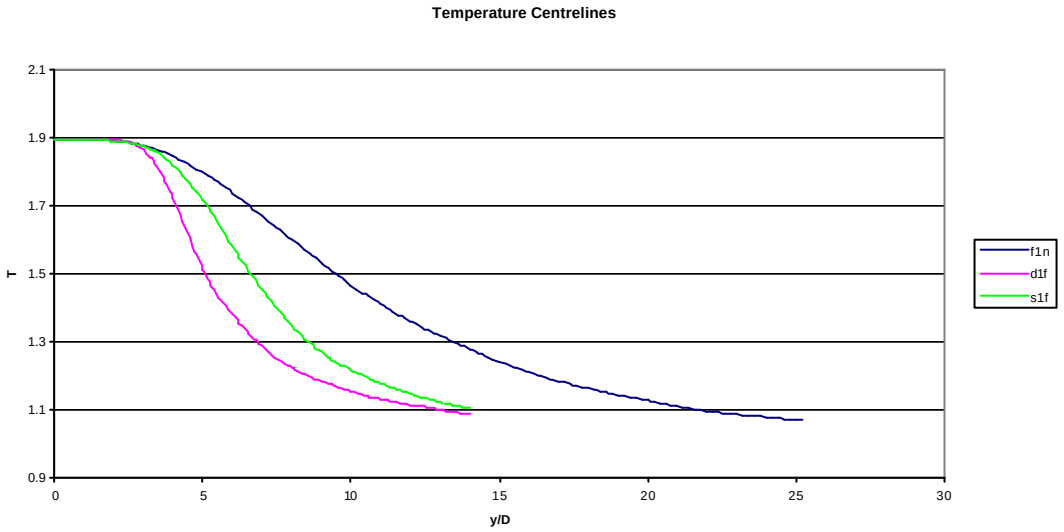

Figure 9.2.5 Temperature centrelines for f1n, dynamic Smagorinsky stress and static SGDH flux models, d1f, dynamic Smagorinsky stress and static SGDH flux models, s1f, static structure function stress and static SGDH flux models.

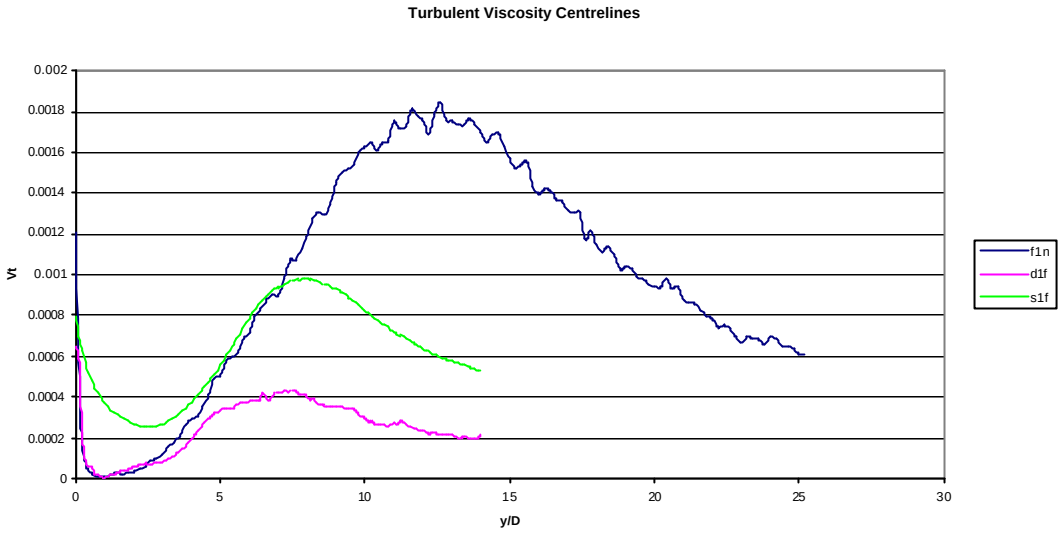

Figure 9.2.6 Turbulent viscosity centrelines for f1n, dynamic Smagorinsky stress and static SGDH flux models, d1f, dynamic Smagorinsky stress and static SGDH flux models, s1f, static structure function stress and static SGDH flux models.

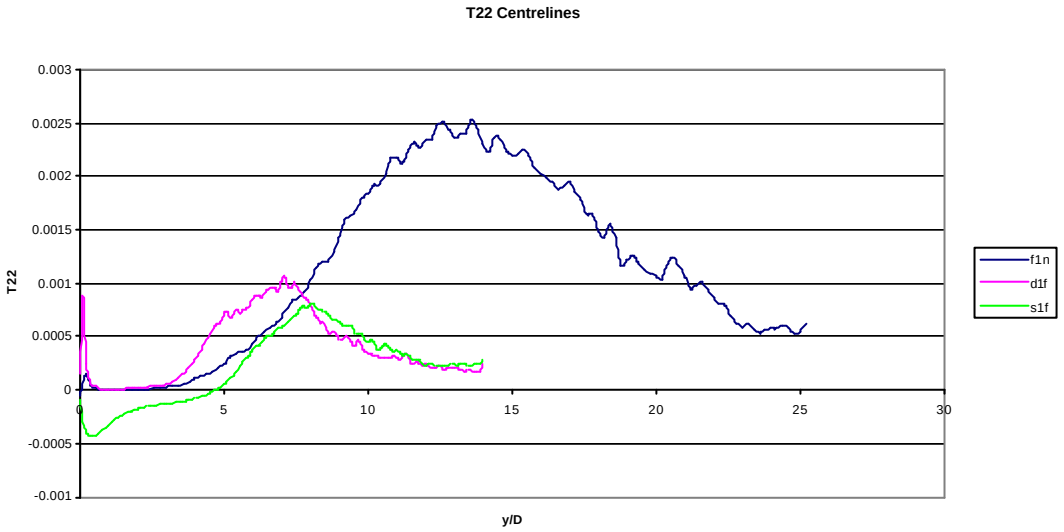

Figure 9.2.7 T22 centrelines for f1n, dynamic Smagorinsky stress and static SGDH flux models, d1f, dynamic Smagorinsky stress and static SGDH flux models, s1f, static structure function stress and static SGDH flux models.

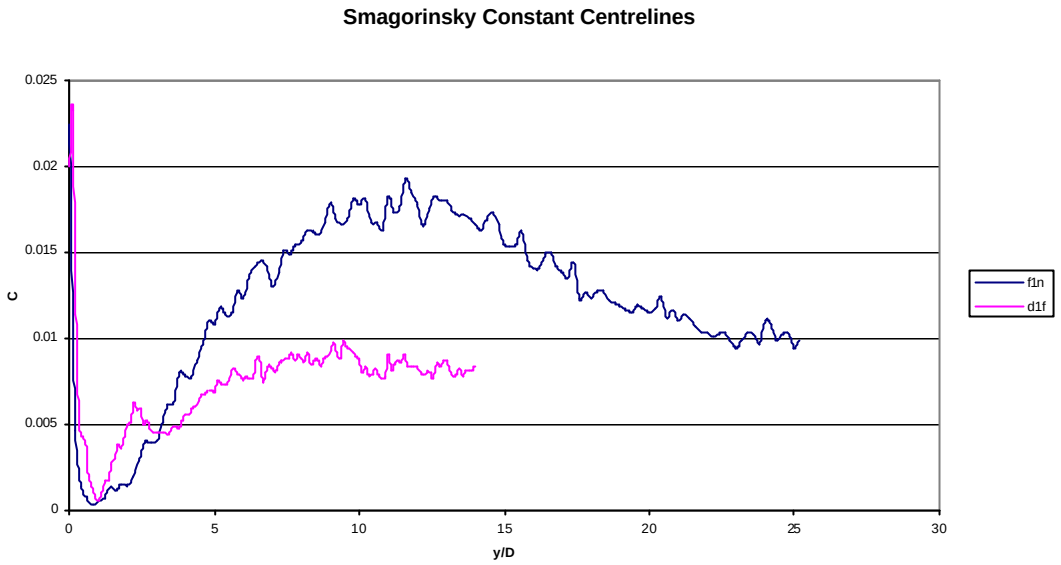

Figure 9.2.8 Smagorinsky constant centrelines for f1n, dynamic Smagorinsky stress and static SGDH flux models, d1f, dynamic Smagorinsky stress and static SGDH flux models.

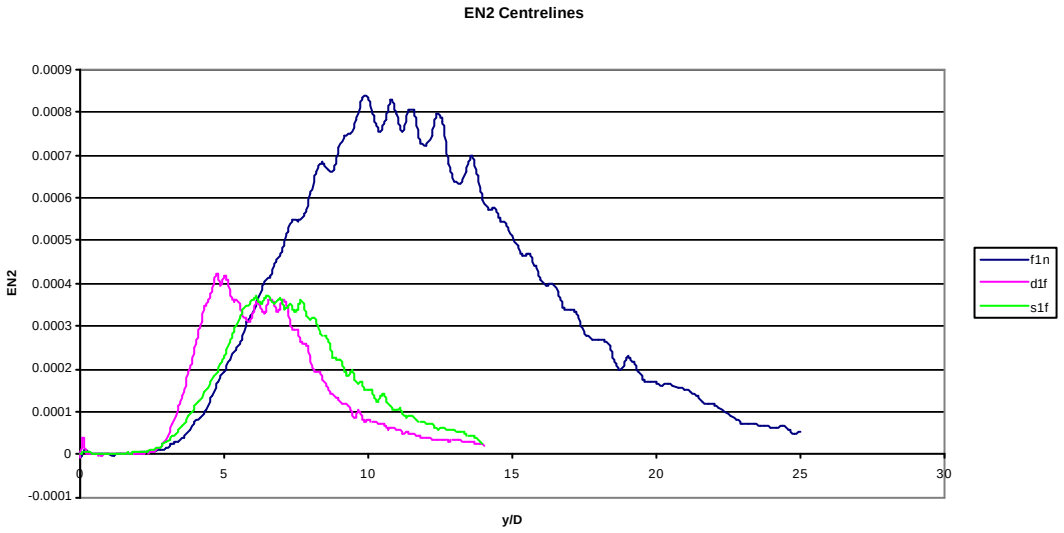

Figure 9.2.9 Vertical flux, EN2, centrelines for f1n, dynamic Smagorinsky stress and static SGDH flux models, d1f, dynamic Smagorinsky stress and static SGDH flux models, s1f, static structure function and static SGDH flux models.

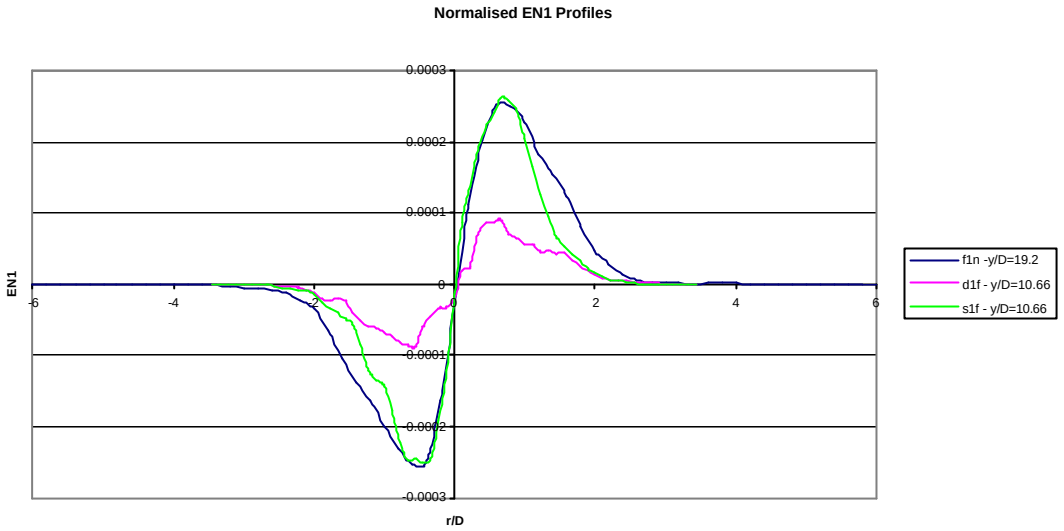

Figure 9.2.10 Normalised radial fluxes, EN1 in the X-axis, for f1n, dynamic Smagorinsky stress and static SGDH flux models, d1f, dynamic Smagorinsky stress and static SGDH flux models, s1f, static structure function stress and static SGDH flux models.

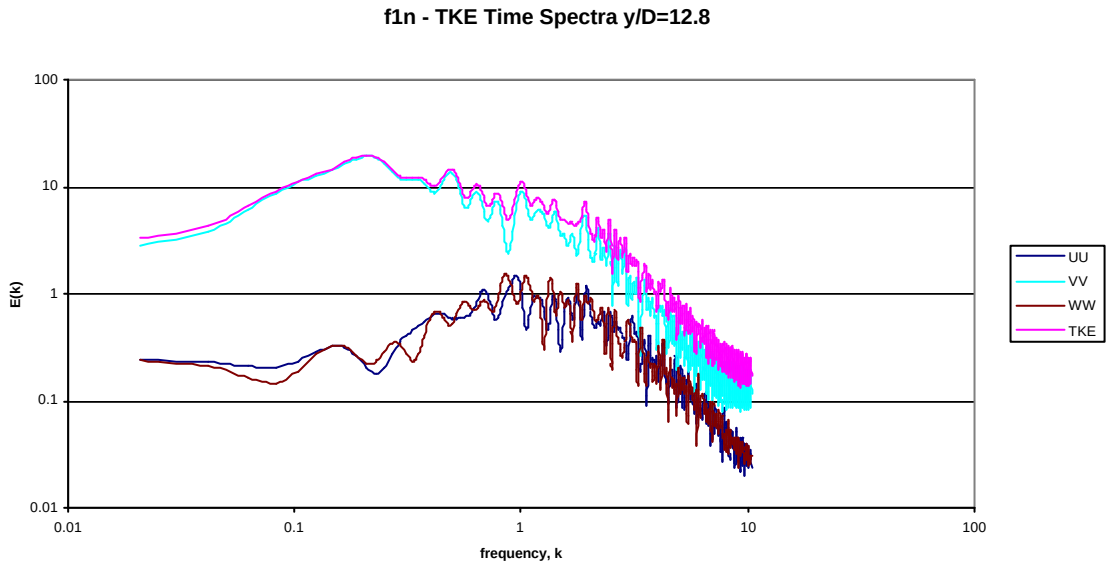

Figure 9.2.11 TKE and component time spectra, y/D=12.8, for f1n, dynamic Smagorinsky stress and static SGDH flux models.

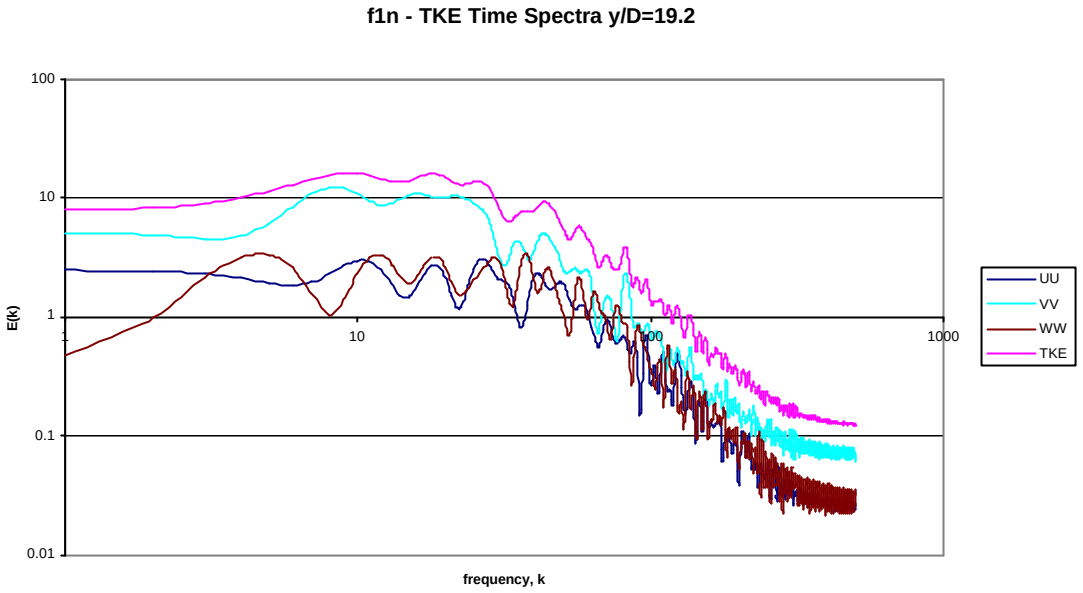

Figure 9.2.12 TKE and component time spectra, y/D=19.2, for f1n dynamic Smagorinsky stress and static SGDH flux models.

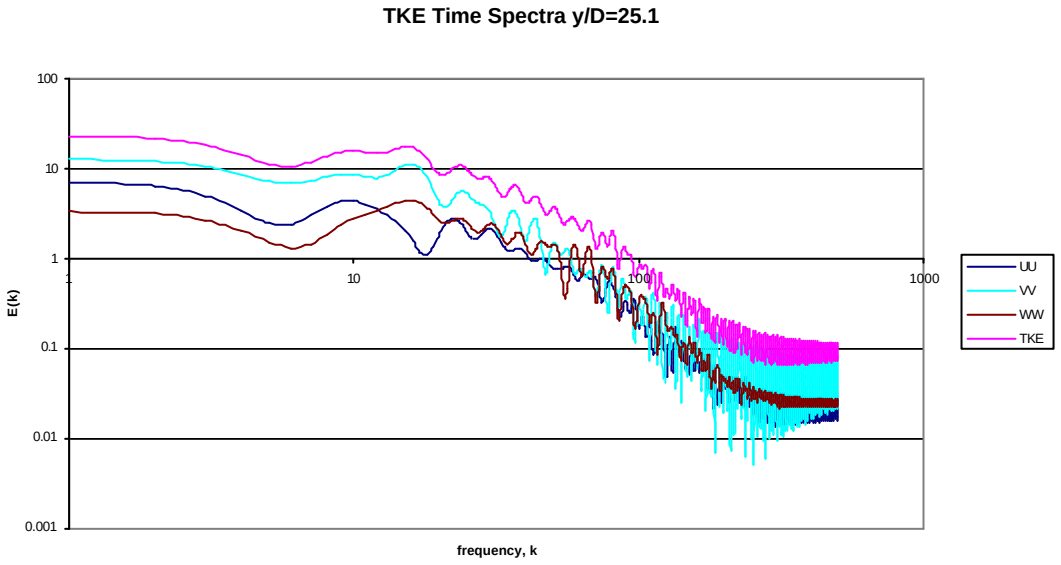

Figure 9.2.13 TKE and component time spectra, y/D=25.1, for f1n, dynamic Smagorinsky stress and static SGDH flux models.

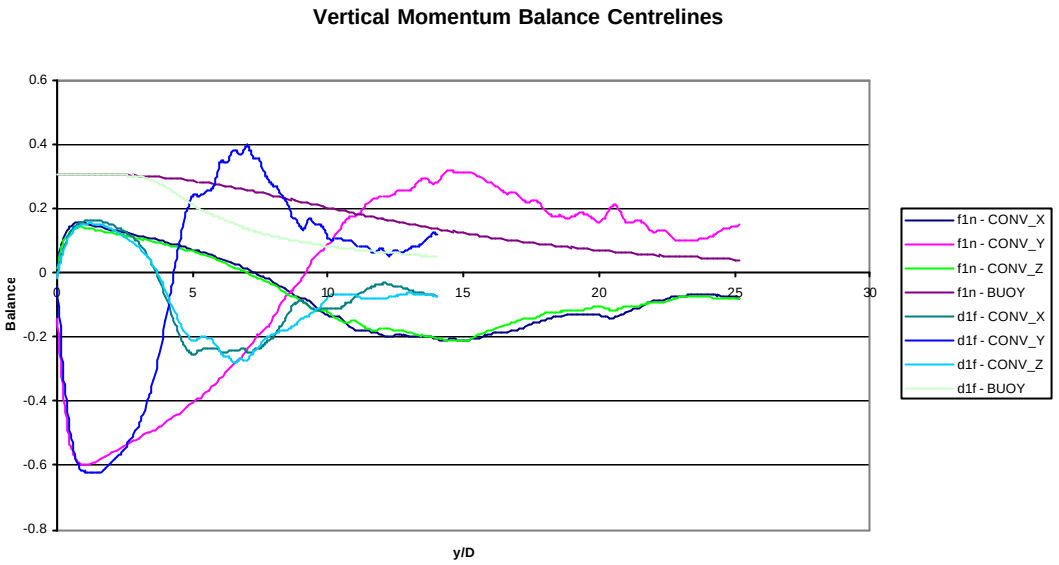

Figure 9.2.14 Vertical Momentum Equation Balance for f1n, dynamic Smagorinsky stress and static SGDH flux models, d1f, dynamic Smagorinsky stress and static SGDH flux models, o1e, static one equation stress and static SGDH flux models.

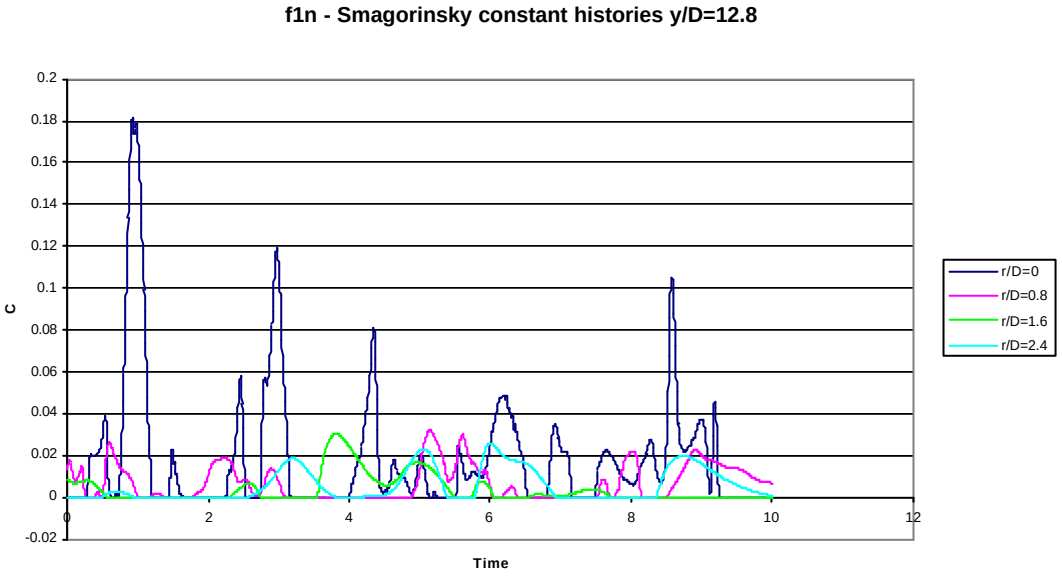

Figure 9.2.15 Smagorinsky constant histories at different radii from the centreline for f1n, dynamic Smagorinsky stress and static SGDH flux models.

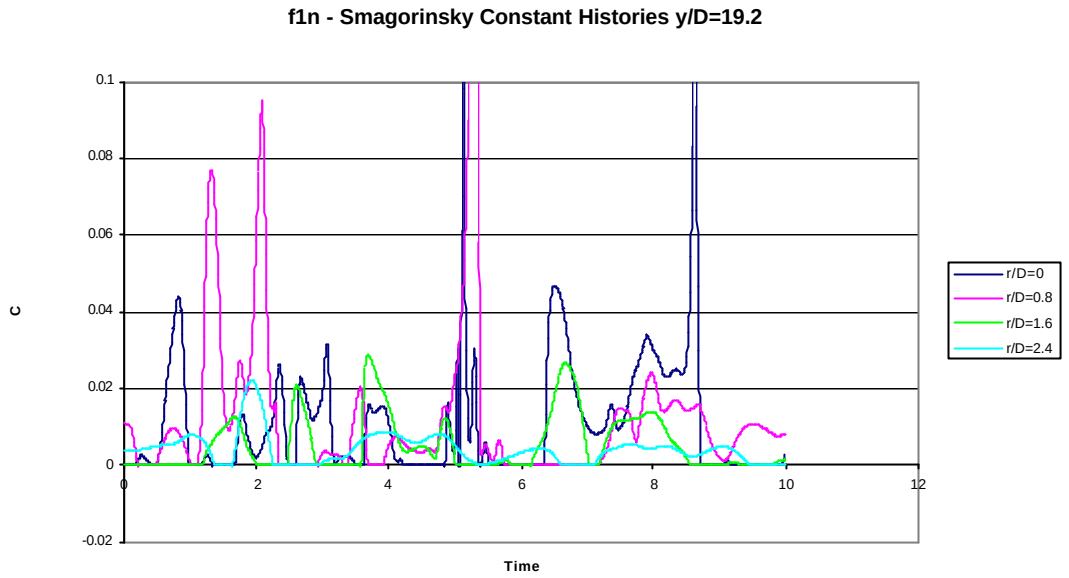

Figure 9.2.16 Smagorinsky constant histories at different radii from the centreline, y/D=19.2, for f1n, dynamic Smagorinsky stress and static SGDH flux models.

9.3 Dynamic SGDH with non-TVD scheme

The dynamic SGDH model simulation, d2f, gave negligible results. It was initially thought that this could have been due to the high level of diffusion incorporated into the TVD convection scheme used in the temperature equation, and it was thought that using a third order upwind scheme which is less diffusive – this is the scheme used for the momentum equations – would improve the models significance to the results. However, using this scheme did not improve the dynamic SGDH model's performance – the flux terms remained negligible. Nevertheless, the difference between schemes is still very relevant to LES modelling, particularly with the emergence of the Monotonically Integrated LES (MILES) technique, which does not use a subgrid model, but relies on TVD schemes for the dissipation. The scheme is shown to be at least as important as the LES model.
The simulation run is identical to d2f, using the dynamic Smagorinsky stress model, and the dynamic SGDH flux model, but uses a 3rd order upwind scheme in the energy equation, and is labelled u1w. The rest of the details are given in section 7.2.

This simulation is, similarly to f1n, not possible without subgrid models. The 3rd order upwind scheme is oscillatory, and temperatures below and above physical bounds are found near the inlet. These are quickly restored to within their physical bounds. The flux model does not increase in magnitude sufficiently to have any appreciable effect on the flow, contrary to the expectation. The implication on the possibility of the flow at all i.e. that it doesn't crash, is that it is the coupling between the velocity and temperature fields which makes the 3rd order upwind scheme unstable and not just the temperature fluctuations alone; the dynamic SGDH does not damp these inflow oscillations. The capability of the dynamic Smagorinsky model to damp the velocity fluctuations has been shown above, and with this, the 3rd order scheme becomes feasible on this coarse grid.
Even though the flux model is still negligible, the simulation results illustrate the significance of the choice of discretisation. The velocity and temperature centrelines are given in figs. 9.3.1 and 9.3.2. They show u1w to go through transition more rapidly than d2f, and afterwards for the decay rate to be slower. This behaviour is identical to the consequences of the different strengths of the eddy models, although

this change in scheme has not affected the Smagorinsky model itself. The turbulent viscosity plot in fig. 9.3.3 shows the two simulations to have very similar magnitudes in relation to their point of transition with u1w marginally larger, but beyond that difference are equivalent.
The SGDH constant centrelines are plotted in fig. 9.3.4, and show that the dynamic procedure does recognise the difference with a consistently increased average but not enough to make the dissipation significant.

The energy spectra at y/D=7.11 and y/D=10.66 are shown in figs. 9.3.5 and 9.3.6. The first plot shows the difference between the vertical and horizontal scales to be less than for previous simulations, and the second plot shows full isotropic turbulence has already been reached. This more rapid development does not appear to have any significant effect on the decay. The d2f simulation is close enough to full isotropic turbulence at this point for the greater dissipation of the model to still be the prominent factor. The temperature spectra of the two simulations are plotted together in fig. 9.3.7. The energy in the large scales is the same, but the TVD scheme dissipates more energy then the 3rd order upwind scheme across the whole inertial range of wavelengths. This greater magnitude of small-scale energy in u1w shows a different behaviour to the ideal of LES with the cut-off filter. If one scheme dissipates more energy than another it would be desirable to see this effect with the spectra cut-off place at a different point, with the rest of the plot overlapping, rather than two different energy distributions. It should be observed, however, that the gradient remains the same. The second part of the temperature range, the –3 gradient, is still elusive.

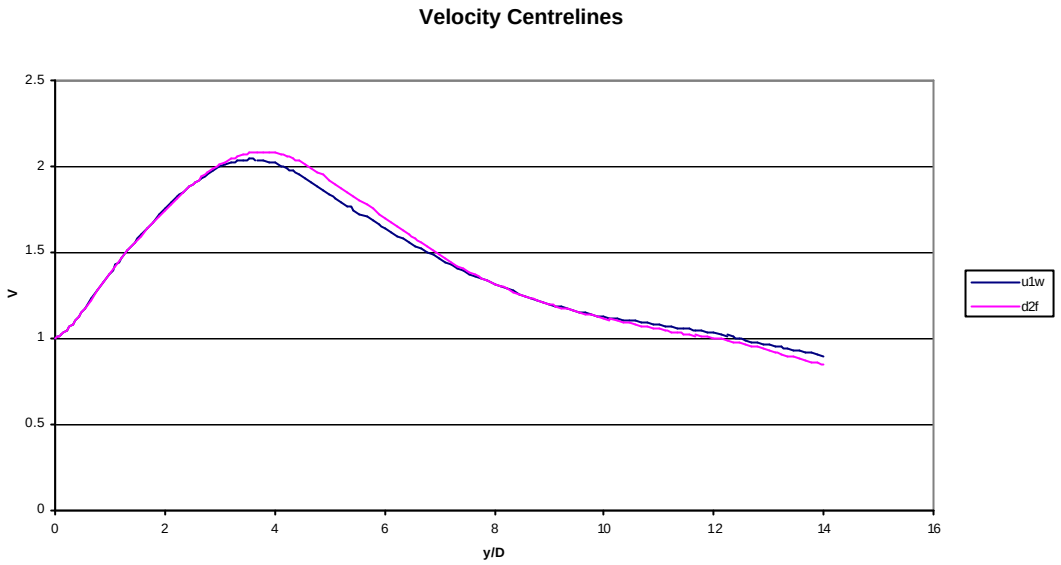

Figure 9.3.1 Vertical velocity centrelines for u1w, 3rd order upwind convection temperature convection scheme, d2f, 2nd order TVD temperature convection scheme.

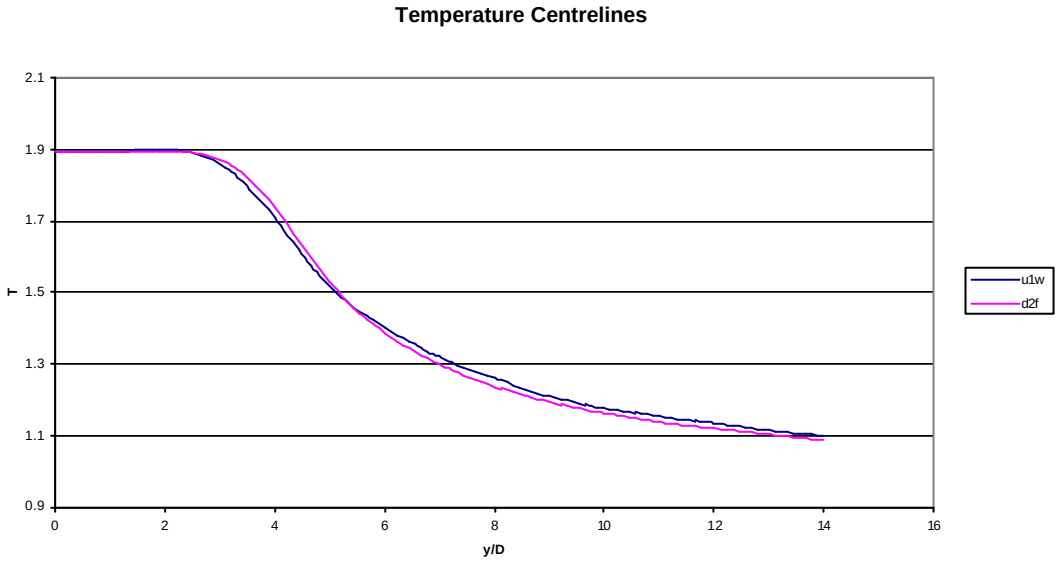

Figure 9.3.2 Temperature centrelines for u1w, 3rd order upwind convection temperature convection scheme, d2f, 2nd order TVD temperature convection scheme.

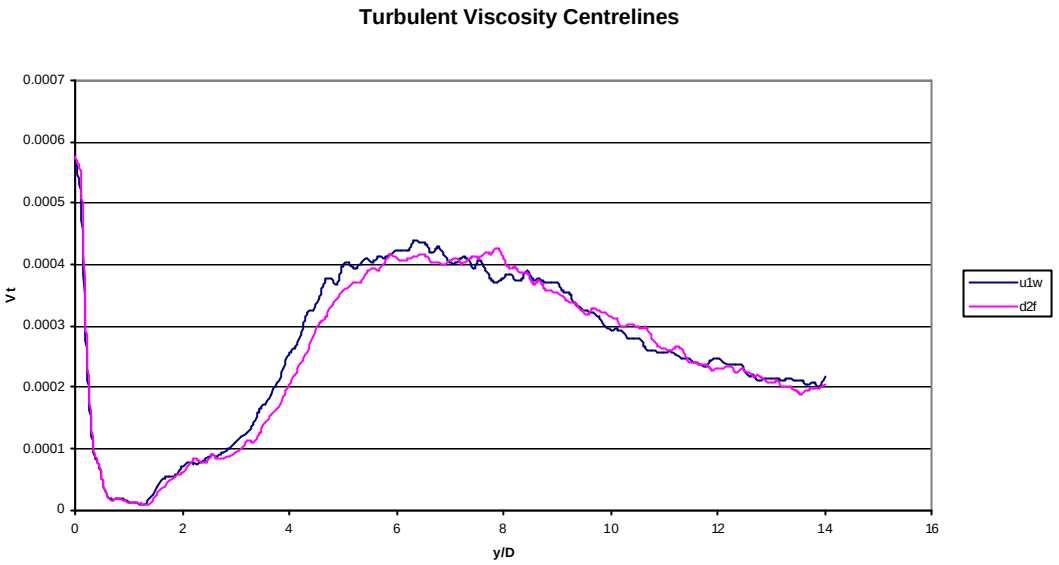

Figure 9.3.3 Turbulent viscosity centrelines for u1w, 3rd order upwind convection temperature convection scheme, d2f, 2nd order TVD temperature convection scheme.

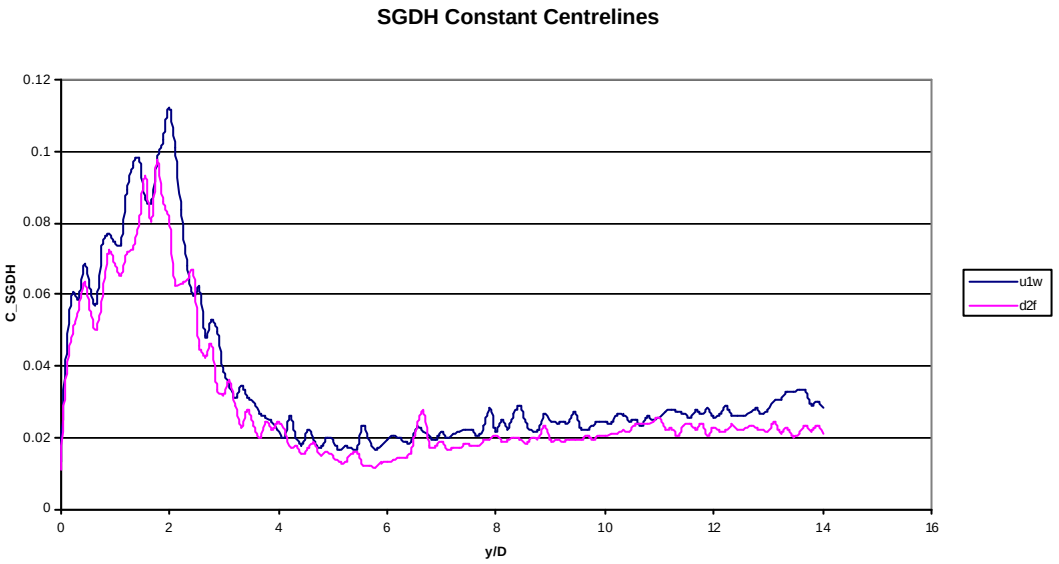

Figure 9.3.4 SGDH constant centrelines for u1w, 3rd order upwind convection temperature convection scheme, d2f, 2nd order TVD temperature convection scheme.

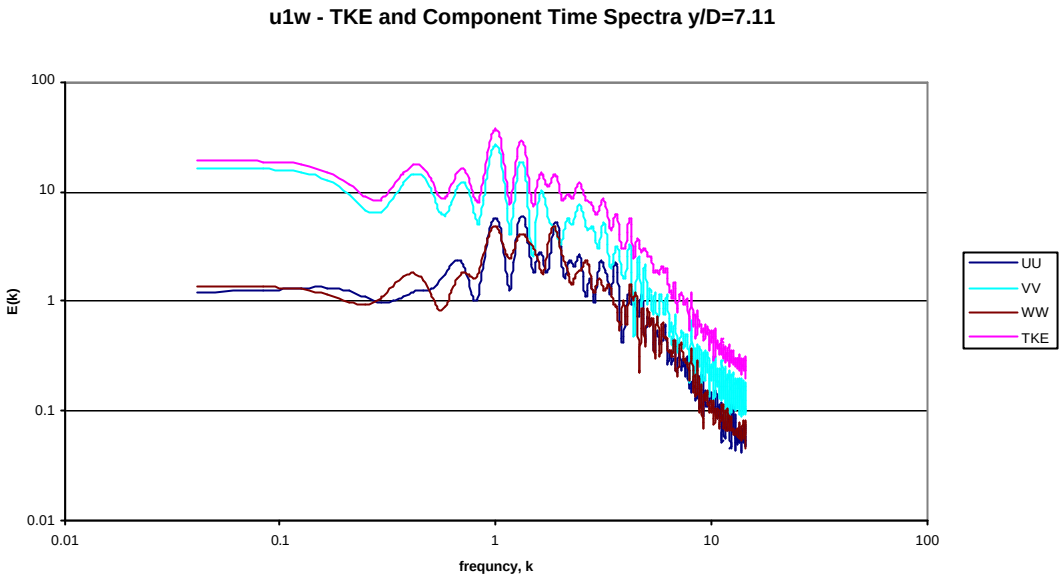

Figure 9.3.5 TKE and component time spectra, y/D=7.11, for u1w, 3rd order upwind convection temperature convection scheme.

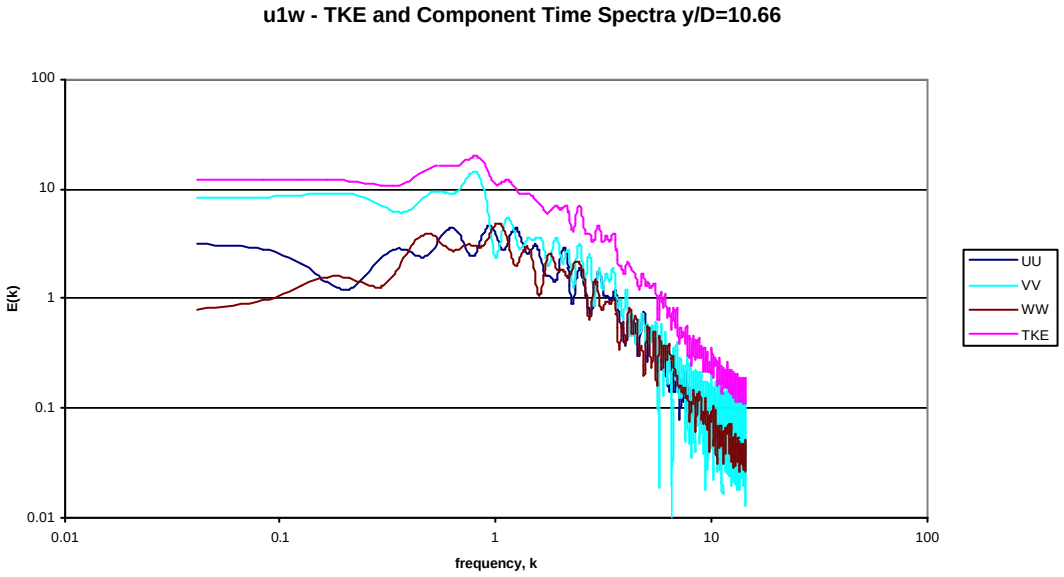

Figure 9.3.6 TKE and component time spectra, y/D=10.66, for u1w, 3rd order upwind convection temperature convection scheme.

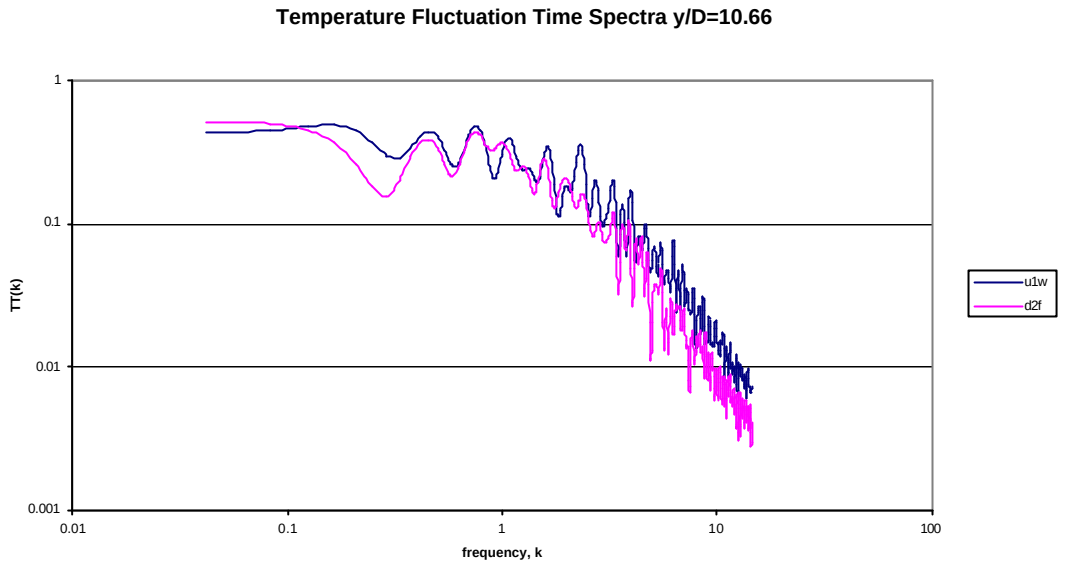

Figure 9.3.7 Temperature fluctuation, TT, time spectra, y/D=10.66, for u1w, 3rd order upwind convection temperature convection scheme, d2f, 2nd order TVD temperature convection scheme.

9.4 Boussinesq Simulation

A simulation is run using the Boussinesq equations, to see if any important effects can be observed, when the assumptions are broken. The same Shabbir and George (1994) experiment is used, with the same parameters as those given in section 8.2. The simulation is given the label b1q. The case is tested using the Smagorinsky model and the SGDH model for the fluxes, and is compared with s1t. The expected delay in transition is not found.

Figs. 9.4.1 and 9.4.2 give the velocity and temperature plots. A significantly reduced acceleration is found, although it accelerates for a longer duration. This is to be expected given the magnitude of the density term not used in the vertical momentum equation. However, the apparent decay appears to start at the same time as for s1t. The temperature decay plot starts to decline after is does for s1t, although it appears to be decaying faster by the end of the domain, although the velocity decays appear to be equal.

The normalised T22 centrelines are given in fig. 9.4.3. These are normalised by the square of the centreline velocity. The normalised vertical Reynolds stress is found to be constant along the centreline in Shabbir and George (1994), and it is likely that this should be the case the subgrid stresses too. The Boussinesq code diminishes the magnitude of the stress in the laminar, non-Boussinesq region, although the difference seen in fig. 9.4.3 will be reduced to a certain extent when the LMN stress is scaled by the density, but not entirely. However, once the developed turbulence region is reached the normalised values are similar. The fluxes, represented by EN2 in fig. 9.4.4, show a similar pattern.

The TKE spectra, including components, are given in figs. 9.4.5-9.4.7 at distances 7.11, 10.66 and 14 y/D respectively. These confirm that the b1q centreline decays have indeed gone through transition at similar points to s1t, despite the lower velocities involved. Similarly to the structure function simulation spectra, in figs 7.2., we can see that there is the same development of the spectra. The first is dominated by the vertical component, in the second the vertical component is only marginally

larger than the horizontal components, and by the end of the domain, the spectra components are isotropically spread in the inertial range. Before the simulation was run, the expectation was that the Boussinesq equations would result in a slower transition, from the lack of extra complexity introduced by the variable density. The apparent sensitivity of the transition point to the flux model used suggested this to be the case. This result suggests that this sensitivity is to the buoyancy component of the equations rather than the coupling of the density with the usual Navier-Stokes terms. Another factor is the decreased vertical velocity allows more time for oscillations to develop, suggesting number of time-steps as another factor in the development of the turbulence, as well as the grid-size, i.e. that decreasing the time-step could increase the oscillatory development. Of course, the degradation in accuracy with decreased time-steps could be a more significant problem, and could serve more to damp the oscillations.

Fig. 9.4.9 plots the TKE spectra at each of the above distances together. The strength of each scale is decreasing, as would be expected. Accuracy of the smallest scales captured is seen to increase as the flow loses its dependence on the initial conditions. Fig. 9.4.9 shows an equivalent plot of the temperature spectra, and shows a similar decrease in the magnitude of energy in the scales.

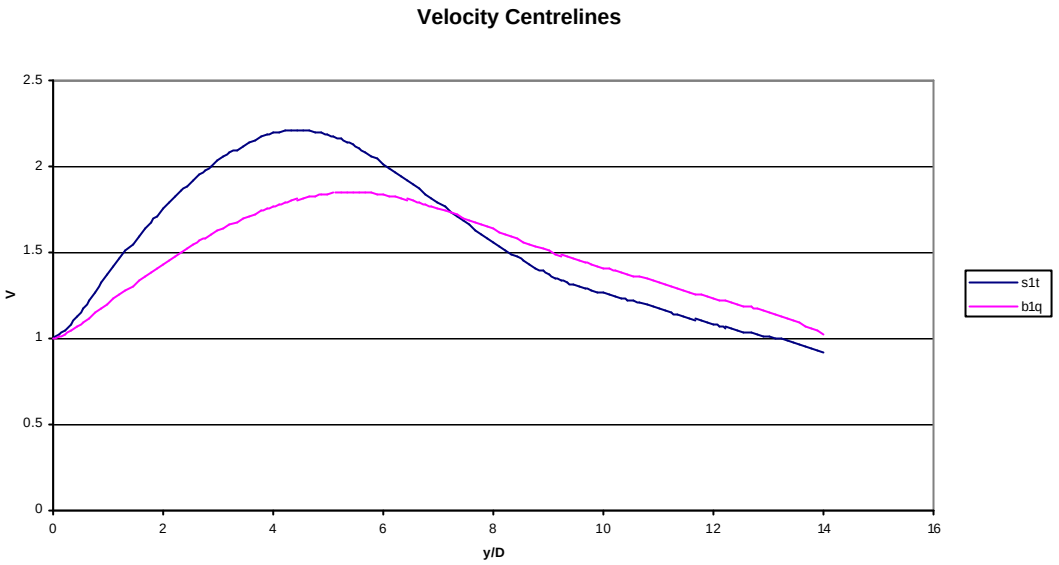

Figure 9.4.1 Vertical velocity centrelines for s1t, LMN flow solver, b1q, Boussinesq flow solver.

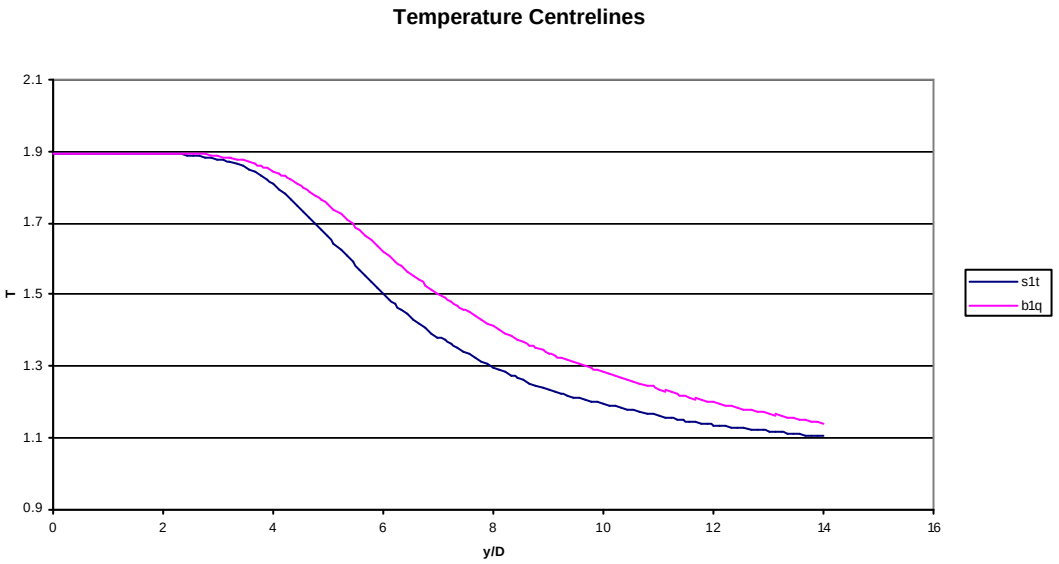

Figure 9.4.2 Temperature centrelines for s1t, LMN flow solver, b1q, Boussinesq flow solver.

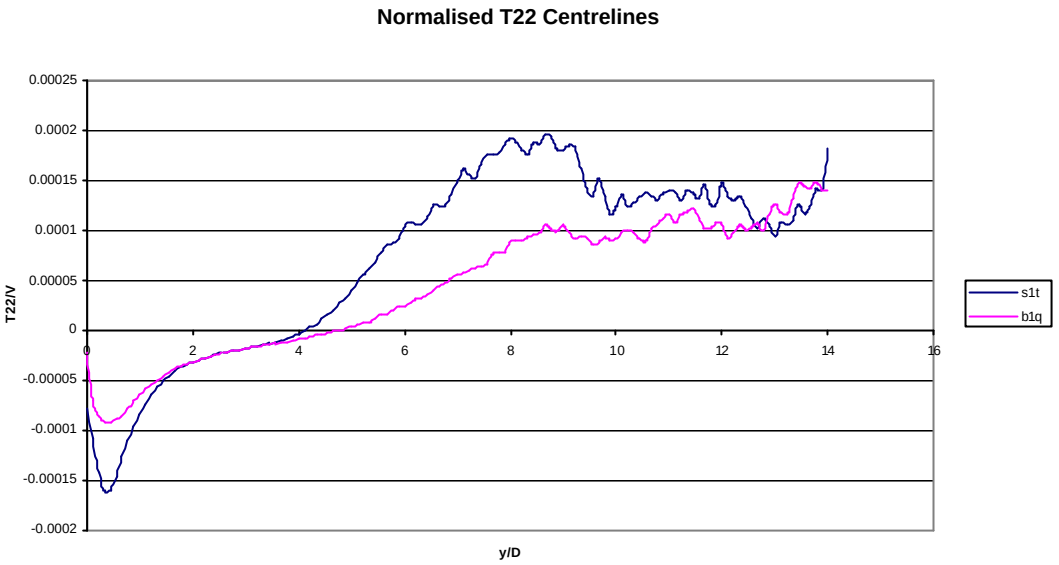

Figure 9.4.3 Normalised T22 centrelines for s1t, LMN flow solver, b1q, Boussinesq flow solver.

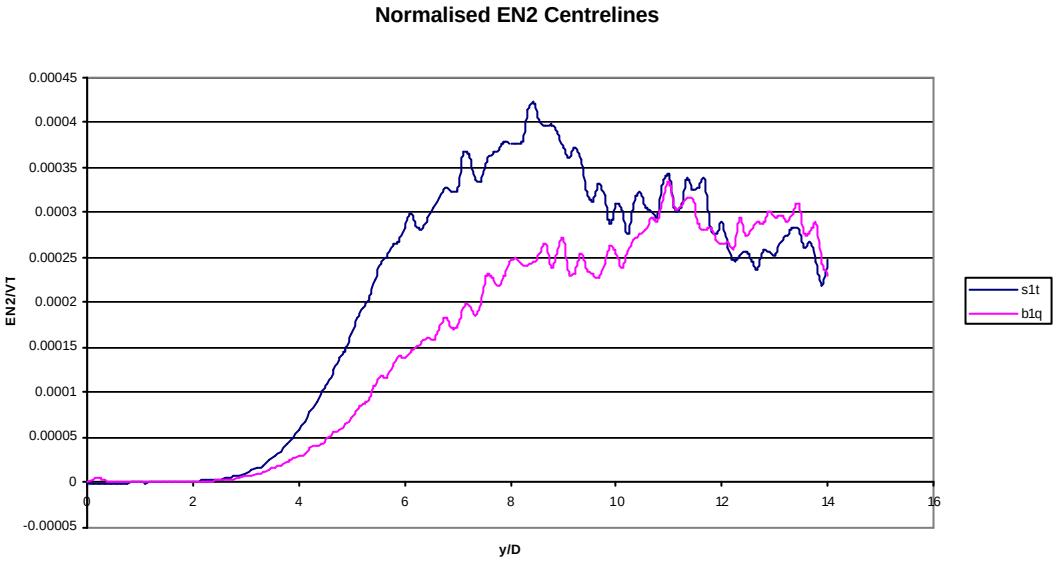

Figure 9.4.4 Normalised EN2 centrelines for s1t, LMN flow solver, b1q, Boussinesq flow solver.

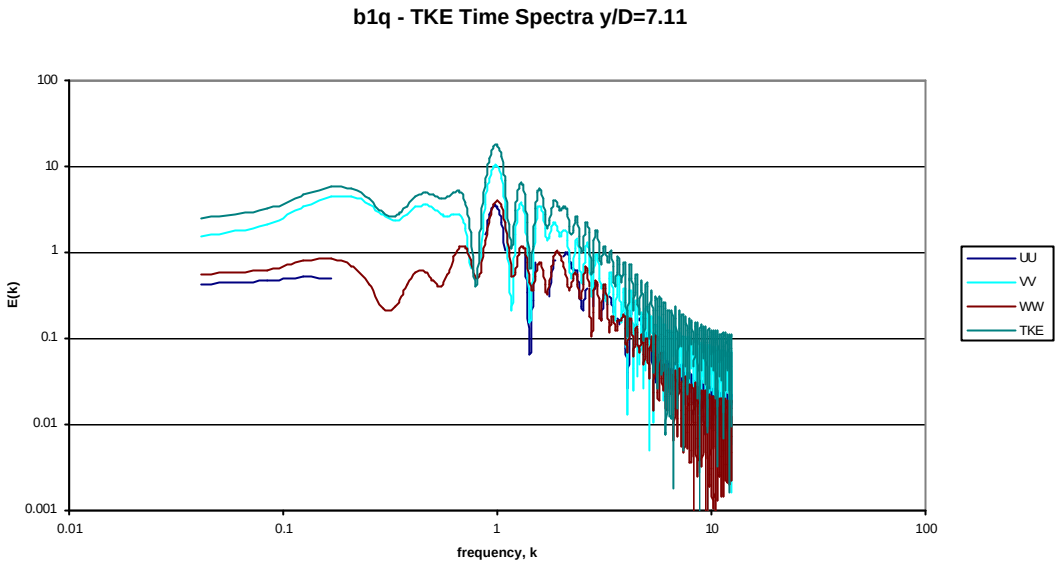

Figure 9.4.5 TKE and component time spectra, y/D=7.11, for b1q, Boussinesq flow solver.

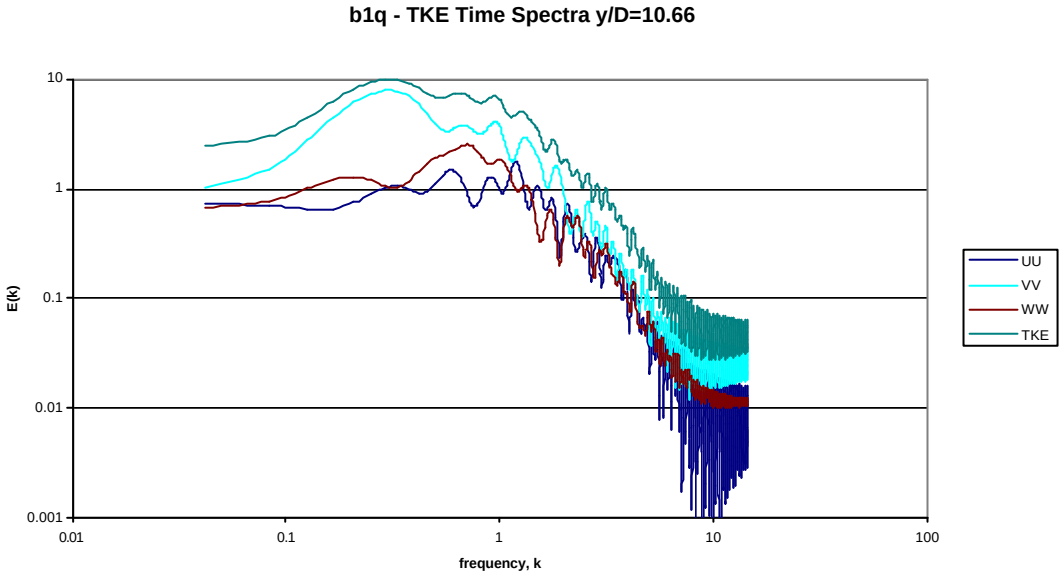

Figure 9.4.6 TKE and component time spectra, y/D=10.66, for b1q, Boussinesq flow solver.

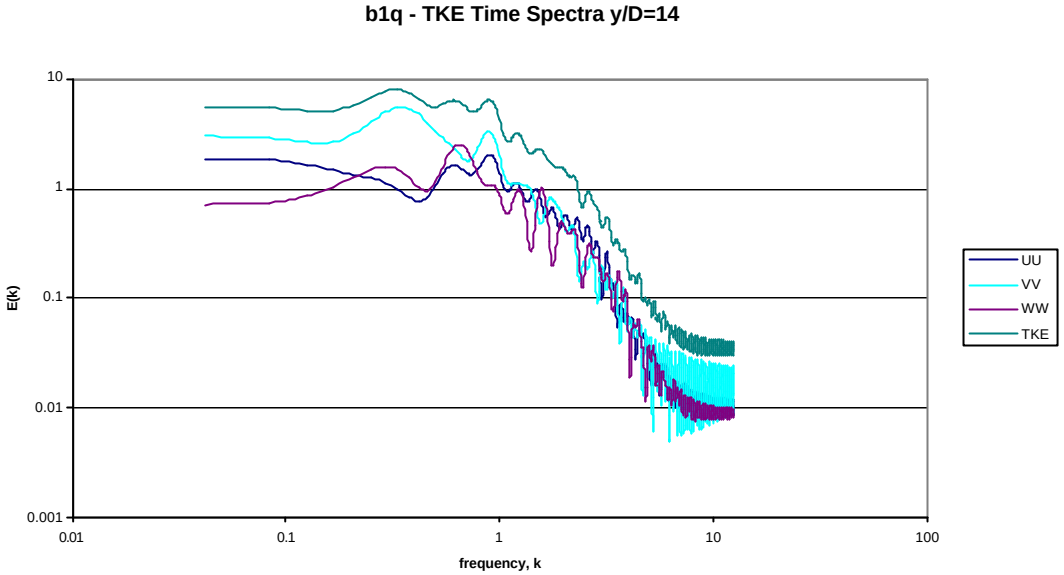

Figure 9.4.7 TKE and component time spectra, y/D=14, for b1q, Boussinesq flow solver.

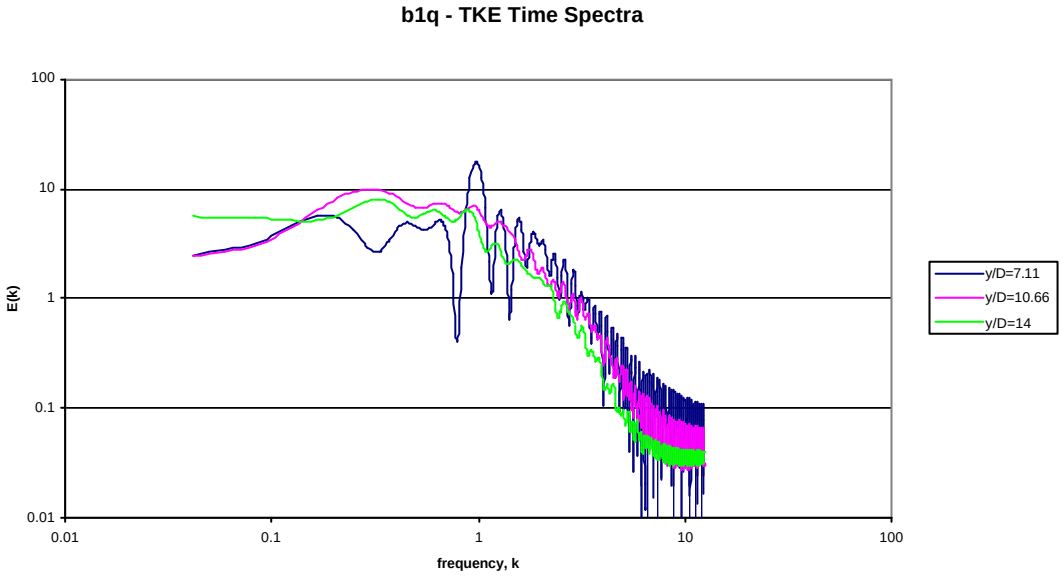

Figure 9.4.8 TKE time spectra at different distances from the source for b1q, Boussinesq flow solver.

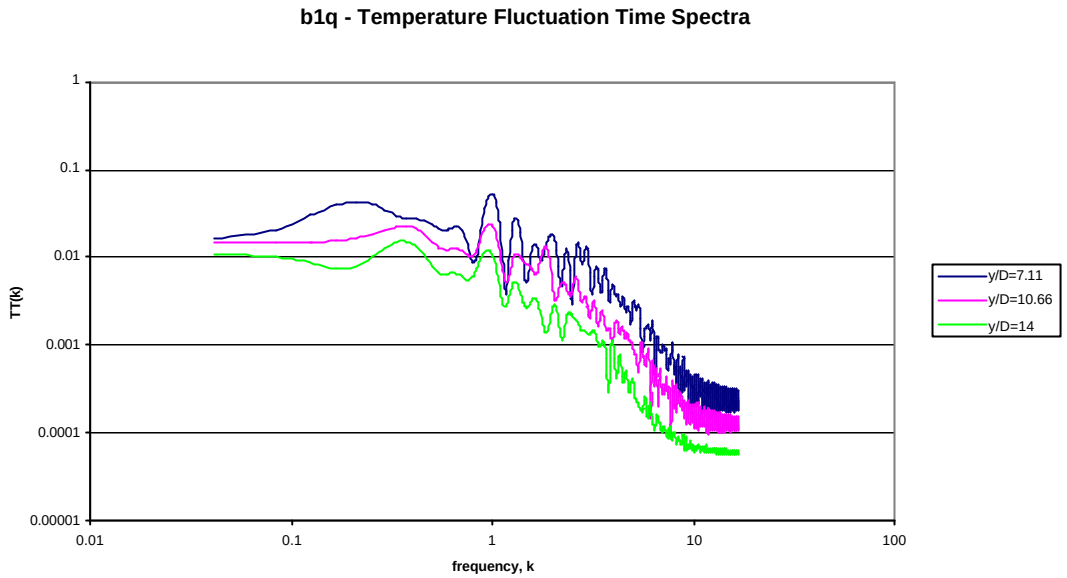

Figure 9.4.9 Temperature fluctuation time spectra at different distances from the source for b1q, Boussinesq flow solver.

9.5 Summary

Three further simulations have been carried out which investigate further issues. The dynamic Smagorinsky model was used on a coarse grid simulation, but the transition region dominated the flow. However, once transition was achieved the model could satisfactorily produce good energy spectra.

In an endeavour to improve the dynamic SGDH model results, a simulation was run using a 3rd order upwind scheme for the temperature convection term, rather than the more diffusive TVD scheme (although the 3rd order upwind scheme is dissipative, good results for the stresses have been found while using it in the momentum equations), but negligible results were found again. This contributes to the argument that the correlation between the temperature fluxes and the turbulent viscosity is not sufficient for the dynamic procedure to work properly. At the same time the strong influence of the numerical scheme was shown.

Also, a test simulation was run with the Boussinesq equations. The breakdown into turbulence occurred at similar times downstream as with the LMN equations, indicating that the LMN equations are not significantly more unstable than the Boussinesq equations are, although the mean acceleration of the plume was considerably less for the Boussinesq equations.

Chapter 10

Conclusion

10.1 Summary

It was the objective of this work to investigate the behaviour and characteristics of the various large eddy simulation turbulence models in a buoyant flow situation. There are very few published works which consider more than two or three LES models at the same time, and to the best of the authors knowledge there are none with the breadth of this work. Two new flux models, the generalised gradient diffusion models, extended from RANS modelling, have been introduced and tested alongside the established models. Of particular concern is the oft-stated argument amongst those who apply LES to practical flow situations, that the choice of LES model makes no difference to the overall flow solution. The original premise for the work was that a relatively coarse grid should better highlight the differences between the models.

An open thermal plume is chosen as the flow on which to investigate the models. This incorporates some general simulation problems, namely the open boundary conditions - turbulent outflow at the top and inflow conditions sufficient for the necessary transition.

For the investigation to be carried out a 3d parallel multigrid code was developed – large eddy simulation must be 3d since turbulence is necessarily 3d. The very large computational costs involved even with relatively coarse grids require very powerful parallel machines. The final code was developed on an SGI Origin 2000, and was successfully ported to an IBM SP machine, and later a new SUN 15k machine. A multigrid Poisson solver is used, one of the fastest advanced techniques available. A number of numerical schemes and discretisations were investigated and a projection scheme eventually settled upon.

A number of LES models were implemented and tested:

Smagorinsky stress model
Buoyancy-modified Smagorinsky stress model
Structure function stress model
One equation stress model
Bardina stress model
Leonard stress model
Mixed stress models
Dynamic Smagorinsky stress model
Dynamic mixed stress model
Dynamic localised stress model
SGDH flux model
GGDH (1/2) flux models
Bardina flux model
Leonard flux model
Mixed flux models
Dynamic SGDH flux model
Dynamic GGDH flux model
Dynamic mixed flux model

A number of factors have been considered in the investigation of the models. Most importantly are the decay rates and the transition point. Momentum and temperature equation balances have been considered. The stresses and fluxes were examined along the centreline and along their profiles and their mechanics considered. Dynamic constant histories are shown with the dynamic models, showing their behaviour in full turbulence and intermittent conditions. Turbulent time spectra are found, showing the nature of the turbulence and the models. Further effects were considered on the models – numerical scheme, grid resolution and the impact of the Boussinesq equations. The characteristics of individual models were also considered.

10.2 Conclusions

The most important conclusion is that the choice of LES model definitely is important, and that the resulting flow can be very significantly affected, although the extent to which the flow is affected depends upon the choice of model. Also that there are still a number of hurdles to bridged in LES modelling – how to handle backscatter has not been resolved (more particularly how to ensure the dissipative eddy constant does not become negative without the need for clipping), since the dynamic mixed models tested do not overcome this problem. The most significant positive result is that the structure models aid transition, indicating that full DNS resolution should not be required in transitional flow simulations to achieve accurate results.

The static models give the widest difference in results. There is a strong correlation between the dissipation of the model and the damping effect on transition, and with the standard constants the one equation model and structure function models are the most dissipative, although it is the conjunction with the SGDH model which most responsible for the delay in transition. Hoiruti (1985) found the static one equation model less dissipative than the Smagorinsky model which is in disagreement with these results, although it was found to be true for the dynamic versions.

The Smagorinsky model is found to give near-identical results to the buoyancy-modified Smagorinsky model contrary to the findings of Bastiaans et al. (2000) who find the model a degradation of the usual Smagorinsky.

The GGDH models are shown to be a good improvement over the SGDH model, and are recommended as an alternative, although the constant values need to be better established.

The mixed models can be interpreted in different ways, the first that there are two separate influences acting on the stresses or fluxes, or secondly considering individually the sum of the two components making up the whole stress or flux. More is said on the latter below. From the first perspective, however, it is the structure models which are the dominant terms on these coarse grids, and these are less dissipative and aid transition. The radial stresses and fluxes are more evenly balanced, though. Piomelli et al. (1991) show that the structure terms (Leonard and Cross terms) should be significantly larger, in agreement with the findings presented here, and that the purely dissipative models adversely affect transition, also shown here.

The dynamic models are recommended unquestionably over the static models for the stresses, in principle. The computational cost is much higher. Transition is suitably captured – i.e. there is little effect from the turbulence model until transition has been reached. The subsequent dissipation rate is less than for the static models. This indicates, and further results show, that the dynamic procedure incorporates the characteristics of the numerical scheme, as predicted by Jiminez (1995), and required by Ragab et al. (1992).

The differences in the impact of the non-mixed dynamic models is much slighter than between the static models, to the extent that in these simulations, there is no indication that one is better than the others. This certainly leaves the dynamic Smagorinsky model computationally superior to the localised dynamic model in this flow domain, and there is no expectation for this to change in other dynamic eddy viscosity model simulations. Neither model has solved the problem of backscatter, but both handle laminar flow and transition well. The high average values of the constants at the boundaries is not detrimental to the evaluation of the turbulent viscosity average, but the larger domain simulation in section 9.2, showed the further boundaries to be an improvement for the entrainment boundary conditions. In the same simulation it was shown that the coarser grid resulted in marginally more clipping.

The dynamic calculation of the subgrid kinetic energy transport dissipation models improves the accuracy, but the resulting stresses are sufficiently similar to the fixed transport model stresses that the main flow averages are not ostensibly different in each case. The constant for the static one equation model is shown to be too high and recommendation is given to use a constant of approximately 0.02.

The non-mixed dynamic flux models give very disappointing results, giving flux magnitudes which are negligible on the flow for both the SGDH model and the second GGDH model. Simulations with non-TVD discretisation schemes were expected to show larger magnitudes in these fluxes, but did not (although different magnitudes of temperature fluctuation were found in the small scales as a consequence of using a different scheme). It is thought that the negative results are caused by a lack of correlation between the turbulent viscosity and temperature fluctuations, but and is shown not to be hindered by the clipping. A dynamic flux model which is not dependent on the fluctuating constant would be hoped to resolve

this issue, for example one could simply evaluate the turbulent viscosity for the dynamic SGDH model without the Smagorinsky constant involved and let the dynamic procedure calculate C/Pr_t instead of $1/\mathrm{Pr}_t$.

The dynamic mixed models give very promising results, with the negative aspects of the overly dissipative eddy models taken out by the dynamic procedure, and the structure components aiding transition. The number of clipped points remains the same or marginally less for the mixed stress model, however. The dynamic procedure overrides the halving in the formulation of the eddy component, and doubles the constant, so that the diffusive eddy components of the model remain at the same magnitude as the dynamic Smagorinsky stresses alone. Also, the formulation of the mixed flux model allows the constant to be evaluated in a manner not dependent on the turbulent viscosity, and results in the eddy component having a non-negligible component, although the level of clipping is high.

The eddy models and the structure models are qualitatively different. The structure models obey the realizability conditions and the eddy models do not. The eddy models are a purely diffusive term which cannot be implementing without changing the nature of the solution (if the turbulent viscosity is non-negligible), whereas the structure models can, even with significant magnitudes. It was shown that it is the relation between the individual stresses which causes a change in flow more than the magnitude of the stresses or fluxes.

From this work the general recommendation for a model, computational expense aside, it would be for the dynamic mixed Smagorinsky/Bardina stress model with the full implementation, i.e. not halving the components, and the full dynamic mixed SGDH/Bardina flux model, although the GGDH would be preferred but was not tested in a mixed model simulation.
However, computational expense is a very considerable factor. If the models with lower memory requirements can be utilized to take advantage of fast cache memory, when others cannot, this may be the more desirable quality, particularly if non-transitional flows are to be simulated where the advantages of dynamic models are less prominent.

10.3 Future Work

Large eddy simulation is a vast area of research, and this work contributes the small beginnings of a potentially massive undertaking, to exhaustively and fully examine different LES models, to understand their capabilities as well as their limitations, and to locate areas where further development is needed. As computer power continues to increase the scope of the test-bed simulations increases too. Limitations of grid size and duration of simulation restricted an exact comparison with experiment. In a simulation with fully developed, self-similar regions of plumes, a good comparison of plume half-widths should show the differences between the dynamic models more strongly than the decay rates do. Either an extension of the domain would clarify these issues further, or less costly, the input of fully turbulent inflow boundaries rather than forced instabilities. A natural way to do this would be to link the turbulent outflow at the top of the domain back to the inflow, shrinking the field to fit the inlet diameter.

In terms of model development and testing flux models are less adequate than the stress models and need further work more urgently than the stress models. The GGDH models are expected to be superior to the SGDH model, and suitable constants should be found for each formulation. The usefulness of the first formulation should be tested further, since the second formulation is computationally more expensive, requiring the SKE equation to be solved. Further development of dynamic strategies for the flux models needs to be pursued. Non-dynamic models will not be sufficient.

The development of the estimation model into a non-implicit method would be very desirable. This is entirely feasible, since the model, when both steps are used, breaks the requirement that the filtered estimated variables equal the resolved filtered field. An explicit method of doing this could be devised, or taken from another source, such as the fractal methods (Scotti and Meneveau, 1997).

Ultimately, the extra cost of LES, based on memory storage rather than operation count needs to be reduced. At the very least, non-uniform grids must be used, and ideally, for the most general applicability, adaptive grids should be used. These will inevitably become the standard grid type as very large domains are solved, requiring significantly different scales of motion to be solved in different regions at different times. What form this will take is as yet unclear, although Cartesian adaptivity with

Cartesian cut cell boundary methods sounds very promising. This would allow the numerical benefits of Cartesian grids and complex geometries together. Also, fully locally evaluated numerical schemes would be highly beneficial for parallelisation purposes, e.g. Brava et al's (1999) scheme. These underlying methods are essential to the ideal situation of maximising the usefulness of LES models, so that the grid size is everywhere such that the resolved scales only capture to the very top of the inertial subrange. Finding a criterion to establish this would be a major undertaking.

Appendix A

Energy Spectra

Initially the spectrum is considered for an homogeneous, isotropic flow. This allows us to consider a one-dimensional energy function. We want something of the form:

$$\int_0^\infty E(k)\partial k = \tfrac{1}{2}\overline{u_i' u_i'} = TKE \qquad \text{(A.1)}$$

$E(k)$ is the energy function.

Its form is derived as follows.

Let $R_{ii}(x, x+\Delta x) = \overline{u_i'(x) u_i'(x+\Delta x)}$ be the correlation function. From the assumptions of homogeneity and isotropy, this correlation can be written purely in terms of the distance (without direction) between the two points. $R_{ii}(x, x+\Delta x) = R_{ii}(\Delta x)$.

We define the spectral function, taking the Fourier transform of the correlation function.

$$\Phi_{ii}(k) = \Im(R_{ii}(\Delta x)) = \frac{1}{(2p)^3}\iiint R_{ii}(\Delta x) e^{-ik\Delta x}\partial\Delta x \qquad \text{(A.2)}$$

Correspondingly, the inverse transform gives:

$$R_{ii}(\Delta x) = \Im^{-1}(\Phi_{ii}(k)) = \iiint \Phi_{ii}(k) e^{ik\Delta x}\partial k \qquad \text{(A.3)}$$

Here, we note $TKE = \tfrac{1}{2}R_{ii}(0)$, and so $TKE = \tfrac{1}{2}\iiint \Phi_{ii}(k)\partial k$ (the exponent goes to zero).

Finally, we change the three-dimensional integral into a single axis integral over the surface of a sphere. Let $k = |k|$. Then

$$TKE = \int_0^\infty 2p k^2 \Phi_{ii}(k)\partial k \qquad \text{(A.4)}$$

which gives us the definition of the energy function.

$$E(k) = 2p k^2 \Phi_{ii}(k) \qquad \text{(A.5)}$$

We can also find the time spectrum, which is what is actually done since the flow is not isotropic or homogeneous, very similarly, and without working in 3d. This helps coding considerably.

We now define $R_{ii}(t,t+\Delta t)=\overline{u_i'(t)u_i'(t+\Delta t)}$, and with only the assumption that there is steady state turbulence (implicitly assumed above), we can write $R_{ii}(t,t+\Delta t)=R_{ii}(\Delta t)$. Now we can take a one-dimensional transform, defining the new spectral function:

$$\Phi_{ii}(k)=\Im(R_{ii}(\Delta t))=\frac{1}{2p}\int R_{ii}(\Delta t)e^{ik\Delta t}\partial\Delta t \qquad \text{(A.6)}$$

and the inverse

$$R_{ii}(\Delta t)=\Im^{-1}(\Phi_{ii}(\Delta t))=\int\Phi_{ii}(k)e^{-ik\Delta t}\partial k \qquad \text{(A.7)}$$

Now

$$TKE=\int_0^\infty 2\Phi_{ii}(k)\partial k \qquad \text{(A.8)}$$

giving the energy function to be

$$E(k)=2\Phi_{ii}(k) \qquad \text{(A.9)}$$

This has the same dimensions as the spatial spectrum, and under the conditions of the Kolmogorov Hypotheses can be expected to give the –5/3 power law.

A discrete Fourier transform must be taken to evaluate the energy spectrum. More details can be found in Brigham (1974).

$$\Im(k/NT)=\sum_{x=0}^{N-1}f(xT)e^{-i2pxk/N},k=0,...,N-1 \qquad \text{(A.10)}$$

and its inverse

$$\Im^{-1}(xT)=\frac{1}{N}\sum_{x=0}^{N-1}f(k/NT)e^{i2pxk/N},x=0,...,N-1 \qquad \text{(A.11)}$$

where T is the period (time step), and k is the frequency.

The transforms used in this work cover 45,000 points in time. 2000 points are used for the transform, and the time correlations are averaged over 4,300 points adding the next point every 10 time steps.

Appendix B

Discretisations

B1. TVD

This scheme is conservative and non-oscillatory in linear convection schemes. In the non-linear convection in the temperature equation, the scheme loses its conservativeness if it is to remain fully TVD.

The temperature convection scheme is then given by (in 1d, assuming a collocated grid point arrangement):

If $u_i > 0$:

$$-u_i \frac{T_i - T_{i-1}}{\Delta x} - \frac{u_i}{2\Delta x}(\Delta x - u_i \Delta t)(s_i - s_{i-1})$$

If $u_i < 0$:

$$-u_i \frac{T_{i+1} - T_i}{\Delta x} - \frac{u_i}{2\Delta x}(\Delta x + u_i \Delta t)(s_{i+1} - s_i)$$

and the 'superbee' flux limiter is given by

$$s_i = \max \bmod(gr1, gr2)$$

$$gr1 = \min \bmod(Tx1, 2Tx2)$$

$$gr2 = \min \bmod(2Tx1, Tx2)$$

$$Tx1 = (T(i+1) - T(i))/\Delta x$$

$$Tx2 = (T(i) - T(i-1))/\Delta x$$

$$\min \bmod(a, b) = \min(abs(a), abs(b))$$

$$\max \bmod(a, b) = \max(abs(a), abs(b))$$

B2. Conservative 3rd Order Upwind

The conservative formulation for the momentum equation in 1d is given by the following (again assuming collocated grid points):

$f_i = r_i u_i u_i$

If $u_i > 0$:

$(2f_{i+1} + 3f_i - 6f_{i-1} + f_{i-2})/6\Delta x$

If $u(i) < 0$:

$(-f_{i+2} + 6f_{i+1} - 3f_i - 2f_{i-1})/6\Delta x$

B3. Non-Conservative 3rd Order Upwind

$f_i = r_i u_i$

If $u_i > 0$:

$f_i(2u_{i+1} + 3u_i - 6u_{i-1} + u_{i-2})/6\Delta x$

If $u_i < 0$:

$f_i(-u_{i+2} + 6u_{i+1} - 3u_i - 2u_{i-1})/6\Delta x$

Appendix C

Simulation Details

This appendix serves to provide the details of the simulations presented in chapter 6, and also to list the main simulations together in one group. All simulations follow the details set out in section 7.2. Differences are stated along with the simulation label and turbulence models.

LABEL	Stress Model	Flux model
l4o	DNS	DNS
Maximum velocity fluctuations are 0.4, and six modes are used in the sinusoidal instabilities		
l6o	Smagorinsky	SGDH
As l4o		
d3n	DNS	DNS
Averages averaged every 2 time-steps rather that every 25		
d1n	DNS	DNS
s1t	Smagorinsky	SGDH
s2t	Buoyancy-modified Smagorinsky	SGDH
s1f	Structure function	SGDH
o1e	One-equation	SGDH
o2e	One-equation	None
f1c	One-equation	GGDH_1
f2c	One-equation	GGDH_2
m1x	Mixed Smagorinsky/Bardina	Mixed Smagorinsky/Bardina
m2x	Mixed Smagorinsky/Leonard	DNS
d1f	Dynamic Smagorinsky	SGDH
d2f	Dynamic Smagorinsky	Dynamic SGDH
l1d	LDM - dynamic SKE models	SGDH
l2d	LDM - static SKE models	SGDH
d1m	Dynamic mixed Smagorinsky/Bardina	SGDH
d2m	Dynamic mixed Smagorinsky/Bardina	Dynamic mixed SGDH/Bardina
f1n	Dynamic Smagorinsky	Dynamic SGDH
This is run on a coarser grid, with a 12.6x25.4x12.6 domain, and the same flow parameters as those in section 7.2		
u1w	Dynamic Smagorinsky	Dynamic SGDH
This uses a 3rd order upwind convection scheme for the temperature equation.		
b1q	Smagorinsky	SGDH
The Boussinesq equations are solved instead of the LMN equations.		

Table C.1 Simulation listings.

References

Ansari, A., & Strang, W. Z., Large-Eddy Simulation of Turbulent Mixing Layers, AIAA Reprot 96-0684, 1996.

Balaras, E., & Benocci, C., Large eddy simulations of flow in a square duct, Proc. Of the thirteenth symposium on turbulence, Univ. of Missouri Rolla, 1992.

Bastiaans, R, J. M., Rindt, C. M. M., Nieuwstadtadt, F. T. M. & van Steenhoven, A. A., Direct and large-eddy simulation of the transition of two- and three-dimensional plumes in a confined enclosure, I. J. Heat Mass Trans., 43, p2375, 2000.

Bastiaans, R. J., M., Rindt, C. C. M., & van Steenhoven, A., A., Experimantal analysis of a confined transitional plume with respect to subgrid-scale modelling, Int. J. Heat Mass Transfer, 41, p3989, 1998.

Basu, A. J. & Mansour, N. N., Large eddy simulation of a forced round turbulent buoyant plume in neutral surroundings, Annual Research Briefs, Centre for Turbulence Research, NASA Ames/Stanford Univ., 1999.

Batchelor, G. K., The Theory of Homogeneous Turbulence, Cambridge University Press, Cambridge, 1953.

Baum, H. R., McGratten, K. B., & Rehm, R. G., Simulation of Smoke Plumes from Large Pool Fires, Twenty Fifth Symposium on Combustion, The Combustion Institute, p1463, 1994.

Boersma, B. J., Direct numerical simulation of a turbulent reacting jet, Annual Research Briefs, Centre for Turbulence Research, NASA Ames/Stanford Univ., 1999.

Boersma, B. J., Brethouwer, G & Nieuwstadt, F. T. M., A numerical investigation on the effect of the inflow conditions on the self-similar region of a round jet, Phys. Fluids , 10(4), 1998.

Boersma, B. J., & Lele, S. K., Large eddy simulation of compressible turbulent jets, Annual Research Briefs, Centre for Turbulence Research, NASA Ames/Stanford Univ., 1999.

Bravo, E., Claeyssen, J. R., & Platte, R B., A direct one-step pressure actualisation for incompressible flow with pressure Neumann condition, J. Comp. and Applied Mathematics, 103, p43, 1999.

Briggs, W. L., A Multigrid Tutorial, Philadelphia, SIAM, 1987.

Brigham, E. O., The Fast Fourier Transform, Prentice-Hall, 1974.

Brown, D. L., Cortez, R., & Minion, M. L., Accurate Projection Methods for the Incompressible Navier-Stokes Equations, J. Comp. Phys., 168, p464, 2001.

Bruneau, C. H., & Fabri, P. Effective Downstream Boundary Conditions for Incompressible Navier-Stokes Equations, Int. J. Num. Methods Fluids, 19, p693, 1994.

Carati, D., & Eijnden, E. V., On the self-similarity assumption in dynamic models for large eddy simulations, Phys. Fluids, 9(7), p2165, 1997.

Carati, D., Ghosal, S., & Moin, P., On the representation of backscatter in dynamic localization models, Phys. Fl., 7(3), p606, 1995.

Carati, D., & Wray, A. A., Time filtering in large eddy simulations, Proc. Summer Programme, Centre for Turbulence Research, NASA Ames/ Stanford Univ., 2000.

Chakravarthy, V. K., & Menon, S., On Large Eddy Simulation of non-homogeneous flows, AIAA Report 97-0652, 1997.

Chen, J C, & Rodi, W, Turbulent Buoyant Jets: a review of experimental data, Heat Mass Transfer, vol. 4, p1, 1980.

Chester, S., Charlette, F., & Meneveau, C., Dynamic Model for LES without Test Filtering: Quantifying the Accuracy of Taylor Series Approximations, Theoret. Comput. Fluid Dynamics, 15, p165, 2001.

Clark, R. A., Ferziger, J. H., & Reynolds, W. C., Evaluation of Subgrid-Scale Turbulence Models Using a Fully Simulated Turbulent Flow, Thermosciences Division, Dept. Mech. Eng., Stanford University, Rept. No. TF-9, 1977.

Cottet, G.-H., & Vasilyev, O. V., Comparison of dynamic Smagorinsky and anisotropic subgrid-scale models, Proc. Summer Program, Centre of Turbulence Research, Stanford, 1998.

Dai, Z, Tseng, L K, & Faeth, G M, Structure of Round, Fully Developed, Buoyant Turbulent Plumes, J. Heat Transfer, 116, p409, 1994.

Daly, B. J., & Harlow, F. H., Transport Equations in Turbulence, Phys. Fluids, 13(11), p2634, 1970.

Davidson, Lars, A Note on Derivation of the Equations for the Subgrid Turbulent Kinetic Energies, Rep. 97/12, Dept. of Thermo and Fluid Dynamics, Chalmers University of Technology, 1997a.

Davidson, Lars, Large Eddy Simulation: A Dynamic One-Equation Subgrid Model for Three-Dimensional Recirculating Flow, 11th Int. Symp. on Turb. Shear Flow, Vol. 3, p26.1, Grenoble, 1997b.

Deardorff, J. W., A numerical study of three-dimensional turbulent channel flow at large Reynolds numbers, J. Fl. Mech., 41(2), p453, 1970.

Deardorff, J. W., The use of subgrid transport equations in a three-dimensional model of atmospheric turbulence, ASME J. Fl. Engng., p429, 1973.

Ding, F., Arya, S. P., & Lin, Y-L, Large-Eddy Simulations of the Atmospheric Boundary Layer Using a New Subgrid-Scale Model, Environmental Fluid Mechanics, 1, p49, 2001.

Domaradzki, J. A. & Loh, K.-C., The subgrid estimation model in the physical space representation, Phys. Fluids, 11(8), 1999.

Domaradzki, J. A. & Rogello, R. S., Local energy transfer and non-local interactions in homogeneous, isotropic turbulence, Phys. Fluids A, 2, 1990.

Domaradzki, J. A. & Saiki, E. M., A subgrid scale model based on the estimation of unresolved scales of turbulence, Phys. Fluids, 9(7), p2148, 1997.

Eidson, T. M., Numerical simulation of the turbulent Rayleigh-Benard problem using subgrid modelling, J. Fluid Mech., 158, p245, 1985.

Ferziger, J. H., & Peric, M., Computational Methods for Fluid Dynamics, 2nd ed., Springer, 1999.

Friedrich, R., Huttl, T. J., Manhart, M., & Wagner, C., Direct numerical simulation of incompressible turbulent flows, Computers & Fluids, 30, p555, 2001.

Frost, W. & Moulden, T. H., Handbook of Turbulence Vol. 1, Plenum Press, New York, 1977.

Fureby, C., & Grinstein, F., Large Eddy Simulation of High-Reynolds-Number Free and Wall-Bounded Flows, J. Comp. Phys., 181, p68, 2002.

George, W. K., Self-preservation of turbulent flows and its relation to initial conditions and coherent structures, in Advances in Turbulence, George, W. K. & Arndt, R., Springer, New York, 1989.

Germano, M., Turbulence: the filtering approach, J. Fluid Mech., 238, p325, 1992.

Germano, M., Piomelli, U., Moin, P., & Cabot, W. H., A dynamic subgrid-scale eddy viscosity model, Phys. Fluids A, 3(7), p1760, 1991.

Ghia, U., Ghia, K. N., & Shin, C. T., High Re Solutions for Incompressible Flow using the Navier-Stokes Equations and a Multigrid Method, J. Comp. Physics, 48, p387, 1982.

Ghosal, S., An Analysis of Numerical Errors in Large Eddy Simulations of Turbulence, J. Comp. Phys., 125(1), p187, 1996.

Ghosal, S., Mathematical and Physical Constraints on Large-Eddy Simulation of Turbulence, AIAA J., 37(4), p425, 1999.

Ghosal, S., Lund, T. S., Moin, P., & Akselvoll, K., A dynamic localization model for large-eddy simulation of turbulent flows, J. Fluid Mech., 286, p229, 1995.

Givoli, D., Non-reflecting Boundary Conditions, J. Comp. Phys., 94, p1, 1991.

Glazier, J. A., Segawa, T., Naert, A., & Sano, M., Evidence against 'ultrahard' thermal turbulence at very high Rayleigh numbers, Nature, 398, p307, 1999.

Gresho, P. M., Incompressible Fluid Dynamics: Some Fundamental Formulation Issues, Ann. Rev. Fluid Mech., 23, p413, 1991.

Harlow, F. H., Welch, J. E., Numerical Calculation of Time-Dependent Viscous Incompressible Flow of Fluid with Free Surface, Phys. Fluids, 8(12), p2182, 1965.

Hanjalic, K, Achievements and Limitations in Modelling and Computation of Buoyant Turbulent Flows and Heat Transfer, Proc. 10^{th} Int. Heat Transfer Conf., 1994.

Hess, R., & Joppoch, W., A comparision of parallel multigrid and a fast Fourier transform algorithm for the solution of the Helmholtz equation in numerical weather prediction, Parallel Computing, 22, p1503, 1997.

Hoiruti, K., Large Eddy Simulation of Turbulent Channel Flow by One-Equation Modelling, J. Phys. Soc. Jap., 54(8), p2855, 1985.

Hoiruti, K., Backward scatter of subgrid-scale energy in wall-bounded turbulence and free shear flow, J. Phys. Soc. Jap., 66(1), p91, 1997.

Horvat, A., Kljenak, & Marn, J., Two-dimensional large-eddy simulation of turbulent natural convection due to internal heat generation, Int. J. Heat Mass Trans., 44, p3985, 2001.

Hu, F. Q., On Absorbing Boundary Conditions for Linearized Euler Equations by a Perfectly Matched Layer, J. Comp. Phys., 129, p201, 1996.

Jaberi, F. A., & Colucci, P. J., Large eddy simulation of heat and mass transport in turbulent flows. Part 2: Scalar field, Int. J. Heat Mass Transfer, 46, p1827, 2003.

Jimenez, J., On why dynamic subgrid-scale models work, Annual Research Briefs, Centre for Turbulence Research, NASA Ames/Stanford Univ., 1995.

Jin, G., & Brava, M., A Nonreflecting Outlet Boundary Condition for Incompressible Unsteady Navier-Stokes Calculations, J. Comp. Phys., 107, p239, 1993.

Jones W. P., & Musange, P., 1988, Closure of the Reynolds-stress and scalar flux equations, Phys. Fluids, 31, p3589, 1988.

Katopodes, F. V., Street, R. L., Ferziger, J. H., Subfilter-scale scalar transport for large eddy simulation, 14th Symposium on boundary layers and turbulence, American Meteorological Society, p472, 2000.

Kawamura, T., Direct Simulation of a Turbulent Inner Flow by finite-difference method, AIAA Report 85-0376, 1985.

Kerr, R. M., Rayleigh number scaling in numerical convection, J. Fluid Mech., 310, p139, 1996.

Kerr, R. M., Domaradzki, J. A., & Barbier, G., Small-scale properties of non-linear interactions and subgrid-scale energy transfer in isotropic turbulence, Phys. Fluids, 8, p197, 1996.

Kim, J., & Moin, P, Application of a Fractional-Step Method to Incompressible Navier-Stokes Equations, J. Comp. Physics, 59, p308, 1985.

Krajnovic, S., Muller, D., & Davidson, L., Comparison of Two One-Equation Subgrid Models in Recirculating Flows, Direct and Large-Eddy Simulation III, p63, Eds: Voke, P. V., Sandham, N. D., Kleiser, L., Kluwer, 1999.

Kwak, D., Reynolds, W. C., & Ferziger, J. H., Numerical Simulation of Turbulent Flow, Thermosciences Division. Dept. Mech. Eng., Stanford University, Report No. TF-5, 1975.

Lele, S. K., Compact Finite Difference Schemes with Spectral-like Resolution, J. Comp. Phys., 103, p16, 1992.

Leonard, A., Energy cascade in large-eddy simulations of turbulent flows, Adv. Geophys., 18, p237, 1977.

Leonard, A., Large-eddy simulation of chaotic convection and beyond, AIAA Report 97-0204, 35th Aerospace Sciences Meeting & Exhibit, Jan. 6-10, Reno, N., 1997.

Lesieur, M. & Metais, O., New Trends in Large Eddy Simulation, Ann. Rev. Fluid Mech., 28, p45, 1996.

Lilly, D. K., On the numerical simulation of buoyant convection, Tellus, XIV(2), p144, 1962.

Lilly, D. K., The Representation of Small-Scale Turbulence in Numerical Simulations, IBM Scientific Computer Symposium on Environmental Sciences, p195, 1967.

Lilly, D. K., A proposed modification of the Germano subgrid-scale closure method, Phys. Fluids A, 4(3), p633, 1992.

Liu, C., Meneveau, C., & Katz, J., On the properties of similarity subgrid-scale models as deduced from measurements in a turbulent jet, J. Fluid Mech., 275, p83, 1994.

Lou, J. Z., & Ferraro, R., A Parallel Incompressible Flow Solver Package with a Parallel Multigrid Elliptic Kernel, J. Comp. Phys., 125, p225, 1996.

Lund, T. S., Ghosal, S., & Moin, P., Numerical experiments with highly variable eddy viscosity models, in Engineering Applications of Large Eddy Simulation, eds. Ragale, S. A., & Piomelli, U., FED Vol. 162, ASME, 1993.

Lund, T. S., & Novikov, E. A., Parametrization of subgrid-scale stress by the velocity gradient tensor, Annual Research Briefs, Centre for Turbulence Research, NASA Ames/Stanford Univ., 1992.

Luo, K. H. & Zhou, X., Large Eddy Simulation of Variable-Density Turbulent Flows Impinging on Wall Plates and Cavity Enclosures, Direct and Large Eddy Simulation IV, Kluwer Academic Publishers, 2001.

Madabhushi, R. K., & Vanka, S. P., Large eddy simulation of turbulence-driven secondary flow in a square duct, Phys. Fluids A, 3(11), p2734, 1991.

Mathieu, J. & Scott, J., An Introduction to Turbulent Flow, Cambridge University Press, 2000.

McGratten, K. B., Baum, H. R., & Rehm, R. G., Numerical Simulation of Smoke Plumes from large Oil fires, Atmospheric Environment, 30, p1, 1996.

Meneveau, C., Statistics of turbulence subgrid-scale stresses: Necessary conditions and experimental tests, Phys. Fluids 6 (2), p815, 1994.

Meneveau, C., & Katz, J., Dynamic testing of subgrid models in large eddy simulation based on the Germano identity, Phys. Fluids, 11(2), p245, 1999.

Meneveau, C., & Lund, T. S., Dynamic model with scale-dependent coefficients in the viscous range, Proc. Summer Program, Centre for Turbulence Research, NASA Ames/Stanford Univ., 1996.

Meneveau, C., Lund, T. S., & Cabot, W. H., A Lagrangian dynamic subgrid-scale model of turbulence, J. Fl. Mech., 319, p353, 1996.

Menon, S., & Kim, W.-W., High Reynolds Number Flow Simulations Using the Localized Dynamic Subgrid-Scale Model, AIAA Report 96-0425, 1996.

Metais, O. & Lesieur, M., Spectral large eddy simulations of isotropic and stably-stratified turbulence, J. Fluid Mech., 239, p157, 1992.

Mittal, R., Large-eddy simulation of flow past a circular cylinder, Annual Research Briefs, Centre for Turbulence Research, NASA Ames/Stanford Univ., 1995.

Moin, P., & Kim, J., Numerical investigation of turbulent channel flow, J. Fluid Mech., 118, p341, 1982.

Moin, P., Squires, W., Cabot, W., & Lee, S., A dynamic subgrid-scale model for compressible turbulence and scalar transport, Phys. Fluids A, 3(11), p2746, 1991.

Morton, B R, Taylor, G I, & Turner, J S, Turbulent gravitational convection from maintained and instantaneous sources, Proc. R. Soc. London A, 234, p1, 1956.

Murikami, S., Overview of turbulence models applied in CWE - 1997, J. Wind Engineering and Industrial Aerodynamics, 74-76, p1, 1998.

Najjar, F. M., & Tafti, D. K., Study of discrete test filters and finite difference approximations for the dynamic subgrid-scale stress model, Phys. Fluids, 8(4), p1076, 1996.

Najm, H.N., Wyckoff, P.S., & Knio, O..M., A Semi-Implicit Numerical Scheme for Reacting Flow. I. Stiff Chemistry, J. Comp. Phys., 143(2), p381, 1998.

Pantokratoras, A, Effects of ambient temperature on vertical buoyant water jets, Int. J. Heat Mass Transfer, 44, p1889, 2001.

Papanicolaou, P N, & List, E J, Investigation of Round Vertical Turbulent Buoyant Jets, J. Fluid Mech., 209, p151, 1988.

Paulucci, S., On the Filtering of Sound from the Navier-Stokes Equations, Sandia National Labs, Report SAND-82-8257, 1982.

Pera, L. & Gebhart, B., On The Stability Of Laminar Plumes: Some Numerical Solutions And Experiments, Int. J. Heat Mass Transfer, 14, p975, 1971.

Peng, S.-H., & Davidson, L., Large eddy simulation for turbulent buoyant flow in a confined cavity, Int. J. Heat Fluid Flow, 22, p323, 2001.

Piomelli, U., Large Eddy Simulation: Achievements and Challenges, Progress in Aerospace Sciences, 35, p335, 1999.

Piomelli, U., Cabot, W. H., Moin, P., & Lee, S., Subgrid-scale backscatter in turbulent and transitional flows, Phys. Fluids A, 3(7), p1766, 1991.

Piomelli, U., & Liu, J., Large-eddy simulation of rotating channel flows using a localized dynamic model, Phys. Fluids, 7(4) , p839, 1995.

Piomelli, U., Moin, P., & Ferziger, J., Large Eddy Simulation of the Flow in a Transpired Channel, AIAA Report 89-0375, 1989.

Pope, S. B., Turbulent Flows, Cambridge University Press, 2000.

Ragab, S. A., Sheen, S.-C., & Sreedhar, M., An investigation of Finite-Difference Methods for Large-Eddy Simulation of a Mixing Layer, AIAA Report 92-0554, 1992.

Rehm, R. G. & Baum, H. R., The Equations of Motion for Thermally Driven, Buoyant Flows, J. Res. Nat. Bur. Stand., 83, p297, 1978.

Rooney, G. G., & Linden, P F, Similarity considerations for non-Boussinesq plumes in an unstratified environment, J. Fluid Mech., 318, p237, 1996.

Rooney, G. G., & Linden, P. F., Strongly Buoyant Plume Similarity and 'Small-fire' Ventilation, Fire Safety Journal, 29, p235, 1997.

Sagaut, P., Large Eddy Simulation for Incompressible Flows: An Introduction, Springer-Verlag, Berlin, 2000.

Sagaut, P., Garnier, E., & Terracol, M., A general algebraic formulation for multi-parameter dynamic subgrid modelling, Int. J. Computational Fluid Dynamics, 13, p251, 2000.

Salvetti, M. V., & Banerjee, S., A priori tests of a new dynamic subgrid-scale model for finite-difference large eddy simulations, Phys. Fluids, 7 (11), 1995.

Sanderson, V. E., Turbulence Modelling of Turbulent Buoyant Jets and Compartment Fires, PhD Thesis, Cranfield University, 2001.

Schmidt H., & Schumann, U., Coherent Structure of the Convective Boundary Layer Derived from Large-Eddy Simulations, J. Fl. Mech., 200, p511, 1989.

Schumann, U., Subgrid-scale model for finite-difference simulations in plane channels and annuli, J. Comp. Phys., 18, p376, 1975.

Schumann, U., Realizability of Reynolds-stress turbulence models, Phys. Fluids, 20(5), p721, 1977.

Scotti, A., & Meneveau, C, Fractal model for coarse-grained nonlinear partial differential equations, Phys. Rev. Lett., 78(5), p867, 1997.

Scotti, A., Meneveau, C., & Lilly, D. K., Geralized Smagorinsky model for anisotropic grids, Phys. Fluids A, 5(9), p2306, 1993.

Shabbir, A. & George, W. K., Experiments on a round turbulent buoyant plume, J. Fluid. Mech., 275, p1, 1994.

Shabbir, A., & Taulbee, D. B., Evaluation of Turbulence Models for Predicting Buoyant Flows, J. Heat Trans, 112, p945, 1990.

Shah, K. B., Ferziger, J. H., A new non-eddy viscosity subgrid-scale model and its application to channel flow, Annual Research Briefs, Centre for Turbulence Research, NASA Ames/Stanford Univ., 1995.

Shang, X.-D., & Xia, K.-Q., Scaling of velocity power spectra in turbulent thermal convection, Physical Review E, 64, 065301, 2001.

Smagorinsky, J., General circulation experiments with the primitive equations, Mon. Weather Rev., 91, p99, 1963.

Spalart, P. R., Strategies for turbulence modelling and simulations, Int. J. Heat Fluid Flow, 21, p252, 2000.

Speziale, C. G., Galilean invariance of subgrid-scale stress models in the large-eddy simulation of turbulence, J. Fluid Mech., 156, p55, 1985.

Speziale, C., G., Turbulence modelling for Time-Dependent RANS and VLES: A Review, AIAA J., 36(2), p173, 1998.

Sweby, P. K., High Resolution Schemes using Flux Limiters for Hyperbolic Conservation Laws, SIAM J. Numer. Anal., 21(5), p995, 1984.

Taylor, G. I., Statistical theory of turbulence: Parts I-III, Proc. R. Soc. London Ser. A, 151, p421, 1935.

Turner, J. S., Buoyancy Effects in Fluids, Cambridge University Press, Cambridge, 1973.

Van der Ven, H., A Family of Large Eddy Simulation Filters with Nonuniform Filter Widths, Phys. Fluids, 7(5), p1171, 1995.

Versteeg, H. K., & Malalasekera, W., An Introduction to Computational Fluid Dynamics, the Finite Volume Method, Longmann Scientific & Technical, 1995.

Vreman, B., Guerts, B., & Kuerten, H., On the formulation of the dynamic mixed subgrid-scale model, Phys. Fluids, 6(12), p4057, 1994a.

Vreman, B., Guerts, B., Kuerten, H., Realizability conditions for the turbulent stress tensor in large-eddy simulation, J. Fluid Mech., 278, p351, 1994b.

Webb, A. T. & Mansour N. N., Towards LES of jets and plumes, Annual Research Briefs, Centre for Turbulence Research, NASA Ames/Stanford Univ., 2000.

Wilcox, D., Turbulence Modelling for CFD, DCW Industries, California, 1993.

Winckelmans, G. S., Wray, A. A., & Vasilyev, O. V., Testing of a new mixed model for LES: the Leonard model supplemented by a dynamic Smagorinsky model, Proc. Summer Program, Centre for Turbulence Research, NASA Ames/Stanford Univ., 1998.

Woods, A. W., A note on non-Boussinesq plumes in an incompressible stratified environment, J. Fluid Mech., 345, p347, 1997.

Wong, V. C., A proposed statistical-dynamic closure method for the linear or nonlinear subgrid-scale stresses, Phys. Fluids A, 4(5), 1992.

Wong, V. C., & Lilly, D, K., A comparison of two dynamic closure methods for turbulent thermal convection, Phys. Fluids, 6(2), 1994.

Worthy, J., Sanderson, V., & Rubini, P. A., Comparison of Modified k-ε Turbulence Models for Buoyant Plumes, Num. Heat Transfer, Part B, 39, p151, 2001.

Xia, K.-Q., & Qiu, X.-L., Turbulent convection with 'disconnected' top and bottom boundary layers, Europhysics Letters, 46(2), p171, 1999.

Yanagita, T., & Kaneko, K., Rayleigh Benard Convection. Patterns, chaos, spatiotemporal chaos and turbulence, Physica D, 82, p288, 1995.

Yoshizawa, A., A statistically-derived subgrid model for the large-eddy simulation of turbulence, Phys. Fluids, 25(9), p1532, 1982.

Zang, Y., Street, R. L., & Koseff, J. R., A dynamic mixed subgrid-scale model and its application to turbulent recirculating flows, Phys. Fluids A, 5(12), p3186, 1993.

Zhang, J., Acceleration of Five-Point Red-Black Gauss-Seidel in Multigrid for Poisson Equation, Applied Mathematics and Computation, 80, p73, 1996.

Zhang, W., Chen, Q., Large Eddy Simulation of Natural and Mixed Convection Airflow Indoors with Two Simple Filtered Dynamic Subgrid Scale Models, Num. Heat Transfer, Part A, 37, p447, 1999.

Zhang, W., Chen, Q., Large eddy simulation of indoor airflow with a filtered dynamic subgrid scale model, I. J. Heat Mass Transfer, 43, p3219, 2000.

Zhou, S.-Q., & Xia, K.-Q., Scaling properties of the temperature field in convective turbulence, Physical Review Letters, 87(6), 064501, 2001.

Zhou, X., Luo, K. H., & Williams, J. J. R., Large-eddy simulation of a turbulent forced plume, Eur. J. Mech. B – Fluids, 20, p233, 2001.